

NOTE TO USERS

This reproduction is the best copy available.

UMI[®]



**A NOVEL HYDROGEL BASED PIEZORESISTIVE
PRESSURE SENSOR PLATFORM
FOR CHEMICAL SENSING**

by

Michael P. Orthner

A dissertation submitted to the faculty of
The University of Utah
in partial fulfillment of the requirements for the degree of

Doctor of Philosophy

Department of Electrical and Computer Engineering

The University of Utah

May 2010

UMI Number: 3406171

All rights reserved

INFORMATION TO ALL USERS

The quality of this reproduction is dependent upon the quality of the copy submitted.

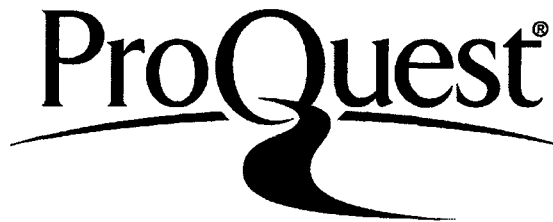
In the unlikely event that the author did not send a complete manuscript and there are missing pages, these will be noted. Also, if material had to be removed, a note will indicate the deletion.



UMI 3406171

Copyright 2010 by ProQuest LLC.

All rights reserved. This edition of the work is protected against unauthorized copying under Title 17, United States Code.



ProQuest LLC
789 East Eisenhower Parkway
P.O. Box 1346
Ann Arbor, MI 48106-1346

Copyright © Michael P. Orthner 2010

All Rights Reserved

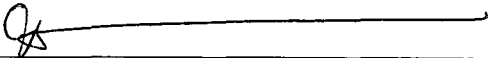
THE UNIVERSITY OF UTAH GRADUATE SCHOOL


SUPERVISORY COMMITTEE APPROVAL

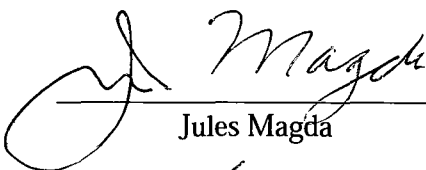
of a dissertation submitted by

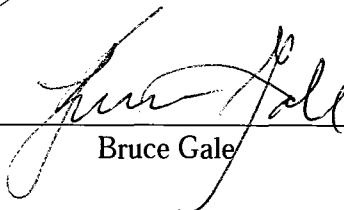
Michael P. Orthner

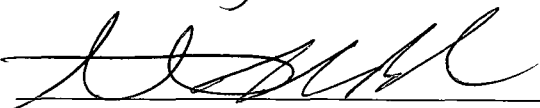
This dissertation has been read by each member of the following supervisory committee and by majority vote has been found to be satisfactory.

_____ 
Chair: Florian Solzbacher

_____ 
Loren Rieth

_____ 
Jules Magda

_____ 
Bruce Gale

_____ 
Steve Blair

THE UNIVERSITY OF UTAH GRADUATE SCHOOL

FINAL READING APPROVAL

To the Graduate Council of the University of Utah:

I have read the dissertation of Michael P. Orthner in its final form and have found that (1) its format, citations, and bibliographic style are consistent and acceptable; (2) its illustrative materials including figures, tables, and charts are in place; and (3) the final manuscript is satisfactory to the supervisory committee and is ready for submission to The Graduate School.

03/30/2010

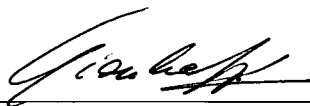
Date



Florian Solzbacher

Chair: Supervisory Committee

Approved for the Major Department



Gianluca Lazzi

Chair/Dean

Approved for the Graduate Council



Charles A. Wight

Dean of The Graduate School

ABSTRACT

New hydrogel-based micropressure sensor arrays for use in the fields of chemical sensing, physiological monitoring, and medical diagnostics are developed and demonstrated. This sensor technology provides reliable, linear, and accurate measurements of hydrogel swelling pressures, a function of ambient chemical concentrations. For the first time, perforations were implemented into the pressure sensors piezoresistive diaphragms, used to simultaneously increase sensor sensitivity and permit diffusion of analytes into the hydrogel cavity.

It was shown through analytical and numerical (finite element) methods that pore shape, location, and size can be used to modify the diaphragm mechanics and concentrate stress within the piezoresistors, thus improving electrical output (sensitivity). An optimized pore pattern was chosen based on these numerical calculations.

Fabrication was performed using a 14-step semiconductor fabrication process implementing a combination of potassium hydroxide (KOH) and deep reactive ion etching (DRIE) to create perforations. The sensor arrays (2×2) measure approximately 3 × 5 mm² and used to measure full scale pressures of 50, 25, and 5 kPa, respectively. These specifications were defined by the various swelling pressures of ionic strength, pH and glucose specific hydrogels that were targeted in this work.

Initial characterization of the sensor arrays was performed using a custom built bulge testing apparatus that simultaneously measured deflection (optical profilometry),

pressure, and electrical output. The new perforated diaphragm sensors were found to be fully functional with sensitivities ranging from 23 to 252 $\mu\text{V}/\text{V-kPa}$ with full scale output (FSO) ranging from 5 to 80 mV.

To demonstrate proof of concept, hydrogels sensitive to changes in ionic strength were synthesized using hydroxypropyl-methacrylate (HPMA), N,N-dimethylaminoethyl-methacrylate (DMA) and a tetra-ethyleneglycol-dimethacrylate (TEGDMA) crosslinker. This hydrogel quickly and reversibly swells when placed environments of physiological buffer solutions (PBS) with ionic strengths ranging from 0.025 to 0.15 M. Chemical testing showed sensors with perforated diaphragms have higher sensitivity than those with solid diaphragms, and sensitivities ranging from 53.3 ± 6.5 to 271.47 ± 27.53 mV/V-M, depending on diaphragm size. Additionally, recent experiments show sensors utilizing Ultra Violet (UV) polymerized glucose sensitive hydrogels respond reversibly to physiologically relevant glucose concentrations from 0 to 20 mM.

FOR MY FAMILY, FRIENDS, AND
LATE FATHER DR. HELMUTH F. ORTHNER

TABLE OF CONTENTS

ABSTRACT.....	iv
LIST OF TABLES.....	xi
LIST OF FIGURES	xii
ACKNOWLEDGEMENTS.....	xx
1. INTRODUCTION	1
1.1 Motivation.....	1
1.2 References.....	13
2. STATE OF THE ART: BIOSENSORS, HYDROGELS AND PIEZORESISTIVE PRESSURE SENSORS	16
2.1 Biomedical Sensors.....	16
2.2 Hydrogels.....	18
2.2.1 Polymer Solvent Mixing Pressure ($\Delta\pi_{\text{mixing}}$)	20
2.2.2 Hydrogel Elasticity ($\Delta\pi_{\text{elastic}}$)	21
2.2.3 Ionic Osmotic Force ($\Delta\pi_{\text{ionic}}$).....	22
2.2.4 Summary	22
2.3 Stimuli Response Hydrogels (pH, ionic strength, glucose).....	22
2.3.1 pH and Ionic Strength Sensitive Hydrogels.....	23
2.3.2 Phenylboronic Acid Based Hydrogels.....	23
2.3.3 Summary.....	24
2.4 State of the Art Hydrogel Based Sensors.....	25
2.4.1 Mechanical Measurements	25
2.4.2 Oscillating Sensor Measurements.....	28
2.4.3 Conductometric Measurements	29
2.4.4 Amperometric Measurements.....	29
2.4.5 Optical Measurements	29
2.4.6 Summary	31
2.5 Piezoresistive Sensors.....	33
2.6 Piezoresistivity.....	33
2.6.1 Transverse and Longitudinal Piezoresistive Coefficients.....	35
2.6.2 Micropressure Sensors (bending plate sensors).....	38
2.7 The Wheatstone Bridge	39
2.7.1 Temperature Compensation.....	40
2.8 Sensor Definitions.....	41
2.8.1 Dynamic Range.....	41
2.8.2 Sensitivity	42
2.8.3 Full-scale Output and Linearity	42

2.8.4	Temperature Coefficient of Sensitivity.....	42
2.8.5	Temperature Coefficient of Offset.....	43
2.8.6	Summary.....	43
2.9	References.....	44
3.	HIGH SPEED WAFER SCALE BULGE TESTING FOR THE DETERMINATION OF THIN FILM MECHANICAL PROPERTIES	50
3.1	Abstract.....	50
3.2	Introduction.....	51
3.3	Experimental.....	54
3.3.1	Bulge Testing System	54
3.3.2	Membrane Preparation.....	56
3.3.3	Testing Methods	58
3.4	Results and Discussion	58
3.4.1	Analytical Model	58
3.4.2	Computer Simulations	60
3.4.3	Empirical Measurements	62
3.4.4	Estimation of Young's Modulus.....	66
3.5	Conclusions.....	70
3.6	References.....	71
4.	DESIGN, SIMULATION AND OPTIMIZATION OF NOVEL PIEZORESISTIVE PRESSURE SENSORS WITH STRESS SENSITIVE PERFORATED DIAPHRAGMS FOR HYDROGEL APPLICATIONS	74
4.1	Abstract.....	74
4.2	Introduction and Device Principal	75
4.3	Design Methods	78
4.4	Sensor Architecture.....	78
4.4.1	Finite Element Models.....	81
4.4.2	Sensing Diaphragm Optimization.....	83
4.4.3	Pore Shape	84
4.4.4	Pore Location.....	85
4.4.5	Pore Diameter	88
4.5	Results Piezoresistor Optimization and Performance.....	93
4.6	Conclusions.....	101
4.7	References.....	103
5.	DEVELOPMENT, FABRICATION, AND CHARACTERIZATION OF PIEZORESISTIVE PRESSURE SENSORS USING PERFORATED DIAPHRAGMS FOR HYDROGEL SENSING.....	107
5.1	Abstract.....	107
5.2	Introduction.....	109
5.3	Sensor Design and Fabrication	111
5.3.1	Oxidation and Implantation	112
5.3.2	Insulation and Metallization	115
5.3.3	Passivation and Pore Etching.....	115
5.3.4	Dicing.....	116

5.4	Sensor Bulge Testing Apparatus.....	116
5.5	Experimental Methods.....	119
5.6	Results and Discussion	121
	5.6.1 Mechanical Deflection.....	121
5.7	Electrical Response.....	126
5.8	Conclusions.....	131
5.9	References.....	133
6.	HYDROGEL BASED PIEZORESISTIVE SENSOR ARRAYS (2×2) WITH PERFORATED DIAPHRAGMS FOR METABOLIC MONITORING (IN-VITRO)	137
6.1	Abstract.....	137
6.2	Introduction.....	139
6.3	Sensor Assembly.....	142
	6.3.1 Sensor Dies	142
	6.3.2 HPMA/DMA/TEGDMA Hydrogels	144
	6.3.3 Backing Plates.....	146
	6.3.4 Wire Bonding.....	147
	6.3.5 Sensor Passivation	147
6.4	Testing Apparatus	148
6.5	Experimental Methods.....	149
6.6	Results and Discussion	150
	6.6.1 Sensitivity	150
	6.6.2 Response Time.....	154
	6.6.3 Stability.....	159
6.7	Conclusions.....	161
6.8	References.....	163
7.	SYNOPSIS OF RESULTS, CONCLUSIONS, AND FUTURE WORK	166
7.1	Overview.....	167
7.2	High Speed Wafer Scale Bulge Testing for the Determination of Thin Film Mechanical Properties.....	168
7.3	Design, Simulation and Optimization of Novel Piezoresistive Pressure Sensors with Stress Sensitive Perforated Diaphragms for Hydrogel Applications.....	169
7.4	Development, Fabrication, and Characterization of Hydrogel Based Piezoresistive Pressure Sensors with Perforated Diaphragms	170
7.5	Hydrogel Based Sensor Arrays (2×2) with Perforated Piezoresistive Diaphragms for Metabolic Monitoring (in-vitro).....	171
7.6	Comparison of Specifications, Simulations, and Empirical Results	172
7.7	Future Work.....	173
	7.7.1 Hydrogels.....	175
	7.7.2 Sensor Design and Manufacturing.....	176
	7.7.3 Passivation/Encapsulation	178
	7.7.4 In-Vivo Testing.....	178

APPENDICES

DESIGN AND PERFORMANCE OF AN LPCVD REACTOR FOR
THE GROWTH OF 3C-SILICON CARBIDE..... 180

EXAMPLE COMSOL CODE FOR PERFORATED DIAPHRAGM SIMULATIONS
..... 187

LIST OF TABLES

1.1. Tradeoffs of several current glucose sensing technologies and hydrogel based glucose sensors.	7
2.1. Comparison of different hydrogel sensing technologies based on [1].....	32
3.1. Initial design specifications of the bulge testing system.	53
3.2. Material parameters used in Comsol 3.3 finite element simulations.....	61
4.1. Hydrogel swelling properties and sensor design specifications. The hydrogel properties were measured using a calibrated pressure sensor coupled to hydrogels under isochoric conditions. The experimental setup for measuring the hydrogel properties is found in [16]. The bottom portion of the table describes the desired perforated diaphragm sensors specifications.....	79
4.2. Min, max and average normal stress developed in the longitudinal and transverse piezoresistors in the three principal directions at an applied pressure of 150 kPa.	98
7.1. Comparison of specified and actual device properties measured using bulge and chemical testing.	174
A.1. Initial performance specifications of the LPCVD reactor used for growth of 3C-SiC on Si.	181
A.2. Experimental plan describing the variation of processing parameters used for 3C-SiC growth. Four variables were studied including the temperature, pressure, flow rate, and precursor concentrations.	182
A.3. Quantified atomic concentrations (XPS) taken from 3C-SiC grown at 1325°C (300 mTorr) with a precursor concentration of 1.16% and total flow rate of 860 sccm. The C:Si ratio was 2.46 and 1.21 on the surface and after ion etching. All films appeared to be carbon rich.	185

LIST OF FIGURES

1.1. Conceptual depiction of the hydrogel based chemical sensor array and integrated electronics for detection of glucose, CO ₂ , ionic strength and pH.	10
2.1. Directions of the electric field E , the current density j , and the applied stresses for a (a) transverse and (b) longitudinally stressed piezoresistors.	37
2.2. Schematic showing the result of applied pressure on a Wheatstone bridge. Typically, two piezoresistors increase in resistance while the other two decrease, depending on orientation and semiconductor type.	39
2.3. Resistors within the Wheatstone bridge all increase with the same ΔR at increased temperatures. Therefore the output voltage (V_0) remains constant and the bridge is temperature compensated.	41
3.1. Photograph of the wafer mounting stage used for bulge testing of silicon nitride-aluminum membranes. Wafers ranging in size from 50 to 150 mm can be mounted while pressure is applied to the backside of the membranes.	54
3.2. Displacement plot illustrating a deflection of 2.68 μm for a quarter of the 1200 \times 1200 μm^2 square membrane calculated using finite element analysis at a pressure of 6894 Pa (1 PSI). The composite structure consists of 720 nm of silicon nitride with 20 nm of aluminum. The bottom and right edges are fixed (clamped) and a symmetry boundary condition placed on the left and top sides.	61
3.3. Height data displayed as (a) 3D plot, (b) solid plot and (c) surface plot from the Zygo Newview 5032 optical pyrometer. This membrane is 1.2 mm length and a laminate structure consisting of 720 nm of Si ₃ N _{4-x} and 20 nm of aluminum loaded at 6894 Pa (1 PSI).	62
3.4. Comparison of the theoretical, simulated, and measured deflection of diaphragms with widths of (A) 350 μm (B) 550 μm and (C) 1200 μm at applied pressures ranging from 689 Pa (0.1 PSI) to 6894 Pa (1.2 PSI). Figure 3.4D shows that standard deviation between measurements is a function of pressure and diaphragm sensitivity. At elevated pressures the standard deviation between measurements is reduced and larger diaphragms are more sensitive and susceptible to minute pressure fluctuations.	64

3.5. Deflection measurements taken for samples located on the left, right and center wafer at a pressure of 6.2 kPa (.9 PSI) (a) and comparison of the measured (-----), simulated(- - -), and analytical (•) deflection of a 1200×1200 μm ² square silicon nitride-aluminum membrane with load ranging from 689 to 6.2 kPa (0.1 to 0.9 PSIG) (b). Analytical and simulated results show little variation.	65
3.6. Calculation of Young’s modulus using equation 1 for diaphragms with widths of 350, 550 and 1200 μm over a pressure range of 0 to 8.5 kPa (0 to 1.23 PSIG). Using this technique calculated values became nonsensical for diaphragms with smaller widths (350 and 550 μm) and at lower pressures (<5 kPa). This is due to the higher measurement variability attributed to reduced pressure control and limitations of instrument resolution. The submicron deflections of the smaller diaphragms lead to higher measurement uncertainty and large variations in young modulus calculations.	67
3.7. Fit of analytical solution (equation 23) to the pressure deflection data for the (a) 350 (b) 550 μm and (c) 1200 μm wide diaphragms. Results show that the system is incapable of resolving the minute nonlinear deflection of the smaller diaphragms with accuracy needed to calculate Young’s modulus. The larger diaphragms have higher nonlinear deflections in micron range and give an estimate of 454 GPa for the Young’s modulus. 69	
4.1. Transduction mechanism utilized in hydrogel based piezoresistive chemical sensors. Environmental changes cause hydrogel swelling creating elevated pressure within the sensor cavity. The diaphragm deflection causes elevated stress to be developed within the piezoresistors whilst the output voltage is maximized though the use of a Wheatstone bridge.	76
4.2. CAD rendering of the hydrogel based pressure sensor designs utilizing analyte diffusion channels that are located within the (a) backside mounting plate and (b) directly in the sensing diaphragm. The design on the left is the previously reported sensor architecture used for detecting hydrogel swelling pressure while the design on the right is novel and implements diffusion pores directly into the diaphragm.	78
4.3. Sensitivity plotted as a function of diaphragm width and thickness for square solid silicon pressure sensors.	81
4.4. Simulated Von Mises stress distribution in a quarter of a 1.0 × 1.0 mm ² square silicon membrane with 30 μm (a) hexagonal, (b) triangular, (c) round, and (d) square pores. Stresses are 2.93X higher in the square pores than in round pores. The highest Von Mises stress is found in the top right pore closest to the diaphragm center as indicated by the arrow.	85

4.5. Von Mises stress distribution of one quarter of a $1.5 \times 1.5 \text{ mm}^2$ diaphragms under a load of 150 kPa. Fixed boundary conditions (BC) are placed on the front two planes representing the edge of the diaphragm while symmetry BCs are placed on the planes located on the inside of the diaphragm (out of view). It is shown that the geometry of diaphragm perforations impacts the stress distribution within the diaphragm while loaded from the backside with 150 kPa. Through manipulation of pore geometry the stress in the piezoresistor locations can be increased. 87

4.6. Deflection of the $1.5 \times 1.5 \text{ mm}^2$ diaphragms with x100 (left) and x52 (right) pores per quarter diaphragm with respect to diaphragm position (x). Pressures from 5 to 500 kPa were applied to the bottom of the diaphragms and plotted. Deflection is higher while piezoresistor stresses are lower for designs with high densities of pores (left). 89

4.7. Normal stress (a,c) perpendicular (S_{nx}) and (b,d) parallel (S_{ny}) to the diaphragm edge. Stresses are calculated as a function of hole size across the (a,b) diaphragm midplane at a pressure of 150 kPa. In (c,d) stresses are calculated at a spacing of $25 \mu\text{m}$ from the diaphragm edge an applied pressure of 5-150 MPa. It was determined that large pores ($40\mu\text{m}$) with a small pitch ($50\mu\text{m}$) do not provide the diaphragm with the mechanical strength needed to develop stresses within the piezoresistors. The large amount of open area in the diaphragm ultimately allows the diaphragm shape to deform. 91

4.8. Finite element results exhibiting Von Mises stress developed in diaphragms with (a) $10 \mu\text{m}$ and (b) $40 \mu\text{m}$ pores. Simulations indicate that as the pores become larger, high tensile stresses are developed in the regions between pores towards the center of the diaphragm. Larger pores and open areas create diaphragms with higher stress and a higher probability of failure. 92

4.9. Influence of pore geometry on piezoresistor stress. (a) Normal compressive stress (S_{nx}) in the piezoresistors located on the topside of the diaphragm $25 \mu\text{m}$ from the diaphragm edge. A load of 150 kPa was applied to the backside of the diaphragm and determined using finite element analysis of designs shown in Figure 4.5. The geometry and location of the pores is used to increase stress in piezoresistors and hence sensor sensitivity. (b) CAD model of the final pore geometry located in a $1.5 \times 1.5 \text{ mm}^2$ diaphragm with $10\mu\text{m}$ thickness. Simulations on were used to optimize the final geometry by modeling one quarter of the diaphragm and using symmetry. 93

4.10. Normal stress distribution (S_{nx}) of the $1.0 \times 1.0 \text{ mm}^2$ 52 pore diaphragm with applied load of 150 kPa. (b) Normal stress distribution (S_{nx}) perpendicular to the diaphragm edge for the $1.0 \times 1.0 \text{ mm}^2$ diaphragms with various pore geometries shown in Figure 4.5. Stress in the piezoresistor regions can be influenced by the pore characteristics. The stress developed in the piezoresistor regions for the 100 pored diaphragm is significantly reduced. 95

4.11. Average normal stresses induced in the longitudinal (left) and transverse (right) piezoresistors as a function of length at an applied pressure of 150 kPa using the $1.0 \times 1.0 \text{ mm}^2$ diaphragm (top). The normal stress (S_{nx}) varies from $>300 \text{ MPa}$ close to the edge to $<150 \text{ MPa}$ moving $75 \text{ }\mu\text{m}$ towards the inside of the diaphragm. This stress gradient is used for calculating the sensitivity of the various sensor designs.	97
4.12. Average normal stresses (a, c, e) perpendicular (S_{nx}) and (b, d, e) parallel (S_{ny}) to the diaphragm edge in the (a,b) longitudinal and (c-e) transverse piezoresistor pairs. Piezoresistors are represented by the black rectangles and arrows represent normal stress in a particular direction. Due to symmetry the longitudinal resistors have the same normal stress while the transverse piezoresistors are dependent on location.	99
4.13. Change in resistance ($\Delta R/R$) of the (a) longitudinal and (b) transverse <i>p</i> -type piezoresistor pairs as a function of applied pressure for design shown in Figure 4.5e with widths of 0.5, 1.0, 1.25, and 1.5 mm and $30\mu\text{m}$ pores. It was determined that the longitudinal resistors have a slightly higher $\Delta R/R$	101
4.14. Porous diaphragm sensor output characteristics describing the (a) output voltage and (b) sensitivity as a function of pressure and diaphragm width. All diaphragms in this model use the design shown in Figure 4.5e with $30 \text{ }\mu\text{m}$ pores with and thickness of $10\mu\text{m}$	102
5.1. CAD mask layout showing the various sensors designs. Sensors with and without perforated diaphragms were fabricated as individual sensors and part of an array. An enlarged image of the $1 \times 1 \text{ mm}^2$ perforated (pores= $30 \text{ }\mu\text{m}$) diaphragm pressure sensor is shown on the right. This optimized pore geometry reduces the stress located within the pores, maintains high stress within the piezoresistors, while maintaining the diaphragm mechanical integrity. An enlargement of the transverse piezoresistor pair is shown below the $1 \times 1 \text{ mm}^2$ sensor magnification.....	113
5.2. Fourteen-step fabrication processes used to manufacture the perforated diaphragm pressure sensors.	114
5.3. Images of the fabricated sensors. (a) Nomarski contrast optical micrograph of the $1.0 \times 1.0 \text{ mm}^2$ perforated diaphragm sensor illustrating the pores after wet etching but before DRIE. (b) Scanning electron microscope image of $1.25 \times 1.25 \text{ mm}^2$ perforated diaphragm sensor before DRIE. (c,d) SEM images of sensors post DRIE.	117
5.4. Illustrated is the CAD design and photographs of the bulge testing apparatus used to measure applied pressure, sensor electrical output, and diaphragm deflection. (a) CAD layout of testing stage. (b) The sensor testing stage is mounted to the optical profilometer. (c) Four sensors are simultaneously mounted to the stage for testing and (d) wire bonded to the PCB board.	118

5.5. Large oscillations were observed in the deflection measurements if pressure fluctuations were present during testing. These pressure fluctuations were found to be caused by N ₂ leaking from the bottom side of the sensors when not properly bonded with dicing wax to the mounting plate.....	121
5.6. Plots of the bulged diaphragm surface for the 1.25×1.25 mm perforated diaphragm (pores = 10 μm) at pressures up to 65.1 kPa. Surface plots (a-f) are shown and exported deflection data along the center of the diaphragm and plotted in relation to position (g). Compressive stress within the passivation layers caused the diaphragm to bulge downward with no applied pressure.	123
5.7. Surface plots recorded during bulge testing of diaphragms with (a)10 μm (b) 30 μm and (c) 40 μm pores at 150 kPa. Data were exported along the center of the diaphragm and (d) plotted in comparison to simulations results. Empirical and simulated results are similar and show that deflection of the diaphragm with 30 μm pores is the largest.	124
5.8. Micrograph of 1×1 mm ² sensor and electrical output voltages determined from bulge testing. (a) Optical micrograph of the 1×1 mm ² (pores = 20μm) with bond pads labeled. (b-f) Sensor outputs for both perforated and solid diaphragm sensors at a supply voltage of 5V. Results show that the sensors behave linearly within this pressure regime and the largest sensors have the highest sensitivities.	127
5.9. Sensitivity of the different diaphragm designs as a function of (a) pore diameter and (b) percentage of open area. The incorporation of pores reduced the sensitivity of sensors. Diaphragms with pores=40μm in diameter had higher sensitivity than other perforated designs with smaller diameter pores. This is due to a modified stress distribution across the piezoresistors.	128
5.10. Elevated pressure (~200kPa) linearity test performed on the 1.5×1.5 mm ² diaphragms with (a) solid (b) 10μm and (c) 40 μm pores. Perforated sensors show higher linearity since pores reduce stiffness of the diaphragm leading to larger geometrical elongation and deformation.	130
6.1. CAD rendering of the hydrogel based pressure sensor designs utilizing analyte diffusion channels that are located within the (a) backside mounting plate and (b) within the diaphragm.	141
6.2. Optical (a) and SEM (b) micrographs of perforated diaphragm pressure sensor array. Inset on left shows a (SEM) micrograph of one of the 1×1 mm ² sensors while (b) shows pores (d=40μm) etched into one quarter of the 1×1 mm ² sensor diaphragm.	143
6.3. Photograph of the HPMa/DMA/TEGDMA hydrogel on glass slide before sample cutting and insertion into the sensors.....	145

6.4. SEM micrograph of the deep reactive ion etched (DRIE) porous backing plate (5×5 mm ²) with pore diameter of 125 μm and a pitch of 200 μm. Shading is indicative of a surface not being completely planar due to this particular wafer being thinned using KOH. The backing plates used for testing do not exhibit this characteristic.....	146
6.5. Photograph of topside of a solid diaphragm sensor assembly with hydrogel inserted and mounted to a perforated backing plate (out of view). Wire bonding was performed using gold insulated wire (d=50 μm). The entire assembly, wires, and PCB are ready for parylene deposition.	149
6.6. Photograph of the testing apparatus used to determine sensor electrical output characteristics. The sensors were placed in solutions of varying ionic strength and the voltage output was simultaneously measured.....	150
6.7 Photographs of sensor assembly post parylene deposition with insulated wires (a) sutured together for additional strength and placed in (b) experimental bottle for chemical testing of ionic strength. The parylene delamination was caused by tape adhesion testing.	151
6.8. Output data used for the calculation of sensitivity for the (a) solid and (b) perforated diaphragm pressure sensors. The perforated diaphragm sensors have a higher sensitivity and larger output for identical environmental testing conditions.	152
6.9. Comparison of sensitivities for perforated diaphragm and solid diaphragm sensors placed in 0.025 and 0.075 M PBS solutions. Perforated diaphragm sensors were more sensitive for all sensors in the array.....	153
6.10. Sensor responses during the first five cycles of testing between 0.15 and 0.025 M PBS solution concentrations (a-d). Exponential fits of (b) cycle 1 (c) cycle 2 and (d) cycle 5 for the swelling and contracting half cycles. Data show the initial cycles have the smallest and slowest response.....	156
6.11. Plot of the calculated time constants (τ) with respect to the first five cycles for the two sensor types. The sensors response time shows significant improvement after an initial conditioning period. Response times for the various sensor types are similar....	158
6.12. Swelling and contracting time constants calculated for the various sized perforated diaphragm sensors within the array after conditioning. The sensors were cycled from 0.15 to 0.025 M PBS and the smaller diaphragms had faster response.....	159
6.13. Plot illustrating the long term stability of the 1.25×1.25 mm ² perforated backing plate sensor with 125 μm pores. The sensor was cycled between 0.15 and 0.025M PBS concentrations and although the sensor responded to changes in ionic strength for ~400 hours it the baseline drifted significantly.....	161
7.1. Proposed SOI wafer perforated diaphragm sensor fabrication procedure.....	177

A.1. Photographs of the (a) double walled 304 stainless steel vacuum chamber, graphite heat shields, and sample holder. Figure (b) shows the chamber lid with the attached graphite heater. Solidworks rendering of the (c) SiC-LPCVD reactor hotzone. The resistive heater is located 25 mm above the rotating sample holder and capable of temperatures >1500 °C. Six 2" wafers can be loaded in the chamber simultaneously. A series of graphite heat shields are used to isolate temperatures to the growth zone.....	182
A.2. (a) Growth rate dependence of the 3C-SiC layers grown at temperatures from 750 to 1325°C. From 1025°C to 1225°C the reaction is strongly temperature dependent and kinetically controlled. The slope of the growth rate with respect to temperature becomes smaller between 1225°C and 1325°C indicating that mass transport was the limiting growth mechanism. (b) Arrhenius plot used to determine an activation energy of 21.5 kcal mol ⁻¹ and 2.15kcal mol ⁻¹ for the kinetic and mass transport limited regimes of the 3C-SiC growth.	183
A.3. Growth rate dependence on (a) pressure and (b) volumetric gas flow rate of 3C-SiC films grown at 1325 °C for 30 minutes. Pressure increase from 300 to 700 mTorr decreased growth rate from 16.9 to 11.4 nm/min respectively. An increase in flow rate from 172 to 860 sccm increased growth rate from 14.3 to 17.6 nm/min.....	183
A.4. Precursor concentration influence on growth rate at 1325°C (300 mTorr) using a total precursor flow of 860 sccm. Increased concentration from 1.16 to 4.63% increased growth rate from 17.7nm/min to 19.7nm/min. A large number of voids are found at the interface of the film and substrate at concentrations >1.16 %.....	183
A.5. SEM images of SiC surface morphology on Si (100) substrates using propane, silane and H ₂ at (a) 1025°C (b) 1125°C (c) 1225°C and (d) 1325°C. Increasing growth temperatures lead to larger more rectangular 3C-SiC crystals	184
A.6. XRD spectra of 3C-SiC films grown at temperatures from 1025 to 1325°C at 300 mTorr with flows of 5 sccm SiH ₄ and C ₃ H ₈ and 850 sccm of H ₂ . Two distinct peaks are present the strained silicon substrate peak (200) and the 3C-SiC (200) at 33.3° and 41.4°, respectively	184
A.7. XRD spectra of 3C-SiC films deposited at pressures and flows ranging from 300 to 700 mTorr and 170 to 860 sccm, respectively. At 300 mTorr the flow rate had a large impact on the (200) 3C-SiC peak while pressure played a less influential role	184
A.8. XPS survey spectrum of sample grown at 1325°C (300 mTorr) at a 1.16% precursor concentration for 30 minutes. The scan was from 1200 to 0 eV using monochromatic Al K α line X-ray source	184
A.9. Carbon 1s peaks shown on the (a) surface and (c) after 240s of Ar etching (<20nm). Silicon 1p peak is shown shifting from (b) 100.9 eV on the surface to (d) 100.3 eV after etching indicating an increase of Si-C bonding	185

A.10. XPS spectra showing surface contamination of the (a) F 1s and (b) O 1s peaks. Sputter etching for 4 minutes significantly reduced the contamination levels detected, suggesting these were surface contaminants 185

A.11. SEM micrographs of voids found at the 3C-SiC/Si interface for films grown at (a) 1125°C (b) 1225°C and (c,d) 1325°C under various growth conditions 186

A.12. SEM micrographs of samples grown at precursor concentration of 4.63% and at temperatures of (a) 1225°C and (b) 1325°C. These deposition conditions caused (a) gas phase nucleation with modified growth sites and (b) films that were highly defective with surface voids protruding into the substrate..... 186

ACKNOWLEDGEMENTS

Many people have helped me throughout my academic career, to whom I am greatly indebted. First and foremost, I have to acknowledge Dr. Florian Solzbacher and Dr. Loren Rieth for their hard work and dedication to making me a better scientist, engineer, and researcher. I also appreciate their friendship which will last a lifetime. I would like to thank the rest of my committee members Dr. Jules Magda, Dr. Bruce Gale, and Dr. Steve Blair, for their suggestions and insightfulness. Gratitude must be shown to affiliates and past/present members of Dr. Solzbacher's research group (Erik, Michael, Jui-Mei, Sohee, Xiao, Sri, Hannwelm, Raj, Sandeep, Rohit, Prashant, and Mahender) who helped make my time enjoyable and who proved excellent sources of both advice and helpful criticism. I owe you all many thanks. Mr. Dennis Romney I am truly appreciative for all your help with my many projects over the course of the years, the great conversations, and making me laugh; you will not be forgotten.

My family and friends have always played a major role in my life and for this reason I dedicate my thesis to them, especially my late father Dr. Helmuth F. Orthner and great uncle Dr. Hans Gritch. I know you would be proud. Mom you have always pushed me to live up to my potential and are a role model whom I've always tried to emulate. Rea and Jeff (and Eva) thanks for always being there for me.

To the love of my life Shea, I am enormously grateful for your constant support, especially through the tough times during the last year. I will always do my best to return your selfless devotion.

CHAPTER 1

INTRODUCTION

1.1 Motivation

The rapid increase of complex automated systems for chemical process control, pharmaceuticals, automotive and biomedical applications requires reliable, robust, low cost sensors. According to recent market analysis of the microelectromechanical (MEMS) and microsystems fields, chemical sensors for medical diagnostics is one of the most rapidly growing market sectors [2]. In the United States demand for chemical sensors is projected to surpass \$5 billion by 2012 from < \$1 billion today [3]. Biosensors will continue to be the largest and fastest growing segment of chemical sensors. A need exists to develop less invasive continuous real time physiological monitoring systems [4]. Driving factors to be considered when designing and developing biosensors for use in medical diagnostic applications include [5, 6]:

- (a) Reducing the risk, complications, and side effects of taking the measurement and/or discomfort of the measurement to the patient. Improve quality of life.
- (b) Increasing speed, frequency, and accuracy of measurements, ideally taking them continuously throughout the day. This enables physicians to make better diagnoses through the use of comprehensive data sets.

- (c) Reducing the measurement complexity allowing self-monitoring by patients in their normal environment. This will decrease overall patient costs by enabling outpatient care.
- (d) Making minimum impact on the patient's lifestyle.
- (e) Decreasing overall cost.

One example of this segment is the field of metabolic sensors (for pH, pCO₂, glucose, etc.) required for the monitoring of metabolic disorders, such as obesity and diabetes. While the goal of this work was not to directly create a glucose sensor, the treatment of diabetes is a prime example of where improved sensor technology would make considerable improvements to the quality of life for millions of people worldwide. Although the sensors resulting from this work are currently being used to measure glucose concentrations in vitro, the primary goal was to develop a sensor platform that could be used for the detection of a wider range of analytes.

It is useful to briefly describe diabetes as a case study and discuss a number of current technologies used for glucose measurement, then compare advantages and disadvantage of these various technologies to the proposed sensor platform. Diabetes describes a category of metabolic diseases described by inadequate control of sugar levels (glucose). In people without diabetes, the blood glucose concentration is usually in the 70 to 120 mg/dL range or approximately 4 to 8 mM. These levels are often much higher for diabetics due to the body's inability to process sugars properly which can lead to a number of complications including heart disease, high blood pressure, stroke, nerve damage, retinopathy, erectile dysfunction, hypo or hyper glycemia, kidney disease, and urologic problems. In 2005, in the US, approximately 20.8 million people (7% of the

population) had diabetes and roughly, \$132 billion dollars was spent on direct and indirect costs relating to diabetes . Over 200,000 Americans die each year from this chronic disease, making diabetes the sixth leading cause of death in the US.

As of now, the standard practice for taking glucose measurements for diabetics is to perform finger prick tests by lancing a finger to draw out a drop of blood. The blood is then applied to a sensor strip which is read by a meter that displays the glucose concentration within seconds. In order to properly monitor sugar levels within the body glucose level spot checks must be performed multiple times daily which leads to a number of dangerous complications. For type 1 diabetics (diagnosed at birth) these spot checks are typically obtained by pricking the finger 3-5 times throughout the day. The electrochemical reaction (using glucose oxidase) is driven by a voltage applied by the meter, and the result is measured by the meter as a current in the electrodes. In another type, a chemical reaction creates a particular color in the test strip and the meter employs optical methods (reflectance spectroscopy) for measurement. The systems are well established because they are inexpensive, small, portable and simple to use. Numerous companies currently market home-use glucose monitoring systems, providing low-cost disposable sensor strips and reusable meters.

Although diabetes treatment has historically been based on blood glucose measurements, the predominant method for commercial continuous monitoring systems is through measurement of glucose levels in interstitial fluid (ISF), the liquid that circulates around cells within body tissues. One reason is that interstitial fluid sampling presents fewer risks to the patient. Continuous sensors can be implanted in the subcutaneous tissue (beneath the skin) instead of inside a vein, reducing the risk of

introducing pathogens into the blood stream and of initiating a clotting response [8]. Secondly, the blood presents a more hostile environment for sensor devices [5]. Glucose has proved to be a difficult analyte to measure in-vivo over a long period of time (>1 week) [9]. Hence, further advances in sensing technology are imperative before these sensors can be used reliably for long-term monitoring of glucose in the body. In brief, it is important to discuss the state of the art commercial continuous glucose sensing technologies and their drawbacks.

Wilkins [10] and Fischer [9-11] have provided a detailed review of many glucose sensing techniques using infrared spectroscopy, excreted physiological fluid analysis (tears, sweat, urine, saliva), microcalorimetry, and optical sensors. Despite the ease of use, speed, and low risk of infection involved with infrared spectroscopy, this technique is hampered by the low sensitivity, poor selectivity, frequently required calibrations, and difficulties with miniaturization. Problems surrounding direct glucose analysis through excreted physiological fluids include a weak correlation between excreted fluids and actual blood glucose concentrations. Exercise and diet that alter glucose concentrations in the fluids also produce inaccurate results. Many of these optical based methods are still experimental and too unreliable for commercialization [13, 14].

The commercially available GlucoWatch™ (Cygnus, Redwood City, CA, USA) uses ion-to-phoresis to measure glucose concentrations. Ions and glucose in the skin are drawn to the cathode and anode contained in the GlucoWatch™ while a low-level electric current is passed through the skin. Interstitial glucose transported to the surface of the skin is measured by an amperometric biosensor and then displayed by the watch. This watch has a built-in audible alarm to alert the wearer when glucose levels deviate

significantly from the normal blood glucose range [11] and greatly increases the daily frequency (>20/day) of blood glucose measurements. A drawback of this method is that it does not permit ISF to directly transfer through the skin, but rather an extract of ISF with a much lower glucose concentrations. Mild skin irritation has also been reported from wearing the GlucoWatch™ [16, 17]. This method also has difficulty taking readings depending on the patient's skin type, temperature and perspiration levels. Recalibration requires using the finger prick test if the watch faults.

Medtronic (Minneapolis, MN, USA) launched the Mini-Med Paradigms Real Time continuous glucose monitoring system (CGMS) that uses wireless technology to transmit calculated blood glucose concentrations from the light-weight transmitter attached to a subcutaneously implanted sensor to an external insulin pump. This is one of the few FDA (<5) approved implantable glucose sensors available today. The insulin pump (Bolus Wizard™) automatically calculates the recommended insulin dosage, based on the transmitted glucose measurement levels. This system has the advantage that it can reduce the chances of inaccurate insulin dosages that arise from operator errors, thereby preventing erroneous blood sugar control. This sensor employs glucose oxidase in an enzymatic reaction that continuously consumes glucose and oxygen and produces gluconic acid and hydrogen peroxide. An electrode exchanges the charges in a reduction reaction created by the increase in hydrogen peroxide creating a current. Even though the enzyme is highly specific, species like ascorbic acid can interfere at the measurement electrode, and the use of selective membranes is necessary. These glucose-restrictive membranes utilize small pores to inhibit glucose diffusion (relative to oxygen) in order to alleviate the oxygen deficit problem and have been shown to have a number of

performance problems. The membranes can become clogged prevent the glucose from reaching the sensing material causing a false or delayed/drifted reading. Therefore a need exists for an equilibrium sensor that does not require external oxygen. In addition, these sensors can cause tissue irritation and infection due to wires, tubes, and/or electric current that must pass through the skin. Another drawback is that currently only the cost of the insulin pump component of this system is covered by insurance companies. The Medtronic CGMS sensor component retails at approximately \$1000 USD, with an additional \$350 per month required for supplies, none of which are reimbursed [18], which is too high for most individuals with diabetes.

The TheraSense FreeStyle NavigatorTM Continuous Glucose Sensor (Abbott Laboratories, Alameda, CA) is a subcutaneous electrochemical sensor that has reduced oxygen dependency by incorporating an osmium (Os) based mediator molecule into the sensor [19-22]. This sensor uses a lower operating potential (+40mV opposed to the 500mV required by most H₂O₂-sensing systems) which reduces oxidation of many electro active molecules responsible for interfering glucose readings. In vivo studies have demonstrated that sensors experience near negligible sensor drift and maintain consistent glucose sensitivity over a 3-day test period. The FreeStyle Navigator was approved by US FDA, in March 2008 and is currently being used on the commercial market.

The above mentioned sensors have their particular drawbacks. Therefore we propose to develop a sensor platform that can possibly be used to measure equilibrium glucose levels without the use of enzymes, IR technology, or external oxygen sources.

This sensor platform employs the use of a new type of “stimuli responsive” hydrogels containing phenylboronic acid (PBA) that binds reversibly to glucose.

Table 1.1 compares the drawbacks of the various current glucose sensing technologies to the new hydrogel based sensor concept which is detailed throughout this dissertation. Hydrogel based implantable glucose sensors have a number of inherent advantages and disadvantages when compared to current glucose sensing technologies. The proposed sensors have the advantage of taking measurements frequently (seconds), do not require the use of external oxygen sources to supplement chemical reactions, do not use oxygen restrictive a membrane, have no ascorbic acid interference, and contains no enzymes that can deactivate.

Table 1.1. Tradeoffs of several current glucose sensing technologies and hydrogel based glucose sensors.

Sensor Type	Finger Prick	IR Based Sensors	Ion-to-phoresis	Electrochemical Enzyme Based	Hydrogel Based Sensors
Noninvasive	no	yes	yes	no	no
Requires glucose-restrictive membrane due to O₂ deficit?	no	no	no	yes	no
Calibration varies with changes in glucose diffusion?	no	no	yes	yes	no
Contains enzymes that can deactivate?	yes	no	no	yes	no
Fructose interference?	no	yes	no	no	yes
Ascorbic acid interference?	yes	no	no	yes	yes/no
Measurement Frequency	3-5 days	3-5 days	1-2 hours	3-5 mins	<1 min
Simultaneous measurement of glucose, pH, CO₂?	no	no	no	no	yes

Another primary advantage of this technology is that hydrogels with various moieties can be used simultaneously to detect a number of physiological analytes (e.g., pH, CO₂, ionic strength). Drawbacks of this technology are that the sensors have to be subcutaneously implanted requiring them to have high biocompatibility. The sensors would ideally be coupled with integrated wireless electronics and therefore would not require any connections through the skin. An additional challenge is that the PBA based swelling hydrogels are also cross sensitive to fructose. Although average fructose concentrations are significantly less (~0.1%) than glucose within the body, it remains of concern.

The hydrogel acts as a chemical-to-mechanical transducer which responds by swelling to contracting to changes in analyte concentration within its environment. Researchers at the University of Utah (Magda et al.) and elsewhere (Siegel, Gerlach, Herber) have been able to synthesize a number of hydrogels that are specifically sensitive to number particular analytes. Changes in glucose concentrations, ionic strength [19] and pH [1] have been shown to impact the swelling characteristics and pressures exerted by these hydrogels. In our sensors the hydrogel allows the detection of analytes in solution by reversibly swelling against the piezoresistive diaphragm creating a change in output voltage. Hence, integration of hydrogels with micropressure sensors creates a unique sensor platform that has the advantage of providing chemical analysis with high measurement frequency without the use of complex measurement equipment. Combinatorial methods can be applied to the multiple sensor output signals of a sensor array to determine cross dependencies of hydrogels as well as giving reference. The success of this sensing method will ultimately depend on the performance, reliability, and

availability of both hydrogel materials, and a sensor platform used for swelling/contracting detection.

This work introduces a sensor platform that when coupled with stimuli responsive hydrogels creates a new category of chemical sensors. For the first time, hydrogel based silicon micro pressure sensor arrays for use in chemical sensing and metabolic monitoring applications were developed and demonstrated. The 2×2 sensor array is capable of simultaneously measuring the swelling pressure of four stimuli responsive hydrogels, and thus different analyte concentration in solution. The concept is shown in Figure 1.1. Ideally, the sensor should be versatile with the ability to measure a wide range of pressures so a single sensor can be used with a number of different hydrogels, which will have different full scale output pressures depending on hydrogel recipe and target analyte.

The general objective of this project is to develop a sensor platform used to detect the swelling pressure of analyte specific hydrogels developed at the University of Utah. Specific aims of this project were defined as:

- (a) Design, optimize, and fabricate silicon based pressure sensors with pressure ranges defined by ionic strength, pH, and glucose sensitive hydrogel swelling pressures.
- (b) Investigate using diffusion pores etched in the sensors' piezoresistive pressure sensing diaphragm to allow diffusion into and out of the hydrogel cavity.
- (c) Develop a small footprint ($3 \times 5 \text{ mm}^2$) piezoresistive pressure sensor array capable of simultaneously measuring ionic strength, pH, and glucose with reference.

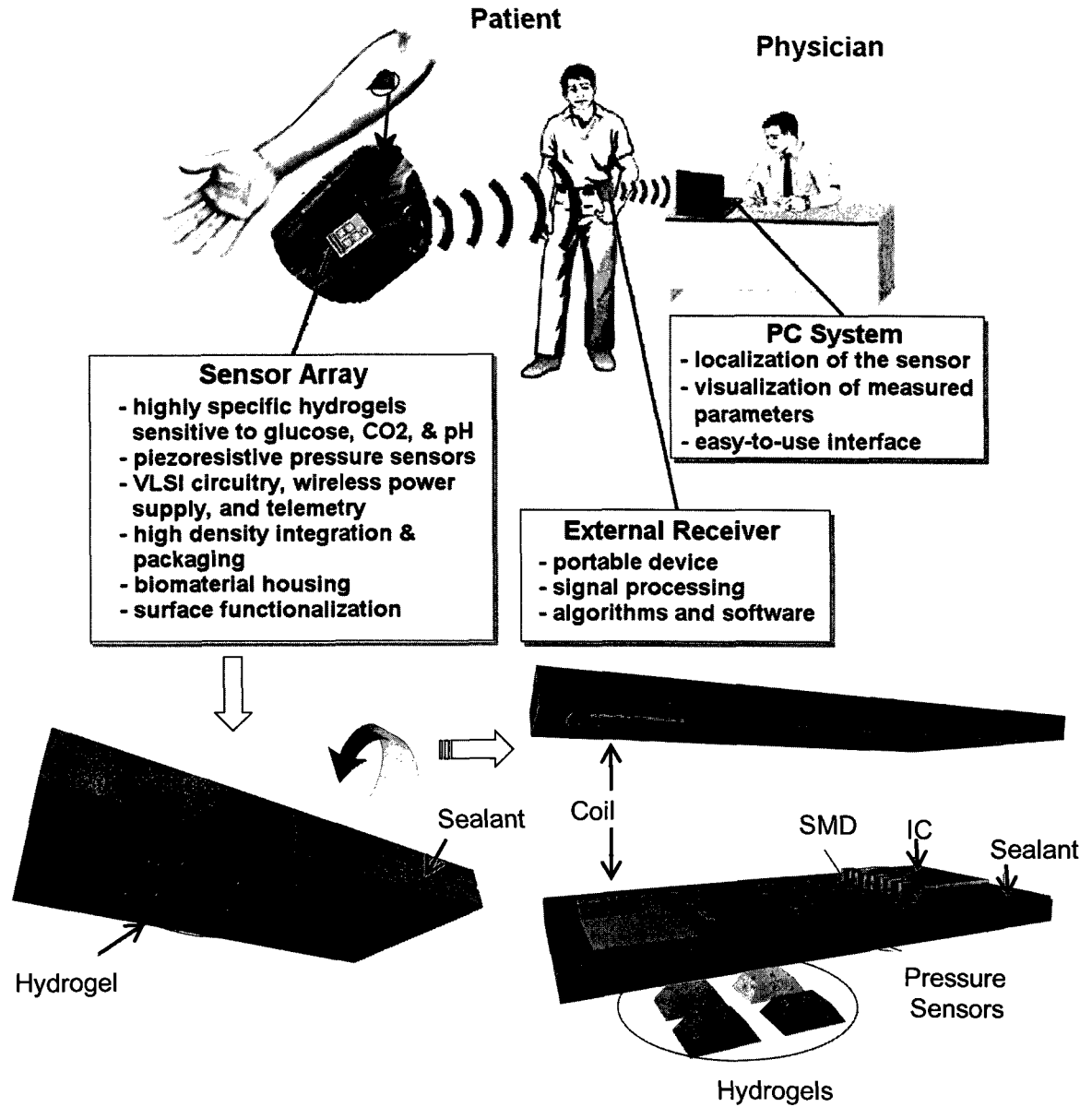


Figure 1.1. Conceptual depiction of the hydrogel based chemical sensor array and integrated electronics for detection of glucose, CO₂, ionic strength and pH.

- (d) Grow and characterize 3C-silicon carbide films for use in a fully front-side processed SiC diaphragm pressure sensor.

Our flexible sensor design incorporates analyte diffusion pores directly into the piezoresistive sensing diaphragm. With only slight modifications to this design and fabrication process, the devices can be optimized for use with a variety of hydrogels creating a platform that reduces sensor development costs by increasing flexibility. The modular sensor array allows easy modification of design parameters which allows sensor use in a variety of application fields. Based on the state of the art requirements for chemical sensing and physiological monitoring the technical sensor specifications were defined. The scope of this proof-of-concept study includes materials investigations, device design, theoretical and finite element analysis, fabrication, physical and chemical testing.

The first priority of this work was to develop functioning sensor arrays that show stable, linear, reversible, repeatable voltage outputs with respect to hydrogel swelling pressure in response to a particular analyte. Therefore testing was performed using well characterized hydrogels sensitive to changes in ionic strength. Experimental methods were developed and equipment and fixtures were constructed for testing the device performance at each stage of development. The transducer concept was tested and working sensors were produced. This work demonstrates the feasibility of the novel sensor concept and design. The processes and designs developed during this research took into account the need for simple and fast transfer to commercial markets.

A number of technical challenges remain, presenting opportunities for further work. An investigation of the effect of diaphragm pore size on response time and

specificity was only done in a simple qualitative fashion at the onset of the project and will need to be carried out in detail. Selected materials limitations and alternative design options were also identified through the characterization of the designs and devices presented here. The presentation of results follows the experimental progress, with chapters defining different aspects of the device concept, design, simulation, fabrication, and testing.

In addition, material is presented in the appendix on the development of a flexible 3C-SiC LPCVD reactor for the deposition of thin film layers for sensor applications. The material was investigated for use as sensor diaphragm but not implemented into the devices presented here and left for future work.

1.2 References

- [1] A. Hullmann, "The Economic Development of Nanotechnology-An Indicators Based Analysis," *EU report*, 2006.
- [2] T. Reuters, "Examine the Chemical Sensors Market in the USA," *Market Report*, vol. 1, 2009.
- [3] R. Bashir, A. Gupta, G. W. Neudeck *et al.*, "On the Design of Piezoresistive Silicon Cantilevers with Stress Concentration Regions for Scanning Probe Microscopy Applications," *J. Micromech. Microeng.*, vol. 10, no. 4, pp. 483-491, 2000.
- [4] R. A. Peura, "Blood Glucose Biosensors-a Review," in *IEEE Case Studies in Medical Instrument Design*, 1991, pp. 51-64.
- [5] H. E. Koschwanetz and W. M. Reichert, "In Vitro, In Vivo and Post Explantation Testing of Glucose-Detecting Biosensors: Current Methods and Recommendations," *Biomaterials*, vol. 28, no. 25, pp. 3687-3703, 2007.
- [6] A. Mokdad, E. Ford, B. Bowman *et al.*, "Prevalence of Obesity, Diabetes, and Obesity-Related Health Risk Factors," *Jama*, vol. 289, no. 1, pp. 76, 2003.
- [7] J. Pickup, L. McCartney, O. Rolinski *et al.*, "In Vivo Glucose Sensing for Diabetes Management: Progress Towards Non-Invasive Monitoring," *British Medical Journal*, vol. 319, no. 7220, pp. 1289, 1999.
- [8] J. N. Roe and B. R. Smoller, "Bloodless Glucose Measurements," *Critical reviews in therapeutic drug carrier systems*, vol. 15, no. 3, pp. 199, 1998.
- [9] E. Wilkins and P. Atanasov, "Glucose Monitoring: State of the Art and Future Possibilities," *Medical Engineering & Physics*, vol. 18, no. 4, pp. 273-288, 1996.
- [10] U. Fischer, "Fundamentals of Glucose Sensors," *Diabetic Medicine*, vol. 8, no. 4, pp. 309-321, 1991.
- [11] S. K. Garg, W. C. Kelly, M. K. Voelmler *et al.*, "Continuous Home Monitoring of Glucose," *Diabetes Care*, vol. 30, no. 12, pp. 3023, 2007.
- [12] P. U. Abel and T. von Woedtke, "Biosensors for In Vivo Glucose Measurement: Can We Cross the Experimental Stage," *Biosensors and Bioelectronics*, vol. 17, pp. 1059-1070, 2002.
- [13] J. A. Tamada, M. Lesho, and M. J. Tierney, "Keeping Watch on Glucose," *Spectrum, IEEE*, vol. 39, no. 4, pp. 52-57, 2002.
- [14] J. A. Tamada, S. Garg, L. Jovanovic *et al.*, "Noninvasive Glucose Monitoring: Comprehensive Clinical Results," *Jama*, vol. 282, no. 19, pp. 1839, 1999.

- [15] K. R. Pitzer, S. Desai, T. Dunn *et al.*, "Detection of Hypoglycemia with the GlucoWatch Biographer," *Diabetes Care*, vol. 24, no. 5, pp. 881, 2001.
- [16] G. Reach and G. S. Wilson, "Can Continuous Glucose Monitoring Be Used for the Treatment of Diabetes?," *Analytical Chemistry*, vol. 64, no. 6, pp. 381A-386A, 2008.
- [17] G. S. Wilson and Y. Hu, "Enzyme-Based Biosensors for in Vivo Measurements," *Chemical Reviews*, vol. 100, no. 7, pp. 2693-2704, 2000.
- [18] B. Feldman, R. Brazg, S. Schwartz *et al.*, "A Continuous Glucose Sensor Based on Wired Enzyme™ Technology-Results from a 3-day Trial in Patients with Type 1 Diabetes," *Diabetes Technology & Therapeutics*, vol. 5, no. 5, pp. 769-779, 2003.
- [19] I. S. Han, M. H. Han, J. Kim *et al.*, "Constant-Volume Hydrogel Osmometer: A New Device Concept for Miniature Biosensors," *Biomacromolecules*, vol. 3, no. 6, pp. 1271-1275, 2002.
- [20] D. Y. Jung, J. J. Magda, and I. S. Han, "Catalase Effects on Glucose-Sensitive Hydrogels," *Macromolecules*, vol. 33, no. 9, pp. 3332-3336, 2000.
- [21] G. Lin, S. Chang, H. Hao *et al.*, "Osmotic Swelling Pressure Response of Smart Hydrogels Suitable for Chronically-Implantable Glucose Sensors," *Sensors and Actuators B: Chemical*, vol. 144, pp. 332-336, 2010.
- [22] G. Lin, S. Chang, C. H. Kuo *et al.*, "Free Swelling and Confined Smart Hydrogels for Applications in Chemomechanical Sensors for Physiological Monitoring," *Sensors & Actuators: B. Chemical*, pp. 186-195, 2008.
- [23] A. Baldi, G. Yuandong, P. E. Loftness *et al.*, "A Hydrogel-Actuated Environmentally Sensitive Microvalve for Active Flow Control," *Journal of Microelectromechanical Systems*, vol. 12, no. 5, pp. 613-21, 2003.
- [24] A. P. Dhanarajan, G. P. Misra, and R. A. Siegel, "Autonomous Chemomechanical Oscillations in a Hydrogel/Enzyme System Driven by Glucose," *Journal of Physical Chemistry A*, vol. 106, no. 38, pp. 8835-8, 2002.
- [25] M. Lei, A. Baldi, T. Pan *et al.*, "A Hydrogel-Based Wireless Chemical Sensor," *Proceedings of the IEEE International Conference on Micro Electro Mechanical Systems (MEMS)*. pp. 391-394.
- [26] G. Yuandong, A. Baldi, B. Ziaie *et al.*, "Modulation of Drug Delivery Rate by Hydrogel-Incorporating MEMS Devices." pp. 406-409.
- [27] M. Guenther, G. Gerlach, C. Corten *et al.*, "Hydrogel-Based Sensor for a Rheochemical Characterization of Solutions," *Sensors & Actuators: B. Chemical*, 2007.

- [28] M. Guenther, G. Gerlach, D. Kuckling *et al.*, "Chemical Sensors Based on Temperature-Responsive Hydrogels," *Proc. SPIE*. p. 61670T.
- [29] M. Guenther, D. Kuckling, C. Corten *et al.*, "Chemical Sensors Based on Multiresponsive Block Copolymer Hydrogels," *Sensors and Actuators B: Chemical*, vol. 126, no. 1, pp. 97-106, 2007.
- [30] J. Sorber, G. Steiner, V. Schulz *et al.*, "Hydrogel-Based Piezoresistive pH Sensors: Investigations Using FT-IR Attenuated Total Reflection Spectroscopic Imaging," *Analytical Chemistry*, vol. 80, no. 8, pp. 2957-2962, 2008.
- [31] Q. Thong Trinh, G. Gerlach, J. Sorber *et al.*, "Hydrogel-Based Piezoresistive pH Sensors: Design, Simulation and Output Characteristics," *Sensors and Actuators B: Chemical*, vol. 117, no. 1, pp. 17-26, 2006.
- [32] G. Gerlach, M. Guenther, J. Sorber *et al.*, "Chemical and pH Sensors Based on the Swelling Behavior of Hydrogels," *Sensors and Actuators B: Chemical*, vol. 111-112, pp. 555-561, 2005.
- [33] S. Herber, J. Bomer, W. Olthuis *et al.*, "A Miniaturized Carbon Dioxide Gas Sensor Based on Sensing of pH-Sensitive Hydrogel Swelling with a Pressure Sensor," *Biomedical Microdevices*, vol. 7, no. 3, pp. 197-204, 2005.
- [34] S. Herber, J. Borner, W. Olthuis *et al.*, "A Micro CO₂ Gas Sensor Based on Sensing of pH-Sensitive Hydrogel Swelling by Means of a Pressure Sensor," *Digest of Technical Papers - International Conference on Solid State Sensors and Actuators and Microsystems, TRANSDUCERS '05*. pp. 1146-1149.
- [35] S. Herber, J. Eijkel, W. Olthuis *et al.*, "Study of Chemically Induced Pressure Generation of Hydrogels Under Isochoric Conditions using a Microfabricated Device," *The Journal of Chemical Physics*, vol. 121, no. 6, pp. 2746-2751, 2004.
- [36] S. Herber, W. Olthuis, and P. Bergveld, "A Swelling Hydrogel-Based PCO₂ Sensor," *Sensors and Actuators B: Chemical*, vol. 91, no. 1-3, pp. 378-382, 2003.
- [37] H. J. v. d. Linden, S. Herber, W. Olthuis *et al.*, "Stimulus-Sensitive Hydrogels and their Applications in Chemical Microanalysis," 2003.
- [38] R. ter Steege, S. Herber, W. Olthuis *et al.*, "Assessment of a New Pototype Hydrogel CO₂ Sensor; Comparison with Air Tonometry," *Journal of Clinical Monitoring and Computing*, vol. 21, no. 2, pp. 83-90, 2007.

CHAPTER 2

STATE OF THE ART: BIOSENSORS, HYDROGELS AND PIEZORESISTIVE PRESSURE SENSORS

In this chapter we briefly discuss the biomedical sensors market to help identify key applications, and then discuss in detail the two main components of hydrogel based chemical sensors. In particular, the chemical sensing element (hydrogel), and different transduction methods used to measure their chemical response. The underlying principles of hydrogel swelling are introduced, with a discussion of the specific pH, ionic strength and glucose sensitive hydrogels synthesized by Magda et al. A state of the art review of hydrogel based chemical sensors and their respective transduction mechanisms are presented. The main drawbacks of these sensors helped determine the specifications and requirements of the new hydrogel based sensor array presented in Chapter 4. The last section of this chapter briefly discusses piezoresistivity and components used in piezoresistive bending plate sensors (micro pressure sensors). This provides a background for the sensing mechanism used in hydrogel based chemical sensors.

2.1 Biomedical Sensors

A biosensor can be described as “a self-contained integrated device, which is capable of providing specific quantitative or semi-quantitative analytical information using a biological recognition element (biochemical receptor), which is retained in direct spatial contact with a transduction element” as defined by the International Union of Pure

and Applied Chemistry (IUPAC) [2]. The interaction of the analyte with the chemical/biological element is designed to produce an effect measured by a transducer, which converts the physical change into a measurable effect, such as an electrical or optical signal. Therefore, by definition the newly developed sensors presented in the report are biosensors.

The biosensor industry for use in medical applications is well established and growing rapidly, with a global market of approximately \$7 billion in 2004, which grew to about \$10 billion by 2008 [3] and demand remains strong for biosensors today. Most commercially available biosensors are based on amperometric enzyme electrodes. However, recent developments using new technologies are numerous and spurring revived growth. A few of those driving technologies are briefly mentioned in this section. Examples of microfabricated devices are also described.

Biomedical sensors are commonly used for medical diagnostics, in order to monitor patients' condition and safety in intensive care, emergency room and surgery settings. Measurement techniques are needed to evaluate numerous physiological markers, including heart rate, blood pressure, glucose levels, pH, CO₂, white blood cell count, hormones, electrolytes, electrical activities, and dissolved gasses. Ideally, physiological measurements would be taken in real time on a continuous basis, and the improved data quality would lead to better diagnosis and treatments. Currently the vast majority of tests can only be performed in clinical settings by trained professionals, either in centralized laboratories, or in hospitals.

Micro-Electro-Mechanical-Systems (MEMS) based technologies are being used for the development of a number of medical applications, and generally refer to devices

that are made up of components between 1 to 100 micrometers in size (i.e., 0.001 to 0.1 mm) and systems ranging in size from roughly 20 micrometers to several millimeters. Many of the technologies used to create these devices stem from the integrated circuit industry, and possess inherent advantages including fabrication that enables new designs to be easily implemented using standard processes, easy reproduction of precise dimensions, diverse set of materials incorporated into fabrication processes, integration of mechanical, electrical, electronic, optical, thermal and fluidic functionalities, the advantage of utilizing high throughput batch manufacturing which reduces costs.

In this past decade, integrated MEMS systems with multiple components and integrated circuits (ICs) have been employed in a broad range of fields from automobile control, national security, to healthcare. More recently, biomedical MEMS (bioMEMS) has evolved into a promising new field which includes numerous areas of research including implantable microsystems, microfluidics, Lab-On-a-Chip (LOC), electronic noses, drug delivery, DNA microarrays, neural interfaces, enzymatic electrodes, and microchemical sensors [3-8].

2.2 Hydrogels

Hydrogels are crosslinked polymeric networks that can undergo a large volume phase transition (swelling) in response to a number of external stimuli and/or environmental conditions including temperature [9], electric field [10], pH [11-16], antigens [17-19], glucose [20-26], and ionic strength [12, 21, 27-31]. The unique behavior of these materials has been researched intensively and used for a large number of applications for sensing, tissue engineering, contact lenses, diapers, and drug delivery. Many hydrogels consist of up to 99% water in their swelled state and up to 500 times

their original mass depending on the chemical composition [32]. The polymer matrix consists of long molecular chains consisting of individual monomers (backbones). The longer backbone chains are held together by crosslinking interconnections between these chains. Crosslinking keeps the chains in the polymer matrix together, preventing the dissolution of the long molecular chains and increasing the mechanical stability of the hydrogel.

Generally, three components are responsible for a hydrogel swelling response: the chemical makeup of polymer chains, their compatibility with water, and the amount of crosslinking species. Additionally, for hydrogels containing fixed ionized groups, a third, ionic component, which depends on degree of ionization, also affects swelling. Flory-Rehner-Donnan theory takes into consideration these three effects and has been used classically to explain the swelling behavior of many hydrogels [29]. According to this theory, the sum of these three individual swelling pressures is zero at equilibrium for any hydrogel network shown in equation 1.

$$\Delta\pi = \Delta\pi_{mixing} + \Delta\pi_{elastic} + \Delta\pi_{ionic} = 0 \quad (1)$$

The equation of state for an ionic hydrogel at equilibrium is expressed mathematically as:

$$\Delta\pi = RT \left[\ln(1 - \phi) + \phi + \chi\phi^2 \right] + \left[V_w P_0 \left(\left(\frac{\phi}{\phi_u} \right)^{\frac{1}{3}} \cdot \left(\frac{\phi}{2\phi_u} \right) \right) \right] \cdot V_w \sum_i (C_i^{ins} - C_i^{out}) \quad (2)$$

where,

$\Delta\pi$ = net ionic osmotic pressure difference driving swelling and shrinking;

R = universal gas constant;

T = temperature;

Φ = polymer volume fraction;

Φ_u = polymer volume fraction in the unperturbed (as prepared) state;

χ = polymer-solvent interaction parameter;

V_w = molar volume of water;

P_0 = crosslinking density or number of active network chains per unit volume;

C_i^{ins} = concentration of the soluble ion 'i' inside the hydrogel;

C_i^{out} = concentration of the soluble ion 'i' outside the hydrogel.

It is in order to briefly discuss the three components of hydrogel swelling pressure.

2.2.1 Polymer Solvent Mixing Pressure ($\Delta\pi_{\text{mixing}}$)

$\Delta\pi_{\text{mixing}}$ is the amount of pressure generated within the hydrogel in response to the mixing of polymer and solvent (water) with one other. For hydrogels, this mixing directly causes swelling and is attributed to two factors. First the mixing entropy is due to the tendency of the polymer and solvent molecules to mix with each other. Secondly, the contact contribution, a quantity that depends on the interactions between the

environment (solvent) and the polymer backbone of the network, one can cause swelling or contracting of the hydrogel in response to particular stimuli.

2.2.2 Hydrogel Elasticity ($\Delta\pi_{\text{elastic}}$)

Crosslinking is typically performed chemically or optically during synthesis of the hydrogels. These chemical linkages have elastic, solid-like behavior at the macroscopic level while retaining liquid-like behavior at the microscopic level. Hydrogel network crosslinking provides the elastic restorative force on the hydrogel, after swelling, driving it towards a most conformal lowest energy entropy state. The $\Delta\pi_{\text{elastic}}$ opposes any swelling or contracting in the network, or shear deformation. Increased crosslinking density usually decreases the degree of swelling of a stimuli responsive hydrogel. Crosslinks are commonly temporary hydrogen bonds [30], hydrophobic interactions [31], or permanent covalent bonds [29]. A specific type of temporary covalent crosslinking has been observed in phenylboronic acid (PBA) containing hydrogels via a glucose bridge at low glucose concentrations and high pH [30]. The degree of crosslinking, and hence the hydrogel mechanical properties depends on glucose concentration in the external environment. The mechanical strength of the hydrogel is also a function of the network elasticity. For instance, the elastic (compression) modulus (E) of the hydrogel is can be approximated as follows [33]:

$$E = \rho_0 RT \left(\frac{\phi}{\phi_u} \right)^{\frac{1}{3}} \quad (3)$$

Hence, a higher crosslinking density, ρ_0 , will increase the hydrogels' modulus, and improve restoring forces against external tension or compression.

2.2.3 Ionic Osmotic Force ($\Delta\pi_{\text{ionic}}$)

Ionic osmotic forces also determine the swelling behavior of hydrogels, and are only observed in hydrogels that have fixed charges located on their polymer chains. These fixed charges are electrically compensated by mobile counter ions, which in turn apply the swelling pressure on the network. This pressure is always positive and promotes uptake of water into the hydrogel network. The precise values of concentrations of ions inside (C^{ins}) and outside (C^{out}) depends on the fixed charges in the gel, which are determined by the degree of substitution of ionizable groups, pH, and ionic content of the external medium.

2.2.4 Summary

Hydrogels are polymeric materials that have potential for use in chemical sensors, due to their high selectivity and configurability. The ability to customize hydrogels' chemical and mechanical characteristics allows for the synthesis of hydrogels optimized for detection of particular target species. Furthermore, hydrogels can readily be miniaturized and directly integrated into piezoresistive pressure sensors.

2.3 Stimuli Response Hydrogels (pH, ionic strength, glucose)

During synthesis, it is possible to manipulate the composition and concentration of chemical moieties, the degree of crosslinking, and the number of ionic charges making it possible to tailor a hydrogel behavior and response to various external stimuli. Magda et al. have specifically developed a number of hydrogels that are sensitive to changes in ionic strength (NaCl), pH, and glucose. Another focus has been on the development of glucose sensitive hydrogels for monitoring of blood glucose levels for diabetes management [19, 22, 23, 26-28]. The pH, ionic strength, and glucose sensitive hydrogels

undergo rapid, reversible, and sharp volume transitions with environmental changes. These volume transitions produce in swelling pressures which are the basis for the chemical-mechanical transduction of our sensors. The specific swelling mechanisms are described for the two different types of hydrogels in the subsequent sections.

2.3.1 pH and Ionic Strength Sensitive Hydrogels

Hydrogels synthesized from hydroxypropyl methacrylate (HPMA), N,N-dimethylaminoethyl methacrylate (DMA) and crosslinker tetra-ethyleneglycol dimethacrylate (TEGDMA) have been shown to reversibly swell in response to changes in pH and ionic strength. The sensing mechanism is based on the protonation of the tertiary amines on the DMA backbone. At low pH value, elevated backbone protonation temporarily increases the osmotic swelling pressure within the hydrogel. At a fixed pH, a larger osmotic swelling pressure can be obtained by increasing the chemical potential of the surrounding water by reducing the environmental ionic strength. In either situation, the increase in osmotic pressure is compensated for by swelling of the gel.

2.3.2 Phenylboronic Acid Based Hydrogels

Phenylboronic acid (PBA) based glucose sensors have emerged as an alternative to the enzyme based glucose sensors. PBA is known to bind reversibly to cis diol bearing sugar molecules to form PBA sugar esters. More specifically, when glucose attaches to the PBA it decreases the pKa value of the boronic acid group, and the fraction of charged borate anions in the hydrogel is increased. This increase in borate anions decreases in the chemical potential of water within the hydrogel making it absorb water and swell. This swelling continues until a balance is reached between the favorable free energy of mixing and the stretching of hydrogel polymer chains. These PBA groups have been previously

incorporated into a hydrogel network to form glucose and fructose sensitive hydrogels. Binding of glucose to PBA has been assessed traditionally either by fluorescence or alteration of charge on the PBA moiety, and hence swelling of the hydrogel.

An apparent problem with this glucose sensing mechanism is that PBA cannot distinguish glucose from other cis diol molecules and may give rise to errors when the glucose measurements are carried out in presence of other sugar molecules, for instance, fructose, which is also found in blood.

In response to the cross sensitivity, another glucose sensing mechanism has been proposed and investigated by synthesizing a hydrogel where glucose can reversibly bind to different side chains of a PBA containing hydrogels creating crosslinking. This crosslink formation, which seems to be specific to glucose and not fructose, manifests itself by shrinking the hydrogel instead of swelling it. Therefore, this mechanism may provide detection of glucose without interference by other sugars.

2.3.3 Summary

The ability to synthesize pH, ionic strength, and glucose sensitive hydrogels in-house gives us the capability to develop a class of chemical sensors that are currently commercially unavailable. This also allows for the synthesis of hydrogels directly in the sensor cavities (in-situ) which has a number of advantages and is discussed in future chapters. Having full design control of both the hydrogels and sensors allows for the optimization of the sensors in a wide range of applications. The hydrogel based sensors specifications were defined using data from previous experiments performed on glucose and ionic strength/ pH sensitive hydrogels.

2.4 State of the Art Hydrogel Based Sensors

Hydrogel based sensors generally consist of two main components, the hydrogel used for chemical detection and a transducer. Mechanical, conductometric, amperometric and optical mechanisms have been used in the past to monitor changes in hydrogel structure. These transduction methods are briefly introduced.

2.4.1 Mechanical Measurements

Mechanical detection of polymer swelling is most common and has been performed in a number of ways. Cai and Grimes attached a salt independent, temperature calibrated pH sensitive hydrogel to a miniature array of four thick film magnetoelastic elements which mechanically vibrate at a resonant frequency dependent on hydrogel mass [16, 33]. They demonstrated a new approach for eliminating the interference of salt on the polymer swelling based pH sensors by using a reference pH independent polyelectrolyte hydrogel. Results showed the sensors had a linear response across a pH range of 5.3 to 7.4 with a slope of 310 Hz/pH. The resolution of the system was 0.1 pH.

Silicon microcantilevers have been used to detect changes of mass, temperature, heat, and/or stress, into bending (static mode) or changes in resonance frequency (dynamic mode). For measurements made in liquids for chemical detection static mode is preferred. Microcantilevers are commonly coupled to an optical or piezoresistive measurement system to determine beam deflection. Peppas et al. fabricated a microcantilever structure with photo lithography defined crosslinked copolymeric hydrogels using silicon-on-insulator (SOI) wafers [34, 35]. As pH around the cantilever was increased the polymer network expanded and resulted in a reversible change in surface stress causing the microcantilever to bend. The sample was allowed to

equilibrate at a given pH. Then deflection of the cantilever was measured by adjusting the focus plane of a microscope from the edge of the cantilever well to the tip of the cantilever. Mechanical amplification of polymer swelling as a function of pH change within the dynamic range was obtained, with a maximum deflection sensitivity of $1 \text{ nm}/5 \times 10^{-5} \text{ -pH}$.

Bending plate sensors can be categorized in two types, capacitive and piezoresistive. The transduction methods are similar that each is based on a flexible diaphragm that is deflected by applied hydrogel swelling pressure. They differ in that piezoresistive transducers measure the stress-dependent resistance in the diaphragm material, while capacitive transducers measure the displacement of the diaphragm with respect to a reference electrode. Piezoresistive devices have the advantage that they provide a linear response, are more easily fabricated, and do not require complicated measurement electronics. In contrast, capacitive sensors use passive circuit elements requiring no additional power requirements. Additionally they are also less sensitive to temperature variations.

Capacitive bending plate sensors use hydrogels to control the distance between the plates. This distance dictates the total sensor capacitance and is directly related to the hydrogel swelling pressure and hence chemical concentration. Capacitive sensors have been coupled to hydrogels by Strong et al. [36] who used the hydrogel to exert contact pressure on a deformable conducting diaphragm, producing a capacitance change. The diaphragm in the sensor design was made of a nickel titanium alloy. The sensors exhibited the greatest sensitivity in the concentration range 0 to 0.5 M of calcium nitrate tetrahydrate, on average of $110 \text{ mN}/\text{M}/\mu\text{l}$.

Piezoresistive based hydrogel sensors have been studied by a number of research groups for over a decade [28, 29, 31, 37-43]. The designs presented in literature all use the same principle: the swelling of a confined hydrogel due to the presence of an analyte causes the deflection of a flexible plate which contains imbedded piezoresistors and consequently the changing of the output voltage of a Wheatstone bridge. Details describing the design and fabrication of piezoresistive pressure sensors are presented later in this chapter. Gerlach et al. have demonstrated the use of commercially available pressure sensor chips with flexible thin silicon bending plates as the mechanical-electrical transducer for the transformation of bending plate deflection into a corresponding electrical output signal [13, 14, 37-39]. Thin films of the photo cross-linkable hydrogels were deposited onto the backside of the silicon bending plate and irradiated with UV light. Aqueous test solutions were pumped through inlet tubes into the silicon chip cavity to induce swelling or contracting of the hydrogels. Using the combination of temperature and pH sensitive hydrogels they created a pH sensor with a long-term stable signal sensitive in the pH range between 2 and 5. Through the use of hydrogel miniaturization time constants of less than a minute were found for thin photo-crosslinked hydrogel films directly deposited on the sensor diaphragms.

Heber et al. fabricated a number of hydrogel based sensors for the detection pH, and CO₂, used in the monitoring and diagnosis of gastrointestinal ischemia [28, 29, 40-42, 44, 45]. A sensor principle for the detection of carbon dioxide was presented where hydrogel pressure generation induced by CO₂ is measured with an existing micropressure sensor. The sensor was placed in a sodium bicarbonate solution and CO₂ was introduced into the solution which decreased the pH. In response, hydrogel microspheres contracted

and the pressure measured decreased. It was experimentally verified that the hydrogel-based carbon dioxide sensor responded well in the medical interesting range between 2 and 20 kPa CO₂ between 25 to 37°C. The response times varied from 1.5 and 4.5 minutes.

2.4.2 Oscillating Sensor Measurements

Oscillating transducers are devices that measure changes in resonant frequency. Changes in the mechanical properties, and hence hydrogel mass or load, result in a shift of this resonance frequency. This can be accompanied by a change of the signal amplitude. Upon applying electric field quartz crystals can be stimulated to oscillate at a particular resonance. Richter et al. used this property to measure changes of hydrogel properties [46]. An increase in the surface load or mass of a quartz crystal should theoretically induce a decrease of the resonance frequency. However, the opposite was observed when coupling the transducer to a hydrogel. This was explained because both the stiffness and the density of the hydrogel strongly decrease with swelling changing the mechanical properties of the hydrogels and hence quartz transducer loading.

Zhao et al. [47] created a MEMS sensor for the detection of glucose utilizing hydrogels featuring a magnetically-driven vibrating microcantilever, which is placed in a microchamber and separated from the environment by a semipermeable membrane. The glucose concentration was determined by detecting viscosity changes in the chamber through the measurement of the cantilever's vibration resonance change. The device is capable of measuring physiologically relevant glucose concentrations from 0 to 25 mM with a resolution 0.025 mM. The response of the sensor to glucose concentration change had a time constant of approximately 4.3 minutes.

2.4.3 Conductometric Measurements

Conductometric measurements have been performed on hydrogels by Sheppard et al. using a thin hydrogel layer deposited on a planar interdigitated electrode array [48-51]. The hydrogel changes volume in response to pH leading to a corresponding increase or decrease in ion mobility inside the hydrogel layer and a change in electrical conductivity. Preliminary results showed that conductivity of pH responsive hydrogels expressed as a fraction of the conductivity of the buffer in which the gels were equilibrated ranged from 1% for the gels in the collapsed state to 70% for the most highly swollen gels over a pH range of 5 to 10. These results suggest that conductivity measurements may provide an alternative to the other methods described for characterizing moderately swollen hydrogels.

2.4.4 Amperometric Measurements

Kikuchi et al. developed an amperometric sensor for the detection of glucose using a hydrogel coated platinum electrode [52]. A hydrogel complex changed its swelling degree with glucose concentration in a physiological buffered solution (PBS) leading to changes in current. It was determined that additions of glucose to PBS induced swelling of the hydrogel leading to increased diffusion of ion species and thus an increase measurable current. It was shown that the observed current changes were proportional to glucose concentration in the physiological important range of 0 to 300 mg/dL (~0 to 16.6 mM).

2.4.5 Optical Measurements

A wide number of optical methods have been explored for the detection of hydrogel swelling. Seitz et al. coupled hydrogels to a reflector and optical fiber.

Changes in polymer volume cause the reflecting diaphragm to move, which in turn changes the intensity of light reflected back into the optical fiber [53]. A second design measured the optical transmission through a hydrogel membrane [54]. The absorbance was measured vs. the wavelength upon exposing the hydrogel membrane to solutions of varying pH (3.0–9.0). At low pH (3.0), the absorbance had the highest value (1.34), while the absorbance decreased significantly (1.10) when the pH was increased to 9.0, indicating polymer swelling.

Asher et al. made significant contributions by incorporating a colloidal crystalline array (CCA) of microspheres into stimuli-responsive hydrogels [55-59]. The CCA diffracts the light at visible wavelengths determined by the lattice spacing d , which gives rise to an intense color. Swelling causes the mean separation between the colloidal spheres to increase shifting the Bragg peak of the diffracted light to longer wavelengths. It was shown that a change of 0.5% in the hydrogel volume shifts the diffraction wavelength by ~ 1 nm.

A new interferometric optical sensor was presented by Schalkhammer et al., in which the swelling of a thin hydrogel layer changes output from an optical thin film system which transforms the variations in volume of the polymer into spectral information [60]. Lowe et al. used reflection holography to characterize polymer swelling [61]. Holographic diffraction gratings which act as a reflector of light were created within the hydrogel. The reflection spectrum of the hologram changes with changing hydrogel volume.

2.4.6 Summary

A wide range of transduction technologies exist to measure physical changes of hydrogels in response to a number of analytes. Table 2.1 quantifies and summarizes a number of these sensors used to measure changes in various pH sensitive hydrogel structures. Since every application requires a specific set of requirements and specifications, it is difficult to directly compare each sensor.

There are a number of advantages using piezoresistive bending plate sensors for the detection of hydrogel swelling pressure when compared to other transduction mechanisms described above:

- (a) Silicon-based piezoresistive pressure sensor technology is mature and well understood making integration of hydrogels feasible and easy to characterize.
- (b) Modular designs are highly configurable and can be optimized and easily modified for particular pressure ranges defined by particular hydrogels.
- (c) The minute size of piezoresistive pressure sensors allows them to be coupled to thinner/smaller hydrogels. These hydrogels have larger surface-to-volume ratios, ultimately improving sensor response times.
- (d) They can be manufactured using bulk processing techniques in large numbers at low costs.
- (e) Have highly linear electrical outputs.
- (f) Utilize simple signal processing circuits, so the sensors can directly connect to unsophisticated monitoring systems.

Table 2.1. Comparison of different hydrogel sensing technologies based on [1].

Sensor type	Transducer signal	Transducer resolution	Sensitivity per pH unit	pH range	Material	~Hydrogel thickness	~Response time	References
Refractometric	refractive index	2.5×10^{-4}	3.11×10^{-2}	7-7.75	HEMA-DMAEMA	300 nm (dry)	~ 80 s	[52]
Holographic	wavelength	6×10^{-3} (1mm/165nm)	165 nm	5 - 7	PHEMA-co-MAA	10 μ m	~ 250 s	[60]
CCA sensor (Bragg diffraction)	wavelength	3.3×10^{-3} (1mm/300nm)	74.2nm	4.3-8.5	PAAm-PCCA	125 μ m	~10 min	[54, 56-58, 62]
Conductometric	resistance	-	100 Ω	7 - 8	HEMA-DMAEMA	8 μ m	~350 s	[47-50]
Quartz-crystal micro balance	frequency	3.3×10^{-6} (0.1Hz/30kHz)	13.2 kHz	2.5- 3.45	PVA-PAA	390 nm (dry)	~500 ms	[45, 46]
Magnetoelastic	frequency	2.4×10^{-4} 0.4Hz/1.7kHz	506 Hz	4.4- 8,5	poly(AA-co-IOA)	1.4 μ m	~120 s	[32]
Microcantilever	deflection	5×10^{-5} (1mm/20 μ m)	20.3 μ m	6 - 6,8	PMAA-PEGDMA	2.2 μ m	~5 min	[33, 34]
Microcantilever	deflection	2.9×10^{-5} (1mm/35 μ m)	1000 nm	6 - 9	AAm-DMAEMA	15 μ m	~10 min	[33, 34]
Bending Plate (piezoresistive)	resistance	1.67×10^{-5} (1 μ V/60mV)	14.55 mV	5.5- 11	PVA-PAA	40 μ m	~ 1 min	[27, 28, 39-41, 43, 44]

2.5 Piezoresistive Sensors

Piezoresistive sensors were some of the first (MEMS) devices and comprise a substantial market share of MEMS sensors in the market today [62]. Piezoresistivity in silicon has been widely used for many types of sensors including pressure sensors, accelerometers, cantilever force sensors, inertial sensors, and strain gauges.

This section describes the fundamental theories and components used in piezoresistive bending plate sensors which were used to detect hydrogel swelling pressure in this work. Specifically the micropressure sensor concept is presented, piezoresistivity is briefly explained, the Wheatstone bridge is described, and sensor terminology used to describe pressure sensors is defined.

2.6 Piezoresistivity

The electrical resistance (R) of a homogeneous material is a function of its dimensions and resistivity (ρ) defined by equation 4:

$$R = \frac{\rho \cdot L}{A} \quad (4)$$

where L is length, and A is average cross-sectional area. The total change in resistance due to applied stress is due to two factors, geometry and resistivity changes. The Poisson's ratio (ν) determines the amount of cross-sectional area the bulk material reduces in proportion to the longitudinal strain as shown in equation 5.

$$\frac{\Delta R}{R} = (1 - 2\nu)\epsilon + \frac{\Delta\rho}{\rho} \quad (5)$$

Poisson's ratio (ν) for most metals ranges from 0.20 to 0.35. For anisotropic silicon, the effective directional Poisson's ratio ranges from 0.06 to 0.36 [63]. The gauge factor (GF) of a strain gauge is defined as:

$$GF = \frac{\left(\frac{\Delta R}{R} \right)}{\epsilon} \quad (6)$$

where ϵ is strain, and $\Delta R/R$ is the resistance change due to strain. The fractional change in resistivity $\Delta\rho/\rho$ for a metal is small on the order of 0.3 and geometric effects alone provide gauge factors of approximately 1.4 to 2.0. Nevertheless, for silicon and germanium in certain directions, $\Delta\rho/\rho$ is 50 to 100 times larger than the geometric term. This shows that the overall resistance of the certain materials can be dominated by the change in resistance due to stress. For semiconductors both elasticity and resistivity are directionally dependent.

Piezoresistivity refers to a phenomenon in which materials change their resistance in response to an applied stress (or strain). Iron and copper were initially used to study the piezoresistive effect in the eighteenth century by Thompson (Lord Kelvin) [64, 65]. In 1954, Charles Smith discovered the piezoresistive effect in silicon and found the pressure sensitivity in silicon piezoresistors to be significantly larger than that of thin metal film resistors [66]. In contrast to metals, whose primary change in resistance is due to deformation of the geometry, piezoresistance in silicon and other semiconductor materials is based on changes in carrier mobilities. A more detailed explanation for the piezoresistance effect of most semiconductors (e.g., silicon) is given by the electron transfer theory [67]. In silicon, the conduction band possesses six minima in directions of

the main crystal axes. The electron transfer theory relates the anisotropic change in resistivity to a redistribution of electrons among the multivalleys in momentum space. As the minima exhibit an ellipsoidal form, the electron mobility is highly anisotropic. But due to the symmetrical distribution of the six valleys, the net mobility is uniform. The application of a tensile stress in the <100> direction causes the multivalley minima to rise in energy in this direction, while the minima perpendicular to the applied strain will drop.

This energy difference causes a change in the distribution of the electrons between the potential wells and this leads to changes in mobility and resistivity. The resistivity in direction of the applied tensile strain is decreased (longitudinal piezoresistance effect). According to this model and the way the ellipsoidal minima are affected, the transverse piezoresistance effect (measured perpendicular to the applied strain) is smaller and has a different sign.

2.6.1 Transverse and Longitudinal Piezoresistive Coefficients

For sensor applications, it is necessary to discuss the longitudinal and the transverse piezoresistance effect in silicon. In single crystalline cubic materials, the relation between the electric field E and the current density j is described by a second order resistivity tensor:

$$E_i = \sum_j \rho_{ij} j_j \quad (7)$$

The first index i represents the direction of the electric field, while the second index j indicates one of the three current density components along the main crystal axes. Cubic crystals show an isotropic electric behavior in a stress free state:

$$E_1 = \rho_0 j_1 \quad E_2 = \rho_0 j_2 \quad E_3 = \rho_0 j_3 \quad (8)$$

A force acting on the crystal leads to an anisotropic change of the resistivity. Along the main crystal axes, the electric field can be described using the elementary piezoresistance coefficients π_{11} , π_{12} and π_{44} :

$$\frac{E_1}{\rho_0} = j_1 \left[1 + \pi_{11} \sigma_1 + \pi_{12} (\sigma_2 + \sigma_3) \right] + \pi_{44} (j_2 \sigma_6 + j_3 \sigma_5) \quad (9)$$

$$\frac{E_2}{\rho_0} = j_2 \left[1 + \pi_{11} \sigma_2 + \pi_{12} (\sigma_1 + \sigma_3) \right] + \pi_{44} (j_1 \sigma_6 + j_3 \sigma_4) \quad (10)$$

$$\frac{E_3}{\rho_0} = j_3 \left[1 + \pi_{11} \sigma_3 + \pi_{12} (\sigma_1 + \sigma_2) \right] + \pi_{44} (j_1 \sigma_5 + j_2 \sigma_4) \quad (11)$$

For the design of piezoresistive sensors that use a Wheatstone bridge, the longitudinal and the transverse piezoresistance effects play an important role and are defined in Figure 2.1. When stressed longitudinally, all components of E , j and σ have the same directions. Using equations 9-11, the electric field E can be described as:

$$\text{Long} \quad E_1 / \rho_0 = j_1 (1 + \pi_{11} \sigma_1) = j_1 (1 + \pi_{long} \sigma_{long}) \quad (12)$$

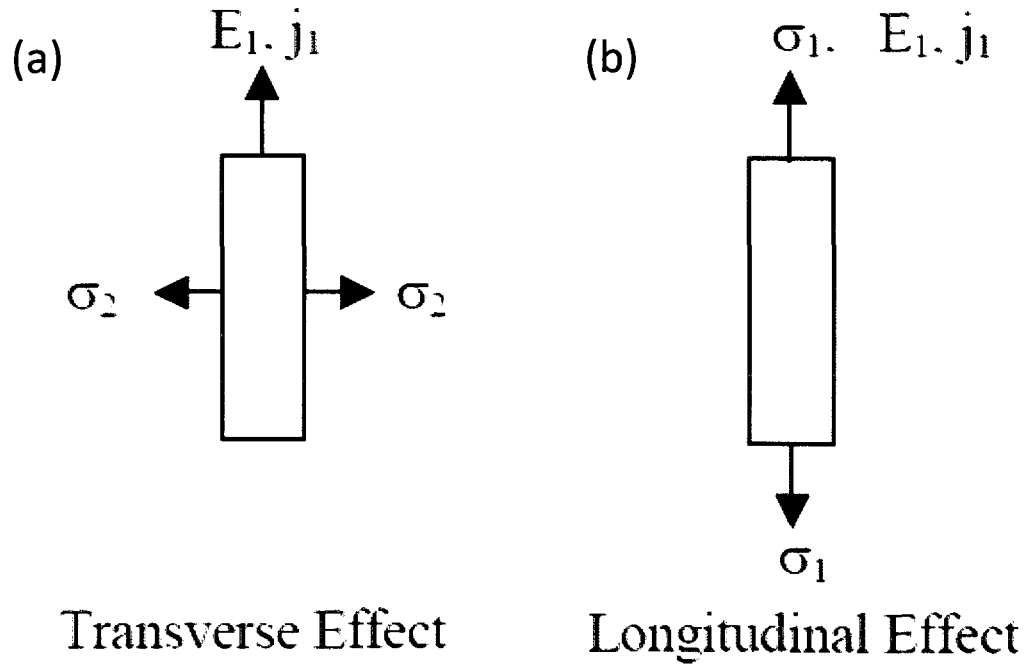


Figure 2.1. Directions of the electric field E , the current density j , and the applied stresses for a (a) transverse and (b) longitudinally stressed piezoresistors.

When stressed transversely, the components of E and j have the same directions, while σ is perpendicular to E and j using equations 9-11, the electric field E can be described as:

$$\text{Trans} \quad E_1/\rho_0 = j_1(1 + \pi_{12}\sigma_2) = j_1(1 + \pi_{trans}\sigma_{trans}) \quad (13)$$

The relative change of resistivity $\Delta\rho/\rho_0$ as appearing in equation 5 for the longitudinal and transverse directions is therefore:

$$\text{Long} \quad (\Delta\rho/\rho_0)_{long} = \pi_{long}\sigma_{long} \quad (14)$$

$$\text{Trans} \quad (\Delta\rho/\rho_0)_{trans} = \pi_{trans}\sigma_{trans} \quad (15)$$

A more general formulation for longitudinal (π_{long}) and transverse (π_{trans}) piezoresistive coefficients for a gauge in an arbitrary crystal direction was developed by Mason and Thurston [68].

$$\text{Long} \quad \pi_{\text{long}} = \pi_{11}' = \pi_{11} - 2(\pi_{11} - \pi_{12} - \pi_{44}) (l_1^2 m_1^2 + l_1^2 n_1^2 + m_1^2 n_1^2) \quad (16)$$

$$\text{Trans} \quad \pi_{\text{trans}} = \pi_{12}' = \pi_{12} + (\pi_{11} - \pi_{12} - \pi_{44}) (l_1^2 l_2^2 + m_1^2 m_2^2 + n_1^2 n_2^2) \quad (17)$$

where l , m , and n are the direction cosines of the direction associated with π_{long} or π_{trans} , with respect to the crystallographic axes.

2.6.2 Micropressure Sensors (bending plate sensors)

A piezoresistive micropressure sensor (bending plate sensor) can be best explained by describing three primary components, the diaphragm, piezoresistors, and Wheatstone bridge. The diaphragm is typically either round or rectangular and thin ($<500\mu\text{m}$) with dimensions typically less than $5 \times 5 \text{ mm}^2$. An external pressure is applied to the diaphragm causing it to deform creating stress in the piezoresistors. Hence, the diaphragm is used to amplify stress within the piezoresistors which converts the magnitude of mechanical stress to relative voltage offset. Today pressure sensor diaphragms are typically made from the same material as the wafer substrate (silicon, silicon carbide, alumina, diamond, etc.) or CVD-based thin films (oxides, nitrides, etc.), but when micropressure sensors were first introduced by Kulite-Bytrex and Microsystems in the late 1950s they were metal [69]. In early piezoresistive sensors semiconductor strain gauges were attached using epoxy adhesive to the surface of a machined metal diaphragm. Four semiconductor strain gauges were utilized, two in tension at the

diaphragm center and two in compression on the metal diaphragms edge. Today piezoresistors are formed by dopant diffusion, ion implantation, or doped epitaxy. Maximum stress occurs at the edge of the diaphragm so piezoresistors are usually located near the edge in a Wheatstone bridge configuration to maximize sensitivity.

2.7 The Wheatstone Bridge

Pfann and Thurston were the first that recognized the benefits of simultaneously using transverse and longitudinal piezoresistors for pressure sensors [70]. Many of their designs used a full Wheatstone bridge with two longitudinal and two transverse piezoresistors to increase sensitivity and compensate for resistance changes due to temperature as shown in Figure 2.2.

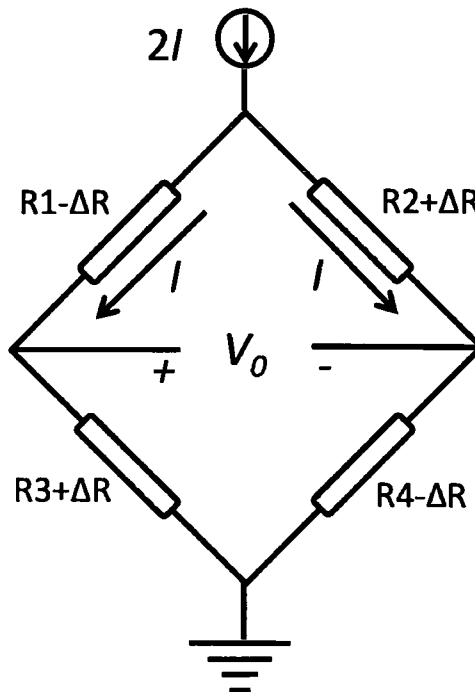


Figure 2.2. Schematic showing the result of applied pressure on a Wheatstone bridge. Typically, two piezoresistors increase in resistance while the other two decrease, depending on orientation and semiconductor type.

In the full bridge configuration, four identical piezoresistors are arranged, two oriented transversely and two longitudinally. When a pressure is applied to the diaphragm, it deforms, and depending on semiconductor type, two of the gauges' resistances will increase while the other two will decrease. This configuration provides enhanced sensitivity and in the absence of an applied stress, the bridge's output is zero.

2.7.1 Temperature Compensation

One of the primary disadvantages of piezoresistive based sensors is their temperature dependence, and hence decreased sensitivity with increased temperature. The Wheatstone bridge is used to mitigate these negative temperature effects. If we assume that all the resistors are the same (i.e. $R_1 = R_2 = R_3 = R_4$). Using a constant current source $2I$, the same current I , will flow in each branch. In the absence of a temperature change, the output voltage is defined by:

$$\Delta V = I(R_1 - R_2) \quad (18)$$

When temperature increases uniformly across the sensors, this causes the resistance to increase, in each of the piezoresistors generating a ΔR . This ΔR is the same for all four resistors, since they are equal in value ΔV is then:

$$\Delta V = I(R_1 + \Delta R) - I(R_2 + \Delta R) = I(R_1 - R_2) \quad (19)$$

Thus, a Wheatstone bridge will generate the same voltage output assuming a uniform temperature and neglecting the effects of temperature on piezoresistor coefficients as shown in Figure 2.3.

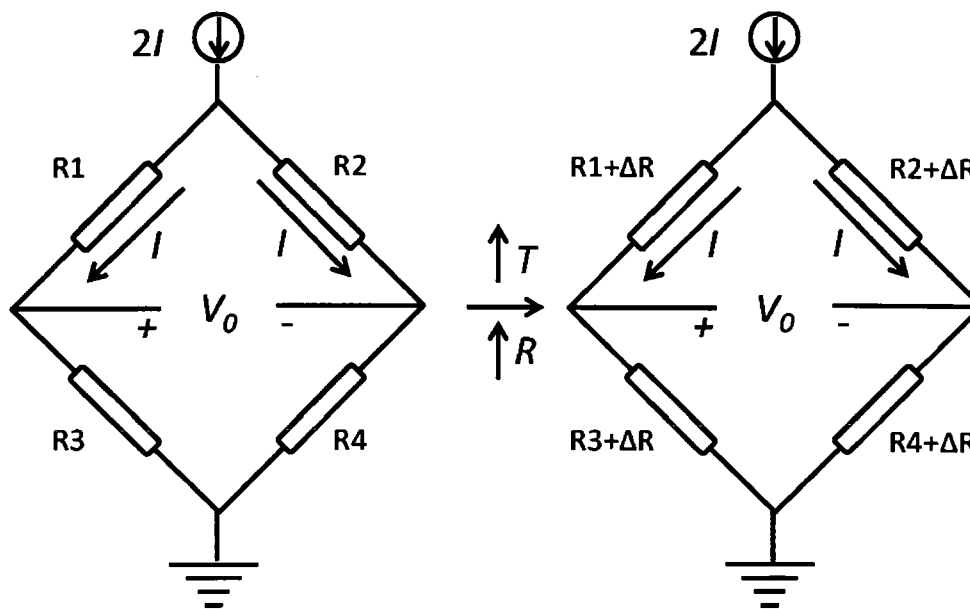


Figure 2.3. Resistors within the Wheatstone bridge all increase with the same ΔR at increased temperatures. Therefore the output voltage (V_0) remains constant and the bridge is temperature compensated.

2.8 Sensor Definitions

The performance criteria in pressure sensors are sensitivity, dynamic range, full-scale output, linearity, and the temperature coefficients of sensitivity and offset. These characteristics depend primarily on the device geometry, piezoresistor locations, and the mechanical/electrical properties of the materials and are useful to define.

2.8.1 Dynamic Range

Dynamic range is the pressure range over which the sensor can provide a meaningful output. It may be limited by nonlinear diaphragm effects, plastic yield and/or catastrophic failure of the diaphragm.

2.8.2 Sensitivity

Sensitivity is defined for pressure transducers as the normalized signal change per unit pressure change to reference signal.

$$S = \frac{1}{\theta} * \frac{d\theta}{dP} \quad (20)$$

Theta (θ) is output signal and $\partial\theta$ is the change in this pressure due to the applied pressure ∂P .

2.8.3 Full-scale Output and Linearity

The full-scale output (FSO) of a pressure sensor is the algebraic difference in the end points of the output over a particular defined pressure range. Linearity refers to the proximity of the device response to a specified straight line. It is the maximum separation between the output and the line, expressed as a percentage of FSO. Piezoresistive sensors have good linearity over a specified range where the deflection of the diaphragm is small relative to its edge length.

2.8.4 Temperature Coefficient of Sensitivity

The temperature sensitivity of a pressure sensor is another performance metric valuable for pressure sensors that are used over a wide range of temperatures. This variance is caused by a number of factors including the resistance change of the piezoresistors due temperature change and thermal expansion mismatches of the materials. The definition of temperature coefficient of sensitivity (TCS) is:

$$TCS = \frac{1}{S} * \frac{dS}{dT} \quad (21)$$

where S is sensitivity, and T is temperature.

2.8.5 Temperature Coefficient of Offset

The offset of a pressure sensor is the value of the output voltage at a reference pressure (conventionally unloaded). Consequently, the TCO is:

$$TCO = \frac{1}{O} * \frac{dO}{dT} \quad (22)$$

where O is offset, and T is temperature.

2.8.6 Summary

Piezoresistance offers a convenient mechanism to convert mechanical pressure to electrical output and was briefly introduced and defined. Utilizing anisotropy of the piezoresistive coefficients in silicon, a Wheatstone bridge offers a simple and effective measurement tool used to determine mechanical pressure while providing temperature compensation. Micropressure sensors using these technologies are mature, robust, and highly configurable making them ideal for the development of hydrogel based chemical sensors.

2.9 References

- [1] "Review of Hydrogel Based Sensors."
- [2] F. Baldini and A. Giannetti, "Optical Chemical and Biochemical Sensors: New Trends." pp. 485-499.
- [3] S. S. Saliterman, "Education, BioMEMS and the Medical Microdevice Revolution," *Expert Rev. Med. Devices*, vol. 2, no. 5, pp. 515-519, 2005.
- [4] A. Gupta, H. Li, R. Gomez *et al.*, "BioMEMS to Bionanotechnology: State of the Art in Integrated Biochips and Future Prospects," *Proc. SPIE - Int. Soc. Opt. Eng. (USA)*. pp. 340-53.
- [5] A. C. R. Grayson, R. S. Shawgo, A. M. Johnson *et al.*, "A BioMEMS Review: MEMS Technology for Physiologically Integrated Devices," *Proceedings of the IEEE*, vol. 92, no. 1, pp. 6-21, 2004.
- [6] R. Bashir, "BioMEMS: State-of-the-Art In Detection, Opportunities and Prospects," *Advanced Drug Delivery Reviews*, vol. 56, no. 11, pp. 1565-1586, 2004.
- [7] K. Wise, "Wireless Integrated Microsystems: Wearable and Implantable Devices for Improved Health Care."
- [8] V. Sridhar and K. Takahata, "A Hydrogel-Based Wireless Sensor using Micromachined Variable Inductors with Folded Flex-Circuit Structures for Biomedical Applications." pp. 70-73.
- [9] A. Richter, D. Kuckling, S. Howitz *et al.*, "Electronically Controllable Microvalves Based on Smart Hydrogels: Magnitudes and Potential Applications," *Journal of Microelectromechanical Systems*, vol. 12, no. 5, pp. 748-753, 2003.
- [10] T. Tanaka, D. Fillmore, S.-T. Sun *et al.*, "Phase Transitions in Ionic Gels," *Physical Review Letters*, vol. 45, no. 20, pp. 1636, 1980.
- [11] B. D. Johnson, D. J. Beebe, and W. C. Crone, "Effects of Swelling on the Mechanical Properties of a pH-Sensitive Hydrogel for Use in Microfluidic Devices," *Materials Science and Engineering: C*, vol. 24, no. 4, pp. 575-581, 2004.
- [12] S. K. De, N. R. Aluru, B. Johnson *et al.*, "Equilibrium Swelling and Kinetics of pH-Responsive Hydrogels: Models, Experiments, and Simulations," *Journal of Microelectromechanical Systems*, vol. 11, no. 5, pp. 544-555, 2002.
- [13] G. Gerlach, M. Guenther, G. Suchanek *et al.*, "Application of Sensitive Hydrogels in Chemical and pH Sensors," *Macromolecular Symposia*, vol. 210, no. 1, pp. 403-410, 2004.

- [14] J. Sorber, G. Steiner, V. Schulz *et al.*, "Hydrogel-Based Piezoresistive pH Sensors: Investigations Using FT-IR Attenuated Total Reflection Spectroscopic Imaging," *Analytical Chemistry*, vol. 80, no. 8, pp. 2957-2962, 2008.
- [15] B. Zhao and J. S. Moore, "Fast pH- and Ionic Strength-Responsive Hydrogels in Microchannels," *Langmuir*, vol. 17, no. 16, pp. 4758-4763, 2001.
- [16] Q. Y. Cai and C. A. Grimes, "A Salt-Independent pH Sensor," *Sensors and Actuators B: Chemical*, vol. 79, no. 2-3, pp. 144-149, 2001.
- [17] T. Miyata, N. Asami, and T. Urugami, "Preparation of an Antigen-Sensitive Hydrogel Using Antigen Antibody Bindings," *Macromolecules*, vol. 32, no. 6, pp. 2082-2084, 1999.
- [18] T. Miyata, N. Asami, and T. Urugami, "A Reversibly Antigen-Responsive Hydrogel," *Nature*, vol. 399, no. 6738, pp. 766-769, 1999.
- [19] T. Miyata, T. Urugami, and K. Nakamae, "Biomolecule-Sensitive Hydrogels," *Advanced Drug Delivery Reviews*, vol. 54, no. 1, pp. 79-98, 2002.
- [20] D. Y. Jung, J. J. Magda, and I. S. Han, "Catalase Effects on Glucose-Sensitive Hydrogels," *Macromolecules*, vol. 33, no. 9, pp. 3332-3336, 2000.
- [21] J. T. Suri, D. B. Cordes, F. E. Cappuccio *et al.*, "Continuous Glucose Sensing with a Fluorescent Thin-Film Hydrogel," *Angewandte Chemie*, vol. 115, no. 47, pp. 6037-6039, 2003.
- [22] D. T. Eddington and D. J. Beebe, "Flow Control with Hydrogels," *Advanced Drug Delivery Reviews*, vol. 56, no. 2, pp. 199-210, 2004.
- [23] A. Guiseppi-Elie, S. Brahim, G. Slaughter *et al.*, "Design of a Subcutaneous Implantable Biochip for Monitoring of Glucose and Lactate," *Sensors Journal, IEEE*, vol. 5, no. 3, pp. 345-355, 2005.
- [24] Y. Zhao, S. Li, A. Davidson *et al.*, "A MEMS Viscometric Sensor for Continuous Glucose Monitoring," *Journal of Micromechanics and Microengineering*, no. 12, pp. 2528, 2007.
- [25] J. Wang, "Electrochemical Glucose Biosensors," *Chemical Reviews*, vol. 108, no. 2, pp. 814-825, 2008.
- [26] G. Lin, S. Chang, H. Hao *et al.*, "Osmotic Swelling Pressure Response of Smart Hydrogels Suitable for Chronically-Implantable Glucose Sensors," *Sensors and Actuators B: Chemical*, vol. 144, pp. 332-336, 2010.
- [27] I. S. Han, M. H. Han, J. Kim *et al.*, "Constant-Volume Hydrogel Osmometer: A New Device Concept for Miniature Biosensors," *Biomacromolecules*, vol. 3, no. 6, pp. 1271-1275, 2002.

- [28] S. Herber, J. Borner, W. Olthuis *et al.*, "A Micro CO₂ Gas Sensor Based on Sensing of pH-Sensitive Hydrogel Swelling by Means of a Pressure Sensor," *Digest of Technical Papers - International Conference on Solid State Sensors and Actuators and Microsystems, TRANSDUCERS '05*. pp. 1146-1149.
- [29] S. Herber, W. Olthuis, P. Bergveld *et al.*, "Exploitation of a pH-Sensitive Hydrogel Disk for CO₂ Detection," *Sensors & Actuators: B. Chemical*, vol. 103, no. 1-2, pp. 284-289, 2004.
- [30] M. Guenther, G. Gerlach, D. Kuckling *et al.*, "Chemical Sensors Based on Temperature-Responsive Hydrogels," *Proc. SPIE*. p. 61670T.
- [31] G. Gerlach, M. Guenther, J. Sorber *et al.*, "Chemical and pH Sensors Based on the Swelling Behavior of Hydrogels," *Sensors and Actuators B: Chemical*, vol. 111-112, pp. 555-561, 2005.
- [32] H. F. Mark and J. I. Kroschwitz, *Encyclopedia of Polymer Science and Engineering*, 2nd ed., New York: Wiley, 1984.
- [33] Q. Y. Cai and C. A. Grimes, "A Remote Query Magnetoelastic pH Sensor," *Sensors and Actuators B: Chemical*, vol. 71, no. 1-2, pp. 112-117, 2000.
- [34] R. Bashir, J. Z. Hilt, O. Elibol *et al.*, "Micromechanical Cantilever as an Ultrasensitive pH Microsensor," *Applied Physics Letters*, vol. 81, no. 16, pp. 3091-3093, 2002.
- [35] J. Z. Hilt, A. K. Gupta, R. Bashir *et al.*, "Ultrasensitive Biomems Sensors Based on Microcantilevers Patterned with Environmentally Responsive Hydrogels," *Biomedical Microdevices*, vol. 5, no. 3, pp. 177-184, 2003.
- [36] Z. A. Strong, A. W. Wang, and C. F. McConaghy, "Hydrogel-Actuated Capacitive Transducer for Wireless Biosensors," *Biomedical Microdevices*, vol. 4, no. 2, pp. 97-103, 2002.
- [37] Q. Thong Trinh, G. Gerlach, J. Sorber *et al.*, "Hydrogel-Based Piezoresistive pH Sensors: Design, Simulation and Output Characteristics," *Sensors and Actuators B: Chemical*, vol. 117, no. 1, pp. 17-26, 2006.
- [38] M. Guenther, G. Gerlach, C. Corten *et al.*, "Hydrogel-Based Sensor for a Rheochemical Characterization of Solutions," *Sensors & Actuators: B. Chemical*, 2007.
- [39] M. Guenther, D. Kuckling, C. Corten *et al.*, "Chemical Sensors Based on Multiresponsive Block Copolymer Hydrogels," *Sensors and Actuators B: Chemical*, vol. 126, no. 1, pp. 97-106, 2007.

- [40] S. Herber, J. Bomer, W. Olthuis *et al.*, "A Miniaturized Carbon Dioxide Gas Sensor Based on Sensing of pH-Sensitive Hydrogel Swelling with a Pressure Sensor," *Biomedical Microdevices*, vol. 7, no. 3, pp. 197-204, 2005.
- [41] S. Herber, J. Eijkel, W. Olthuis *et al.*, "Study of Chemically Induced Pressure Generation of Hydrogels Under Isochoric Conditions using a Microfabricated Device," *The Journal of Chemical Physics*, vol. 121, no. 6, pp. 2746-2751, 2004.
- [42] S. Herber, W. Olthuis, and P. Bergveld, "A Swelling Hydrogel-Based PCO₂ Sensor," *Sensors and Actuators B: Chemical*, vol. 91, no. 1-3, pp. 378-382, 2003.
- [43] G. Lin, S. Chang, C. H. Kuo *et al.*, "Free Swelling and Confined Smart Hydrogels for Applications in Chemomechanical Sensors for Physiological Monitoring," *Sensors & Actuators: B. Chemical*, pp. 186-195, 2008.
- [44] H. J. v. d. Linden, S. Herber, W. Olthuis *et al.*, "Stimulus-Sensitive Hydrogels and their Applications in Chemical Microanalysis," 2003.
- [45] R. ter Steege, S. Herber, W. Olthuis *et al.*, "Assessment of a New Pototype Hydrogel CO₂ Sensor; Comparison with Air Tonometry," *Journal of Clinical Monitoring and Computing*, vol. 21, no. 2, pp. 83-90, 2007.
- [46] A. Richter, A. Bund, M. Keller *et al.*, "Characterization of a Microgravimetric Sensor Based on pH Sensitive Hydrogels," *Sensors and Actuators B: Chemical*, vol. 99, no. 2-3, pp. 579-585, 2004.
- [47] Y. J. Zhao, A. Davidson, J. Bain *et al.*, "A MEMS Viscometric Glucose Monitoring Device." pp. 1816-1819 Vol. 2.
- [48] M. J. Lesho and N. F. Sheppard, "Adhesion of Polymer Films to Oxidized Silicon and its Effect on Performance of a Conductometric pH Sensor," *Sensors and Actuators B: Chemical*, vol. 37, no. 1-2, pp. 61-66, 1996.
- [49] N. F. Sheppard Jr, "Design of a Conductimetric Microsensor Based on Reversibly Swelling Polymer Hydrogels." pp. 773-776.
- [50] N. F. Sheppard, M. J. Lesho, P. McNally *et al.*, "Microfabricated Conductimetric pH Sensor," *Sensors and Actuators B: Chemical*, vol. 28, pp. 95-102, 1995.
- [51] N. F. Sheppard, M. J. Lesho, R. C. Tucker *et al.*, "Electrical Conductivity of pH-Responsive Hydrogels," *Journal of Biomaterials Science, Polymer Edition*, vol. 8, pp. 349-362, 1997.
- [52] A. Kikuchi, K. Suzuki, O. Okabayashi *et al.*, "Glucose-Sensing Electrode Coated with Polymer Complex Gel Containing Phenylboronic Acid," *Analytical Chemistry*, vol. 68, no. 5, pp. 823-828, 1996.

- [53] O. Oktar, P. Caglar, and W. R. Seitz, "Chemical Modulation of Thermosensitive Poly(N-isopropylacrylamide) Microsphere Swelling: a New Strategy for Chemical Sensing," *Sensors and Actuators B: Chemical*, vol. 104, no. 2, pp. 179-185, 2005.
- [54] Z. M. Shakhsher, I. Odeh, S. Jabr *et al.*, "An Optical Chemical Sensor Based on Swellable Dicarboxylate Functionalized Polymer Microspheres for pH Copper and Calcium Determination," *Microchimica Acta*, vol. 144, no. 1, pp. 147-153, 2004.
- [55] V. L. Alexeev, A. C. Sharma, A. V. Goponenko *et al.*, "High Ionic Strength Glucose-Sensing Photonic Crystal," *ANALYTICAL CHEMISTRY*, vol. 75, no. 10, pp. 2316-2323, 2003.
- [56] S. A. Asher, V. L. Alexeev, A. V. Goponenko *et al.*, "Photonic Crystal Carbohydrate Sensors: Low Ionic Strength Sugar Sensing," *Journal of the American Chemical Society*, vol. 125, no. 11, pp. 3322-3329, 2003.
- [57] J. H. Holtz and S. A. Asher, "Polymerized Colloidal Crystal Hydrogel Films as Intelligent Chemical Sensing Materials," *Nature*, vol. 389, no. 6653, pp. 829-832, 1997.
- [58] K. Lee and S. A. Asher, "Photonic Crystal Chemical Sensors: pH and Ionic Strength," *Macromolecules*, vol. 27, pp. 1446-1454, 1994.
- [59] J. P. Walker and S. A. Asher, "Acetylcholinesterase-Based Organophosphate Nerve Agent Sensing Photonic Crystal," *Analytical Chemistry*, vol. 77, no. 6, pp. 1596-1600, 2005.
- [60] T. Schalkhammer, C. Lobmaier, F. Pittner *et al.*, "Metal Island Coated Polymer Sensor for Direct Determination of the Volume Effect of Chaotropic Agents," *Microchimica Acta*, vol. 121, no. 1, pp. 259-268, 1995.
- [61] A. G. Mayes, J. Blyth, R. B. Millington *et al.*, "Metal Ion-Sensitive Holographic Sensors," *Analytical Chemistry*, vol. 74, no. 15, pp. 3649-3657, 2002.
- [62] A. A. Barlian, W. T. Park, J. R. Mallon *et al.*, "Review: Semiconductor Piezoresistance for Microsystems," *Proceedings of the IEEE*, vol. 97, no. 3, pp. 513-552, 2009.
- [63] W. A. Brantley, "Calculated Elastic Constants for Stress Problems Associated with Semiconductor Devices," *Journal of Applied Physics*, vol. 44, no. 1, pp. 534-535, 1973.
- [64] H. Tomlinson, "On the Increase in Resistance to the Passage of an Electric Current Produced on Wires by Stretching.[Abstract]," *Proceedings of the Royal Society of London*, vol. 25, pp. 451-453, 1876.

- [65] H. Tomlinson, "The Influence of Stress and Strain on the Action of Physical Forces," *Proceedings of the Royal Society of London*, vol. 33, no. 216-219, pp. 276, 1881.
- [66] C. S. Smith, "Piezoresistance Effect in Germanium and Silicon," *Physical Review*, vol. 94, no. 1, pp. 42, 1954.
- [67] C. Herring and E. Vogt, "Transport and Deformation-Potential Theory for Many-Valley Semiconductors with Anisotropic Scattering," *Physical Review*, vol. 101, no. 3, pp. 944, 1956.
- [68] W. P. Mason and R. N. Thurston, "Use of Piezoresistive Materials in the Measurement of Displacement, Force, and Torque," *The Journal of the Acoustical Society of America*, vol. 29, no. 10, pp. 1096-1101, 1957.
- [69] H. A. Nielsen and H. A. Neilsen, "From Locomotives to Strain Gages," Vantage Press Inc., 1985.
- [70] W. G. Pfann and R. N. Thurston, "Semiconducting Stress Transducers Utilizing the Transverse and Shear Piezoresistance Effects," *Journal of Applied Physics*, vol. 32, no. 10, pp. 2008-2019, 1961.

CHAPTER 3

HIGH SPEED WAFER SCALE BULGE TESTING FOR THE DETERMINATION OF THIN FILM MECHANICAL PROPERTIES

3.1 Abstract

A wafer scale bulge testing system has been constructed to study the mechanical properties of thin films and microstructures. The custom built test stage was coupled with a pressure regulation system and optical profilometer which gives high accuracy three dimensional topographic images collected on the timescale of seconds. Membrane deflection measurements can be made on the wafer scale (50 mm to 150 mm) with up to nanometer-scale vertical resolution. Gauge pressures up to 689 kPa (100 PSI) are controlled using an electronic regulator with an accuracy of approximately 0.344 kPa (.05 PSI). Initial testing was performed on square diaphragms 350, 550, and 1200 μm in width comprised of 720 \pm 10 nm thick low pressure chemical vapor deposited (LPCVD) silicon nitride with \sim 20 nm of e-beam evaporated aluminum. These initial experiments were focused on measuring the system limitations and used to determine what range of deflections and pressures can be accurately measured and controlled. Gauge pressures from 0 to \sim 8.3 kPa (1.2 PSI) were applied to the bottom side of the diaphragms and their deflection was subsequently measured. The overall pressure resolution of the system is good (\sim 350 Pa) and small fluctuations exist at pressures below 5 kPa leading to a larger

standard deviation between deflection measurements at low pressures. Analytical calculations and computed finite element analysis (FEA) deflections closely matched those empirically measured. Using an analytical solution that relates pressure deflection data for the square diaphragms the Young's modulus was estimated for the films assuming a Poisson's ratio of $\nu=0.25$. Calculations for the Young's modulus for the smaller diaphragms proved difficult because the pressure deflection relationship remained in the linear regime over the tested pressure range. Hence, the calculations result in a very large error when used to estimate the Young's modulus for the smaller membranes. For the largest membrane tested the deflection pressure data set was fitted to the analytical solutions and estimated to be 454 GPa for the $1200 \times 1200 \mu\text{m}^2$ diaphragms. This analytical model ignored the reflective sputtered aluminum layer which increases the film modulus; therefore calculations were slightly higher than previously reported values.

3.2 Introduction

The mechanical properties of thin films are an important metric used in design and fabrication of sensors and microelectromechanical systems (MEMS), and play a large role in overall device behavior [1-3]. It is well known that thin film material properties vary significantly from their bulk counterparts [4] and thin films can withstand higher failure stresses than the same bulk material [5]. Bulge testing is a technique that can quickly derive information on mechanical properties of thin films including Young's modulus, biaxial modulus, yield strength, fracture strength, and residual stress. In bulge testing, a membrane is fastened into place, pressure is applied, and the resulting deflection is measured. The residual stress can be determined from measuring deflection

at low pressures, while the deformations at higher pressures are used to determine the biaxial modulus . This technique has the unique advantage of extracting these material characteristics simultaneously from membrane deflection.

Data derived from the pressure-deflection relationship are also useful for the development of micropressure sensors. The mechanics that define and stresses induced in the sensing diaphragms are strongly correlated to both deflection and curvature of the bulge. For piezoresistive pressure sensors, it is useful to perform bulge testing to determine sensor sensitivity by correlating their output voltage to applied pressure; the resulting diaphragm deflection can be helpful in determining stress found within the piezoresistors.

In the past, bulge testing thin films was susceptible to sample irregularities (thickness, defects) and a number of problems existed related to sample mounting [6, 7]. This created a need for samples to be fabricated with tight tolerances and high uniformity. Microfabrication technologies address these requirements directly by using processes that are highly optimized and repeatable. The silicon wafer acts as an excellent substrate for thin films due to its high strength, homogeneity and wet etching characteristics. Silicon wafers oriented with a [100] surface allow the anisotropic etching along the (110) planes of the substrate using potassium hydroxide (KOH). Many diaphragms can be simultaneously fabricated across the wafer from the deposited thin films which are defined by sidewalls at angles of 54.74° to the surface.

Typically, laser interferometers, atomic force microscopes (AFM), and mechanical profilometers have been used to analyze the deflection of individual films under load [8-10]. Brown *et al.* hold a patent on a system used to perform bulge testing

on the wafer scale using noncontact profilometry similar to the one presented within this report [11]. Alternative methods to calculate stress and strain relationships include X-ray diffraction, nano-indentation and wafer curvature techniques [9, 12-15]. The American Society for Testing and Materials (ASTM) standard for determination of mechanical properties of bulk materials are tensile and bend tests which prove difficult to perform on thin films [16].

Our bulge test system directly integrates an optical profilometer (Zygo, NewView 5032, Middlefield, CT, USA) and wafer scale mounting stage with a pressure control subsystem (Tescom, ER 3000, Elk River, MN, USA). The apparatus allows the determination of film properties through measuring the deflection of thin diaphragms accurately with a 3D dataset. The initial system specifications are presented in Table 3.1.

This tool also allows us to enhance our thin film deposition techniques and sensor designs by better characterizing thin film mechanical behavior. Large variations in membrane deflection across a wafer indicate that thin film material variation exists either in thickness or microstructure. However, use as an in-situ monitoring tool requires the backside etching of the wafer after each deposition.

Table 3.1. Initial design specifications of the bulge testing system.

System Requirement	Value
Wafer Size (mm)	50-150
Diaphragm Size (mm)	0.1-2
Measurement Time (min)	< 1
Deflection Range (μm)	0.01-1000
Deflection Resolution (nm)	< 5
Pressure Range (kPa)	0-200
Pressure Resolution (kPa)	0.5

This report discusses the design of the apparatus and gives the initial low pressure test results used to determine system capabilities. Analytical and finite element models of membrane deformation are compared empirical measurements. Young's modulus is then calculated for the films using three sizes of square silicon nitride diaphragms.

3.3 Experimental

3.3.1 Bulge Testing System

The bulge testing system is comprised of three main components including the diaphragm mounting stage, pressure regulation system, and optical profilometer. The mounting stage is used to secure wafers ranging in size from 50 to 150 mm and made from aluminum and is presented in Figure 3.1.

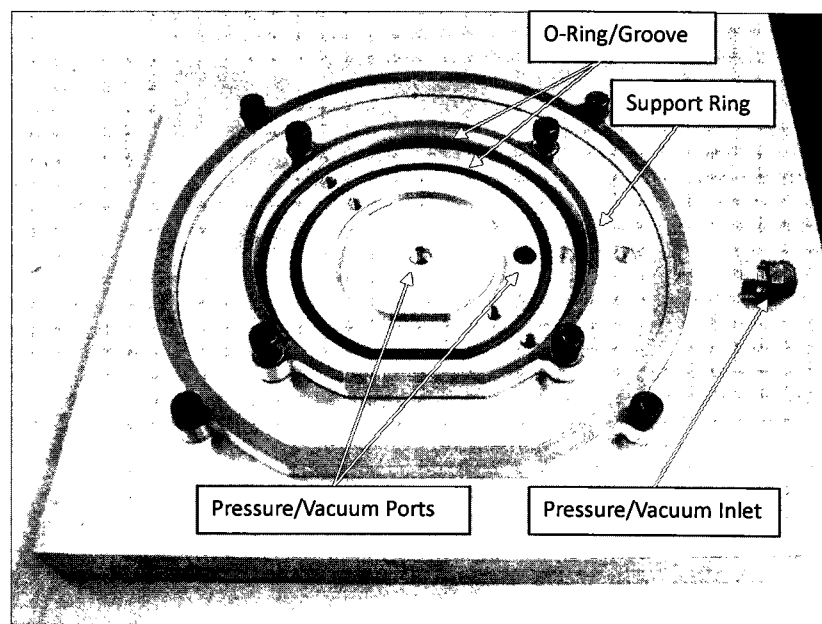


Figure 3.1. Photograph of the wafer mounting stage used for bulge testing of silicon nitride-aluminum membranes. Wafers ranging in size from 50 to 150 mm can be mounted while pressure is applied to the backside of the membranes.

Aluminum clamping rings with flat bottom surfaces approximately 8 mm wide are used to apply uniform pressure to the topside of the wafer circumference creating a compression seal against the o-rings. The aluminum clamping rings are tightened down manually with four screws. This compression insures that small leaks are minimized between the wafer and stage which may lead to pressure fluctuations and deflection error. With this mounting system it is also possible to achieve downward deflection by applying vacuum to the backside of the wafer. Wafer curvature was measured (without applied pressure) using mechanical profilometry (P-20, Tencor, Milpitas, CA, USA) after mounting and showed that the wafer clamping ring compression did not significantly alter the initial wafer curvature. Ports 10 mm in diameter located in between differently sized mounting rings are used to apply pressure to the space beneath the wafer. When smaller wafers are tested, ports located on the periphery are sealed using small plugs with integrated o-rings.

Individual test samples can also be mounted to a stainless steel dummy wafer using a two part epoxy. The dummy wafer serves as an “adapter” between the test sample and the wafer level bulge tester. The adapter is made from 304 stainless steel and has a 150 μm hole located in its center.

Pressure is applied to the mounting stage using an electro-pneumatic regulator (ER3000, Tescom, McKinney, TX, USA) with the ability to modulate pressures up to 689 kPa (100 PSIG) with 344 Pa (0.05 PSIG) accuracy. The regulator was microprocessor controlled and used a proportional-integral-derivative (PID) method to compare the internal pressure sensor signal to the set point controlling a pair of inlet and outlet solenoid valves. The system has the capability to use a high accuracy external

pressure transducer and dome loaded pressure regulator to accurately control pressures over a wider range. Internal control parameters such as PID settings, zero, and span can be remotely controlled via a PC through an RS-485 interface. Data recording and custom pressure routines can also be easily implemented.

A Newview 5032 (Zygo Instruments Inc, Middlefield, CT, USA) system was used to perform noncontact white light optical profilometry on deflected membranes. The system has the advantage of making fast measurements (< 10 s) without physical contact and is able to make lateral measurements over the 150 mm diameter wafer. Our instrument had the 5X and 20X objectives installed which allows us to analyze diaphragms 250 μm to 2.5 mm in size and deflections in the nanometer range. This report only discusses square diaphragms that are 350 to 1200 μm in width bulged at low pressure ($< 10\text{kPa}$).

3.3.2 Membrane Preparation

The $\text{Si}_3\text{N}_{4-x}$ films used in this study were deposited on *n*-type (1-10 Ωcm) 100 mm diameter silicon wafers by low pressure chemical vapor deposition (LPCVD). This LPCVD nitride also acts as the KOH bulk silicon etch mask. The deposition was performed at 825°C for 2 hours with an approximate deposition rate of 6 nm/min. The precursors used were dichlorosilane (DCS) and ammonia at a 6:1 ratio (DCS: NH_3) with flow rates of 60 and 10 sccm, respectively. The stoichiometry of the Si:N is 1.0:1.07 according to X-ray photo electron spectroscopy (XPS) data. An average $\text{Si}_3\text{N}_{4-x}$ tensile stress of 311 ± 7 MPa was calculated for two wafers using Stoneys equation [17]. Stress in these films is attributed to the mismatch between the coefficients of thermal expansion of the Si substrate and the film and intrinsic stress within the film [18]. Five additional

wafers with deposited LPCVD nitride were coated with Shipley 1813 positive photo resist was spun on at 3000 rpm for 30 seconds and soft baked for 90 seconds at 110°C. Three sizes of square etch openings were patterned on the wafers using chrome masks which corresponded to diameter of 350, 550, and 1200 μm . Alignment of the square diaphragms to the wafer flat was performed using an Electronic Visions 420 (EV Group Inc, Tempe, AZ, USA) mask aligner on the backside of the wafer. Each of the wafers' was patterned with an orthogonal array membranes aligned to the wafers edge with a pitch of 5 mm. The silicon nitride provides high selectivity when used as a potassium hydroxide (KOH) masking layer and acts as the structural material for free-standing square membranes in this experiment. The photoresist was exposed using a UV light source for 9 seconds with an intensity of 75 mJ/cm^2 for patterning. Then it was developed using Shipley 352 developer for 1 minute. Resist was hard baked for 5 minutes at 90°C. Reactive ion etching was performed using an Oxford 100 at a pressure of 5 mTorr and power of and 100 W. A mixture of SF_6 and O_2 are used to open etch windows on the backside of the wafer.

A Tencore P-20 (Tencor, Milpitas, CA, USA) contact profilometer verified a nitride film thickness of 720 ± 10 nm measuring across the windows. Initial wafer thickness measurements using a dial indicator (series-543, Mitutoyo, Kanagawa, Japan) yield a total wafer thickness of 423 ± 1 μm . A square opening was wet etched through the back side of the wafer using 60% concentration KOH solution at 87°C. The backside openings were etched for 7.75 hours giving an average etch rate of ~ 1.1 $\mu\text{m}/\text{min}$. The $\text{Si}_3\text{N}_{4-x}$ membranes appeared yellow and semitransparent. Due to the transparency the $\text{Si}_3\text{N}_{4-x}$ membranes optical profilometry could not be used directly on the membranes.

Therefore e-beam evaporation of 20 nm of aluminum was performed in a Denton evaporator (Denton Vacuum, Moorestown, NJ, USA) system at a voltage of 6.5kV and current of 0.1 A to make the membranes opaque. A 20 nm thick film was deposited in 15 seconds at a rate of at a rate of ~ 13 A/min, measured using a quartz crystal thickness monitor.

3.3.3 Testing Methods

Wafers with silicon nitride diaphragms were loaded into the bulge testing stage and mounted in the Zygo Newview 5032 motorized XY table. The membranes were aligned under the microscope objective in field of view and then placed into focus. Pressures were applied on the backside of the membranes and all scans were performed using the 20X objective and zoom of 1.3X with a scan height of 20 μm . The membrane height data were recorded at pressure intervals of 645 Pa (0.1 PSI). After measurements were complete, data were exported using Zygo MetroPro™ software which allows a 2D cross section to be taken in the diaphragm center.

3.4 Results and Discussion

To quantify the accuracy of the new bulge test system, deflection results from the membranes were compared between analytical models, FE analysis, and empirical data. These pressure-deflection data were also used to calculate the effective Young's modulus of the laminate silicon nitride-aluminum membranes.

3.4.1 Analytical Model

A number of analytical models have been developed to study deflection and stress characteristics in square membranes as a function of applied pressure. The relationship

between the external pressure and the membrane deflection initially was studied by Timoshenko who developed an analytical solution. In the small elastic deflections, where the pressure and deflection are linearly related there also exists an exact solution presented by Levy in the form of a series, which is also given in Timoshenko's book on plates and shells. Tabata was able to calculate biaxial modulus and Poisson's ratio from deflection characteristics of rectangular membranes [19, 20]. Pan *et al.* compared the analytical solution with finite element method (FEM) analysis and found that the functional form of the analytical solution is correct, but the constants needed minor correction [21]. Several additional models were also developed to improve accuracy of material characterization from the load-displacement data [6, 7, 10, 22-25]. Maier-Schneider *et al.* developed a solution in determining pressure-deflection characteristics for square silicon nitride membranes [26] shown in equation 1. This solution is similar in form to more current solutions found by Vlassak *et al.* [6].

$$P = 3.45 \left(\frac{\sigma_r \cdot t}{a^2} \right) d + 2.48 \left(\frac{E t}{a^4} \right) d^3 \quad (23)$$

where P is the load pressure, t the thickness, E Young's modulus, σ_r the residual stress, 3.45 and 2.48 were empirically found numerical constants that depend on Poisson's ratio and membrane aspect ratio, and d is the maximum center deflection at one half of the membrane's edge length. The aluminum layer is less than 5% of the membrane thickness and Young's modulus is significantly lower (70 GPa) [16, 25]. Therefore this model is still applicable although it neglects the additional reflective aluminum layer.

3.4.2 Computer Simulations

Finite element analysis was carried out on the $\text{Si}_3\text{N}_4\text{-x}/\text{Al}$ membrane structures using Comsol 3.4a (Comsol, Burlington, MA, USA). One quarter of the square membrane is modeled because four-fold symmetry can be utilized to reduce the complexity of the model and reduce total number of calculations. Since the membranes are subjected to relatively low pressures the deformation of silicon wafer support frame can be neglected as determined by initial simulations. Fixed boundary conditions are placed on two of the adjacent membrane edges (clamped) mimicking the silicon wafer frame. On the remaining two internal edges symmetry boundary conditions were used. For analysis, the membrane was first meshed using square mapping then divided into rectangular elements in all three dimensions. This meshing was used because it is the most efficient in terms of node quantity and calculation efficiency for this geometry. Large deformation conditions were utilized since the deflections of the membranes were several times that of the membrane thickness over the simulated pressure range. According large deflection theory, the work created by the application uniform pressure on the membrane is transformed to the elastic energy of the membrane, which consists of the material stretching [27]. The stretching is due to the extending of the middle plane of the membrane and bending due to the out-of-plane displacement. Material parameters used for computer simulations are shown in Table 3.2. The static pressure load is applied to backside of the membrane up to 8.28 kPa (1.2 PSI) in increments of 0.689 kPa (0.1 PSI). A parametric study was used to determine the deflection over this pressure range. The deflection results at ~6.2 kPa (0.9 PSI) are shown in Figure 3.2.

Table 3.2. Material parameters used in Comsol 3.3 finite element simulations.

Simulation Parameter	Value
Modulus $\text{Si}_3\text{N}_{4-x}$ (GPa)	297
$\text{Si}_3\text{N}_{4-x}$ Residual Stress (MPa)	311 ± 7
Modulus Al (GPa)	79
Membrane Width (μm)	350 to 1200
$\text{Si}_3\text{N}_{4-x}$ Thickness (nm)	720
Al Thickness (nm)	20

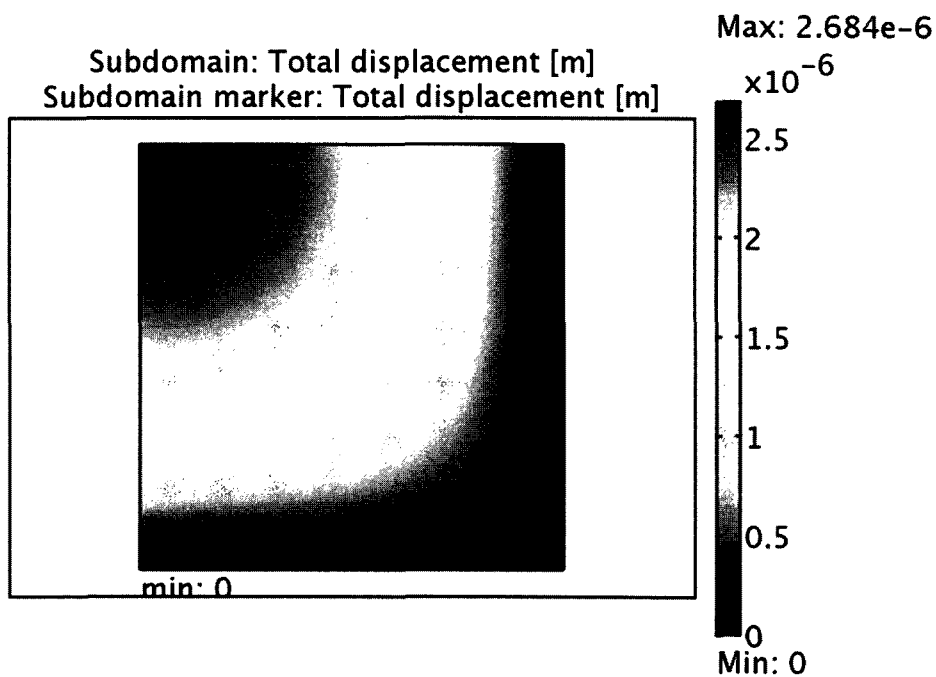


Figure 3.2. Displacement plot illustrating a deflection of $2.68 \mu\text{m}$ for a quarter of the $1200 \times 1200 \mu\text{m}^2$ square membrane calculated using finite element analysis at a pressure of 6894 Pa (1 PSI). The composite structure consists of 720 nm of silicon nitride with 20 nm of aluminum. The bottom and right edges are fixed (clamped) and a symmetry boundary condition placed on the left and top sides.

3.4.3 Empirical Measurements

Measurements of the $720 \pm 10 \text{ nm}$ thin films require that low pressures ($< 10 \text{ kPa}$) can be applied without the interference of noise from the outside environment. The primary objective of these initial tests was to qualify the system and determine any sources of error and/or noise. Deflections data can be displayed in a number of different formats including a 3D mesh plots, solid plots, and surface plots shown in Figure 3.3. The optical image of the bulged $1200 \times 1200 \mu\text{m}^2$ diaphragm shows that aluminum layers were deposited with large compressive stress, consistent with the delamination and buckling observed in the Figure 3.3b.

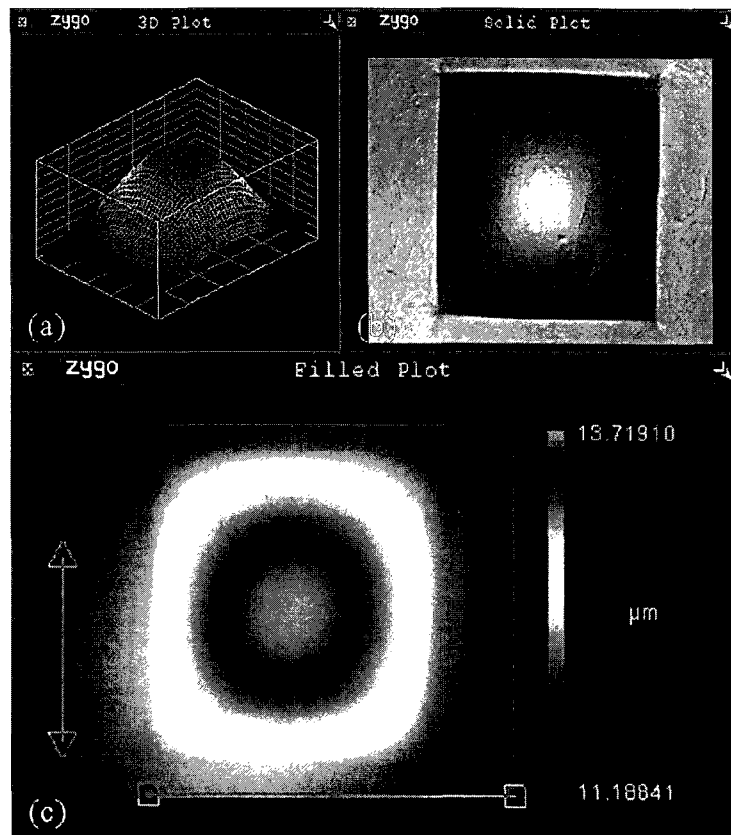


Figure 3.3. Height data displayed as (a) 3D plot, (b) solid plot and (c) surface plot from the Zygo Newview 5032 optical pyrometer. This membrane is 1.2 mm length and a laminate structure consisting of 720 nm of $\text{Si}_3\text{N}_{4-x}$ and 20 nm of aluminum loaded at 6894 Pa (1 PSI).

Due to the significant aluminum film buckling and the thickness of the layer being approximately 2.7 % of silicon nitride we disregarded the 20 nm sputtered aluminum layer for analytical calculations. The finite element simulations took the aluminum layer into account but assumed the aluminum residual stress was negligible. The deflection for the square diaphragms 350, 550, and 1200 μm in width are presented in Figure 3.4 (a-c) for pressures ranging from 0 to 8.3 kPa (1.2 PSI). Deflection results show little variation between theoretical, simulated and measured results. Figure 3.4d shows the standard deviation between measurements for the various membranes. When comparing the analytical and FEA diaphragm deflection models, FEA deflections were slightly lower, which may be due to the additional aluminum layer that had to be added on top of the diaphragm. In general, the deflections of the membranes were slightly lower than analytical calculations but higher than simulations and within 2% of calculated values.

We additionally observed through data analysis that minute pressure fluctuations impacted the deflection data and a number of trends existed. First, as the membranes become larger they become more susceptible to minute pressure fluctuations and the membranes have a higher standard deviation between identical measurements shown in Figure 3.4d. Secondly, at lower pressures, measurements have higher variation in deflection. We suspect this discrepancy in measurements is caused by pressure variations due to control limitations of the electronic pressure regulator. Since the deviation of empirical measurements is small (10^{-2}) with respect to the mean deflection values this system is capable of measuring minute deflections at low pressures (<10 kPa) reliably.

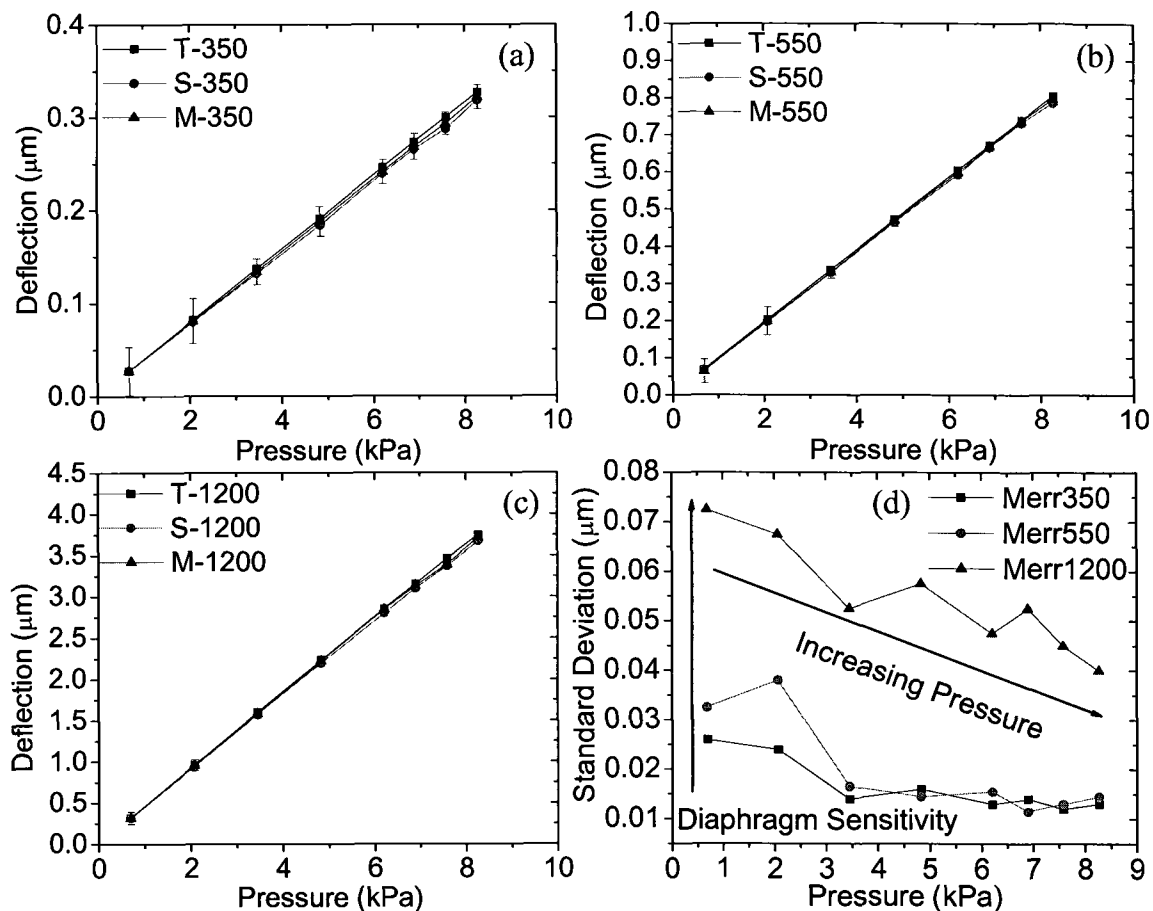


Figure 3.4. Comparison of the theoretical, simulated, and measured deflection of diaphragms with widths of (A) 350 μm (B) 550 μm and (C) 1200 μm at applied pressures ranging from 689 Pa (0.1 PSI) to 6894 Pa (1.2 PSI). Figure 3.4D shows that standard deviation between measurements is a function of pressure and diaphragm sensitivity. At elevated pressures the standard deviation between measurements is reduced and larger diaphragms are more sensitive and susceptible to minute pressure fluctuations.

No trends appear to exist in relation to wafer position and the deflection values have similar standard deviations when compared to previous samples.

The system allows the export of data from the cross section of the bulged diaphragm in order to analyze the shape of the deflected diaphragms. The shape of the deflected diaphragms generated by the FEA models was also compared with the real membrane shape along the centerline shown in Figure 3.5B. Although these data can potentially become slightly skewed with respect to the origin of the coordinate system since the user manually defines the centerline of the bulge, deflection results closely match those predicted by finite element analysis.

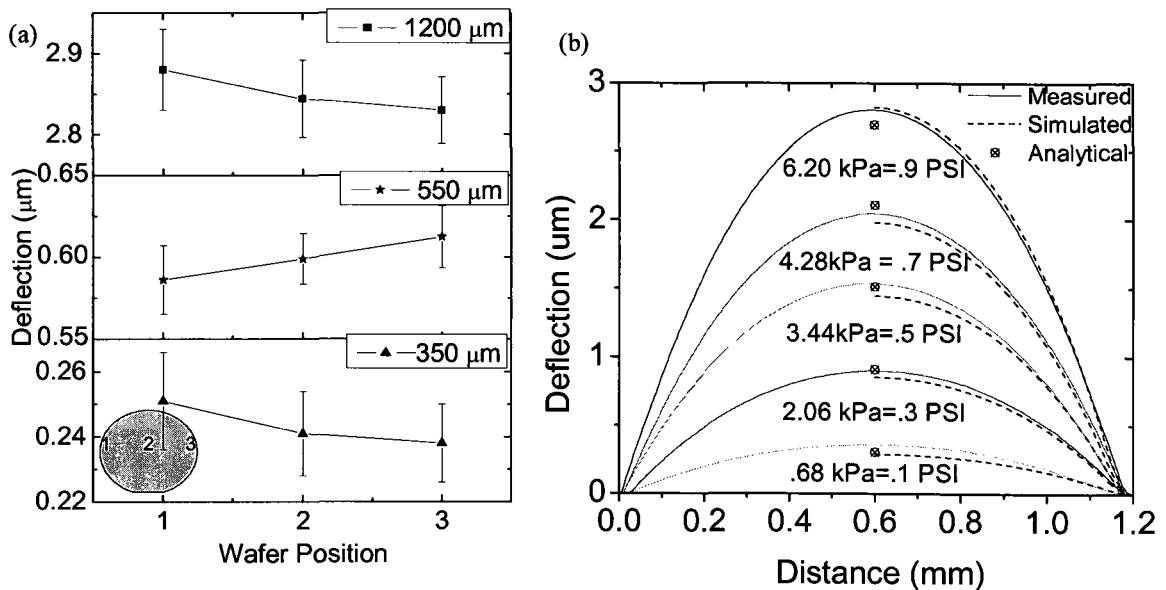


Figure 3.5. Deflection measurements taken for samples located on the left, right and center wafer at a pressure of 6.2 kPa (.9 PSI) (a) and comparison of the measured (-----), simulated(- - -), and analytical (•) deflection of a $1200 \times 1200 \mu\text{m}^2$ square silicon nitride-aluminum membrane with load ranging from 689 to 6.2 kPa (0.1 to 0.9 PSIG) (b). Analytical and simulated results show little variation.

Any slight misalignment of exported bulge shape could possibly be alleviated with software routines that automatically determine the membrane centerline.

3.4.4 Estimation of Young's Modulus

Since testing was performed on square membranes the estimation of Poisson's ratio is required in order to solve for the Young's modulus using equation 1. A value of $\nu = 0.25$ was used for Poisson's ratio which leads to values of 3.45 and 2.48 for the constants of equation 23[26]. Solving equation 23 for the Young's modulus (E) we obtain the expression where a is one half the diaphragm width, P is applied pressure, and d is the measured deflection:

$$E = \frac{0.4032 \left(-P + \frac{3.45 \theta t d}{a^2} \right) a^4}{t d^3} \quad (24)$$

Through further simplification:

$$E = \frac{0.0201 \left(-69. \theta t d + 20. P a^2 \right) a^2}{t d^3} \quad (25)$$

We assume that the residual tensile stress of ($\theta = 311 \pm 7$ MPa) and thickness $t = 720$ nm of the films are identical therefore substitute into 25 obtaining a function that describes the modulus (E) as a function of P , a , and d .

$$\frac{2240.14 \left(-1.93 \cdot 10^5 d + 250. P a^2 \right) a^2}{d^3} \quad (26)$$

From equation 4 we calculated the Young's modulus for deflections of the various membrane sizes as shown in Figure 3.6.

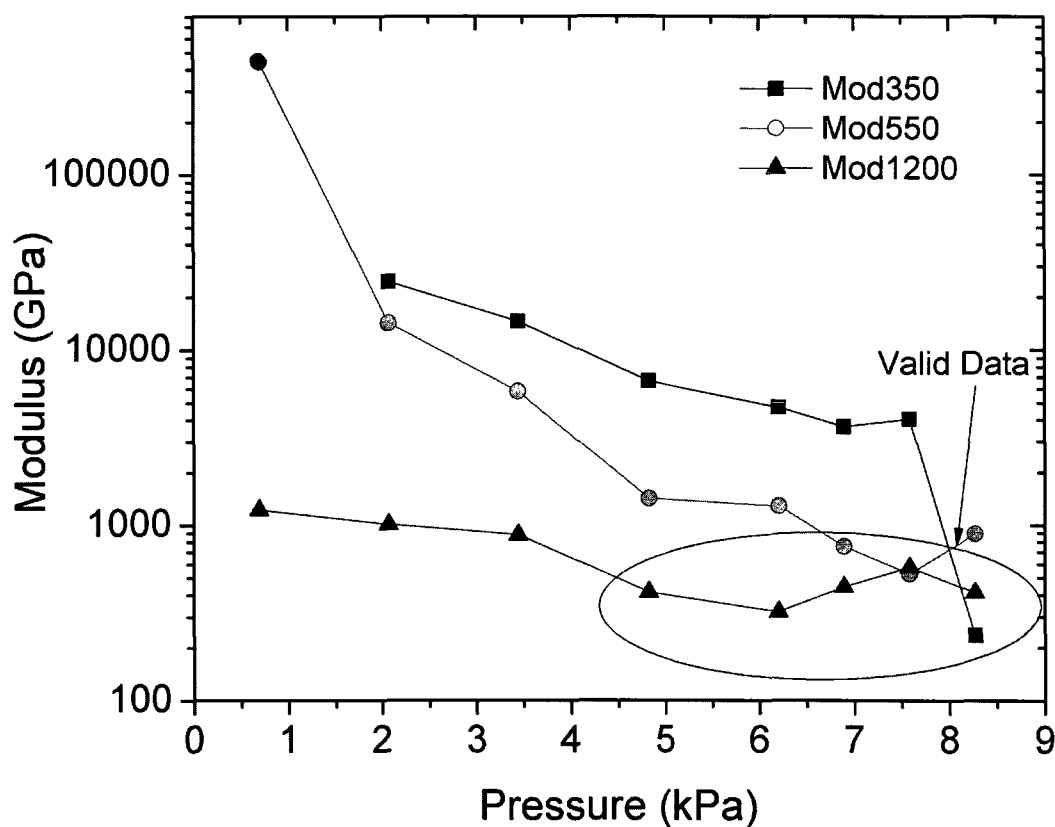


Figure 3.6. Calculation of Young's modulus using equation 1 for diaphragms with widths of 350, 550 and 1200 μm over a pressure range of 0 to 8.5 kPa (0 to 1.23 PSIG). Using this technique calculated values became nonsensical for diaphragms with smaller widths (350 and 550 μm) and at lower pressures (<5 kPa). This is due to the higher measurement variability attributed to reduced pressure control and limitations of instrument resolution. The submicron deflections of the smaller diaphragms lead to higher measurement uncertainty and large variations in young modulus calculations.

We were able to determine that we could only reasonably calculate the Young's modulus for the largest diaphragms, with the highest applied pressures, and most nonlinear deflections. The smaller diaphragms at these low pressures were only found to deflect in the linear regime; therefore calculation of the Young's modulus was inaccurate with high error. Specifically the $1200 \times 1200 \mu\text{m}^2$ diaphragm had average calculated Young's modulus ranging from 321 to 576 GPa from 4.5 to 8.5 kPa. While trying to calculate the Young's modulus for specific data points we determined that a combination

of inability to control low pressures exactly and limitations in the submicron resolution of the optical profilometer created incorrect or shifted modulus results for many of the individual data points.

In order to more accurately determine the Young's modulus of thin films the pressure was plotted as a function of deflection and fitted using equation 23 across the entire range of measurements as shown in Figure 3.7. The fits were very accurate with r-square values >99% and this technique showed improved results over the point evaluation methods described above. The Young's modulus was calculated across the entire pressure range and was 454 GPa for the $1200 \times 1200 \mu\text{m}^2$ while the moduli of the $550 \times 550 \mu\text{m}^2$ and $350 \times 350 \mu\text{m}^2$ diaphragms were 9.05 GPa and 3.32×10^3 GPa, respectively, which are nonsensical. The 454 GPa estimate for Young's modulus of the $1200 \times 1200 \mu\text{m}^2$ appears high and is likely due to variation created by the sputtered aluminum layer which is ignored in the analytical solution. To improve the accuracy of the Young's modulus calculations future tests should use larger diaphragms at higher pressures which are more nonlinear. Although fitting the pressure-deflection function (equation 23) achieved better results with the empirical data, it was determined that the system was incapable of precisely measuring the deflection and pressure with of the smaller diaphragms, due to being in the linear regime.

Without significant measurable nonlinearity we were unable to solve for Young's modulus in smaller diaphragms. Therefore in future tests to increase the deflection nonlinearity higher pressures and larger diaphragms should be used. This nonlinearity will increase the contribution of Young's modulus on the membrane deformation, which will allow more accurate quantification of this value.

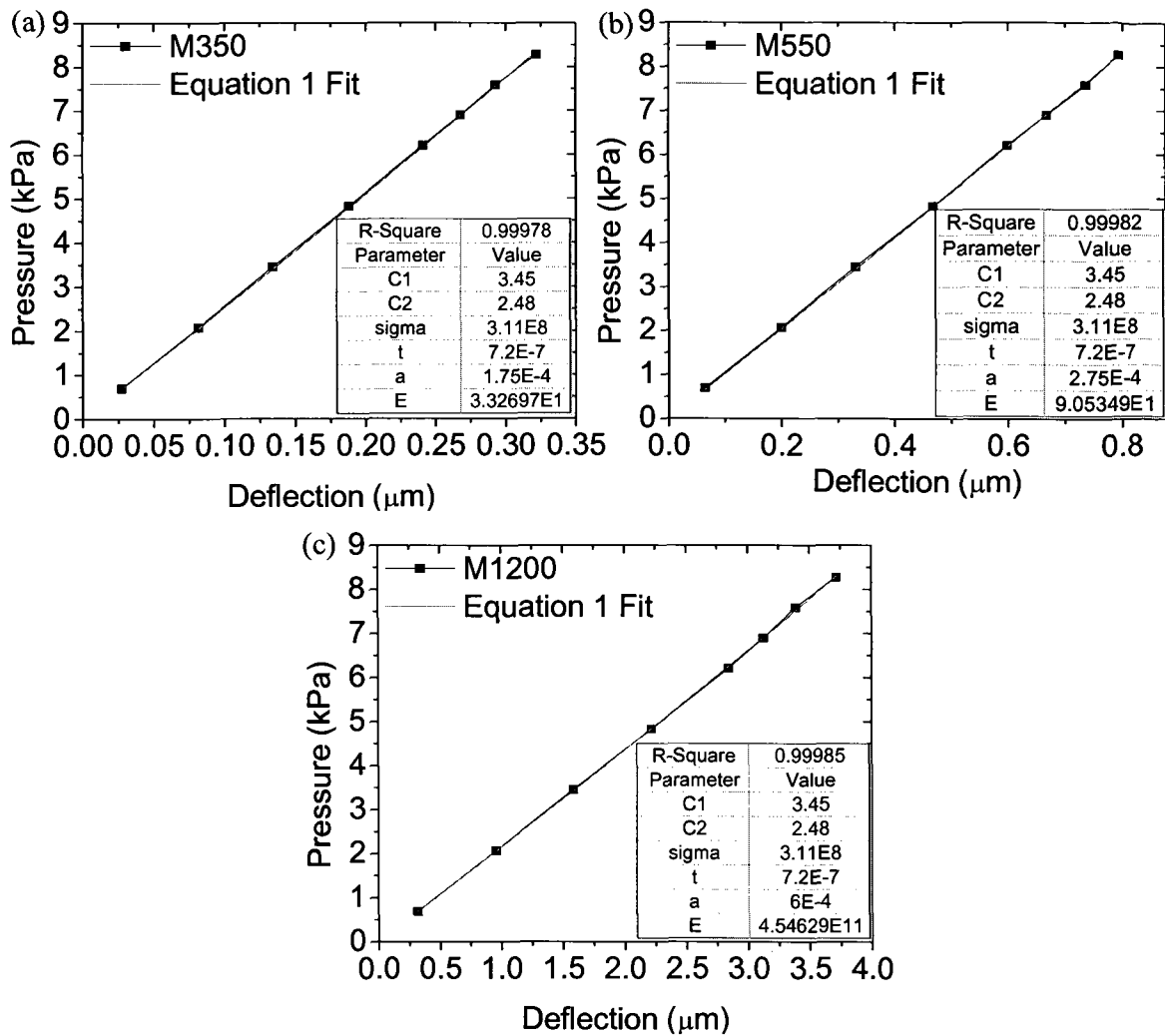


Figure 3.7. Fit of analytical solution (equation 23) to the pressure deflection data for the (a) 350 (b) 550 μm and (c) 1200 μm wide diaphragms. Results show that the system is incapable of resolving the minute nonlinear deflection of the smaller diaphragms with accuracy needed to calculate Young's modulus. The larger diaphragms have higher nonlinear deflections in micron range and give an estimate of 454 GPa for the Young's modulus.

3.5 Conclusions

We design, fabricated, and tested a bulge testing system that can rapidly measure deflections and curvature of thin membranes principally on Si at the wafer scale over a large range of pressures. The performance of this system was characterized by measuring the bulge deflection of thin silicon nitride diaphragms 720 nm thick with a reflective e-beam evaporated aluminum layer (20 nm) at low pressures (<8.3 kPa). Deflection results from the silicon nitride membranes with a reflective sputtered aluminum layer show excellent correlation between the empirical membrane deflection measurements and analytical and FEA model results. The overall pressure resolution of the system is good (~350 Pa) and small fluctuations exist at pressures below 5 kPa leading to a larger standard deviation between deflection measurements at low pressures. Deflection measurements taken at various locations across the wafer have little variation and similar standard deviations between measurements. Unfortunately for the smaller diaphragms measured deflections were in the linear regime and therefore an accurate calculation of Young's modulus was unsuccessful. Fitting experimental data directly to the analytical square membrane pressure-deflection relationship gives r-square value >99% and the Young's modulus of the 1200×1200 μm^2 film was calculated to be 454 GPa.

3.6 References

- [1] H. Guckel, T. Randazzo, and D. W. Burns, "A Simple Technique for the Determination of Mechanical Strain in Thin Films with Applications to Polysilicon," *Journal of Applied Physics*, vol. 57, no. 5, pp. 1671-1675, 1985.
- [2] H. Guckel, D. Burns, C. Rutigliano *et al.*, "Diagnostic Microstructures for the Measurement of Intrinsic Strain in Thin Films," *Journal of Micromechanics and Microengineering*, no. 2, pp. 86, 1992.
- [3] H. D. Espinosa, B. C. Prorok, and M. Fischer, "A Methodology for Determining Mechanical Properties of Freestanding Thin Films and MEMS Materials," *Journal of the Mechanics and Physics of Solids*, vol. 51, no. 1, pp. 47-67, 2003.
- [4] R. P. Vinci and J. J. Vlassak, "Mechanical Behavior of Thin Films," *Annual Review of Materials Science*, vol. 26, no. 1, pp. 431-462, 1996.
- [5] E. Arzt, "Size Effects in Materials Due to Microstructural and Dimensional Constraints: A Comparative Review," *Acta Materialia*, vol. 46, no. 16, pp. 5611-5626, 1998.
- [6] J. J. Vlassak and W. D. Nix, "A New Bulge Test Technique for the Determination of Young's Modulus and Poisson's Ratio of Thin Films," *J. Mater. Res.*, vol. 7, no. 12, 1992.
- [7] R. Edwards, G. Coles, and W. Sharpe, "Comparison of Tensile and Bulge Tests for Thin-Film Silicon Nitride," *Experimental Mechanics*, vol. 44, no. 1, pp. 49-54, 2004.
- [8] A. J. Kalkman, A. H. Verbruggen, and G. C. A. M. Janssen, "High-Temperature Bulge-Test Setup for Mechanical Testing of Free-Standing Thin Films," *Review of Scientific Instruments*, vol. 74, no. 3, pp. 1383-1385, 2003.
- [9] E. W. Schweitzer and M. Goken, "In Situ Bulge Testing in an Atomic Force Microscope: Microdeformation Experiments of Thin Film Membranes," *Journal of Materials Research*, vol. 22, no. 10, pp. 2902-11, 2007.
- [10] W. N. Sharpe, Jr., B. Yuan, and R. L. Edwards, "A New Technique for Measuring the Mechanical Properties of Thin Films," *Journal of Microelectromechanical Systems*, vol. 6, no. 3, pp. 193-199, 1997.
- [11] S. Brown, C. Muhlstein, K. Lynch *et al.*, "System and Method for Performing Bulge Testing of Films, Coatings and/or Layers," Google Patents, 2002.
- [12] R. Saha and W. D. Nix, "Effects of the Substrate on the Determination of Thin Film Mechanical Properties by Nanoindentation," *Acta Materialia*, vol. 50, no. 1, pp. 23-38, 2002.

- [13] O. Kraft, M. Hommel, and E. Arzt, "X-ray Diffraction as a Tool to Study the Mechanical Behaviour of Thin Films," *Materials Science and Engineering A*, vol. 288, no. 2, pp. 209-216, 2000.
- [14] M. F. Doerner, D. S. Gardner, and W. D. Nix, "Plastic Properties of Thin Films on Substrates as Measured by Submicron Indentation Hardness and Substrate Curvature Techniques," *Journal of Materials Research*, vol. 1, no. 6, pp. 845-851, 1986.
- [15] A. Karimi, O. R. Shojaei, T. Kruml *et al.*, "Characterisation of TiN Thin Films Using the Bulge Test and the Nanoindentation Technique," *Thin Solid Films*, vol. 308-309, pp. 334-339, 1997.
- [16] D. LaVan and W. Sharpe, "Tensile Testing of Microsamples," *Experimental Mechanics*, vol. 39, no. 3, pp. 210-216, 1999.
- [17] G. C. Janssen, M. M. Abdalla, F. van Keulen *et al.*, "Celebrating the 100th Anniversary of the Stoney Equation for Film Stress: Developments from Polycrystalline Steel Strips to Single Crystal Silicon Wafers," *Thin Solid Films*, vol. 517, no. 6, pp. 1858-1867, 2009.
- [18] J. M. Olson, "Analysis of LPCVD Process Conditions for the Deposition of Low Stress Silicon Nitride. Part I: Preliminary LPCVD Experiments," *Materials Science in Semiconductor Processing*, vol. 5, no. 1, pp. 51-60, 2002.
- [19] O. Tabata, K. Kawahata, S. Sugiyama *et al.*, "Mechanical Property Measurements of Thin Films using Load-Deflection of Composite Rectangular Membrane." pp. 152-156.
- [20] S. P. Timoshenko and S. Woinowsky-Krieger, "Theory of Plates and Shells," *Engineering Societies Monographs*, New York: McGraw-Hill, 1959, 2nd ed., 1959.
- [21] J. Y. Pan, P. Lin, F. Maseeh *et al.*, "Verification of FEM Analysis of Load-Deflection Methods for Measuring Mechanical Properties of Thin Films." pp. 70-73.
- [22] S. M. Jay, A. Z. Christian, K. Thomas *et al.*, "Examination of Bulge Test for Determining Residual Stress, Young's Modulus, and Poisson's Ratio of 3C-SiC Thin Films," *Journal of Aerospace Engineering*, vol. 16, no. 2, pp. 46-54, 2003.
- [23] M. K. Small, "Analysis of the Accuracy of the Bulge Test in Determining the Mechanical Properties of Thin Films," *Journal of Materials Research*, vol. 7, no. 6, pp. 1553-63, 1992.
- [24] Z. Wei, Y. Jinling, S. Guosheng *et al.*, "Fracture Properties of Silicon Carbide Thin Films Characterized by Bulge Test of Long Membranes." pp. 557-560.

- [25] Y. Xiang, X. Chen, and J. J. Vlassak, "Plane-Strain Bulge Test for Thin Films," *Journal of Materials Research*, vol. 20, no. 9, pp. 2360-2370, 2005.
- [26] D. Maier-Schneider, J. Maibach, and E. Obermeier, "A New Analytical Solution for the Load-Deflection of Square Membranes," *Journal of Microelectromechanical Systems*, vol. 4, no. 4, pp. 238-241, 1995.
- [27] K. Suzuki, T. Ishihara, M. Hirata *et al.*, "Nonlinear Analysis of a CMOS Integrated Silicon Pressure Sensor," *IEEE Transactions on Electron Devices*, vol. 34, no. 6, pp. 1360-1367, 1987.

CHAPTER 4

**DESIGN, SIMULATION AND OPTIMIZATION OF NOVEL
PIEZORESISTIVE PRESSURE SENSORS WITH STRESS
SENSITIVE PERFORATED DIAPHRAGMS FOR
HYDROGEL APPLICATIONS**

4.1 Abstract

We report on the design and simulation of novel pressure sensors that incorporate perforated diaphragms for the detection of various hydrogel swelling pressures. Holes etched in silicon diaphragms permit the exchange of ions and/or target molecules between an external medium and the hydrogels. As with conventional micropressure sensors stresses are induced in *p*-type piezoresistors but in our case pressure is generated from hydrogel swelling. This stress is transduced into resistance change and hence voltage output through the use of a full Wheatstone bridge. A combination of theoretical and finite element models were used to optimize sensor sensitivity and voltage output by studying parameters including diaphragm thickness and size, diffusion channel metrics and piezoresistor geometries. To our knowledge this is the first time any group has reported on using an array of pores located in the bending plate to allow the passage of analytes into a pressure sensor cavity. It was shown through finite element simulations that pore shape, location, and size can be used modify the diaphragm mechanics and thus electrical output. The optimized geometry had diffusion pores removed from along the

diaphragm midline, edges, and close to piezoresistors. This specific pattern was used because it significantly reduces stresses developed around the pores while maintaining the diaphragm's mechanical integrity. It was also found that pores can act as piezoresistor stress concentrators leading to increased sensitivities. We determined that when using large pores ($40\ \mu\text{m}$) combined with small pitches ($50\ \mu\text{m}$) the diaphragm stiffness is reduced leading to decreased stress concentrations within the piezoresistors due to larger diaphragm deformations. With a diaphragm thickness of $10\ \mu\text{m}$ and widths of 0.5, 1.0, 1.25, and 1.5 mm the optimized designs had average sensitivities of 0.13, 0.65, 0.98, and 1.23 mV/V-kPa, respectively.

4.2 Introduction and Device Principal

Hydrogels are polymeric materials which consist of a three-dimensional network of crosslinked molecules that can absorb large amounts of water. Synthesis is performed either by crosslinking between individual molecules or via reaction polymerization which simultaneously creates the backbone chains and crosslinked molecules. Many hydrogels are biocompatible and suitable for use in implantable biomedical sensors and autonomous drug delivery devices. One group of hydrogels known as "stimuli-responsive" hydrogels have been shown to swell or shrink in response to a number of environmental and chemical stimuli including temperature, electric field [1, 2], pH [3-7], glucose [8-15], and ionic strength [4, 9, 16-18]. This transduction mechanism makes these materials appealing for chemical analysis and is utilized in a number of different sensors including: quartz crystal microbalances (resonance) [19], holographic Bragg diffraction (optical) [20], electrode impedance (electrical) [11, 21], and piezoresistive based cantilevers or membranes (mechanical-electrical) [5, 22-25]. Our proposed sensor design utilizes a

silicon diaphragm that is stressed due to pressure caused by hydrogel swelling. The square diaphragm acts as a stress magnifier changing the resistivity of the imbedded piezoresistors and consequently the output voltage. The complete transduction mechanism for the sensor is illustrated in Figure 4.1. Several advantages of using piezoresistive pressure (bending plate) sensors are highly linear output, low cost measurement electronics, low power, configurability over large pressure ranges, a small form factor (<1mm), and they are easily bulk manufactured reducing costs.

This sensing mechanism has been implemented to detect CO² [17, 18, 26], pH [7, 25], glucose [16], and ionic strength (NaCl concentrations) [8, 16, 27]. One commonality between these designs is that they use solid pressure sensing diaphragms to detect hydrogel swelling. They also require a semipermeable backing plate to permit analyte diffusion into the hydrogel cavity. Backing plates in the past has been made from wire mesh [16], nonporous polymers [27], micromachined silicon [26], or glass and attached using adhesives or anodic bonding.

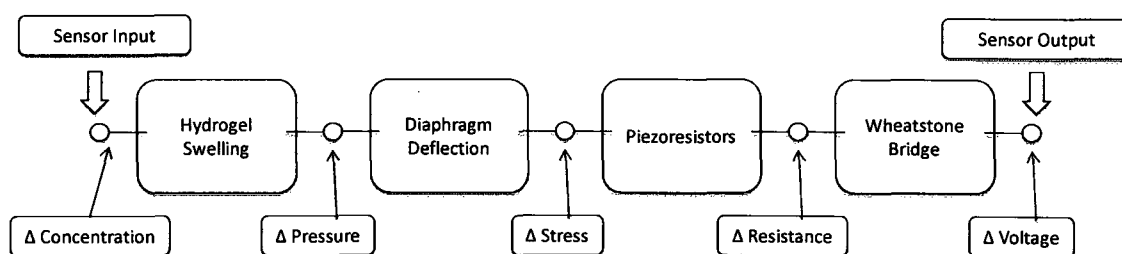


Figure 4.1. Transduction mechanism utilized in hydrogel based piezoresistive chemical sensors. Environmental changes cause hydrogel swelling creating elevated pressure within the sensor cavity. The diaphragm deflection causes elevated stress to be developed within the piezoresistors whilst the output voltage is maximized through the use of a Wheatstone bridge.

Although the mesh backing keeps the hydrogel in contact with the sensor's diaphragm a number of issues exist with the current technologies. First the fabrication procedure is complex requiring a number of individual components to be fabricated and attached in the latter stages. Secondly permeable mesh can flex reducing the amount of pressure transferred to the sensor diaphragm reducing sensitivity [27]. The backing plate diffusion pore diameter is also important since if it is too large then the hydrogel has the ability to exude through the backing reducing overall swelling pressure within the cavity. Magda *et al.* found this was true for almost all of the stainless steel wire cloth meshes commonly available and demonstrated this condition when comparing a 40 to an 80 mesh wire cloth used to enclose the hydrogel onto a commercial pressure sensor. Under the same experimental conditions the 40 wire mesh gives a pressure output of 35kPA while the 80 mesh cloth produced roughly 60kPA. The 40 mesh cloth had a mean opening of 381 μm , and an open area of 36% while 80 mesh wire cloth has a square pore opening of 178 μm with 31% open area. It was directly shown that this pore size influences the pressure created in the within hydrogel cavity. Although the open area of the meshes only differed by 5% the output pressure was 185% higher for the 80 mesh. This experiment demonstrates that pore size directly impacts the sensor output. This effect is presumably less pronounced as the diffusion channels become smaller. The pore density, size, and length dictate the diffusion rate of the analyte into the cavity. In the remainder of this chapter we describe design and simulation of a novel sensor concept used for detection of hydrogel swelling pressure that integrates the holed backing plate and sensing diaphragm shown in Figure 4.2b.

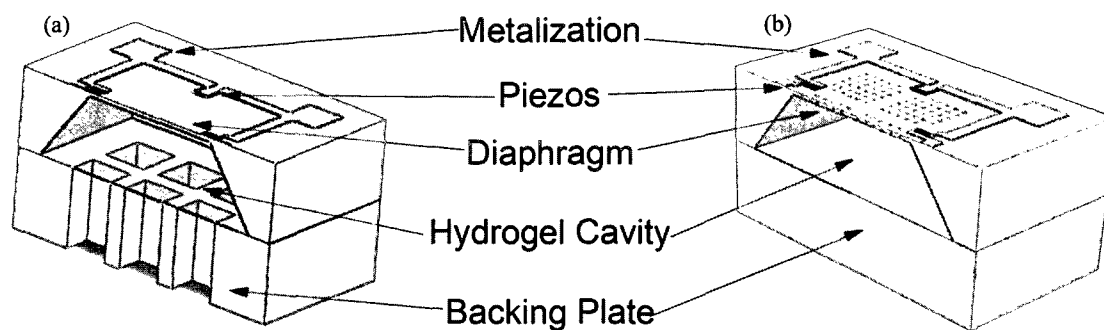


Figure 4.2. CAD rendering of the hydrogel based pressure sensor designs utilizing analyte diffusion channels that are located within the (a) backside mounting plate and (b) directly in the sensing diaphragm. The design on the left is the previously reported sensor architecture used for detecting hydrogel swelling pressure while the design on the right is novel and implements diffusion pores directly into the diaphragm.

4.3 Design Methods

Individual sensor pressure ranges were defined by measurements previously performed on hydrogels at the University of Utah and reported by Magda *et al.* for glucose [15, 16], pH [16, 27] and ionic strength [27]. Swelling pressures were determined with a system that couples a calibrated commercial pressure sensor (Measurement Specialties Model : EPB-B01-5P-/L02F, Les Clayes-Sous-Bois, France) to the hydrogels under isochoric conditions [16, 27]. Analyte concentrations were varied, diffused into the gel, and swelling pressure was recorded. Specifications for the porous diaphragm pressure sensor are roughly based on these results and found in Table 4.1.

4.4 Sensor Architecture

Our proposed sensor design uses a square silicon diaphragm that contains a Wheatstone bridge with piezoresistors located midway between the diaphragm edges. This region is close to the area where the stress is largest when pressure is applied to the center of the membrane.

Table 4.1. Hydrogel swelling properties and sensor design specifications. The hydrogel properties were measured using a calibrated pressure sensor coupled to hydrogels under isochoric conditions. The experimental setup for measuring the hydrogel properties is found in [16]. The bottom portion of the table describes the desired perforated diaphragm sensors specifications.

Synthesized Hydrogel Properties	min.	max.	unit
pH Gel Pressure Output	0	20000	Pa
Ionic Strength (NaCl) Gel Pressure Output	0	150000	Pa
Glucose Sensitive Gel Pressure Output	0	5000	Pa
Gel Thicknesses	300	1000	um
Sensor Parameters	min.	max.	unit
Overall Die Size (per sensor)	1 x 1 x .5	2 x 3 x .5	mm
Sensitivity	0.1	NA	mv/(V-Kpa)
Full Scale Output	50	500	mv
Bridge resistance	3000	8000	Ω
Offset voltage	-40	+40	mV
Temperature coefficient of offset (TCO)	-0.1	0.1	%F.S.O/K
Temperature coefficient of sensitivity (TCS)	-0.2	-0.1	%F.S.O/K
Temperature coefficient of bridge resistance (TCB)	+0.08	+0.14	%K
Pressure-hysteresis	<.1	<.5	\pm %F.S.O/K
Temperature-hysteresis	-0.8	+0.8	%F.S.O
Linearity error	-0.5	0.5	%F.S.O
Power Supply	1	10	V

To maximize bridge output the boron piezoresistors (*p*-type) are oriented to the <110> directions of a high resistivity n-type wafer using ion implantation. Resistors positioned perpendicularly to diaphragm edges (longitudinally) are in the direction of maximum stress whose resistance increases with pressure (*p*-type). The other two resistors parallel to the diaphragm edges are oriented transversely and decrease in resistance with applied pressure. The differential output voltage signal from the bridge at low pressures is ideally zero (perfectly balanced) and highest when maximum pressure is applied. The bridge resistance change $\Delta R/R$ and hence voltage output is defined by the longitudinal and transverse piezoresistive coefficients π_{long} (Pa^{-1}) and π_{trans} (Pa^{-1}), times the calculated average normal stress (S_{nx}, S_{ny}) in the piezoresistors at a particular location.

For a longitudinally oriented resistor (current flow and stress along length of resistor) the $\Delta R/R$ is defined in equations 27. For transverse piezoresistors $\Delta R/R$ is defined in 28.

$$\frac{\Delta R_{long}}{R_o}(x) = \pi_{long} S_{nx}(x) + \pi_{trans}(S_{ny}(x) + S_{nz}(x)) \quad (27)$$

$$\frac{\Delta R_{trans}}{R_o}(x) = \pi_{long} S_{ny}(x) + \pi_{trans}(S_{nx}(x) + S_{nz}(x)) \quad (28)$$

Conventionally two parameters critical to square diaphragm pressure sensor performance are diaphragm width and thickness. Larger and thinner diaphragms create pressure sensors which are more sensitive as shown in equation 29 [28]. This approximation gives the maximum sensitivity of a square piezoresistive pressure sensor and is valid for solid silicon diaphragms free of intrinsic stress. In this estimation piezoresistor length is neglected, and stresses are treated as points located at the midpoint of the diaphragm sides in regions of highest stress. This allows us to determine the maximum sensitivity in regard to the initial width and thickness and provides initial parameters for the finite element simulations.

$$S_{piezo} = \frac{\Delta V_{out}}{V_{Source}P} = .1539 \pi_{44}(1 - \nu) \left(\frac{L}{h}\right)^2 \quad (29)$$

The source and output voltage are defined as V_{Source} and V_{out} where P is the applied pressure. The piezoresistor coefficient π_{44} for p-type resistors oriented in the $\langle 110 \rangle$ directions on and (100) silicon wafer is well known ($138 \times 10^{-11} \text{Pa}^{-1}$) [29]. A plot of equation 29 for solid square diaphragms ranging in thickness from 2.5 to 15 μm with widths of up to $2 \times 2 \text{ mm}^2$ is shown in Figure 4.3.

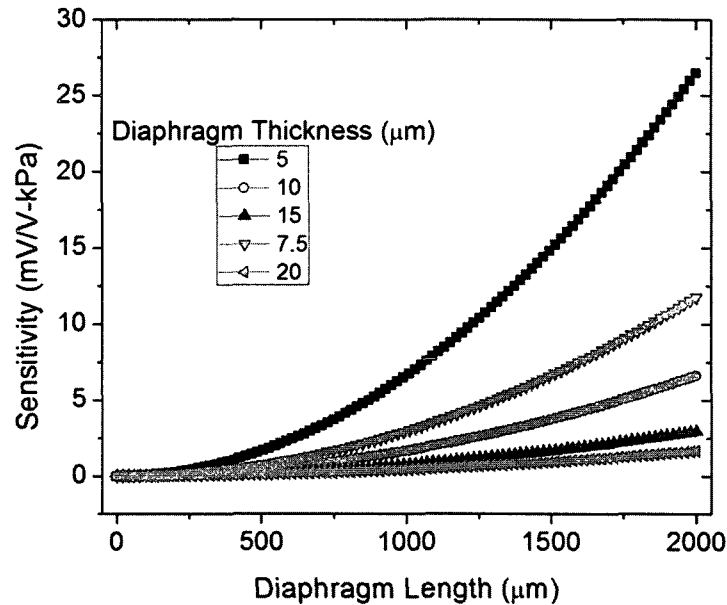


Figure 4.3. Sensitivity plotted as a function of diaphragm width and thickness for square solid silicon pressure sensors.

A Poisson's ratio of 0.22 was used for single crystal silicon. This plot indicates that with a silicon diaphragm $1 \times 1 \text{ mm}^2$ and thickness of $10 \text{ } \mu\text{m}$ it is possible to fabricate a sensor capable $>1 \text{ mV/V-kPa}$ sensitivity.

4.4.1 Finite Element Models

Finite element analysis (FEA) has the ability to solve problems that do not have explicit analytical solutions. In our case the FEA solutions were used to solve the complex pored diaphragm designs while giving additional verification to the analytical models of simplified solid diaphragms. FEA also allows us to study a number of design parameters with relative ease by changing geometries and boundary conditions of the models. In our simulations three-dimensional models of the diaphragms were created using Solidworks 2008 then imported into COMSOL 3.4a for finite element analysis.

Parameters that varied included diaphragm width and thickness, pore shape, location, and size. The structural mechanics module in COMSOL was used to define material properties, apply boundary conditions, solve the system of equations, and examine the solution. Determination of stress and strain distributions throughout the diaphragm as well as deflection are critical parameters used to investigate and validate initial designs. The optimization of pore parameters was performed by creating number of designs and studying the impact on the von Mises stresses (S_{vm}) and normal stress (S_n) created within the diaphragm under load. The S_{vm} is typically used to determine failure of materials which undergo plastic deformation but proves useful in our case for determining area most likely to fail under loading. The yield strength of single crystalline silicon ($\sigma = 7\text{GPa}$) [30] is high but the engineering design fracture stress was not allowed to exceed 600 MPa to provide a large factor of safety. Young's modulus of silicon was treated isotropically due to the cubic nature of silicon with a value of 168 GPa ([31]). To accurately predict the $\Delta R/R$, output voltage, and sensor sensitivity the parallel and perpendicular normal stress (S_{nx}, S_{ny}) experienced by the piezoresistors are multiplied by the piezoresistive coefficients. Using symmetrical boundary conditions (BC) it was possible to reduce the computational complexity by modeling a quarter of the diaphragm. The two edges not subject to the symmetry BCs are fixed and simply supported. A follower load was applied to the diaphragm surface to keep the applied pressure normal to the surface during deflection. This force is applied to the bottom face of the diaphragm that is in contact with the hydrogel material creating compressive stress in the piezoresistors on the top surface. Applied BCs and material properties were identical for all simulations. Initial "proof of concept" simulations show it was possible to incorporate

pores into the diaphragm without compromising the structural integrity of the silicon while loaded.

4.4.2 Sensing Diaphragm Optimization

Although pores on the microscale have been created for a number of applications including microsieves [32, 33], drug delivery devices [34], and optics [35] to our knowledge no group has incorporated pores into the sensing diaphragm of pressure sensor. Creating a pressure sensor with diffusion holes incorporated into the diaphragm is a novel and complex design problem where a number of tradeoffs exist. If the density of holes is too high and located in high stress areas, the mechanical strength and electrical sensitivity is compromised. Alternatively, if few small holes are fabricated, the analytes cannot diffuse quickly into the hydrogel cavity slowing overall sensor response time. This new design has distinct advantages over using a permeable mesh backing including:

- (a) Pores are directly integrated into the diaphragm during sensor fabrication. Therefore the sensor does not require a separate permeable membrane to support the hydrogel. This design has fewer losses of stress and signal by eliminating bending of a separate membrane.
- (b) Analyte diffusion rate into the hydrogel cavity is controlled by manipulating pore size and density.
- (c) Placement of pores can be used to modify stress/strain distributions within the diaphragm.
- (d) Pore geometry can be easily modified making a single sensor useful over various pressure ranges. This makes one sensor design adaptable for various hydrogels.

4.4.3 Pore Shape

Cracks in mechanical structures are often a source of failure and initiate and propagate from the locations with high stress and/or strain concentrations [36]. Reduction of these stresses is critical in preventing premature diaphragm breakdown. Finite element models have been used to compare stress concentrations (Figure 4.4) of different shaped pores within a $1.0 \times 1.0 \text{ mm}^2$ diaphragm ($20 \mu\text{m}$ thick) with a pressure of 150 kPa follower load applied to the bottom face. Fixed simply supported boundary conditions were placed on the left and bottom edge while symmetry BCs were placed on the top and right side. This simulation demonstrates that the stresses located within the pores are largely dependent on shape. The square, triangular, hexagonal and circular pores are placed in identical locations and with a $30 \mu\text{m}$ radii. The highest Von Mises stress was located at the same node in the upper right hand pore which is indicated with arrows in the figure. Square pores generate a Von Mises stress under these loading conditions of 299.3 MPa while circular holes exhibit a stress of 102.3 MPa. Localized Mises stress is 2.93 times higher in the square pores than when compared to the circular versions. Although the stress is not higher than the failure stress it demonstrates that round pores will reduce the amount of concentrated stress within the pores.

Pores made from shapes with sharp corners such as hexagons, triangles, or squares will concentrate stress and become a likely mode of failure. It is conclusive that the circular pores have the lowest inherent stress when placed into diaphragm using these boundary conditions.

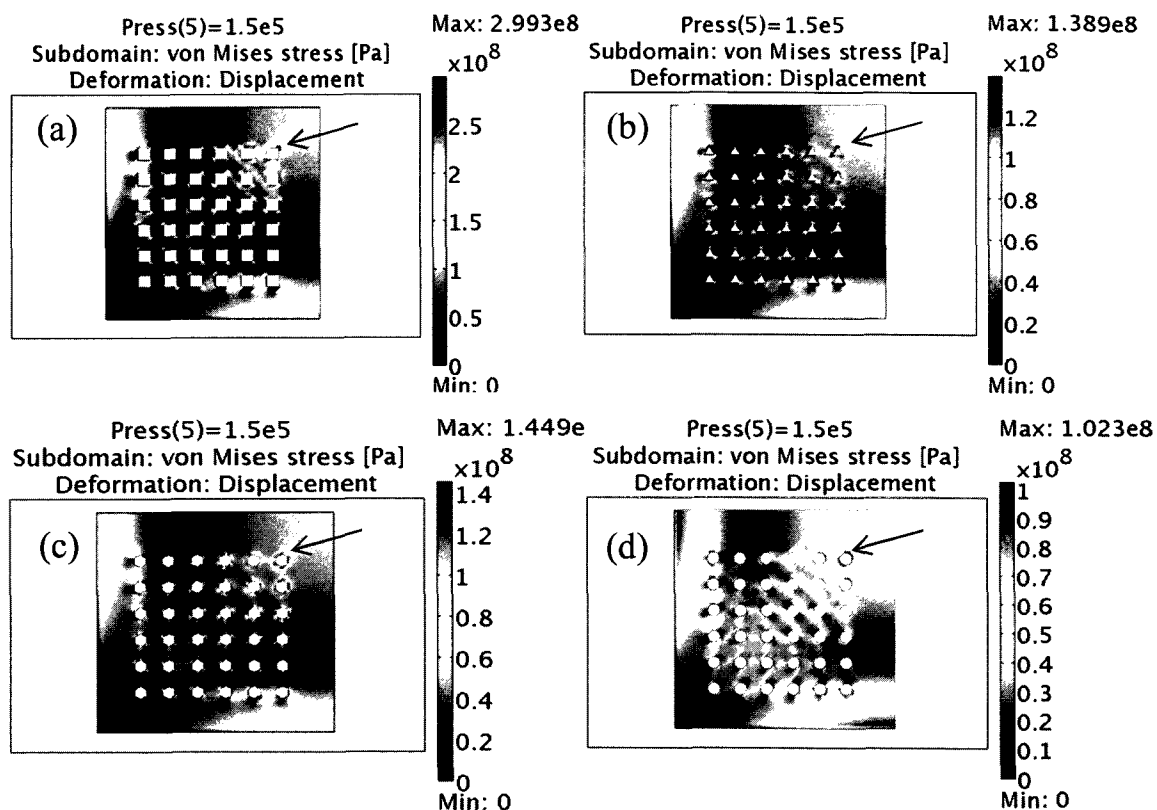


Figure 4.4. Simulated Von Mises stress distribution in a quarter of a $1.0 \times 1.0 \text{ mm}^2$ square silicon membrane with $30 \mu\text{m}$ (a) hexagonal, (b) triangular, (c) round, and (d) square pores. Stresses are 2.93X higher in the square pores than in round pores. The highest Von Mises stress is found in the top right pore closest to the diaphragm center as indicated by the arrow.

4.4.4 Pore Location

One of the critical design parameters for our sensors is the locations of the pores in the diaphragm. These pores not only play a role in the diffusion of analytes in the hydrogel cavity but also can be used to manipulate the stress distribution within the diaphragm. The ideal design should utilize a large open area with short pores allowing fast analyte diffusion rates. We hypothesize that though optimization pores can be directly integrated into diaphragm, leading to increased stresses found in the piezoresistors. This can be accomplished while keeping the stresses found in the pores within design limits ($<600 \text{ MPa}$). As with previous simulations a follower load of 150

kPa is applied to the bottom of the $1.5 \times 1.5 \text{ mm}^2$ diaphragm. In this simulation a larger diaphragm was used to magnify the changes in stress from variations in pore location. Although a number of other sizes of diaphragms were studied in this paper we discuss six designs that are shown in Figure 4.5(a-f). To compare the effect of location pores ($30 \mu\text{m}$) were placed in orthogonal rows with a $50 \mu\text{m}$ pitch spaced $50 \mu\text{m}$ from the edge.

Designs were optimized by removing pores in the highest stress locations and investigating the effects on the stress distributions in the diaphragm specifically around the piezoresistors. It is clearly shown in Figure 4.5a-e that the removal of pores influences the distribution and magnitude and location of Von Mises stress (S_{vm}).

When comparing the maximum S_{vm} generated by the different diaphragm designs we observed that it varied from $\sim 580 \text{ MPa}$ for the 100 pore design (Figure 4.5a) to $\sim 350 \text{ (MPa)}$ for the 52 pores (Figure 4.5e) version. The maximum Von Mises stress (S_{vmmax}) for the 100 pore design was positioned between pores closest to the diaphragms fixed edge. This location is most probable for failure and other designs that placed pores close to the fixed midline edge (Figure 4.5b) had similar results. Pores were removed in areas of highest stress particularly along the diaphragm edges and midlines.

It was determined that removing pores along the midlines focused normal stress perpendicular (S_{nx}) to the diaphragm edge towards the diaphragm center increasing stresses located in the piezoresistive regions. Results showed that it is possible through the proper placement of the holes we can manipulate piezoresistor stress. In general three trends were found to exist. First pores located along the midlines reduced stress in the piezoresistive regions due to diaphragm stretching.

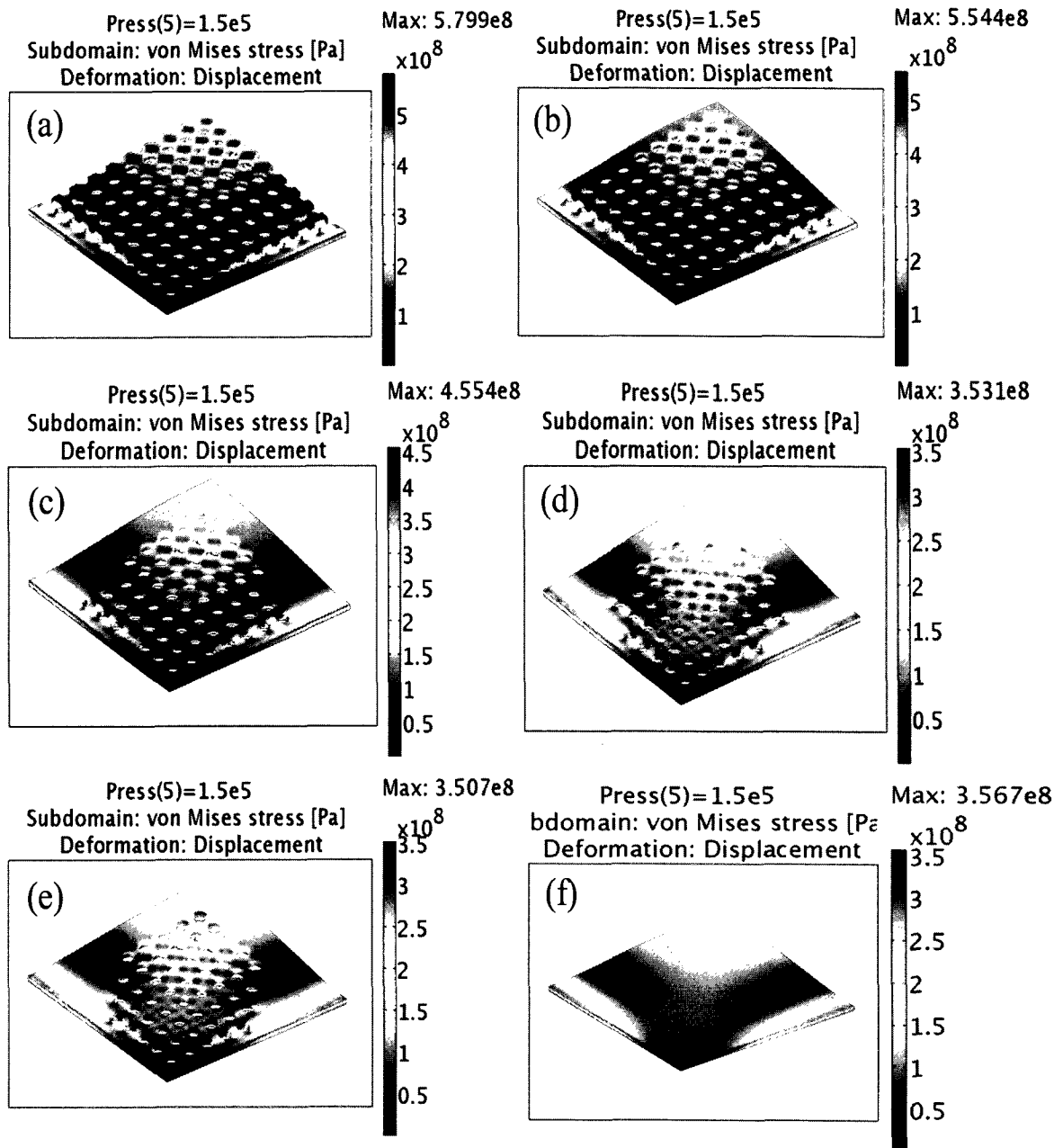


Figure 4.5. Von Mises stress distribution of one quarter of a $1.5 \times 1.5 \text{ mm}^2$ diaphragms under a load of 150 kPa . Fixed boundary conditions (BC) are placed on the front two planes representing the edge of the diaphragm while symmetry BCs are placed on the planes located on the inside of the diaphragm (out of view). It is shown that the geometry of diaphragm perforations impacts the stress distribution within the diaphragm while loaded from the backside with 150 kPa . Through manipulation of pore geometry the stress in the piezoresistor locations can be increased.

Secondly pores close to the midpoint of the diaphragm edges developed extremely high levels of stress when compared to other regions and were removed. Finally, high densities of large pores develop unacceptable levels of interpore stress. These stresses reduced stiffness in the middle of the center causing higher deflection and less localized piezoresistor stress concentrations as shown in Figure 4.6. In response to the observed trends the final designs used a diaphragm patterned without pores along the symmetry plane and close to the diaphragm edge midpoint found in Figure 4.5e. In the solid diaphragm (Figure 4.5f) the maximum S_{vm} is confined to the diaphragm edge while for a 52-pore diaphragm the stress is less confined to the edge spread towards the center of the diaphragm. This design minimizes stress within the pores while maintaining high stress levels needed in the piezoresistors. It is envisioned that since pores are created in the final fabrication step this could be used for tuning a single pressure sensor to be responsive over wide range of pressures. This first generation pore pattern is conservative because it substantially reduces the maximum stress found in regions around the pores while only minutely modifying stress distribution in the piezoresistor regions. It is envisioned that more radical designs would place pores closer to the piezoresistors which would increase induced stress and hence voltage output.

4.4.5 Pore Diameter

The pore diameter plays a primary role in controlling the diffusion rate of analyte into the sensor cavity but also influences the stiffness of the diaphragm. This is useful for customizing the sensor to hydrogels with varying swelling pressures and mechanical properties.

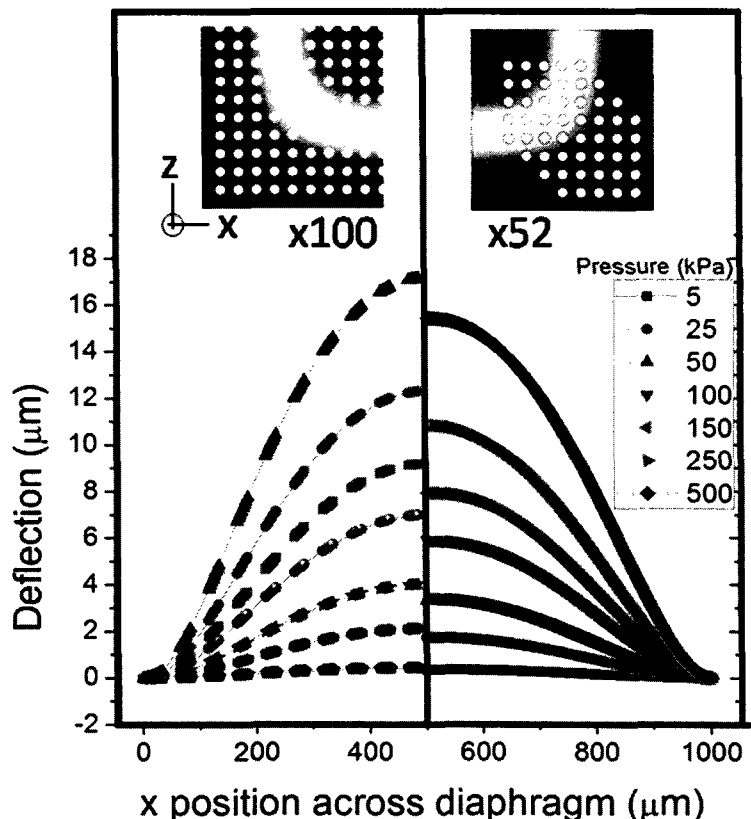


Figure 4.6. Deflection of the $1.5 \times 1.5 \text{ mm}^2$ diaphragms with x100 (left) and x52 (right) pores per quarter diaphragm with respect to diaphragm position (x). Pressures from 5 to 500 kPa were applied to the bottom of the diaphragms and plotted. Deflection is higher while piezoresistor stresses are lower for designs with high densities of pores (left).

For example, hydrogels with a higher modulus can be used with larger pores because the gel is harder to exude through the pores. Softer gels (lower modulus) on the other hand must be coupled with smaller pores. Large pores reduce the diaphragm stiffness and reduce stress within the piezoresistors modifying the applicable pressure range. Fabrication repeatability and reliability dictate the initial sensor pore size and the first designs used pores 10 to 40 μm (diameter) with a pitch of 50 μm . Pores on this scale can be readily manufactured using a combination of lithography and deep reactive ion etching (DRIE) etching. Furthermore, it should be possible using this same fabrication

technique to create pores submicron in diameter making the diaphragm behave as a semipermeable membrane.

To investigate the effect of pore size on sensor performance FEA was used to calculate stresses found in the diaphragm and within piezoresistors. Simulations presented were performed again on a $1.5 \times 1.5 \text{ mm}^2$ diaphragm that is loaded at the bottom face with a uniform follower load that ranges from 5-250 kPa. A plot of the normal stress perpendicular S_{nx} and parallel S_{ny} to the diaphragm edge along the midline is shown in Figure 4.7a and Figure 4.7b, respectively. Stress located $25 \mu\text{m}$ from the diaphragm edge on the midline (approximate piezoresistor regions) are shown as a function of pressure and holes size in both the S_{nx} (Figure 4.7c) and S_{ny} (Figure 4.7d) directions. There appears to be a relatively small change in stress concentrations when comparing the diaphragm that is solid to versions with 10, 20 and $30 \mu\text{m}$ pores. Alternatively, the design with $40 \mu\text{m}$ pores is shown to reduce both compressive and tensile stresses developed in the diaphragm during loading. This reduction in developed stress will also decrease the sensor sensitivity when applied with the same loading conditions. When coupled with a hydrogel these loading boundary conditions may not be completely accurate. The hydrogel will exert the same force on the diaphragm that has $40 \mu\text{m}$ holes than the solid diaphragm but the force density in each circumstance is different. This is because the same pressure is applied to the diaphragm irrespective of pore size if we assume the hydrogel doesn't exude through the pores. Therefore the force/volume is highest on the diaphragm with the least amount volume since the swelling pressure for a particular gel remains constant at static conditions.

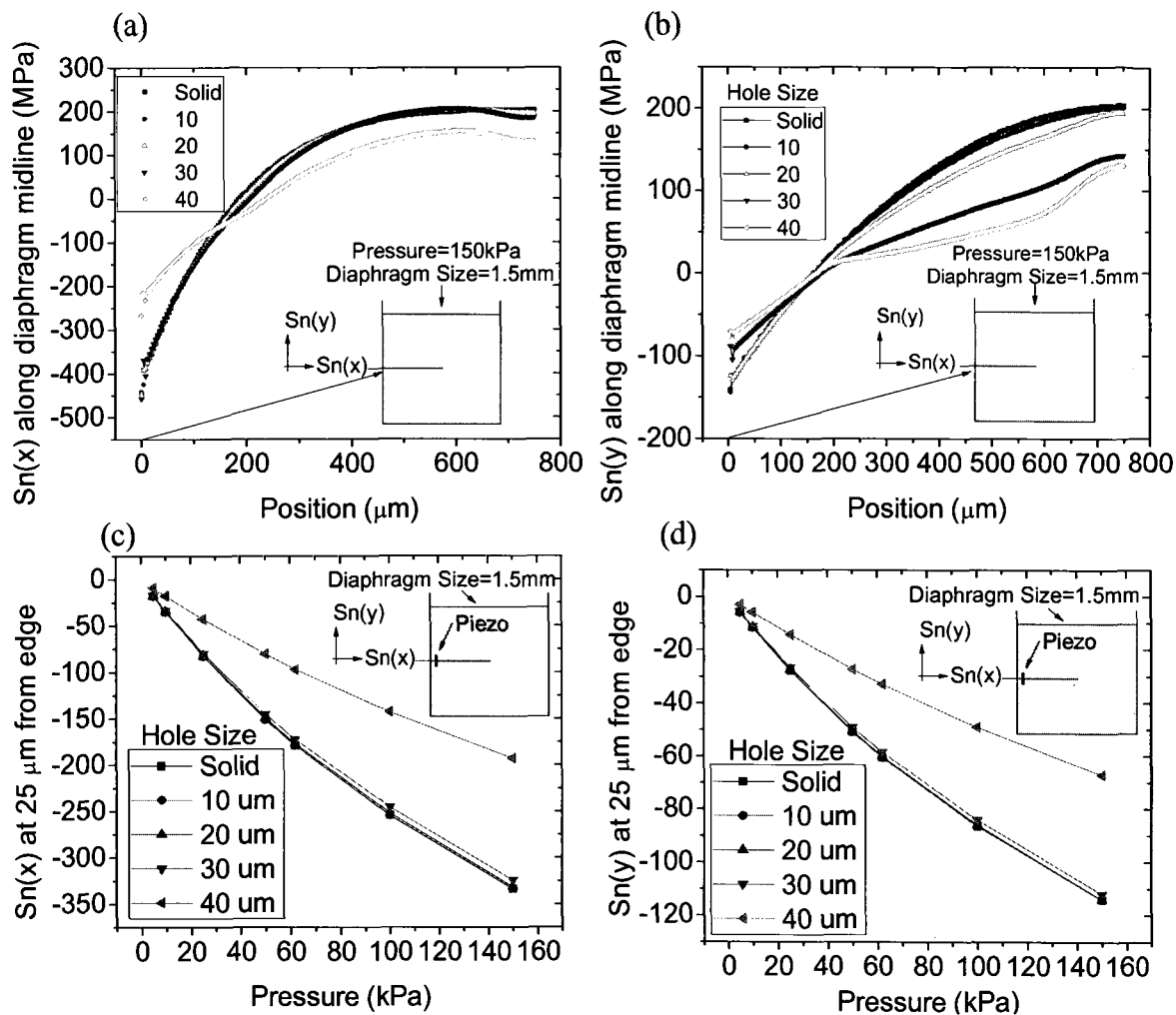


Figure 4.7. Normal stress (a,c) perpendicular (S_{nx}) and (b,d) parallel (S_{ny}) to the diaphragm edge. Stresses are calculated as a function of hole size across the (a,b) diaphragm midplane at a pressure of 150 kPa. In (c,d) stresses are calculated at a spacing of 25 μm from the diaphragm edge at an applied pressure of 5-150 MPa. It was determined that large pores (40 μm) with a small pitch (50 μm) do not provide the diaphragm with the mechanical strength needed to develop stresses within the piezoresistors. The large amount of open area in the diaphragm ultimately allows the diaphragm shape to deform.

In this scenario the highest forces are witnessed by the diaphragm with largest pores. The actual amount of deformation of the gel through the pores is difficult to estimate and should be studied empirically since hydrogels' mechanical properties vary significantly. For comparative purposes our simulations assume that a constant pressure is applied to the bottom surface of the diaphragm and hence the total applied force is highest for the solid diaphragm.

Von Mises stress is shown in Figure 4.8 for the $1.5 \times 1.5 \text{ mm}^2$ diaphragm with pore diameters of $10 \text{ }\mu\text{m}$ and $40 \text{ }\mu\text{m}$. When $40 \text{ }\mu\text{m}$ pores are used only a $10 \text{ }\mu\text{m}$ of silicon exists between pores at the narrowest point and the deflection strain is distributed across this material leading to high stress conditions.

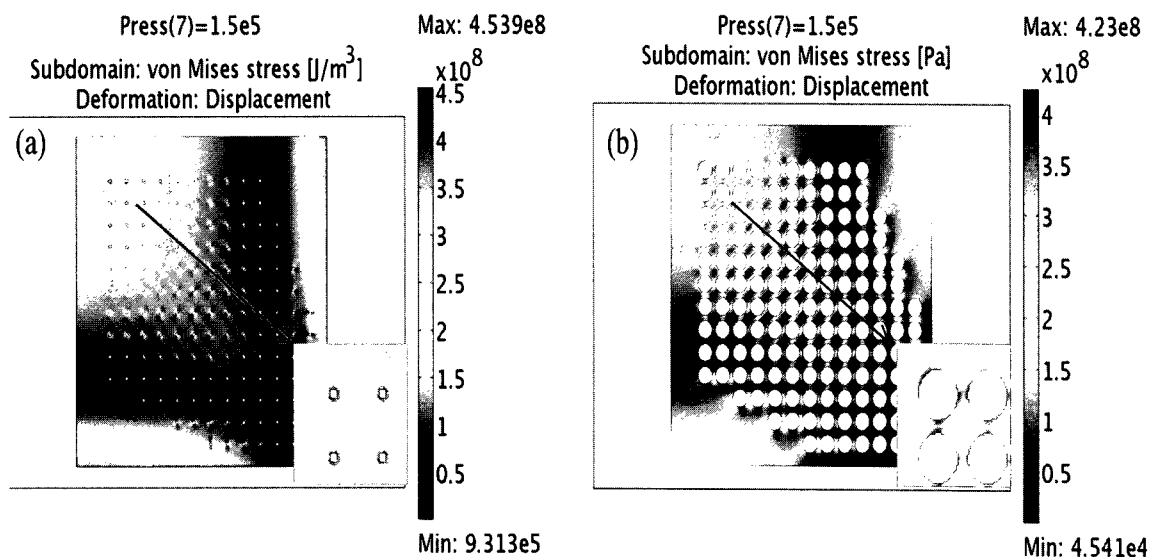


Figure 4.8. Finite element results exhibiting Von Mises stress developed in diaphragms with (a) $10 \text{ }\mu\text{m}$ and (b) $40 \text{ }\mu\text{m}$ pores. Simulations indicate that as the pores become larger, high tensile stresses are developed in the regions between pores towards the center of the diaphragm. Larger pores and open areas create diaphragms with higher stress and a higher probability of failure.

4.5 Results Piezoresistor Optimization and Performance

To effectively determine the sensor performance (output voltage, sensitivity) stresses induced in the piezoresistors must be accurately predicted. Comparing the six designs in Figure 4.5 the normal perpendicular stress (S_{nx}) 25 μm from the diaphragms' edge were calculated. This distance from the edge was chosen because for because it represents the approximate center point of the piezoresistors. Values range from -164 MPa for to -278 MPa for the various designs. Normal stress is calculated in the perpendicular direction because it is dominant and shown in Figure 4.9a. This demonstrates the ability of pore density and location to influence the stresses induced in the piezoresistor.

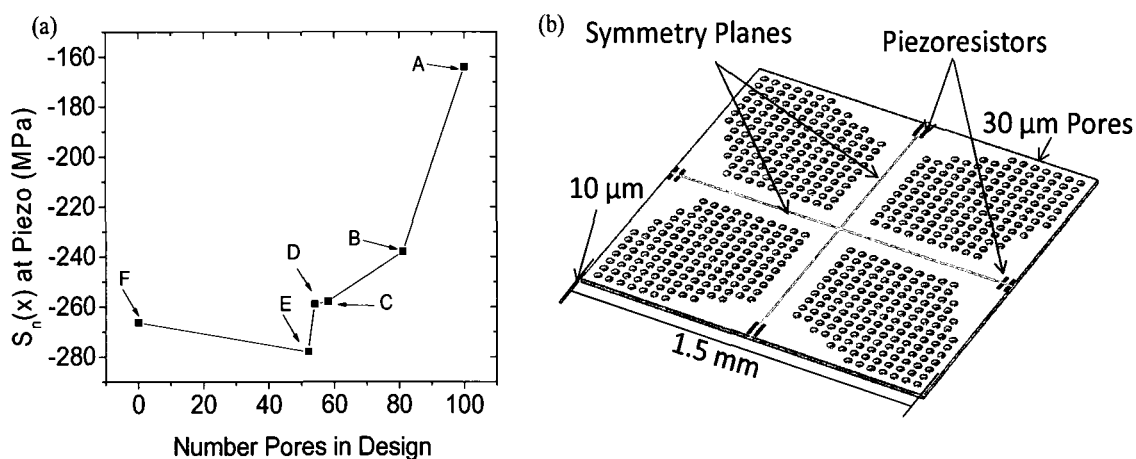


Figure 4.9. Influence of pore geometry on piezoresistor stress. (a) Normal compressive stress (S_{nx}) in the piezoresistors located on the topside of the diaphragm 25 μm from the diaphragm edge. A load of 150 kPa was applied to the backside of the diaphragm and determined using finite element analysis of designs shown in Figure 4.5. The geometry and location of the pores is used to increase stress in piezoresistors and hence sensor sensitivity. (b) CAD model of the final pore geometry located in a $1.5 \times 1.5 \text{ mm}^2$ diaphragm with 10 μm thickness. Simulations on were used to optimize the final geometry by modeling one quarter of the diaphragm and using symmetry.

The lowest piezoresistor stress averaged at the three adjacent nodes was (-164 MPa) was found in the design with 100 pores placed in the diaphragm (Figure 4.5a). This design mechanically deformed much more than the other designs reducing the piezoresistor stresses. The design with 52 pores (Figure 5E) was found to increase S_{nx} in the piezoresistor by 12 MPa when compared to the solid diaphragm. This design was used as the basis for the final pore geometry shown in Figure 4.9b for the $1.5 \times 1.5 \text{ mm}^2$ diaphragm with $30 \mu\text{m}$ pores.

Figure 4.10a shows S_{nx} distribution across the diaphragm for the porous $1.0 \times 1.0 \text{ mm}^2$ diaphragms while loaded from the below with 150 kPa. Figure 4.10b plots the S_{nx} across the diaphragm length to study the how the piezoresistors are impacted by the various designs. The enlarged box represents region in which the piezoresistors are located which is influenced by pore design. In general the S_{nx} distribution across the diaphragms is similar for all the designs with exception of the version with 100 pores. The high density of pores of this design reduces the stresses in the piezoresistive regions while increasing stress in the pores. For the final designs two piezoresistors were connected in series creating a pair close to the diaphragm edge. This was necessary to obtain a required output voltage and the specified bridge resistance of $3 \text{ k}\Omega$. The smaller piezoresistor footprint in this design also improves sensor output by localizing the induced stresses when compared to using one long piezoresistor.

However, the piezoresistors are not single points but rectangular areas. Therefore signal output voltage and sensitivity will be lower than is predicted using a point source.

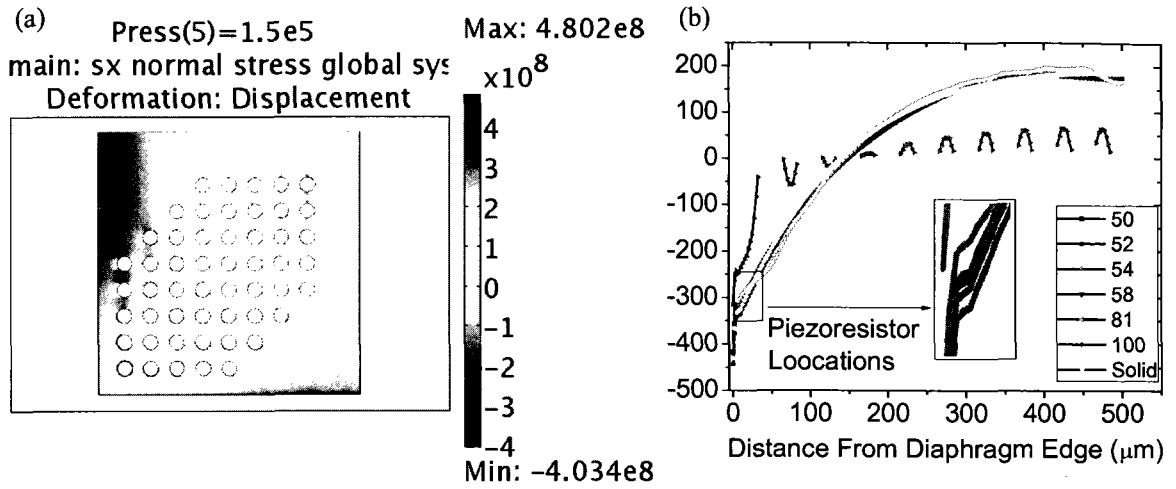


Figure 4.10. Normal stress distribution (S_{nx}) of the $1.0 \times 1.0 \text{ mm}^2$ 52 pore diaphragm with applied load of 150 kPa. (b) Normal stress distribution (S_{nx}) perpendicular to the diaphragm edge for the $1.0 \times 1.0 \text{ mm}^2$ diaphragms with various pore geometries shown in Figure 4.5. Stress in the piezoresistor regions can be influenced by the pore characteristics. The stress developed in the piezoresistor regions for the 100 pored diaphragm is significantly reduced.

In final sensitivity calculations the effect of piezoresistor length is considered and stress data from FEA are input into the following equation [37]:

$$\frac{\Delta V}{V} = \frac{\Delta R}{R} = \frac{\pi_T \left(\sum_{i=1}^n S_{nx_i} A_i \right) + \pi_l \left(\sum_{i=1}^n S_{ny_i} A_i \right)}{A_i} \quad (30)$$

where π_l and π_T are the transverse and longitudinal piezoresistor coefficients, S_{nxi} and S_{nyi} are the parallel and perpendicular normal stresses of i^{th} element found within the piezoresistors and A_i are the area of the i^{th} element. This calculation technique compensates for the stress averaging across the piezoresistors and better predicts sensor output. We determined that piezoresistor pairs (2 resistors each $10 \times 75 \mu\text{m}^2$) spaced $10 \mu\text{m}$ from the diaphragm edge with a spacing of $20 \mu\text{m}$ would generate stresses needed for the specified output and could be manufactured reliably.

The design implements eight piezoresistors in total but only the longitudinal and transverse pairs need to be investigated in order to calculate the sensor output performance. The longitudinal piezoresistor (LR1, LR2) stresses are equivalent because they are mirrored along the symmetry plane.

Alternatively each of the transverse piezoresistor pairs has a unique stress distribution and the resistor closer to the diaphragm edge has higher normal stress. Figure 4.11 gives the averaged stress distribution along the length of the piezoresistors in the 52 pore $1 \times 1 \text{ mm}^2$ diaphragm under a 150 kPa load. Compressive stresses in the longitudinal piezoresistors significantly decrease from -307 MPa to -107 MPa over its 75 μm length. It is apparent that the length of the perpendicular resistors cannot be neglected for the sensitivity calculations in this design.

A summary of normal stresses in piezoresistors for the three principal directions is shown in Table 4.2 for the 1 mm diaphragm with 52 pores. Piezoresistor stresses were then calculated for porous diaphragms with widths of 0.5, 1.0, 1.25 and 1.5 mm. Stresses in the z direction (normal to the diaphragm) are insignificant and are ignored for sensitivity calculations. We integrate the length of piezoresistors to get the average longitudinal and transverse stresses that are then used calculate the resistance change at an applied pressure.

Figure 4.12 displays normal stresses parallel and perpendicular to the diaphragm edge for the piezoresistors in relation to applied pressure for the four diaphragm sizes.

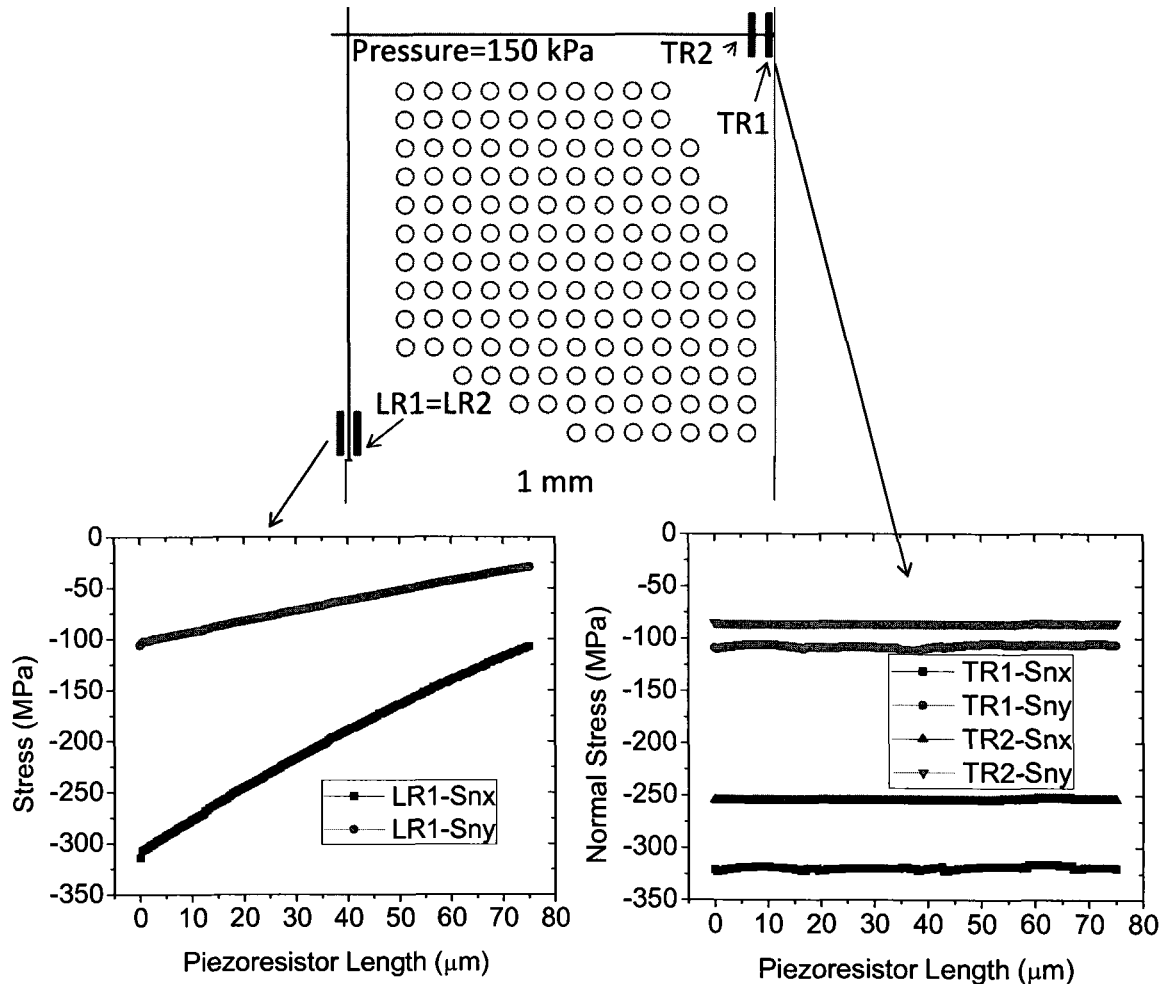


Figure 4.11. Average normal stresses induced in the longitudinal (left) and transverse (right) piezoresistors as a function of length at an applied pressure of 150 kPa using the $1.0 \times 1.0 \text{ mm}^2$ diaphragm (top). The normal stress (S_{nx}) varies from $>300 \text{ MPa}$ close to the edge to $<150 \text{ MPa}$ moving $75 \mu\text{m}$ towards the inside of the diaphragm. This stress gradient is used for calculating the sensitivity of the various sensor designs.

The black rectangles in the figure correspond to the piezoresistors with arrows representing the stress in a particular direction. For the longitudinal piezoresistors the parallel and perpendicular stresses are the same due to symmetry but this is not the case for the transverse resistors which have four unique average stresses. Substituting the average longitudinal and transverse stresses (Figure 4.12) into equation 4, we can obtain the $\Delta R/R$ for each of the resistor pairs.

Table 4.2. Min, max and average normal stress developed in the longitudinal and transverse piezoresistors in the three principal directions at an applied pressure of 150 kPa.

Piezoresistor	Stress Tensor	Min (MPa)	Max (MPa)	Average (MPa)
Longitudinal LR1=LR2	S _{nx}	-107	-307	-200
Longitudinal LR1=LR2	S _{ny}	-106	-29.2	-65
Longitudinal LR1=LR2	S _{nz}	-.015	-.045	-.027
Transverse TR1	S _{nx}	-316	-323	-319
Transverse TR1	S _{ny}	-105	-112	-107
Transverse TR1	S _{nz}	-.013	-.035	-.024
Transverse TR2	S _{nx}	-253	-255	-254
Transverse TR2	S _{ny}	-84	-86	-84
Transverse TR2	S _{nz}	-.006	-.012	-.09

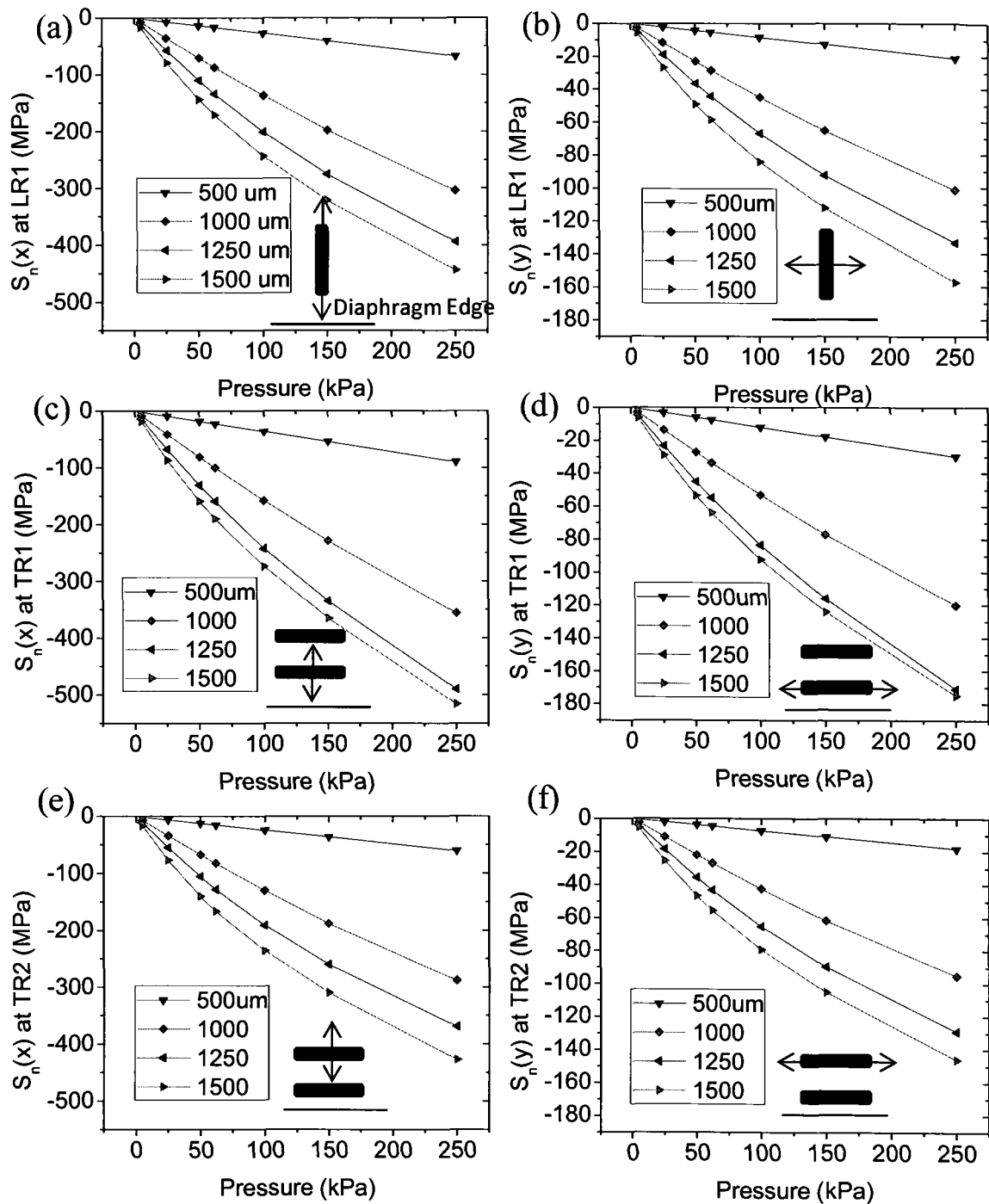


Figure 4.12. Average normal stresses (a, c, e) perpendicular (S_{nx}) and (b, d, e) parallel (S_{ny}) to the diaphragm edge in the (a,b) longitudinal and (c-e) transverse piezoresistor pairs. Piezoresistors are represented by the black rectangles and arrows represent normal stress in a particular direction. Due to symmetry the longitudinal resistors have the same normal stress while the transverse piezoresistors are dependent on location.

The longitudinal and transverse piezoresistive coefficients for *p-type* silicon at low doping concentrations and room temperature defined by Smith [29] are: $\pi_l = 1/2(\pi_{11} + \pi_{12} + \pi_{44}) = 71.8 \times 10^{-11} \text{ Pa}^{-1}$ and $\pi_t = 1/2(\pi_{11} + \pi_{12} - \pi_{44}) = -66.3 \times 10^{-11} \text{ Pa}^{-1}$, where $\pi_{11} = 6.6 \times 10^{-11} \text{ Pa}^{-1}$, $\pi_{12} = -1.1 \times 10^{-11} \text{ Pa}^{-1}$, and $\pi_{44} = 138.1 \times 10^{-11} \text{ Pa}^{-1}$. The resistance change ($\Delta R/R$) with regard to applied pressure has been calculated for the longitudinal and transverse piezoresistor pairs shown in Figure 4.13. The resistor pairs are well balanced giving outputs that are similar in magnitude but opposite in sign. Sensors with 1.25×1.25 and $1.5 \times 1.5 \text{ mm}^2$ diaphragm are more sensitive than the smaller diaphragms but also have higher nonlinearity across the 5-250 kPa pressure range. Designing pressure sensors in the low pressure range is often a compromise between sensitivity and nonlinearity. This nonlinearity arises from large diaphragm deflections of thin membranes and is caused by the finite elongation of the central interior plane [38-40]. Simulations were used to determine stresses induced in the piezoresistors used large deflection theory taking into account the diaphragm deformation. Although simulations showed nonlinearity at higher pressures for the larger diaphragms (1.25, 1.5 mm) they are intended for use at lower pressures $< 50 \text{ kPa}$ where it is of less concern. Since the piezoresistor pairs were slightly unbalanced the $\Delta R/R$ values were inserted into equation 31 [41] to improve output voltage calculations.

$$\Delta V = \frac{r}{(1+r)^2} \left(\frac{\Delta R1}{R1} - \frac{\Delta R2}{R2} + \frac{\Delta R3}{R3} - \frac{\Delta R4}{R4} \right) V_{in} \quad (31)$$

This equation takes into account the small variability between resistor pairs where $r = R2/R1 = R3/R4$, V_{in} is the bridge-input voltage and V_{out} is the differential output voltage.

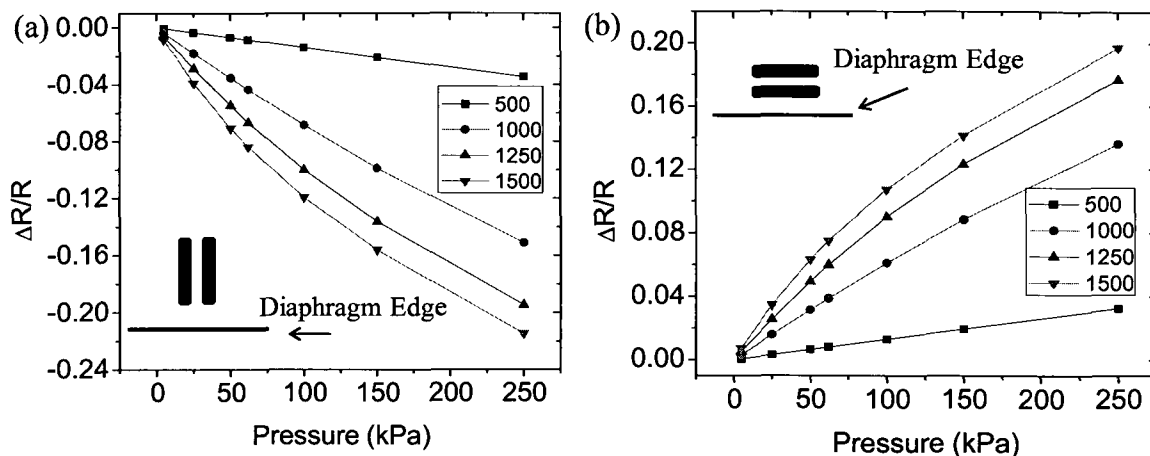


Figure 4.13. Change in resistance ($\Delta R/R$) of the (a) longitudinal and (b) transverse p -type piezoresistor pairs as a function of applied pressure for design shown in Figure 4.5e with widths of 0.5, 1.0, 1.25, and 1.5 mm and 30 μm pores. It was determined that the longitudinal resistors have a slightly higher $\Delta R/R$.

The input voltage was set at 1V and the sensor output and sensitivity is shown in Figure 4.14. Sensitivity analysis indicates that the 1.25 and 1.5mm sensors are predominately linear up to $\sim 100\text{kPa}$ above which diaphragm stretching occurs and reduces stress in the piezoresistors and hence voltage output.

4.6 Conclusions

This chapter describes the design, modeling, and development of a novel silicon-based porous diaphragm piezoresistive pressure sensor concept for use with hydrogels. Finite element results show that it is possible to incorporate a perforation or diffusion pores into the diaphragm while maintaining mechanical stresses needed in the piezoresistors. Six proposed designs were compared to conventional solid diaphragm sensors. We found that the optimal design exhibits removed pores from the midlines of the diaphragm, close to the edges, and around piezoresistors.

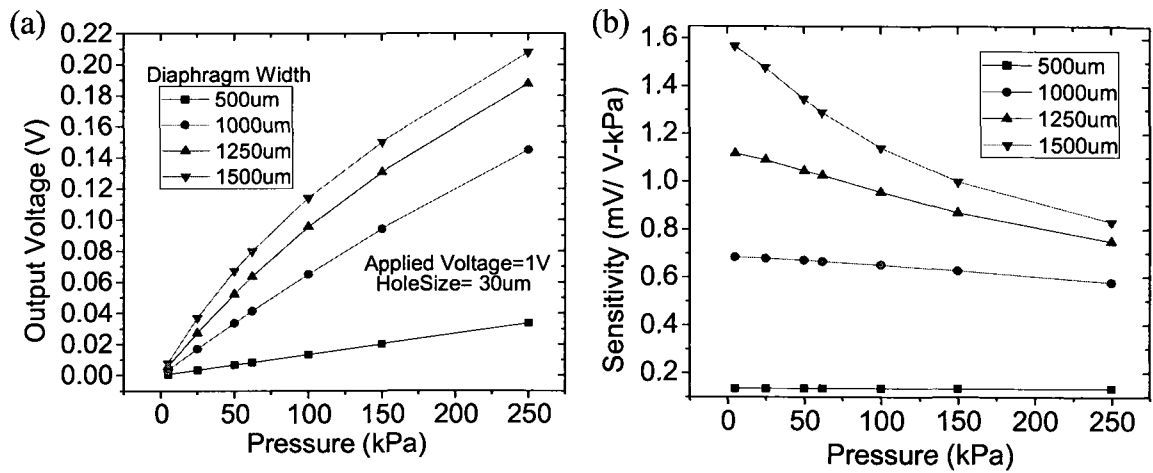


Figure 4.14. Porous diaphragm sensor output characteristics describing the (a) output voltage and (b) sensitivity as a function of pressure and diaphragm width. All diaphragms in this model use the design shown in Figure 4.5e with 30 μm pores with and thickness of 10 μm .

This is a conservative design because it significantly reduces the amount of stresses located in the pore regions while minutely increasing the electrical output. This particular geometry was implemented to other diaphragm sizes in order to measure pressures ranging from 5 to 250 kPa. To our knowledge this the first time a pressure sensor with perforated diaphragm for combined stress/pressure sensing and diffusion of analytes into the sensor cavity has been reported. The final designs show qualified sensitivity of .1-1.23 mV/V-kPa.

4.7 References

- [1] T. Tanaka, D. Fillmore, S.-T. Sun *et al.*, "Phase Transitions in Ionic Gels," *Physical Review Letters*, vol. 45, no. 20, pp. 1636, 1980.
- [2] J. Kopecek and J. Yang, "Hydrogels as Smart Biomaterials," *Polymer International*, vol. 56, pp. 1078-1098, 2007.
- [3] B. D. Johnson, D. J. Beebe, and W. C. Crone, "Effects of Swelling on the Mechanical Properties of a pH-Sensitive Hydrogel for Use in Microfluidic Devices," *Materials Science and Engineering: C*, vol. 24, no. 4, pp. 575-581, 2004.
- [4] S. K. De, N. R. Aluru, B. Johnson *et al.*, "Equilibrium Swelling and Kinetics of pH-Responsive Hydrogels: Models, Experiments, and Simulations," *Journal of Microelectromechanical Systems*, vol. 11, no. 5, pp. 544-555, 2002.
- [5] G. Gerlach, M. Guenther, G. Suchanek *et al.*, "Application of Sensitive Hydrogels in Chemical and pH Sensors," *Macromolecular Symposia*, vol. 210, no. 1, pp. 403-410, 2004.
- [6] J. Sorber, G. Steiner, V. Schulz *et al.*, "Hydrogel-Based Piezoresistive pH Sensors: Investigations Using FT-IR Attenuated Total Reflection Spectroscopic Imaging," *Analytical Chemistry*, vol. 80, no. 8, pp. 2957-2962, 2008.
- [7] B. Zhao and J. S. Moore, "Fast pH- and Ionic Strength-Responsive Hydrogels in Microchannels," *Langmuir*, vol. 17, no. 16, pp. 4758-4763, 2001.
- [8] D. Y. Jung, J. J. Magda, and I. S. Han, "Catalase Effects on Glucose-Sensitive Hydrogels," *Macromolecules*, vol. 33, no. 9, pp. 3332-3336, 2000.
- [9] J. T. Suri, D. B. Cordes, F. E. Cappuccio *et al.*, "Continuous Glucose Sensing with a Fluorescent Thin-Film Hydrogel," *Angewandte Chemie*, vol. 115, no. 47, pp. 6037-6039, 2003.
- [10] D. T. Eddington and D. J. Beebe, "Flow Control with Hydrogels," *Advanced Drug Delivery Reviews*, vol. 56, no. 2, pp. 199-210, 2004.
- [11] A. Guiseppi-Elie, S. Brahim, G. Slaughter *et al.*, "Design of a Subcutaneous Implantable Biochip for Monitoring of Glucose and Lactate," *Sensors Journal, IEEE*, vol. 5, no. 3, pp. 345-355, 2005.
- [12] Y. J. Zhao, A. Davidson, J. Bain *et al.*, "A MEMS Viscometric Glucose Monitoring Device." pp. 1816-1819 Vol. 2.
- [13] Y. Zhao, S. Li, A. Davidson *et al.*, "A MEMS Viscometric Sensor for Continuous Glucose Monitoring," *Journal of Micromechanics and Microengineering*, no. 12, pp. 2528, 2007.

- [14] J. Wang, "Electrochemical Glucose Biosensors," *Chemical Reviews*, vol. 108, no. 2, pp. 814-825, 2008.
- [15] G. Lin, S. Chang, H. Hao *et al.*, "Osmotic Swelling Pressure Response of Smart Hydrogels Suitable for Chronically-Implantable Glucose Sensors," *Sensors and Actuators B: Chemical*, vol. 144, pp. 332-336, 2010.
- [16] I. S. Han, M. H. Han, J. Kim *et al.*, "Constant-Volume Hydrogel Osmometer: A New Device Concept for Miniature Biosensors," *Biomacromolecules*, vol. 3, no. 6, pp. 1271-1275, 2002.
- [17] S. Herber, J. Borner, W. Olthuis *et al.*, "A Micro CO₂ Gas Sensor Based on Sensing of pH-Sensitive Hydrogel Swelling by Means of a Pressure Sensor," *Digest of Technical Papers - International Conference on Solid State Sensors and Actuators and Microsystems, TRANSDUCERS '05*. pp. 1146-1149.
- [18] S. Herber, W. Olthuis, P. Bergveld *et al.*, "Exploitation of a pH-Sensitive Hydrogel Disk for CO₂ Detection," *Sensors & Actuators: B. Chemical*, vol. 103, no. 1-2, pp. 284-289, 2004.
- [19] A. Richter, A. Bund, M. Keller *et al.*, "Characterization of a Microgravimetric Sensor Based on pH Sensitive Hydrogels," *Sensors and Actuators B: Chemical*, vol. 99, no. 2-3, pp. 579-585, 2004.
- [20] J. Cong, X. Zhang, K. Chen *et al.*, "Fiber Optic Bragg Grating Sensor Based on Hydrogels for Measuring Salinity," *Sensors and Actuators B: Chemical*, vol. 87, no. 3, pp. 487-490, 2002.
- [21] F. W. Scheller, U. Wollenberger, A. Warsinke *et al.*, "Research and Development in Biosensors," *Current Opinion in Biotechnology*, vol. 12, no. 1, pp. 35-40, 2001.
- [22] G. Gerlach, M. Guenther, J. Sorber *et al.*, "Chemical and pH Sensors Based on the Swelling Behavior of Hydrogels," *Sensors and Actuators B: Chemical*, vol. 111-112, pp. 555-561, 2005.
- [23] M. Guenther, D. Kuckling, C. Corten *et al.*, "Chemical Sensors Based on Multiresponsive Block Copolymer Hydrogels," *Sensors and Actuators B: Chemical*, vol. 126, no. 1, pp. 97-106, 2007.
- [24] M. Guenther, G. Gerlach, D. Kuckling *et al.*, "Chemical Sensors Based on Temperature-Responsive Hydrogels," *Proc. SPIE*. p. 61670T.
- [25] Q. Thong Trinh, G. Gerlach, J. Sorber *et al.*, "Hydrogel-Based Piezoresistive pH Sensors: Design, Simulation and Output Characteristics," *Sensors and Actuators B: Chemical*, vol. 117, no. 1, pp. 17-26, 2006.
- [26] S. Herber, W. Olthuis, and P. Bergveld, "A Swelling Hydrogel-Based PCO₂ Sensor," *Sensors and Actuators B: Chemical*, vol. 91, no. 1-3, pp. 378-382, 2003.

- [27] G. Lin, S. Chang, C. H. Kuo *et al.*, "Free Swelling and Confined Smart Hydrogels for Applications in Chemomechanical Sensors for Physiological Monitoring," *Sensors & Actuators: B. Chemical*, pp. 186-195, 2008.
- [28] G. Shih-Chin and L. Chengkuo, "Analytical Solutions of Sensitivity for Pressure Microsensors," *Sensors Journal, IEEE*, vol. 1, no. 4, pp. 340-344, 2001.
- [29] C. S. Smith, "Piezoresistance Effect in Germanium and Silicon," *Physical Review*, vol. 94, no. 1, pp. 42, 1954.
- [30] K. E. Petersen, "Silicon as a Mechanical Material," *Proceedings of the IEEE*, vol. 70, no. 5, pp. 420-457, 1982.
- [31] M. J. Madou, *Fundamentals of Microfabrication : The Science of Miniaturization*, 2nd ed., Boca Raton, Fla. ; London: CRC Press, 2002.
- [32] H. D. Tong, H. V. Jansen, V. J. Gadgil *et al.*, "Silicon Nitride Nanosieve Membrane," *Nano Lett.*, vol. 4, no. 2, pp. 283-287, 2004.
- [33] C. van Rijn, M. van der Wekken, W. Nijdam *et al.*, "Deflection and Maximum Load of Microfiltration Membrane Sieves made with Silicon Micromachining," *Microelectromechanical Systems, Journal of*, vol. 6, no. 1, pp. 48-54, 1997.
- [34] S. L. Tao and T. A. Desai, "Microfabricated Drug Delivery Systems: from Particles to Pores," *Advanced Drug Delivery Reviews*, vol. 55, no. 3, pp. 315-328, 2003.
- [35] Y. Ezo, M. Koshiishi, M. Mita *et al.*, "Recent Development of Micropore Optics using MEMS Technologies." p. 62661B.
- [36] Z. Yang, C.-B. Kim, C. Cho *et al.*, "The Concentration of Stress and Strain in Finite Thickness Elastic Plate Containing a Circular Hole," *International Journal of Solids and Structures*, vol. 45, no. 3-4, pp. 713-731, 2008.
- [37] S. M. Sze and K. K. Ng, *Physics of Semiconductor Devices*: Wiley-Interscience, 2007.
- [38] S. P. Timoshenko and S. Woinowsky-Krieger, "Theory of Plates and Shells," *Engineering Societies Monographs*, New York: McGraw-Hill, 1959, 2nd ed., 1959.
- [39] J. A. Voorthuyzen and P. Bergveld, "The Influence of Tensile Forces on the Deflection of Circular Diaphragms in Pressure Sensors," *Sensors Actuators*, pp. 201-13, 1984.
- [40] S. Samaun, K. D. Wise, and J. B. Angell, "An IC Piezoresistive Pressure Sensor for Biomedical Instrumentation," *Biomedical Engineering, IEEE Transactions on*, vol. BME-20, no. 2, pp. 101-109, 1973.

- [41] C.-C. Lee, C.-T. Peng, and K.-N. Chiang, "Packaging Effect Investigation of CMOS Compatible Pressure Sensor using Flip Chip and Flex Circuit Board Technologies," *Sensors and Actuators A: Physical*, vol. 126, no. 1, pp. 48-55, 2006.

CHAPTER 5

DEVELOPMENT, FABRICATION, AND CHARACTERIZATION OF PIEZORESISTIVE PRESSURE SENSORS USING PERFORATED DIAPHRAGMS FOR HYDROGEL SENSING

5.1 Abstract

Hydrogels have been demonstrated to swell in response to a number of external stimuli including pH, CO₂, glucose, and ionic strength making them useful for detection of metabolic analytes. In order to measure the hydrogel swelling pressure, we have fabricated and tested novel perforated diaphragm piezoresistive pressure sensors and arrays that couple the pressure sensing diaphragm with a perforated semipermeable membrane. The 2×2 arrays measure approximately 3 × 5 mm² and consist of four square sensing diaphragms with widths of 1.0, 1.25, and 1.5 mm used to measure full scale pressures of 50, 25, and 5 kPa, respectively. These four diaphragms with ranging sensitivities allow the sensor arrays to be coupled to a diverse number of hydrogels, with different swelling pressures. Round micropores were etched with the sensing diaphragm to allow analyte diffusion into the sensor cavity where the hydrogel material is located. The pore geometry and placement were optimized with the use of finite element analysis to reduce stress located in the perforated region while maintaining elevated stress concentrations within the piezoresistors. The 14-step front side wafer process was carried out by a commercial foundry service (MSF, Frankfurt (Oder), Germany).

Diaphragm pores were created using a combination of potassium hydroxide (KOH) etching and deep reactive ion etching (DRIE). The sensing diaphragm was fabricated using silicon. Four p-type piezoresistor pairs were ion implanted in regions of high stress as determined using finite element analysis. The metallization consists of sputtered aluminum-silicon (1 μm thick) alloy, thermal oxide (120 nm) and plasma enhanced (PE) nitride (600nm) were used on for diaphragm insulation and passivation. Characterization of sensor arrays was performed without the use of hydrogels using a custom bulge testing apparatus that simultaneously measured deflection, pressure, and electrical output. These initial test results are discussed, then used to quantify the sensor sensitivity and show proof-of-concept. From these initial tests the diaphragms were found to have a small negative deflection which is attributed to compressive stress found in the passivation layers. Measured deflections were compared to finite element simulations and found to be within 10% with the addition of a 281 MPa compressive stress in the modeled passivation layers. Simulations also showed that the sensitivity was slightly improved for the perforated diaphragm designs while empirical electrical characterization showed that the perforated diaphragm sensors were slightly less sensitive than solid diaphragm sensors. This discrepancy is believed to be due to the influence of compressive stress found within passivation layers and poor etching uniformity. The new perforated diaphragm sensors were fully functional with sensitivities ranging from 23 to 252 $\mu\text{V}/\text{V-kPa}$ (FSO= 5 to 80mV), and show a higher nonlinearity at elevated pressures than identical sensors with solid diaphragms. Sensors ($1.5 \times 1.5 \text{ mm}^2$) with perforated diaphragms (pores=40 μm) have a nonlinearity of approximately 10% while for the identical solid diaphragm sensor it was roughly 3 % over the entire 200 kPa range. This

is the first time piezoresistive pressure sensors with integrated diffusion pores for detection of hydrogel swelling pressure have been fabricated and tested.

5.2 Introduction

Recent developments of specialized hydrogels for medical and chemical sensing applications has created a need to quantify physical changes that occur (within the hydrogel) in response to changing environmental conditions. These “stimuli-responsive” hydrogels have been shown to swell or shrink in response to a number of environmental and chemical stimuli including temperature [1], electric field [2], pH [3-8], glucose [9-15], and ionic strength [4, 10, 16-19]. Numerous studies have been performed on these hydrogels. Magda *et al.* [17] designed and tested a miniature biosensor for glucose concentration measurements in blood using the combination of a pressure transducer and a pH glucose gel. Herber *et al.* [18-22] created a number of sensors used for monitoring carbon dioxide concentrations. Gerlach *et al.* [6, 7, 16, 23-25] used hydrogels to measure to measure the changes in pH. Other transduction mechanisms used to measure the physical transitions in hydrogels include: quartz crystal microbalances (resonance) [26], holographic Bragg diffraction (optical) [27], electrode impedance (electrical) [12, 28], permittivity [29], and piezoresistive based cantilevers or membranes (mechanical-electrical) [6, 16, 24, 25, 30].

One sensor concept that directly addresses this need directly couples hydrogels to micropressure sensors. These devices use the principle that chemically induced changes in the hydrogel causes an osmotic pressure increase or decrease leading to swelling or contracting, respectively. This swelling of the gel when confined under isochoric conditions leads to an increased pressure in the sensor cavity. The hydrogel is placed in

contact with the sensing diaphragm (<5 mm) which converts these pressure fluctuations to changes in resistance which are measured using a Wheatstone bridge. The diaphragm acts as a stress intensifier and the piezoresistors are placed in regions of highest stress, which are typically located close to the midpoint of the diaphragm edge. The thin piezoresistive diaphragm and hydrogel cavity required are typically created using KOH etching of the bulk silicon [23-25]. Researchers have previously mechanically cut gels to size and manually positioned them in the cavity [6, 23-25, 30] or alternatively polymerized the hydrogel solution directly in the cavity [18, 21].

A commonality to these designs is after hydrogel insertion a backing plate is attached to the backside of the sensor. This backing plate allows the diffusion of analyte into/out of the hydrogel cavity. Backing plates in the past has been made from wire meshes, nonporous polymers, micromachined silicon, or glass and attached using adhesives or anodic bonding. Although the mesh backing keeps the hydrogel in contact with the sensor diaphragm a number of problems exist with the current technology. First, the fabrication procedure is complex requiring a number of individual components to be fabricated and assembled individually. Secondly, the permeable mesh has been shown to flex, reducing the amount of pressure transferred to the sensor diaphragm and hence reducing sensitivity [31]. If the pores are too large, the gels have been shown to exude through the mesh reducing pressure within the cavity [31]. Therefore it is important to accurately control the size of the pores. We previously reported on the optimization and geometry of a novel perforated diaphragm pressure sensor through the use of finite element analysis [32]. It was shown that it is possible to incorporate pores directly into the sensing diaphragm without sacrificing sensitivity or mechanical robustness. Another

observation was with appropriate placement, pores can act as stress concentrators and increase stress induced in the piezoresistors, potentially yielding higher sensitivity. The remainder of this article describes the fabrication and initial bulge testing of the first generation perforated diaphragm pressure sensors. A subsequent paper will describe the physical behavior of the sensors while coupled with the hydrogels tested in wet sensing environments.

5.3 Sensor Design and Fabrication

Square perforated diaphragm pressure sensors with widths of 0.5, 1.0, 1.25, and 1.5 mm were fabricated to measure hydrogel swelling pressures ranging from 5 to 150 kPa. Specifically two types of dies were fabricated during the process. First, “individual” sensor dies had sensors with widths of 0.5, 1.0, 1.25, and 1.5 mm and designed to have full scale pressures of 150, 50, 25 and 5 kPa, respectively. These sensors were intended to be singulated. Secondly, “array” dies contained four diaphragms: two $1 \times 1 \text{ mm}^2$, one $1.25 \times 1.25 \text{ mm}^2$ and one $1.5 \times 1.5 \text{ mm}^2$ in a more compact layout measuring approximately $3 \times 5 \text{ mm}^2$. The arrays are intended to be used with various types of hydrogels simultaneously with different swelling pressure characteristics. The bulk micromachined cavities of the arrays are separated by $200 \mu\text{m}$ thick silicon frame created during the backside KOH etching. Finite element analysis showed that an insignificant amount of deflection occurs within the frame. Therefore cross sensitivities should be small and individual sensor sensitivity should be unaffected. These sensor designs were created conservatively with a large factor of safety and a burst pressure >10 times that of the specified full pressure. The 14-step front side fabrication process was carried out on 5 wafers by a commercial foundry (MSF, Frankfurt (Oder),

Germany). The pores were created in diaphragms using deep reactive ion etching (DRIE) and the hydrogel cavity was etched using potassium hydroxide (KOH). Perforated sensors included etched pores of 10, 20, 30, and 40 μm in diameter within the diaphragms to allow the diffusion of analyte in to the hydrogel cavity using an optimized geometry previously discussed. This pore size was chosen for three primary reasons. First, they can easily be etched using DRIE. Secondly, they provide a wide range to open surface areas allowing us to study the effect of pore incorporation and lastly they are small enough to prohibit the hydrogel from exuding through the membrane. Solid diaphragm sensors were also fabricated using identical design parameters as a control. All design parameters including diaphragm thickness, piezoresistor dimensions, pores location, and metallization remained consistent. The optimized pattern of pores (30 μm) is shown for the perforated $1 \times 1 \text{ mm}^2$ sensor in Figure 5.1. This design was used because it significantly reduced the stress located on the pores without significantly modifying the normal longitudinal and transverse stress found in the piezoresistors. Figure 5.1 also illustrates the different types of sensor test structures fabricated including Kelvin, contact chain, diode and alignment test structures.

5.3.1 Oxidation and Implantation

Four-inch (100 mm) *n*-type wafers oriented in the (100) direction with a resistivity of 3-6 $\Omega\text{-cm}$ were used as substrates. They were $400 \pm 25 \mu\text{m}$ thick and double side polished with a total thickness variation (TTV) of $< 5 \mu\text{m}$. The wafers were cleaned using an RCA 1 ($\text{NH}_4\text{OH}:1, \text{H}_2\text{O}_2: 2, \text{H}_2\text{O}:10$) etch bath for 3 minutes. The first step in fabrication was to deposit a $500 \pm 20 \text{ nm}$ silicon oxide using wet oxidation at 1000°C .

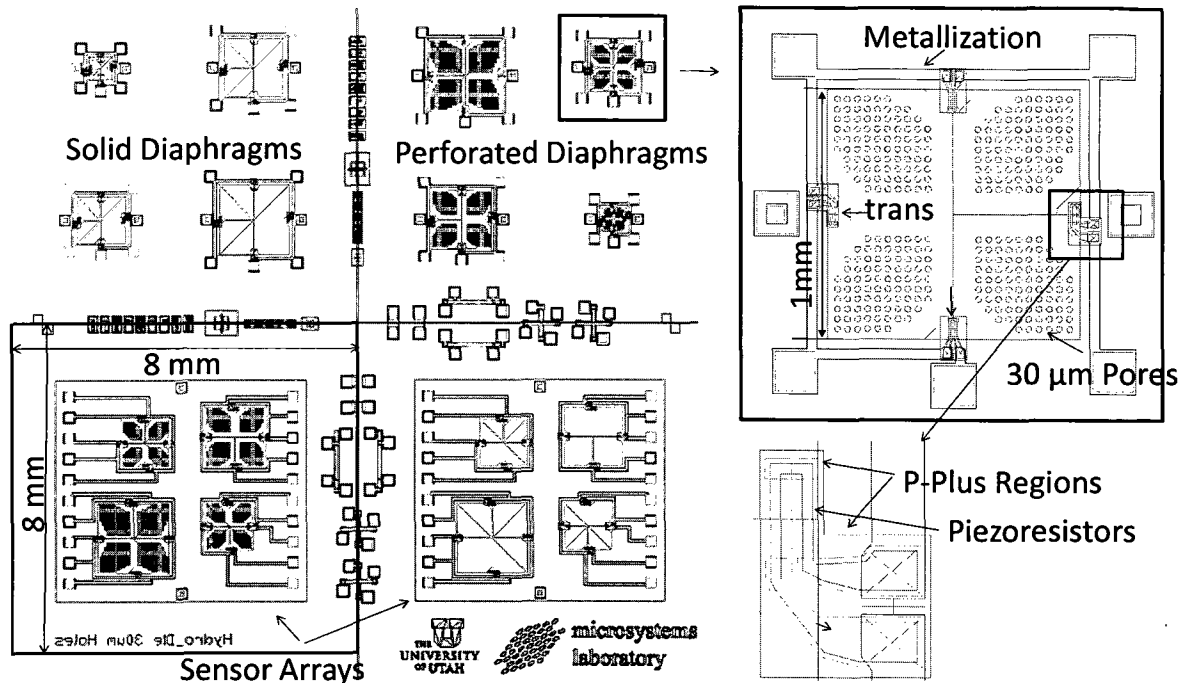


Figure 5.1. CAD mask layout showing the various sensors designs. Sensors with and without perforated diaphragms were fabricated as individual sensors and part of an array. An enlarged image of the $1 \times 1 \text{ mm}^2$ perforated (pores= $30 \mu\text{m}$) diaphragm pressure sensor is shown on the right. This optimized pore geometry reduces the stress located within the pores, maintains high stress within the piezoresistors, while maintaining the diaphragm mechanical integrity. An enlargement of the transverse piezoresistor pair is shown below the $1 \times 1 \text{ mm}^2$ sensor magnification.

Lithography was performed on the silicon oxide using AZ 6612 photo resist as an implantation mask and etched using a buffered oxide etch (BOE 7:1 NH_4F :7, HF :1). This oxide layer isolates the metallization from the silicon substrate and opens the active diaphragm regions. A piranha etch (H_2O_2 , H_2SO_4) was used to remove the resist and another RCA 1 cleaning was performed. The highly conductive p^+ plus regions were defined using AZ 6612 resist and the first implantation was performed at an accelerating voltage of 80 keV with a dose of $5.5 \times 10^{14} \text{ cm}^{-2}$ as shown in Figure 5.2.

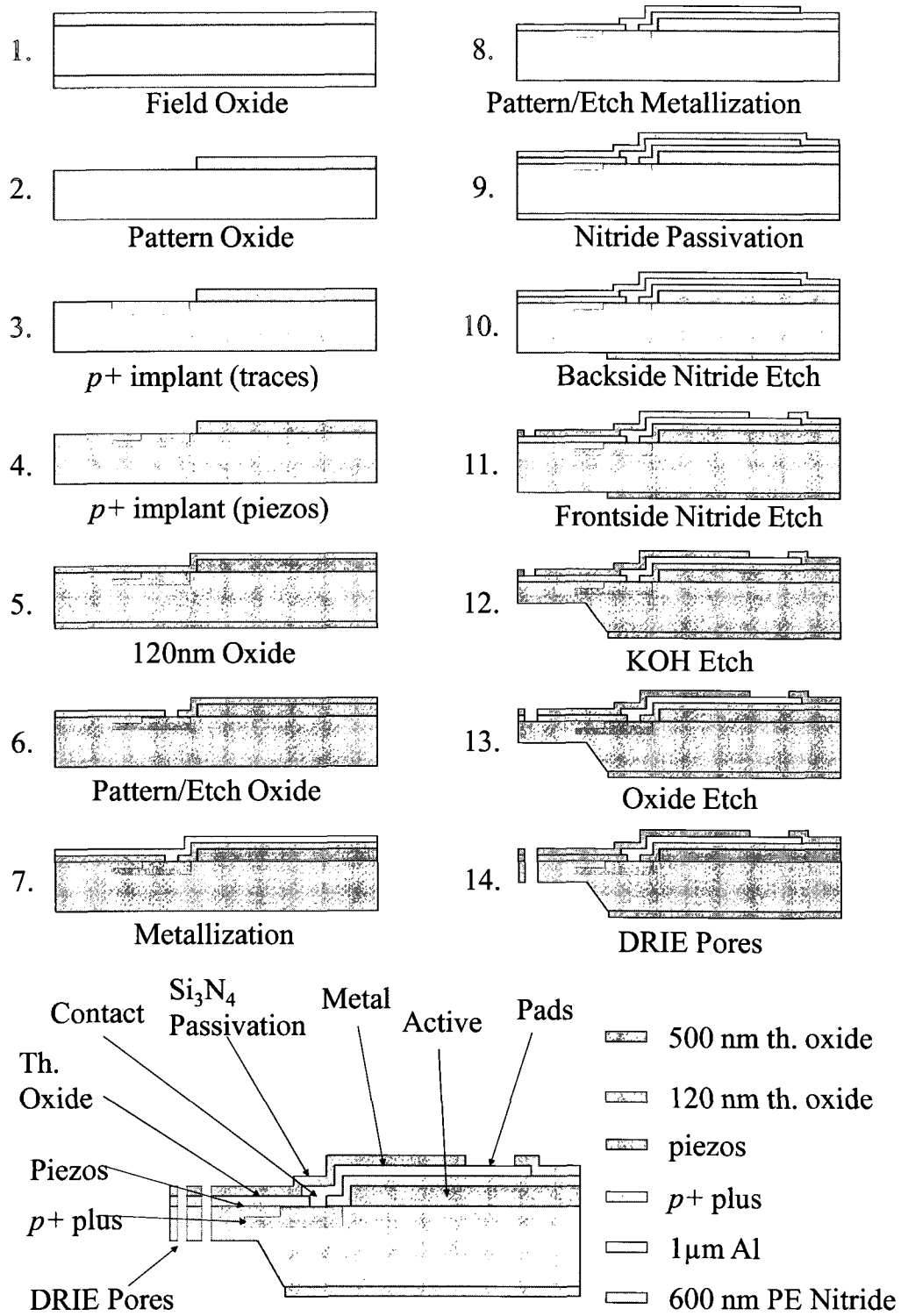


Figure 5.2. Fourteen-step fabrication processes used to manufacture the perforated diaphragm pressure sensors.

The second implantation was performed at 90 keV and dose $2.5 \times 10^{15} \text{ cm}^{-2}$ designed to yield resistivity of $4 \times 10^{-3} \Omega\text{-cm}$ and depth of $0.2 \mu\text{m}$ for the piezoresistors.

5.3.2 Insulation and Metallization

After ion implantation the photoresist was removed using AZ stripper and cleaned in an O_2 plasma, followed by the growth of a $100 \pm 5 \text{ nm}$ thick thermal silicon oxide at 1000°C using dry oxidation. This layer is used to passivate the diaphragm and create another dielectric insulation layer for the metallization. The contact traces are situated on top of both oxidations layers to reduce leakage currents to the substrate.

An additional patterning step is performed using AZ 2020 to open contact windows to the piezoresistors followed by a blanket deposition of a $1 \mu\text{m}$ sputtered aluminum-silicon alloy. Patterning and development of the aluminum metallization traces was performed using AZ 2020 resist and aluminum etchant. The wafer was then briefly (1 min) cleaned to remove any silicon particles using equal parts of HF and HNO_3 . After the removal of photoresist using AZ stripper the aluminum was annealed in forming gas ($\text{H}_2 + \text{N}_2$ mixture) at 400°C . These are steps 5-8 as shown in Figure 5.2.

5.3.3 Passivation and Pore Etching

Passivation of the metallization is critical for our sensors since their intended use is within wet environments (saline) in-vitro and/or in-vivo. Therefore a 600 nm silicon nitride was deposited using plasma enhanced chemical vapor deposition (PECVD) at 400°C on both the topside and backside of the wafers. Windows were etched on the backside of the wafer using reactive ion etching (RIE) at pressure of 100 mTorr, at 100 W, using a mixture of CF_4 and O_2 , creating a mask for the bulk micromachining using

potassium hydroxide (KOH) wet etching. This process creates the cavity housing the hydrogel and controls the diaphragm thickness.

An AZ 2020 photoresist mask was used on the front-side of the wafer to define windows for contact etching and openings for the diaphragm pores. The nitride is etched with RIE and a subsequent BOE etching removes the 100 nm thermal oxide located within the pores. Bulk KOH etching was performed at 70°C (40% concentration) resulting in an etch rate of 35 to 40 $\mu\text{m}/\text{hour}$ leaving a membrane of $15 \pm 3 \mu\text{m}$ thickness. Photoresist (MA-P 1275) was then applied to the topside of the wafer and removed only over the pores for a Bosch™ DRIE etch process to etch the silicon and finalize the pores using (SF_6) and (C_4F_8). The photoresist was removed on the topside using AZ striper. Optical and scanning electron micrographs are displayed in Figure 5.3 showing sensors pre and post DRIE etching.

5.3.4 Dicing

In order to perform bulge testing “individual” and “array” dies measuring $8 \times 8 \text{ mm}^2$ were singulated from the wafer using a semi automatic Disco dicing saw at a feed rate of 2.5cm/sec.

5.4 Sensor Bulge Testing Apparatus

Investigating the performance of the perforated pressure sensors starts with characterizing the deflections of the diaphragms in response to the applied pressures. Accurate quantification of the deflection-pressure relationship provides important information on bending behavior giving insight to analytical and finite element model validity.

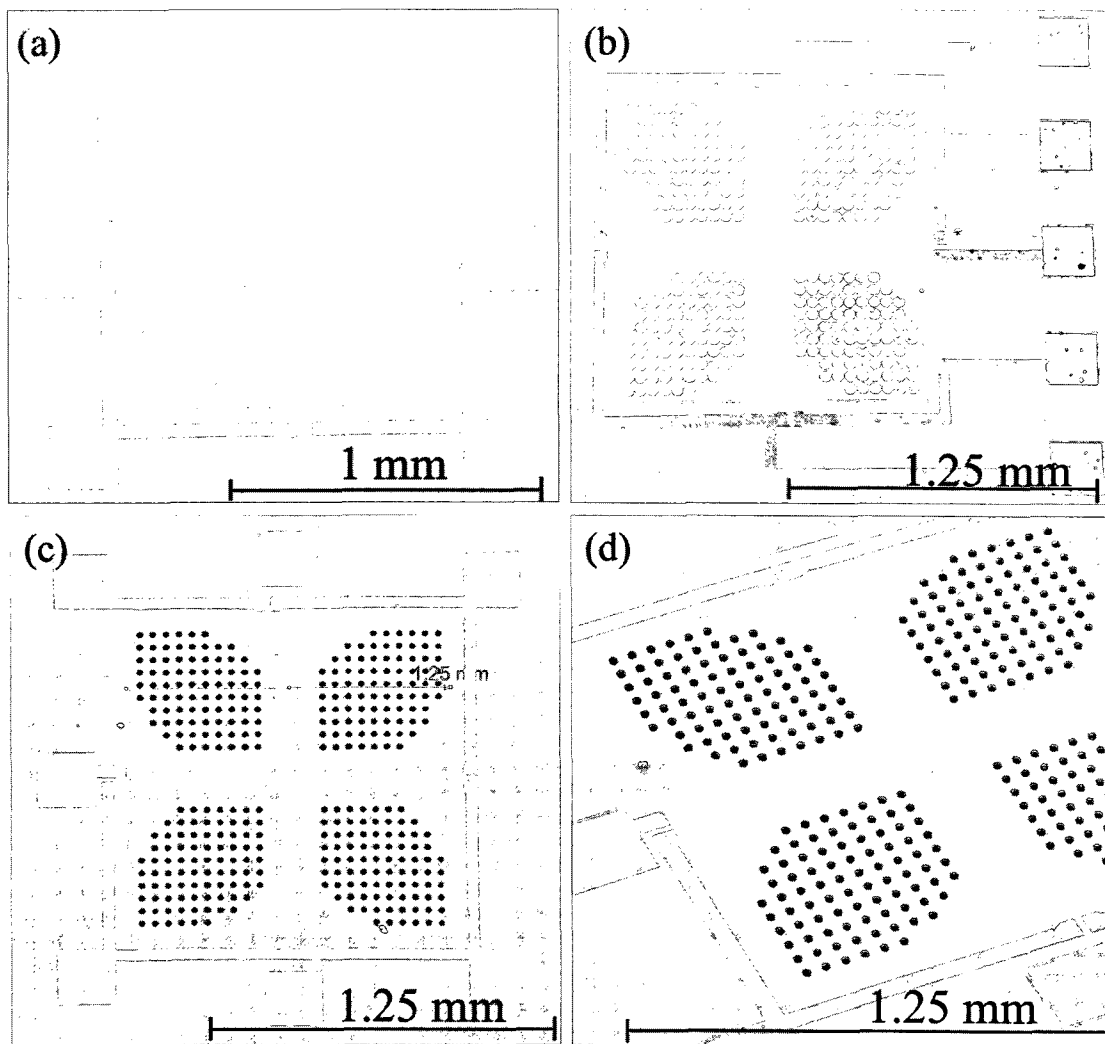


Figure 5.3. Images of the fabricated sensors. (a) Nomarski contrast optical micrograph of the $1.0 \times 1.0 \text{ mm}^2$ perforated diaphragm sensor illustrating the pores after wet etching but before DRIE. (b) Scanning electron microscope image of $1.25 \times 1.25 \text{ mm}^2$ perforated diaphragm sensor before DRIE. (c,d) SEM images of sensors post DRIE.

Sensor characterization was performed using a custom bulge testing station that couples an optical profilometer, an electronic pressure regulator, and electronics used to measure the sensor output shown in Figure 5.4a. The design and performance of this system are found in [33]. The system applies a regulated pressure to the backside of the diaphragms while measuring the sensors electrical output, calibrated applied pressure, and diaphragm deflection.

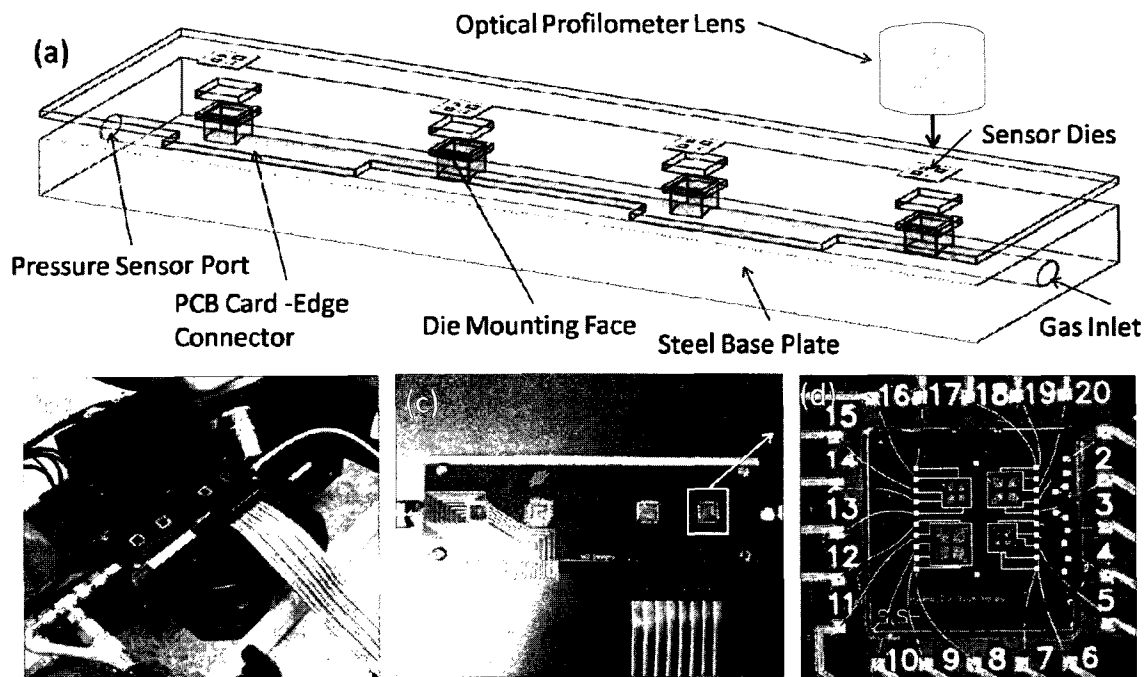


Figure 5.4. Illustrated is the CAD design and photographs of the bulge testing apparatus used to measure applied pressure, sensor electrical output, and diaphragm deflection. (a) CAD layout of testing stage. (b) The sensor testing stage is mounted to the optical profilometer. (c) Four sensors are simultaneously mounted to the stage for testing and (d) wire bonded to the PCB board.

The pressure can accurately be controlled with a resolution of approximately 290 Pa. An optical profilometer (Zygo Newview 5032, Stamford, CT) measures the three-dimensional diaphragm deflection with nanometer resolution. The $8 \times 8 \text{ mm}^2$ sensor dies were mounted to a stainless steel mounting plate using dicing wax (Nikka Seiko, Step wax No. 1, Tokyo, Japan) at 140°C to create an airtight seal. A calibrated pressure transducer (Omega PX429) with a range of 0-30 PSI and 0.08% full scale accuracy is mounted to the steel plate and connected to the channel that links the backside of the sensors. A Keithley 2400 digital source meter powers and records the output (4-20 mA) from the pressure transducer during experiments. Four sensor dies can be attached to the mounting plate and exposed to the same pressure channel.

The sensors are ultrasonically wedge wire bonded using 50 μm diameter insulated gold wire (PF003774, Kanthal, Palm Coast, Florida, USA) from the bond pads to the custom printed circuit board (PCB) that is screwed on top of the steel mounting plate shown in Figure 5.4d. Although the particular tests presented here do not necessarily require the use of insulated gold wires, they will be needed for future wet tests. Hence, the sensors were assembled with this wire. The PCB board has a total of 80 electrical connections using two double-sided 40 contact card edge connectors (Figure 5.4b-c). This high density output gives us the ability to measure characteristics of all piezoresistors simultaneously.

The card edge connectors are connected to a 40 pin terminal block which is attached to a Keithley 4200 semiconductor parameter analyzer which has four independent source measure units (SMUs) giving us the ability to record data from each piezoresistor while testing. This system allows us to characterize and calibrate the sensors before testing in-vitro/in-vivo while coupled with hydrogels.

5.5 Experimental Methods

We compared diaphragm deflections (μm), output voltages (V), and sensitivities ($\mu\text{V}/\text{V}\text{-kPa}$) between perforated and solid diaphragm sensors. Measurements were performed on “individual” and “array” sensor dies containing both perforated and solid diaphragms with sizes of $0.5\times 0.5\text{ mm}^2$, $1\times 1\text{ mm}^2$, $1.25\times 1.25\text{ mm}^2$, and $1.5\times 1.5\text{ mm}^2$ and DRIE etched pores have sizes of 10, 20, 30 and 40 μm . While testing sensors, compressed N_2 was supplied via the gas inlet (Figure 5.4a) with pressures up to 200 kPa then exited through pores in the diaphragms while pressure was being measured by the calibrated pressure transducer. As pressure was increased N_2 flowed through perforated

diaphragms and the system was allowed to reach steady state equilibrium. In these tests we assume that at equilibrium (steady state) pressure gradients along the length of the testing stage N₂ gas chamber are minimal and be neglected. Therefore, pressure applied to the bottom face of the diaphragms is identical to that witnessed by the calibrated pressure transducer. This assumption was validated by measuring the identical perforated sensor in all stage four positions at a single pressure; we found no output signal variation dependent on location.

Although analytical models exist that describe the deflection of solid square diaphragms [34-36], to our knowledge no models have been developed for the deflection of perforated diaphragms. Finite element modeling using COMSOL 3.4a (Burlington, MA, USA) was used to evaluate and optimize designs by modeling deflections, and stress within the diaphragms. Details on the finite element models demonstrating proof of concept are presented in [32].

Results show that it is possible to incorporate pores into the diaphragm without compromising the mechanical integrity or electrical sensitivity. Simulations used in this article use the same boundary conditions as previously reported [32] but an additional 120 nm oxide and a 600 nm thick silicon nitride passivation layers were included.

Since these sensors will be used with hydrogels, the boundary conditions of the FE models may not be completely accurate. Specifically the models do not take drag forces / differential pressures across the aperture into account, because they were designed for use with hydrogels.

5.6 Results and Discussion

5.6.1 Mechanical Deflection

While testing the pressure signal, noise varied by roughly $\pm 20 \mu\text{A}$, corresponding to a variation of $\pm 0.26 \text{ kPa}$ for pressures $< 100 \text{ kPa}$ which is less than 1% and neglected. At higher pressures $> 150 \text{ kPa}$ two sources of pressure noise became apparent. The system base noise levels became larger, on the order of $\pm 100 \mu\text{A}$ corresponding to fluctuations of $\pm 1.29 \text{ kPa}$. Although there was a significant increase of noise from the pressure sensor output it was still $< 1\%$ of the overall output. The second source of noise was large pressure oscillations which at pressures ($> 150 \text{ kPa}$) would cause large oscillations in deflection as shown in Figure 5.5 for the most sensitive $1.5 \times 1.5 \text{ mm}^2$ sensor.

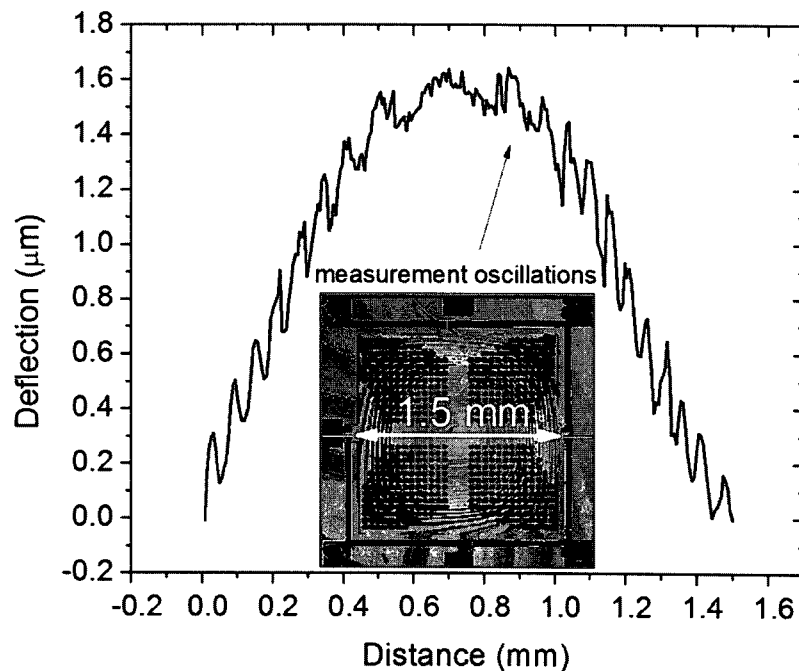


Figure 5.5. Large oscillations were observed in the deflection measurements if pressure fluctuations were present during testing. These pressure fluctuations were found to be caused by N_2 leaking from the bottom side of the sensors when not properly bonded with dicing wax to the mounting plate.

We eliminated these large pressure fluctuations and deflection oscillations using an improved method of sealing of the sensor dies to the mounting plate. After heating the steel mounting plate to 150°C dicing wax (stepwax #1, Nikka Seiko, Tokyo, Japan) was applied to the and then sensors were attached. The improved adhesion of the sensor die to the mounting plate prevented the leakage of N₂, which we suspect caused the pressure fluctuations and diaphragm oscillations. The deflection measurements taken after the dies were mounted using step wax had very stable deflections and were easily measured. Solid diaphragms were tested in a similar fashion but the system was closed and pressure was increased and held constant.

Measurements of the solid and perforated diaphragms using the new mounting technique showed little diaphragm vibration and significantly less noise from the pressure sensor output. Figure 5.6 shows the deflection of a 1.25×1.25 mm² diaphragm with 10 μm pores loaded with pressure ranging from 0 to 64.1 kPa (9 PSI). The diaphragm deflection clearly increases with pressure on a scale that can be easily and accurately measured using the optical profilometer. With no applied pressure the diaphragm has a negative deflection (bows downward) approximately (~100nm), which is attributed to the compressive stress developed in the passivation layers. In previous simulations, only membranes without residual stress were modeled and it is well known that the presence of tensile or compressive stress significantly alters the deflection behavior of membranes [37]. During deposition compressive stress was formed by a mismatch between the coefficients of thermal expansion of the Si substrate, SiO₂, and Si₃N₄ films or/and intrinsic stresses within the film.

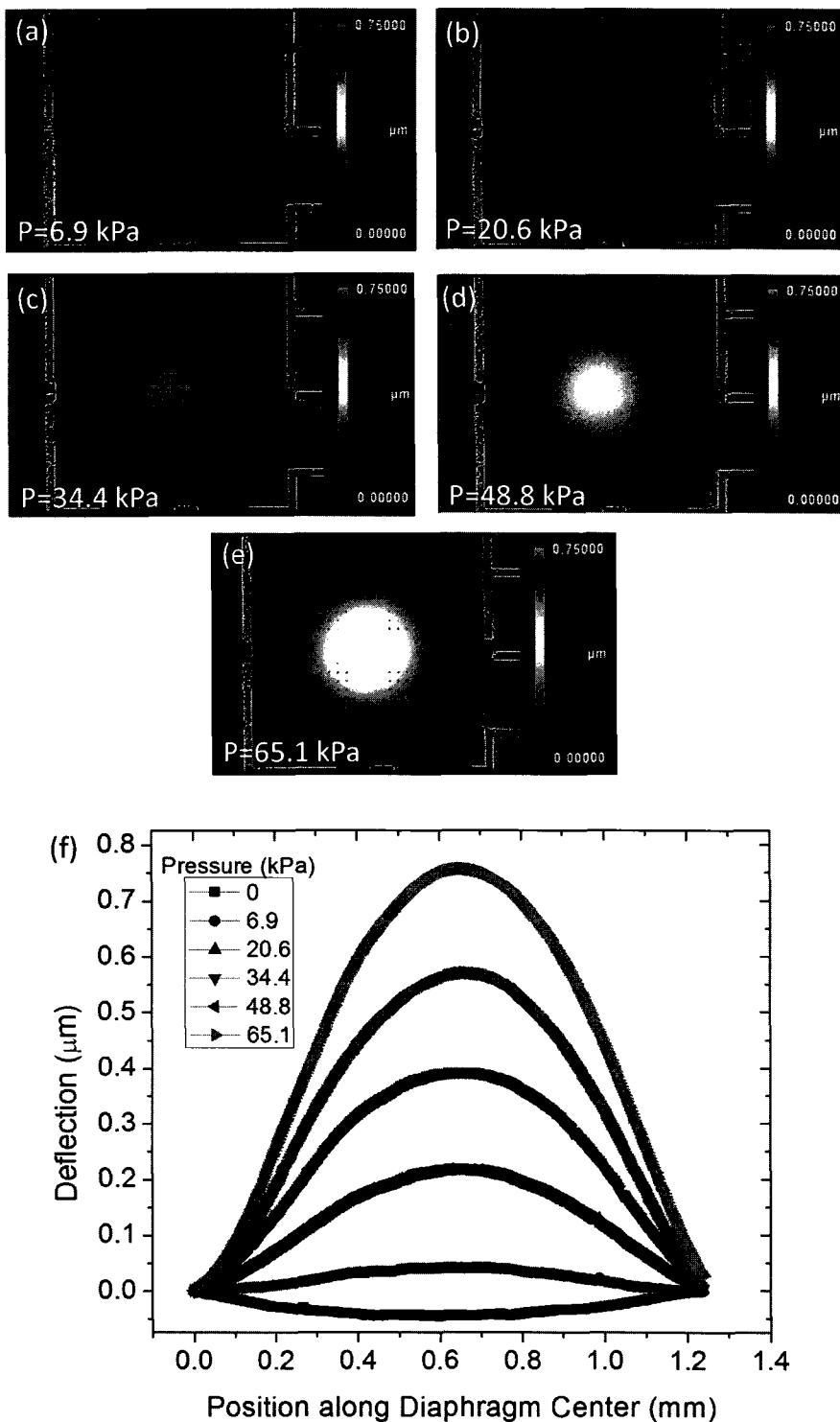


Figure 5.6. Plots of the bulged diaphragm surface for the 1.25×1.25 mm perforated diaphragm (pores = $10 \mu\text{m}$) at pressures up to 65.1 kPa. Surface plots (a-f) are shown and exported deflection data along the center of the diaphragm and plotted in relation to position (g). Compressive stress within the passivation layers caused the diaphragm to bulge downward with no applied pressure.

The intrinsic residual stress Si_3N_4 films are known to vary significantly and are affected by the film composition [38, 39]. For our diaphragms, the PECVD Si_3N_4 films (600 nm) and SiO_2 (120 nm) passivation layers are close to 5% the diaphragm thickness the source of compressive stress. A better fit between the simulated data and empirical results was achieved using 281 MPa compressive stress in the Si_3N_4 layer. Figure 5.7 compares the empirical and simulated deflection behavior of the $1.5 \times 1.5 \text{ mm}^2$ diaphragm with respect to hole size at a pressure of 150 kPa. Diaphragms with pores (a) $10 \mu\text{m}$ (b) $30 \mu\text{m}$ and (c) $40 \mu\text{m}$ in diameter had maximum deflections of 1.85, 2.23, and $1.92 \mu\text{m}$, respectively.

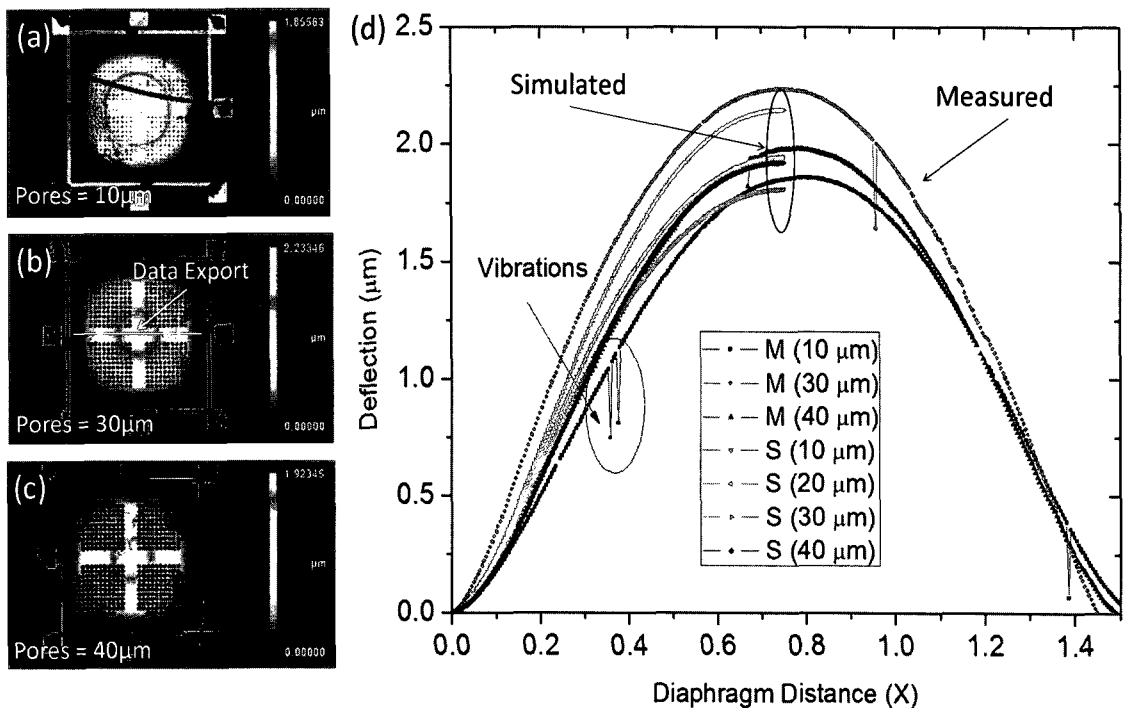


Figure 5.7. Surface plots recorded during bulge testing of diaphragms with (a) $10 \mu\text{m}$ (b) $30 \mu\text{m}$ and (c) $40 \mu\text{m}$ pores at 150 kPa. Data were exported along the center of the diaphragm and (d) plotted in comparison to simulations results. Empirical and simulated results are similar and show that deflection of the diaphragm with $30 \mu\text{m}$ pores is the largest.

It was determined that the simulated deflections and empirical measurement are well correlated and have similar bending shapes. The perforated diaphragms bending shapes have slightly higher curvature than solid diaphragms due to the incorporation of pores which makes the diaphragms slightly more compliant and less rigid. Sensor diaphragms used in this study have from 1.5 to 33% open surface area and the sensors with 40 μm pores while the most compliant actually deflect less than diaphragms with 30 μm pores. This is due to a combination of loading effects and diaphragm stiffness. The diaphragms with higher open surface area experience less force on the bottom diaphragm surface due to the applied pressure. Then again, they are also less stiff and more easily deformed.

The same trends were observed in empirical measurements and in finite element analysis which applied pressure to the diaphragms' bottom face. Although the effect is small these trends were observed in experiment and are more pronounced when comparing the largest diaphragms since they are the most pressure sensitive, and have the highest pore density and largest deflections.

Another observation is that at higher pressures the empirically measured deflection is minutely higher than that of simulated values while at lower pressures it is the inverse. We hypothesize that this is due to higher frictional drag forces caused by the N_2 flowing through in the diaphragm perforations which are not accounted for in the simulations. At elevated testing pressures the N_2 gas flows through the pores at higher velocities leading to increased drag forces which may also cause a modified flow pattern [40]. We observed no measurable deflection hysteresis in the testing of the diaphragms.

5.7 Electrical Response

In parallel to measuring deflection the sensors electrically characterized. Seven bond pads were implemented in the design allowing us to characterize the performance of each piezoresistor individually, and the bridge output voltage as shown in Figure 5.8. Pads 6 and 7 were used as substrate contacts which verified that there was insignificant current leakage from the piezoresistors and metallization. The resistance of the unloaded longitudinal piezoresistors was measured across pads 1-2 and 4-5 had an average resistance of $3.16 \pm 0.05 \text{ k}\Omega$ while the transverse piezoresistors had a resistance of 3.02 ± 0.05 , slightly unbalancing the Wheatstone bridge. The piezoresistors were within approximately 5% of the $3 \text{ k}\Omega$ design specification. The imbalance was likely due to preloading caused by initial compressive stresses present in the passivation layers. For sensitivity testing pads 3 and 4 were grounded, voltage of 5V was applied to pad 1, and voltage output is measured between pads 2 (decreasing) and 5 (increasing) with respect to applied pressure. Figure 5.8 gives the output voltages of the individual solid and perforated sensors from 0 to 62 kPa. The measured bridge offset ranged from 91 to 104 mV at a supply voltage of 5V. We also estimated the electrical output characteristics of the perforated diaphragm pressure sensors from data derived from the finite element simulations. These results established that sensors with a diaphragm thickness of $10 \text{ }\mu\text{m}$ should give voltage outputs ranging from 0.13 to 1.23 mV/V-kPa for sensors with dimensions of 0.5×0.5 and $1.5 \times 1.5 \text{ mm}$ ($30 \text{ }\mu\text{m}$ pores), respectively. The measured output voltages were approximately 80% less than these approximated values. This is presumably due the fabricated diaphragm thickness of $15 \pm 3 \text{ }\mu\text{m}$.

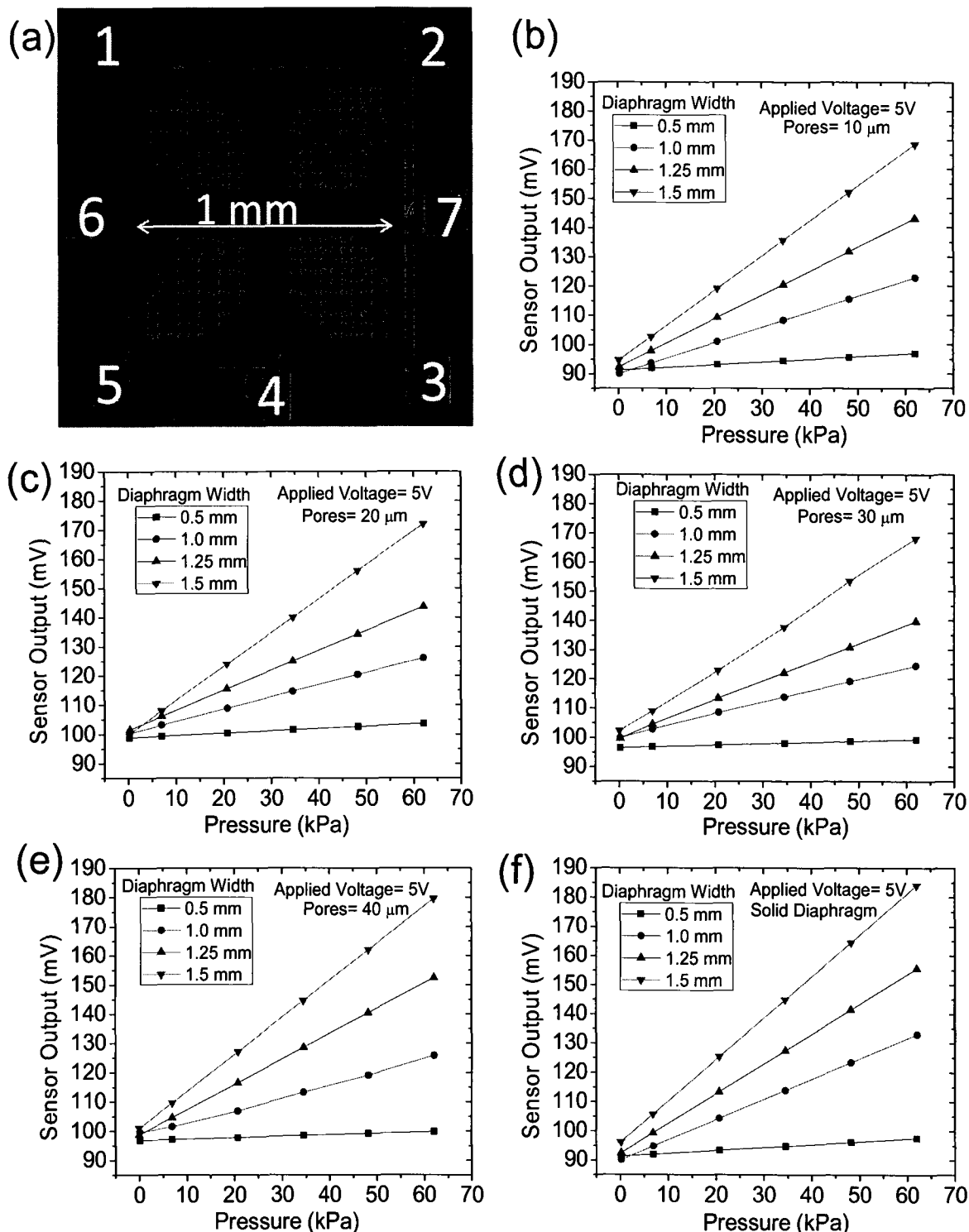


Figure 5.8. Micrograph of $1 \times 1 \text{ mm}^2$ sensor and electrical output voltages determined from bulge testing. (a) Optical micrograph of the $1 \times 1 \text{ mm}^2$ (pores = $20 \mu\text{m}$) with bond pads labeled. (b-f) Sensor outputs for both perforated and solid diaphragm sensors at a supply voltage of 5 V . Results show that the sensors behave linearly within this pressure regime and the largest sensors have the highest sensitivities.

When comparing the sensitivity over this pressure range (0-64 kPa), solid diaphragm sensors (without pores) had only slightly improved sensitivity shown in Figure 5.9. This was apparent for all diaphragm widths and is further proof that diaphragm thickness was the primary cause of reduced sensitivity. Examination of data revealed that initial incorporation of pores reduced sensitivity by 16, 28, 34, and 19% for the 10, 20, 30 and 40 μm sized pores when compared to the solid diaphragms. Sensitivity and output voltages are similar for both the individual sensors and arrays (Figure 5.9), and although the sensitivity is reduced the perforated diaphragm sensors are fully functional and easily measured. Another interesting effect is that sensitivity suddenly increases for the 40 μm pores. Simulation data showed that pores incorporated in the diaphragm increased longitudinal stresses perpendicular to the diaphragm edge while reducing the parallel transverse stress.

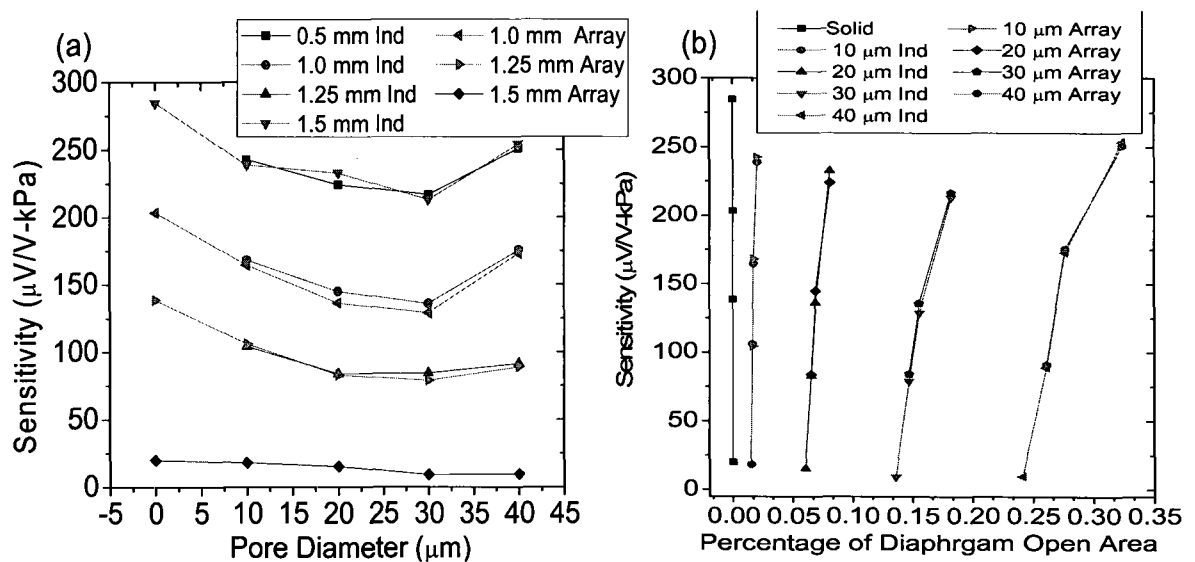


Figure 5.9. Sensitivity of the different diaphragm designs as a function of (a) pore diameter and (b) percentage of open area. The incorporation of pores reduced the sensitivity of sensors. Diaphragms with pores=40 μm in diameter had higher sensitivity than other perforated designs with smaller diameter pores. This is due to a modified stress distribution across the piezoresistors.

The output nonlinearity was calculated using the End Point Linearity (EPL) model and all sensors tested have a nonlinearity $< 1\%$ for pressures < 65 kPa which is the range most significant to measure hydrogel swelling. Elevated pressure testing (up to 200kPa) was performed to study broadened sensor nonlinearity and failure characteristics. All dies were subjected to the elevated pressures without failure. Diaphragms 1.5×1.5 mm² both solid and perforated (10, 40 μ m pores) were compared because they are the most sensitive and most prone to nonlinearity. Results of the test are shown in Figure 5.10.

We found that the perforated sensors have higher nonlinearity than the solid diaphragm sensors. In pressures measurements taken to 200 kPa the calculated nonlinearity is 3.49, 6.30, and 10.02 % for the 1.5×1.5 mm² sensors that are solid and perforated with 10 and 40 μ m pores, respectively. Nonlinearity in the solid diaphragm sensors is often due to large diaphragm deflections that cause stresses to be partially supported by membrane axial stresses (balloon effect) in response to the applied pressure. This is caused by the finite elongation in the central interior diaphragm plane. For solid square diaphragms approximate formulas have been derived to calculate nonlinearity using the strain-energy method [41] but for perforated diaphragms these models do not apply. The reduced stiffness of the larger pored diaphragms may explain why the electrical output from the 40 μ m pored diaphragm is significantly more nonlinear than the output from the 10 μ m and solid diaphragm designs. A second source of nonlinearity for the perforated sensors may stem from nonlinearity of the piezoresistive effect.

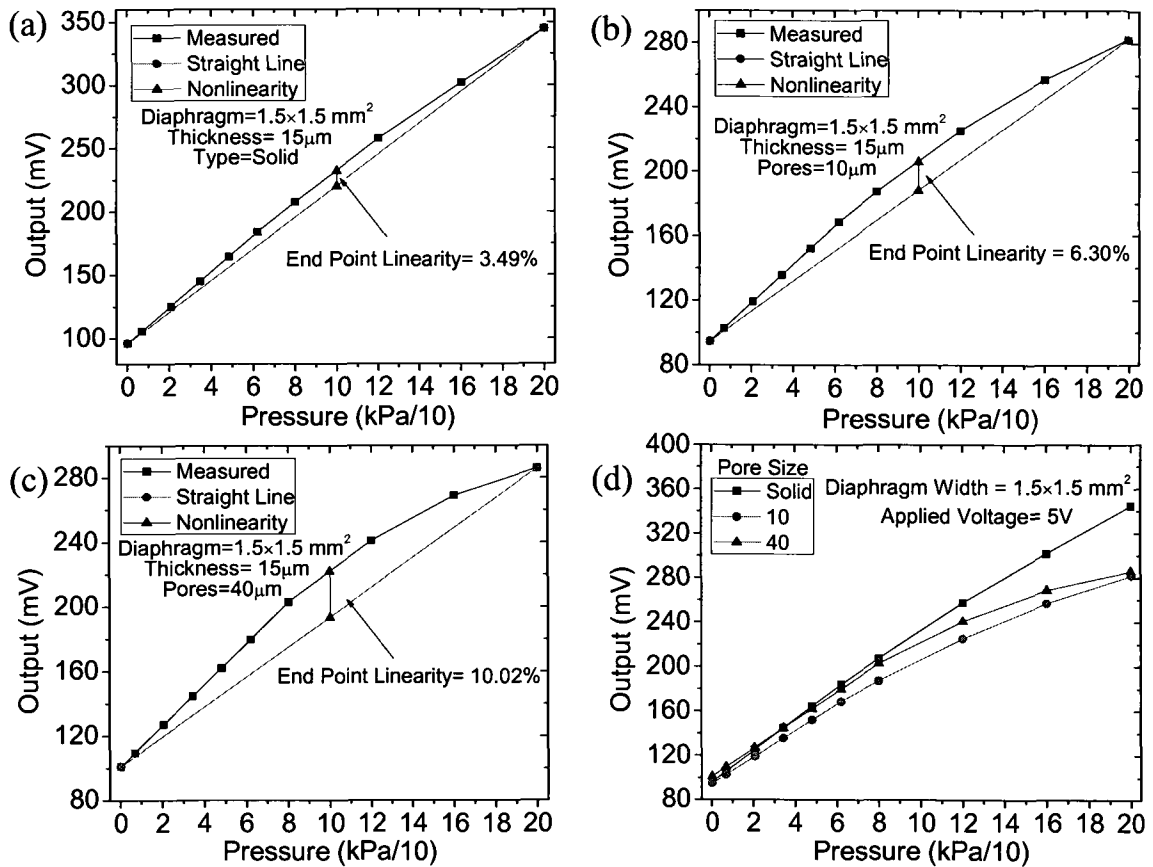


Figure 5.10. Elevated pressure (~ 200 kPa) linearity test performed on the 1.5×1.5 mm² diaphragms with (a) solid (b) 10µm and (c) 40 µm pores. Perforated sensors show higher linearity since pores reduce stiffness of the diaphragm leading to larger geometrical elongation and deformation.

It has been shown for high values of mechanical stresses (high pressures), resistivity changes are no longer proportional to the applied stress, and second and third order effects cannot be ignored. The diaphragms with 40 µm pores generate higher sensitivities and therefore more stress in the piezoresistors as shown in Figure 5.10a, and therefore may also behave more nonlinearly.

Additional sources of nonlinearity in the pressure sensors may be due to the piezoresistor positions deviating from the diaphragm edge location, causing asymmetry in the sensitivities of the different resistors within the Wheatstone bridge. Ideally, the

sensors were designed to have all resistors located at the same locations with respect to diaphragm edge. Fluctuations in substrate thickness, pore alignment, diaphragm thickness, and backside alignment accuracy in defining the diaphragm etch masks lead to piezoresistor position variation and may have contributed to the nonlinearity of the perforated diaphragm sensors [42].

The response time of the sensors is limited to the hydrogels' ability to create swelling pressure. This intrinsic property is specific to particular hydrogels and is complex and a function of hydrogel kinetics, diffusivity of the hydrogel, amount of crosslinking, and ionic character. To improve the response times thinner gels are used with a higher proportion of surface area, which increases the diffusion rate of analyte into the hydrogel. Therefore the diaphragms with larger open areas should permit higher diffusion rates and reduce sensor response times.

5.8 Conclusions

We have presented fabrication details and initial bulge testing results for novel sensors that incorporate diffusion channels into the sensing diaphragm for the detection of hydrogel swelling pressure. Sensors were created using a 14 step-fabrication process, and pores were etched in the diaphragm using a combination of DRIE and KOH etching. Bulge testing using N_2 shows that the diaphragms are under compressive stress attributed to the diaphragms passivation layers (SiO_2 and Si_3N_4). Bulge testing showed all perforated diaphragms are mechanically robust and able to withstand pressures >200 kPa. The diaphragm deflections were also dependent on pore size. Empirical and simulated results showed that the diaphragms with $30 \mu m$ pores had the highest deflections. This is due to a combination of effects. As the pore size increases the mechanical compliance is

increased but loading force decreases because of a larger open area. For the 30 μm diaphragms the effect of reduced stiffness is more significant than the reduced loading force. Simulated deflections are within 10% of empirically measured values for the fabricated diaphragms. Sensitivities ranged from 23 to 252 $\mu\text{V}/\text{V-kPa}$ for the perforated diaphragm pressure sensors. Incorporation of pores reduced sensitivity when compared to solid diaphragms. We found that for our design with 40 μm pores sensitivity was higher than for other pore sizes presumably due to over etching of the perforated diaphragm. This chapter shows that it is possible to incorporate pores into a pressure sensor diaphragm to allow chemical diffusion into the bulk etched hydrogel cavity. While the perforations do slightly reduce sensitivity, sensors remain fully functional. Electrical output measurements conducted at hydrogel relevant output pressures (up to 65 kPa) showed that the perforated diaphragm sensors have little nonlinearity (<1 %) for their designed pressure ranges. It was also found that increased pore size leads to higher nonlinearity at pressures tested up to 200 kPa. A separate paper “Novel Hydrogel Based Piezoresistive Sensor Array (2×2) with Integrated Perforated Diaphragm for Metabolic Monitoring (in vitro)” discusses the results from initial in-vitro chemical testing.

5.9 References

- [1] A. Richter, D. Kuckling, S. Howitz *et al.*, "Electronically Controllable Microvalves Based on Smart Hydrogels: Magnitudes and Potential Applications," *Journal of Microelectromechanical Systems*, vol. 12, no. 5, pp. 748-753, 2003.
- [2] T. Tanaka, D. Fillmore, S.-T. Sun *et al.*, "Phase Transitions in Ionic Gels," *Physical Review Letters*, vol. 45, no. 20, pp. 1636, 1980.
- [3] B. D. Johnson, D. J. Beebe, and W. C. Crone, "Effects of Swelling on the Mechanical Properties of a pH-Sensitive Hydrogel for Use in Microfluidic Devices," *Materials Science and Engineering: C*, vol. 24, no. 4, pp. 575-581, 2004.
- [4] S. K. De, N. R. Aluru, B. Johnson *et al.*, "Equilibrium Swelling and Kinetics of pH-Responsive Hydrogels: Models, Experiments, and Simulations," *Journal of Microelectromechanical Systems*, vol. 11, no. 5, pp. 544-555, 2002.
- [5] Q. Y. Cai and C. A. Grimes, "A Salt-Independent pH Sensor," *Sensors and Actuators B: Chemical*, vol. 79, no. 2-3, pp. 144-149, 2001.
- [6] G. Gerlach, M. Guenther, G. Suchanek *et al.*, "Application of Sensitive Hydrogels in Chemical and pH Sensors," *Macromolecular Symposia*, vol. 210, no. 1, pp. 403-410, 2004.
- [7] J. Sorber, G. Steiner, V. Schulz *et al.*, "Hydrogel-Based Piezoresistive pH Sensors: Investigations Using FT-IR Attenuated Total Reflection Spectroscopic Imaging," *Analytical Chemistry*, vol. 80, no. 8, pp. 2957-2962, 2008.
- [8] B. Zhao and J. S. Moore, "Fast pH- and Ionic Strength-Responsive Hydrogels in Microchannels," *Langmuir*, vol. 17, no. 16, pp. 4758-4763, 2001.
- [9] D. Y. Jung, J. J. Magda, and I. S. Han, "Catalase Effects on Glucose-Sensitive Hydrogels," *Macromolecules*, vol. 33, no. 9, pp. 3332-3336, 2000.
- [10] J. T. Suri, D. B. Cordes, F. E. Cappuccio *et al.*, "Continuous Glucose Sensing with a Fluorescent Thin-Film Hydrogel," *Angewandte Chemie*, vol. 115, no. 47, pp. 6037-6039, 2003.
- [11] D. T. Eddington and D. J. Beebe, "Flow Control with Hydrogels," *Advanced Drug Delivery Reviews*, vol. 56, no. 2, pp. 199-210, 2004.
- [12] A. Guiseppi-Elie, S. Brahim, G. Slaughter *et al.*, "Design of a Subcutaneous Implantable Biochip for Monitoring of Glucose and Lactate," *Sensors Journal, IEEE*, vol. 5, no. 3, pp. 345-355, 2005.
- [13] Y. J. Zhao, A. Davidson, J. Bain *et al.*, "A MEMS Viscometric Glucose Monitoring Device." pp. 1816-1819 Vol. 2.

- [14] Y. Zhao, S. Li, A. Davidson *et al.*, "A MEMS Viscometric Sensor for Continuous Glucose Monitoring," *Journal of Micromechanics and Microengineering*, no. 12, pp. 2528, 2007.
- [15] J. Wang, "Electrochemical Glucose Biosensors," *Chemical Reviews*, vol. 108, no. 2, pp. 814-825, 2008.
- [16] G. Gerlach, M. Guenther, J. Sorber *et al.*, "Chemical and pH Sensors Based on the Swelling Behavior of Hydrogels," *Sensors and Actuators B: Chemical*, vol. 111-112, pp. 555-561, 2005.
- [17] I. S. Han, M. H. Han, J. Kim *et al.*, "Constant-Volume Hydrogel Osmometer: A New Device Concept for Miniature Biosensors," *Biomacromolecules*, vol. 3, no. 6, pp. 1271-1275, 2002.
- [18] S. Herber, J. Borner, W. Olthuis *et al.*, "A Micro CO₂ Gas Sensor Based on Sensing of pH-Sensitive Hydrogel Swelling by Means of a Pressure Sensor," *Digest of Technical Papers - International Conference on Solid State Sensors and Actuators and Microsystems, TRANSDUCERS '05*. pp. 1146-1149.
- [19] S. Herber, W. Olthuis, P. Bergveld *et al.*, "Exploitation of a pH-Sensitive Hydrogel Disk for CO₂ Detection," *Sensors & Actuators: B. Chemical*, vol. 103, no. 1-2, pp. 284-289, 2004.
- [20] S. Herber, J. Bomer, W. Olthuis *et al.*, "A Miniaturized Carbon Dioxide Gas Sensor Based on Sensing of pH-Sensitive Hydrogel Swelling with a Pressure Sensor," *Biomedical Microdevices*, vol. 7, no. 3, pp. 197-204, 2005.
- [21] S. Herber, J. Eijkel, W. Olthuis *et al.*, "Study of Chemically Induced Pressure Generation of Hydrogels Under Isochoric Conditions using a Microfabricated Device," *The Journal of Chemical Physics*, vol. 121, no. 6, pp. 2746-2751, 2004.
- [22] S. Herber, W. Olthuis, and P. Bergveld, "A Swelling Hydrogel-Based PCO₂ Sensor," *Sensors and Actuators B: Chemical*, vol. 91, no. 1-3, pp. 378-382, 2003.
- [23] M. Guenther, G. Gerlach, C. Corten *et al.*, "Hydrogel-Based Sensor for a Rheochemical Characterization of Solutions," *Sensors & Actuators: B. Chemical*, 2007.
- [24] M. Guenther, D. Kuckling, C. Corten *et al.*, "Chemical Sensors Based on Multiresponsive Block Copolymer Hydrogels," *Sensors and Actuators B: Chemical*, vol. 126, no. 1, pp. 97-106, 2007.
- [25] Q. Thong Trinh, G. Gerlach, J. Sorber *et al.*, "Hydrogel-Based Piezoresistive pH Sensors: Design, Simulation and Output Characteristics," *Sensors and Actuators B: Chemical*, vol. 117, no. 1, pp. 17-26, 2006.

- [26] A. Richter, A. Bund, M. Keller *et al.*, "Characterization of a Microgravimetric Sensor Based on pH Sensitive Hydrogels," *Sensors and Actuators B: Chemical*, vol. 99, no. 2-3, pp. 579-585, 2004.
- [27] J. Cong, X. Zhang, K. Chen *et al.*, "Fiber Optic Bragg Grating Sensor Based on Hydrogels for Measuring Salinity," *Sensors and Actuators B: Chemical*, vol. 87, no. 3, pp. 487-490, 2002.
- [28] F. W. Scheller, U. Wollenberger, A. Warsinke *et al.*, "Research and Development in Biosensors," *Current Opinion in Biotechnology*, vol. 12, no. 1, pp. 35-40, 2001.
- [29] X. Huang, S. Li, J. S. Schultz *et al.*, "A Dielectric Affinity Microbiosensor," *Applied Physics Letters*, vol. 96, no. 3, pp. 033701, 2010.
- [30] M. Guenther, G. Gerlach, D. Kuckling *et al.*, "Chemical Sensors Based on Temperature-Responsive Hydrogels," *Proc. SPIE*, p. 61670T.
- [31] G. Lin, S. Chang, C. H. Kuo *et al.*, "Free Swelling and Confined Smart Hydrogels for Applications in Chemomechanical Sensors for Physiological Monitoring," *Sensors & Actuators: B. Chemical*, pp. 186-195, 2008.
- [32] M. Orthner, L. Rieth, S. Buetefisch *et al.*, "Design, Simulation and Optimization of a Novel Piezoresistive Pressure Sensor with Stress Sensitive Perforated Diaphragm for Wet Sensing and Hydrogel Applications," *Sensors and Actuators B: Chemical*, vol. Submitted Manuscript, 2009.
- [33] M. Orthner, L. Rieth, and F. Solzbacher, "High Speed Wafer Scale Bulge Testing Apparatus for the Determination of Thin Film Mechanical Properties," *Review of Scientific Instruments*, vol. Submitted Manuscript, 2009.
- [34] S. P. Timoshenko and S. Woinowsky-Krieger, "Theory of Plates and Shells," *Engineering Societies Monographs*, New York: McGraw-Hill, 1959, 2nd ed., 1959.
- [35] C. Hin-Leung and K. D. Wise, "Scaling Limits in Batch-Fabricated Silicon Pressure Sensors," *Electron Devices, IEEE Transactions on*, vol. 34, no. 4, pp. 850-858, 1987.
- [36] D. Maier-Schneider, J. Maibach, and E. Obermeier, "A New Analytical Solution for the Load-Deflection of Square Membranes," *Journal of Microelectromechanical Systems*, vol. 4, no. 4, pp. 238-241, 1995.
- [37] J. J. Vlassak and W. D. Nix, "A New Bulge Test Technique for the Determination of Young's Modulus and Poisson's Ratio of Thin Films," *J. Mater. Res.*, vol. 7, no. 12, 1992.
- [38] M. Stadtmueller, "Mechanical Stress of CVD-Dielectrics," *Journal of the Electrochemical Society*, vol. 139, no. 12, pp. 3669-3674, 1992.

- [39] J. M. Olson, "Analysis of LPCVD Process Conditions for the Deposition of Low Stress Silicon Nitride. Part I: Preliminary LPCVD Experiments," *Materials Science in Semiconductor Processing*, vol. 5, no. 1, pp. 51-60, 2002.
- [40] C. Van Rijn, *Nano and Micro Engineered Membrane Technology*: Elsevier Science, 2004.
- [41] K. Suzuki, T. Ishihara, M. Hirata *et al.*, "Nonlinear Analysis of a CMOS Integrated Silicon Pressure Sensor," *IEEE Transactions on Electron Devices*, vol. 34, no. 6, pp. 1360-1367, 1987.
- [42] S. Marco, J. Samitier, O. Ruiz *et al.*, "High-Performance Piezoresistive Pressure Sensors for Biomedical Applications using very Thin Structured Membranes," *Measurement Science and Technology*, no. 9, pp. 1195, 1996.

CHAPTER 6

HYDROGEL BASED PIEZORESISTIVE SENSOR ARRAYS (2×2) WITH PERFORATED DIAPHRAGMS FOR METABOLIC MONITORING (IN-VITRO)

6.1 Abstract

This report details the first experimental results from novel hydrogel sensor array (2×2) which incorporates analyte diffusion pores into a piezoresistive diaphragm for the detection of hydrogel swelling pressures and hence chemical concentrations. The sensor assembly was comprised of three components, the active four sensors, HPMA/DMA/TEGDMA hydrogel, and backing plate.

Each of the individual sensors of the array can be used with various hydrogels used to measure the presence of a number of stimuli including pH, ionic strength, and glucose concentrations. In this paper and to properly characterize the sensor assembly, hydrogels sensitive to changes ionic strength were synthesized using hydroxypropyl methacrylate (HPMA), N,N-dimethylaminoethyl methacrylate (DMA) and crosslinker tetra-ethyleneglycol dimethacrylate (TEGDMA) and inserted into the sensor assembly. This hydrogel quickly and reversibly swells when placed environments of physiological buffer solutions (PBS) with ionic strengths ranging from 0.025 to 0.15 M, making it ideal for proof-of-concept testing and initial characterization.

The assembly was wire bonded to a printed circuit board and coated with 3 ± 0.5 μm of Parylene using chemical vapor deposition (CVD) to protect the sensor and electrical connections during ionic strength wet testing. Two versions of sensors were fabricated for comparison, the first incorporated diffusion pores into the diaphragm, and the second used a solid diaphragm with perforated backing plate.

This new design (perforated diaphragm) was shown to have slightly higher sensitivity than solid diaphragm sensors with separate diffuse backing plates when coupled with the hydrogel. The sensitivities for the 1×1 mm^2 , 1.25×1.25 mm^2 , 1.5×1.5 mm^2 perforated diaphragm sensors were 53.3 ± 6.5 , 171.7 ± 8.8 , and 271.47 ± 27.53 mV/V-M , respectively. These results show that perforations in the diaphragm can be used not only to allow the diffusion of analyte into the cavity but to increase mechanical stress in the piezoresistive diaphragm, thereby increasing sensor output signal.

The time constants for swelling (τ -swelling) and contracting (τ -contracting) were calculated by fitting the sensor output half cycles to an exponential growth function. We found that the sensors' response was initially retarded during the preliminary hydrogel conditioning period then improved after 3 to 5 cycles with values of approximately 9 and 7 minutes for τ -swelling and τ -contracting. For all sensors tested τ -swelling $>$ τ -contracting. This may be due to the increased loading on the hydrogel from the diaphragm during the swelling process. During contraction the diaphragm aids the hydrogel by reversibly applying mechanical pressure and therefore reducing τ -contracting. Long term stability testing showed the sensors remained functional for upwards of two weeks in the test phosphate buffer solution (PBS).

6.2 Introduction

Hydrogels are polymeric materials that consist of a cross linked polymer network that absorbs/desorbs water in response to changes in surrounding environmental conditions. This diffusion of water within hydrogels causes swelling to occur in response to a shift in chemical potential and hence osmotic pressure. One classification of hydrogels known as “smart” or “stimuli responsive” reversibly swell in response to changes in environmental concentrations of specific target molecules. Using these “smart” hydrogels, sensor selectivity can be enhanced by attaching moieties to the hydrogel that selectively bind the analyte of interest including pH, glucose, CO₂ [1-4]. Many hydrogels are also biocompatible and highly suitable for use in implantable biomedical sensors and autonomous drug delivery devices. The response time of hydrogels was shown to improve through miniaturization by increasing the ratio of surface area to volume which increases the effective diffusion rate. Many approaches have been used to measure modifications in hydrogels optical, electrical, and mechanical properties including: holographic Bragg diffraction (optical) [5], electrode impedance (electrical) [6, 7], quartz crystal microbalances (resonance) [8], and piezoresistive based cantilevers or membranes (mechanical-electrical) [4, 9-12]. One of the most appealing transduction mechanisms used to detect hydrogel swelling is obtained by confining a thin piece (<500 μ m) of smart hydrogel between porous membrane and the diaphragm of a miniature piezoresistive pressure transducer. In this design the change in the environmental analyte concentration causes chemical diffusion through the pores of the membrane changing the osmotic swelling pressure within the hydrogel. This change in

chemical potential (osmotic pressure) causes swelling and an increase of mechanical pressure within the hydrogel cavity as measured by the pressure transducer.

Figure 6.1 shows two versions of “chemo-mechanical sensors” that we have fabricated that embody this sensing mechanism. The two designs differ from one another by the location of the analyte diffusion pores. The first design (Figure 6.1a) uses a periodic array of diffusion channels located on the backing plate while the new design (Figure 6.1b) incorporates the diffusion pores directly into the piezoresistive membrane. Previous reports have shown that sensors based on Figure 6.1a have been successfully developed to detect variations of pH [10, 12-14] and CO₂ [15-19]. The novel perforated diaphragm pressure sensor (Figure 6.1b) we believe has a number of advantages when comparing the designs. It was previously reported that the shape, size and location of these diffusion channels can be used to manipulate the stress distribution within the diaphragm allowing the sensor to be tuned to a particular hydrogel [20]. We also envision that the pores within the diaphragm can be fabricated using a combination of potassium hydroxide (KOH) and deep reactive ion etching (DRIE) on a scale which make them behave as a semipermeable membrane. An additional advantage of this design is with the integration of the pores with the diaphragm the fabrication of a backing plate is not required. The hydrogels used in this study are composed of HPMA/DMA/TEGDMA and reversibly respond to pH and changes in ionic strength because they contain tertiary amines (on DMA) that becomes protonated. At low pH value this elevated protonation temporarily increases the osmotic swelling pressure within the hydrogel.

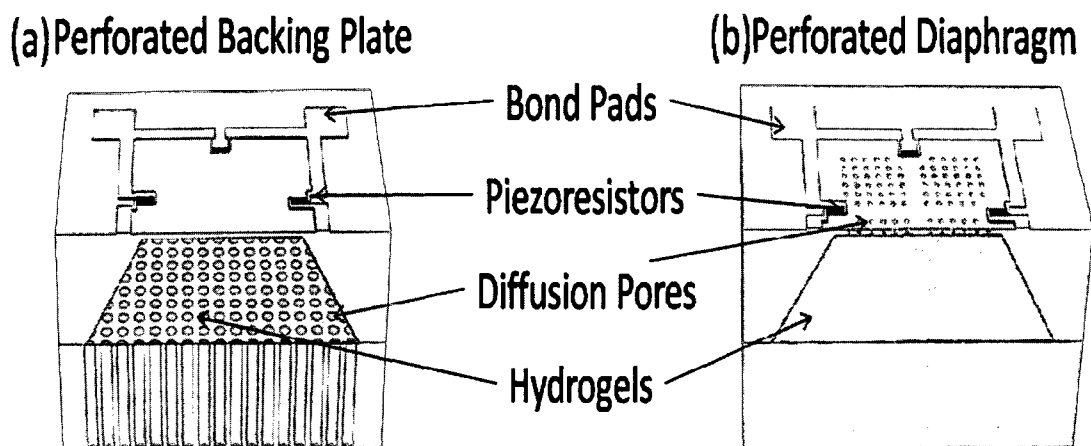


Figure 6.1. CAD rendering of the hydrogel based pressure sensor designs utilizing analyte diffusion channels that are located within the (a) backside mounting plate and (b) within the diaphragm.

At a fixed pH, a larger osmotic swelling pressure is also obtained by increasing the chemical potential of the surrounding water by reducing the environmental ionic strength. In either situation, the increase in osmotic pressure is compensated for by swelling of the gel and hence increased pressure found with the isochoric sensor cavity. From previous work on hydrogels of the same composition tests were performed to quantify the swelling pressure and overall response characteristics of the gels [21]. In this experiment the gels were confined between a calibrated micropressure sensor and a variety of wire meshes inside of a $\sim 3\text{mm}$ stainless steel cylinder. The end of the stainless steel cylinder that contained the wire mesh and hydrogel are placed in solutions of varying ionic concentration. The pressure created within the cylinder was measured and recorded with respect to time. In all cases the measured results were taken from hydrogels with a thickness of approximately $400\mu\text{m}$. The physiological buffer solution (PBS) was subjected to cyclic changes in ionic strength between 0.05 and 0.15M at fixed

pH of 7.4. The response characteristics of the hydrogel were well characterized in this study for a number of alternate steel meshes and nanoporous paper membranes. It was also observed that the pressure response increases with the amount of initial hydrogel loading or how tightly the hydrogel was confined against the pressure sensor. Hydrogel swelling pressure ranged from 21 to 112 kPa with response times (τ_{50}) from 2.9 to 9.5 minutes. This experiment showed that both the initial loading pressure and diffusion channel characteristics play a primary role in the overall sensor behavior. Although hydrogels used to measure changes in ionic strength may not be as physiologically significant as those that measure glucose or CO₂ they have high swelling pressures, are easily synthesized, and well characterized making them ideal for preliminary sensor array characterization.

In this paper we present the fabrication and passivation of the hydrogel sensor arrays and discuss initial test results from sensors coupled with HPMA/DMA/TEGDMA hydrogels. Output characteristics for both solid and perforated diaphragm (Figure 6.1b) sensors are reported in response to changes of ionic strength for various PBS mixtures.

6.3 Sensor Assembly

6.3.1 Sensor Dies

Sensor assemblies were comprised of three main components. First, square silicon micropressure sensor arrays were used for the detection hydrogel swelling pressures. These sensor dies were designed with both solid and perforated square silicon diaphragms with widths of 1.0, 1.25, and 1.5 mm used to measure pressures of 150, 50, 25, 5 kPa, respectively, shown in Figure 6.2.

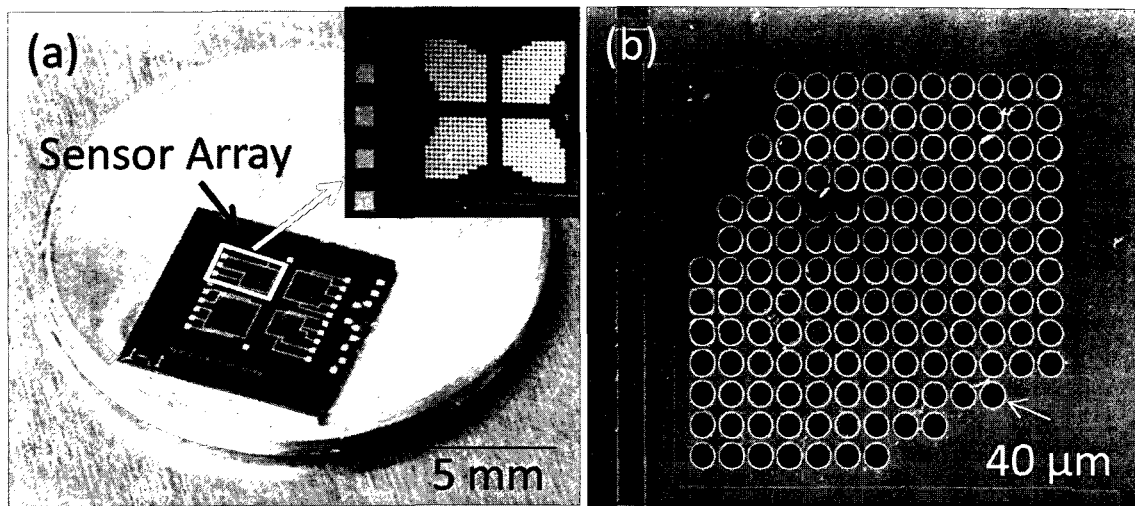


Figure 6.2. Optical (a) and SEM (b) micrographs of perforated diaphragm pressure sensor array. Inset on left shows a (SEM) micrograph of one of the $1 \times 1 \text{ mm}^2$ sensors while (b) shows pores ($d=40 \mu\text{m}$) etched into one quarter of the $1 \times 1 \text{ mm}^2$ sensor diaphragm.

A 14-step fabrication process was performed using standard integrated circuit technologies and microelectromechanical systems (MEMS) processes found in [22]. The 2×2 array measures approximately $3 \times 5 \text{ mm}^2$ and individual diaphragms were separated by a $200 \mu\text{m}$ silicon frame that was bulk etched using KOH from the backside. A measured thickness of diaphragms was $15 \pm 3 \mu\text{m}$ determined using scanning electron microscopy (SEM). Analyte diffusion pores of 10, 20, 30, and $40 \mu\text{m}$ in diameter were etched into diaphragms using deep reactive ion etching (DRIE). The pore geometry was optimized using finite element analysis and discussed in [20] and showed that stress within the piezoresistors could be increased while stresses around the pores could be minimized. Empirical bulge testing using N_2 showed that the solid diaphragm sensors had slightly improved sensitivity when compared to the perforated diaphragm sensors and was likely due to the loading conditions used in test as described in [22]. Bulge testing experiments determined that the passivation layers contained 281 MPa of

compressive stress and the perforated diaphragm sensors were functional with sensitivities ranging from 23 to 252 $\mu\text{V}/\text{V}\cdot\text{kPa}$. Passivation layers (SiO_2 and Si_3N_4) were deposited on the topside of the sensor to protect the ion implanted piezoresistors from external environmental ion diffusion. This layer also was used for masking of the DRIE micropores.

6.3.2 HPMA/DMA/TEGDMA Hydrogels

The second component of the sensor assembly is the HPMA/DMA/TEGDMA hydrogel which is currently synthesized in thin sheets with thickness of 400 μm . The chemicals used for the preparation of hydrogel were obtained as follows: hydroxypropyl methacrylate (HPMA), N,N-dimethylaminoethyl methacrylate (DMA) and crosslinker tetra-ethyleneglycol dimethacrylate (TEGDMA) were purchased from Polysciences, Inc (Warrington, PA). Initiator system containing Ammonium peroxydisulfate (APS) and N,N,N',N',-tetra-methylethylenediamine (TEMED), along with Delbecco's phosphate-buffered saline solution were all obtained from Sigma-Aldrich (St Louis, MO). All the chemicals were used as received. Polyelectrolyte pH-responsive and ionic strength sensitive hydrogels containing HPMA/DMA/TEGDMA at a nominal mole ratio of 70/30/2 were synthesized via free radical cross-linking copolymerization at room temperature as in [23],[24]. In brief, appropriate amounts of monomers HPMA and DMA, crosslinker TEGDMA as well as accelerator TEMED were mixed in a vial to obtain pregel solution, which was then purged with N_2 gas for about 10min. Shortly thereafter, the initiator APS was added to the pregel solution and the mixture was vortexed for about 5 seconds before being rapidly injected into a cavity (thickness 400 \pm 10 μm) between two square glass plates of surface area 64 cm^2 . The hydrogel slab

was removed from the glass plate after approximately 4 hours of reaction, then washed with PBS solution for at least 2 days to remove unreacted chemicals prior to testing. In order to speed up the cleaning process and for preconditioning, hydrogels were subjected to five swelling/deswelling cycles by varying ionic strength of PBS between 0.15M and 0.05M before insertion into the sensor assembly.

After synthesis and initial conditioning gels were placed in a 0.15M solution of PBS to ensure they were in a contracted state. Next the gels were laid on a glass slide (Figure 6.3) in an air environment at room temperature for 60 minutes to improve the adhesion to the slide. The process reduced the water content of the gel through evaporation and made the gels easier to cut using a surgical scalpel. The gels were then trimmed into squares under a microscope with dimensions roughly 1×1 , 1.25×1.25 and $1.5 \times 1.5 \text{ mm}^2$ and placed into the sensors' backside KOH etched cavity.

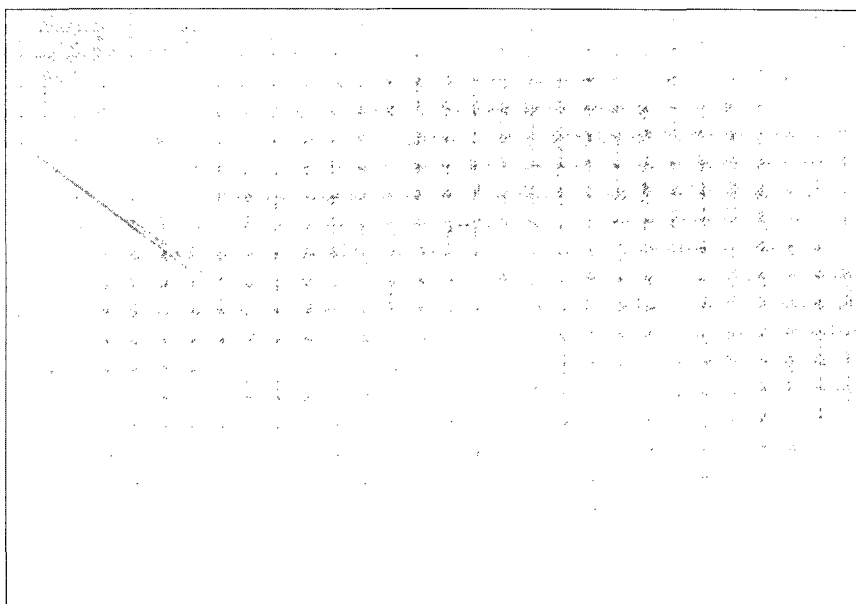


Figure 6.3. Photograph of the HPMA/DMA/TEGDMA hydrogel on glass slide before sample cutting and insertion into the sensors.

6.3.3 Backing Plates

The final part of the sensor assembly is the backing plate used to hold the hydrogel in contact with the pressure sensing diaphragm. Two configurations of this component were fabricated, one for the solid diaphragm, and the other for perforated diaphragm sensors. The sensors with solid silicon diaphragms require that the diffusion pores are fabricated directly into the backing plate, while perforated diaphragm sensors allow analyte diffusion into the hydrogel cavity directly through the diaphragm. The backing plates for the solid diaphragm sensors were fabricated with pores that ranged in size from 100 to 175 μm in diameter in 25 μm increments with a 200 μm pitch. These pore dimensions were used because they were easily micro machined using DRIE (Bosch process) in $5 \times 5 \text{ mm}^2$ arrays (Figure 6.4).

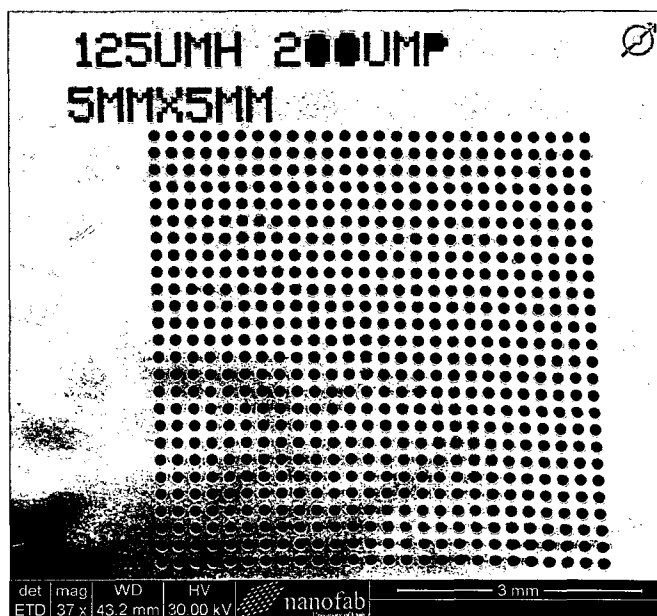


Figure 6.4. SEM micrograph of the deep reactive ion etched (DRIE) porous backing plate ($5 \times 5 \text{ mm}^2$) with pore diameter of 125 μm and a pitch of 200 μm . Shading is indicative of a surface not being completely planar due to this particular wafer being thinned using KOH. The backing plates used for testing do not exhibit this characteristic.

The backing plates were the same thickness as the wafer ($400\pm 15\ \mu\text{m}$) and covered the backside of all four sensors simultaneously. Backing plates for the perforated diaphragm sensors were made using the same wafers without any pores. The backing plates were singulated into $8\times 8\ \text{mm}^2$ using Disco (Tokyo, Japan) dicing saw and attached to the sensors using silicone adhesive (NuSil MED-4211, Carpinteria, CA, USA) and allowed to cure for 48 hours before testing.

6.3.4 Wire Bonding

Each sensor array has a total of 20 electrical inputs/outputs, 4 for each sensor which include: V_{in} , Gnd , V_{out+} , V_{out-} . To interface the 2×2 arrays a custom designed FR-4 printed circuit board (PCB) was fabricated with a total of 100 bond pads. After cleaning the sensors and PCB using isopropyl alcohol and deionized water sensors were ultrasonically wedge wire bonded using a semiautomatic wire bonding machine (West.Bond, Inc., Anaheim, CA). Insulated gold wires ($d=50\ \mu\text{m}$) were employed because they add another layer protection needed for solution testing. Utmost care was taken not to fracture sensor diaphragms during wire bonding since they are thin ($\sim 15\ \mu\text{m}$) and can easily break.

6.3.5 Sensor Passivation

The sensor assembly requires a long term stable encapsulation to avoid device deterioration in the harsh physiological testing environment. The passivation layer acts as a dielectric barrier to isolate the metal electrical traces of sensor array from the wet external environment. Ideally, the encapsulation material needs to be thin ($< 5\ \mu\text{m}$), conformal, pinhole free, low stress and deposited at near room temperature, since the

entire diaphragms are coated it is important the passivation does not alter the mechanical properties of the diaphragms and hence the electrical output. Chemical vapor deposited (CVD) parylene (para-xylylene) thin films were used because they can be deposited at room temperature, and the coating process involves no curing, solvents, or additives. Consequently, the concerns associated with thermal piezoresistor diffusion, diaphragm stress, and contamination is minimized. Parylene also exhibits a low permeability to moisture make it an ideal choice for such applications. After assembly, the sensor, wiring and PCB are coated with parylene C (poly para-xylylene) as shown in Figure 6.5. A Para tech Coating, LabTop 3000 (Aliso Viejo, CA) system is used vaporize the parylene solid dimer at 150° C then pyrolyze it into stable monomeric diradical, para-xylylene at 680°C. These monomers then enter the deposition chamber at room temperature and get adsorbed and polymerized on the sample simultaneously. A monitor sample is also coated along with the sensors and was used to verify the encapsulation layer thickness as being approximately $3\pm 0.5 \mu\text{m}$. An added benefit of this passivation process is it also mechanically enhances the strength the wire bonds need for the repeated chemical testing.

6.4 Testing Apparatus

For each sensor array a 26-pin latch connector is soldered to the custom PCB and connected to ribbon cable that interfaces a data acquisition unit (Agilent technologies, Inc, 34970A, Santa Clara, CA) through a 20-channel multiplexer (Agilent technologies, Inc, 34901A, Santa Clara, CA). A high accuracy DC power supply (B&K Precision Corporation, 1621, Yorba Linda, CA) was used to apply the 1 V input voltage.

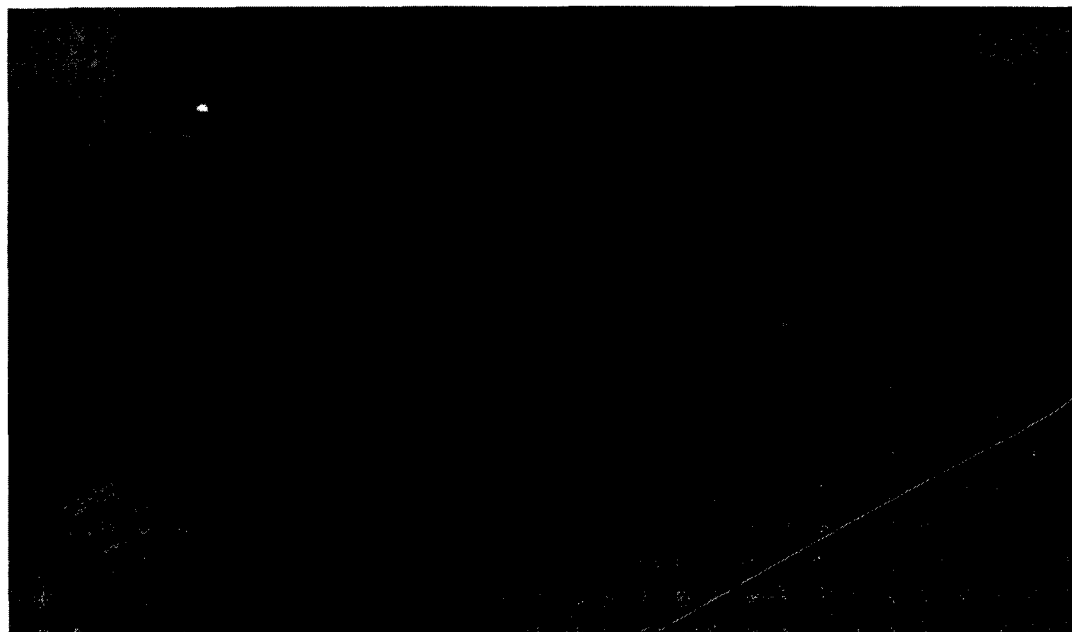


Figure 6.5. Photograph of topside of a solid diaphragm sensor assembly with hydrogel inserted and mounted to a perforated backing plate (out of view). Wire bonding was performed using gold insulated wire ($d=50\ \mu\text{m}$). The entire assembly, wires, and PCB are ready for parylene deposition.

The data acquisition unit is connected to a personal computer using a GPIB cable to monitor and record data. “Benchlink Data logger 3” software (Agilent technologies, Inc, 34825A, Santa Clara, CA) was used to record and plot real-time test data. The testing apparatus is shown in Figure 6.6.

6.5 Experimental Methods

The hydrogel swelling pressure was measured in relation to changes of ionic strength of PBS solutions. These initial tests are used to qualify the sensor designs and provide proof of concept for the perforated diaphragm sensors. Therefore, sensors of the two varying designs were subjected to identical experimental conditions and compared. Solution tests were conducted using phosphate buffer solution (PBS) with a human physiological pH value of 7.4 and ranging in ionic strength from 0.025 to 0.15M.

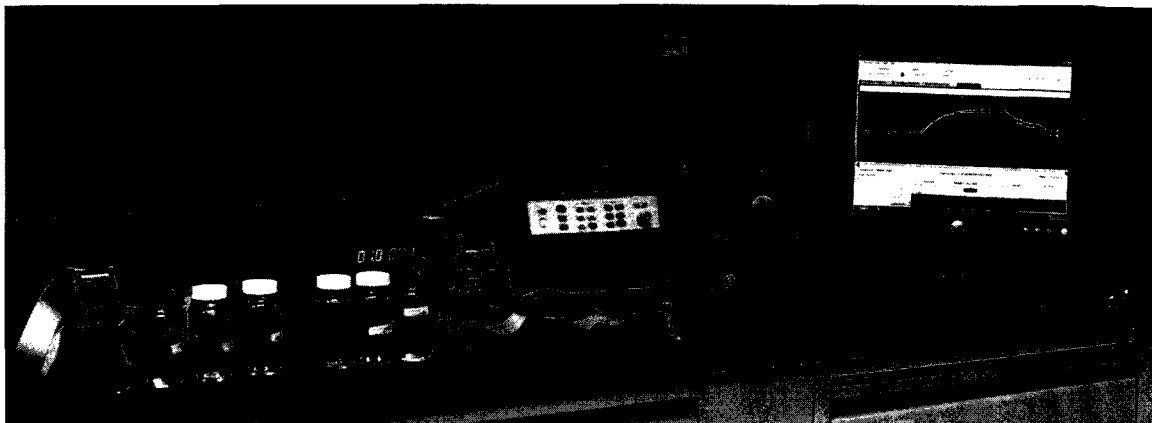


Figure 6.6. Photograph of the testing apparatus used to determine sensor electrical output characteristics. The sensors were placed in solutions of varying ionic strength and the voltage output was simultaneously measured.

PBS solution with 0.15M was purchased from Sigma Aldrich (St. Louis, MO, USA) made of NaH_2PO_4 , HCl, and NaCl and diluted with deionized water to create solutions with reduced ionic strength. The solutions were mixed in 100 ml plastic experimental bottles and then sensor assemblies were placed directly into the bottles at room temperature without additional agitation as shown in Figure 6.7.

6.6 Results and Discussion

6.6.1 Sensitivity

Sensitivity testing was performed to determine how well sensor arrays can discriminate between solutions of varying ionic strengths. These measurements were taken after the initial hydrogel conditioning cycles. Figure 6.8 shows sensor voltage output with respect to change ionic strength of the PBS solution for the two different sensor designs.

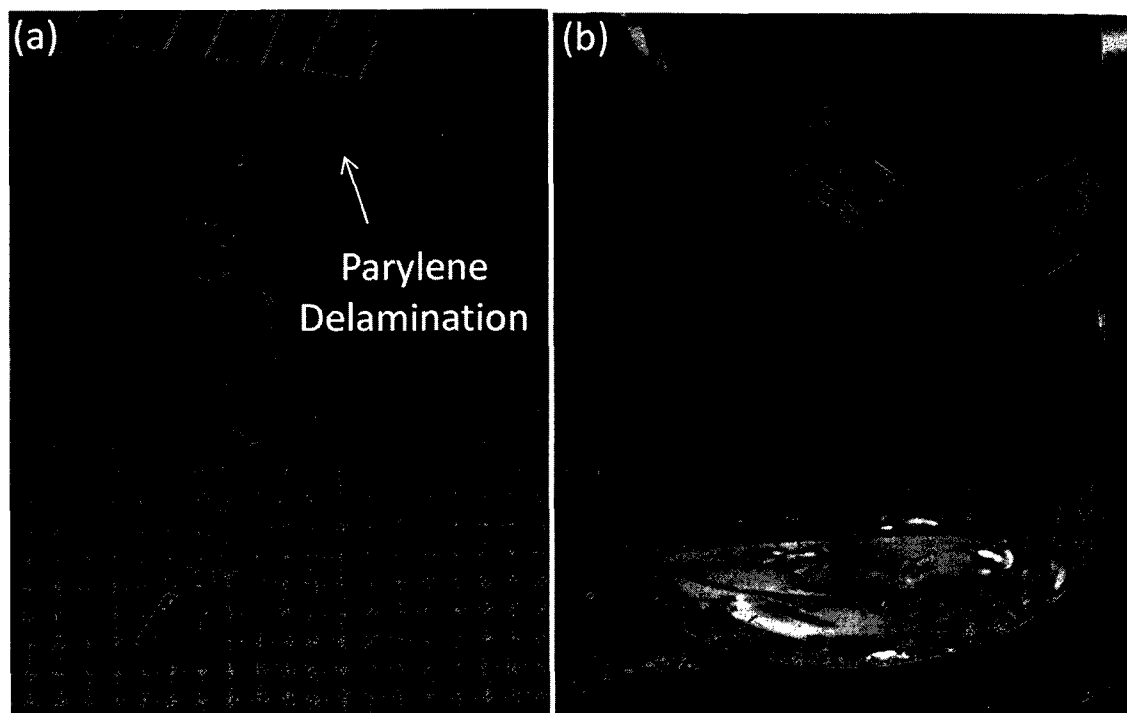


Figure 6.7 Photographs of sensor assembly post parylene deposition with insulated wires (a) sutured together for additional strength and placed in (b) experimental bottle for chemical testing of ionic strength. The parylene delamination was caused by tape adhesion testing.

The perforated diaphragm sensors have pore size of $40\ \mu\text{m}$ and the perforated backing plate sensors have pores of $175\ \mu\text{m}$, with pitches of $200\ \mu\text{m}$ and $50\ \mu\text{m}$, respectively. The perforated diaphragms have an open area of approximately 64% while the backing plates have an open area of 60%. The diaphragms are much thinner ($15\ \mu\text{m}$) than the backing plates ($400\ \mu\text{m}$) which may increase diffusion rate and hence the response time but at equilibrium should not affect overall sensitivity. The sensors were allowed to equilibrate in $0.15\ \text{M}$ PBS for 1 hour and then the arrays were placed into the solution containing $0.025\ \text{M}$ PBS causing the hydrogels to swell and subsequent increase in voltage output. The ionic concentrations were then reversibly decreased and the final step the solution was then returned to its initial concentration of $0.15\ \text{M}$.

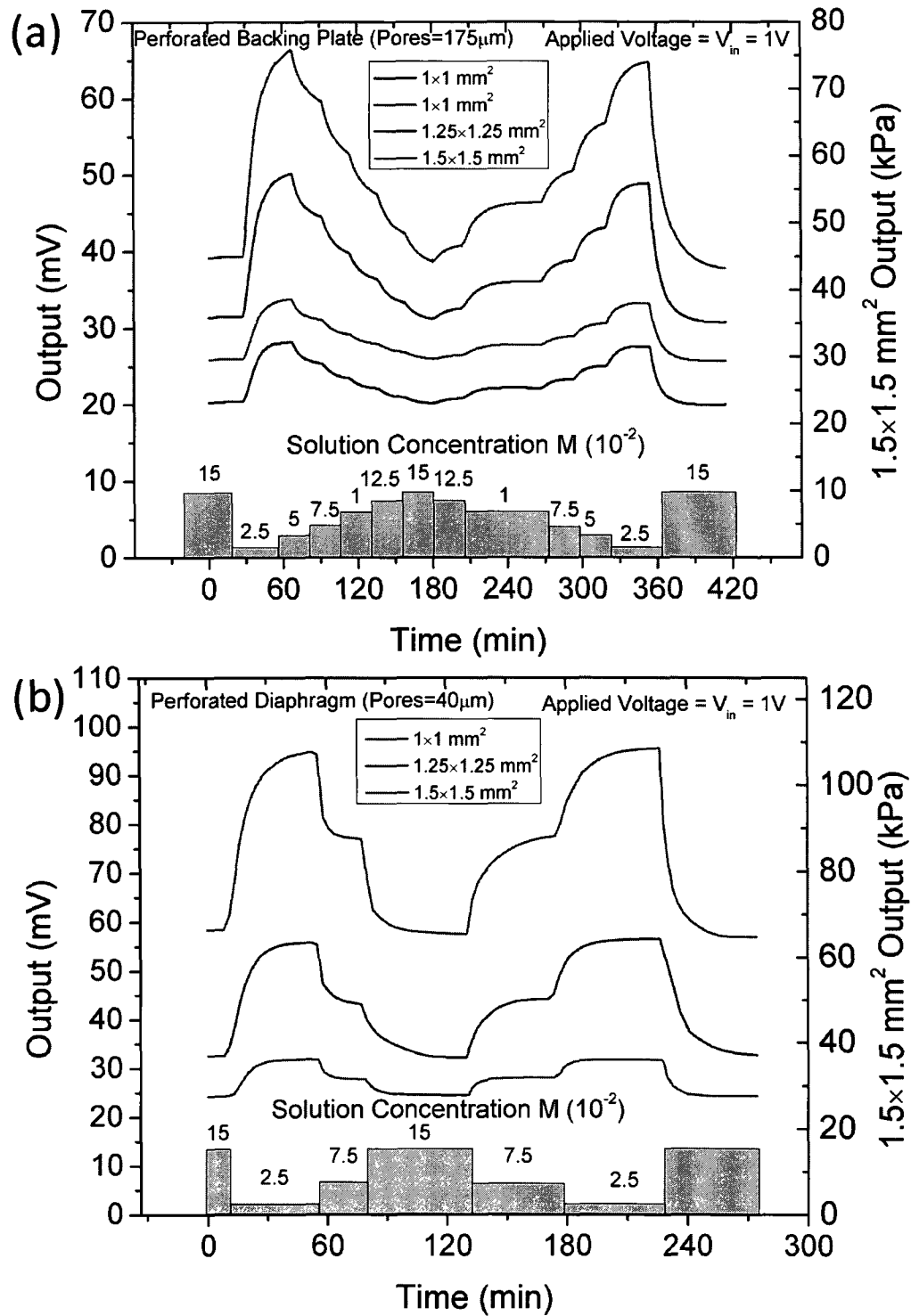


Figure 6.8. Output data used for the calculation of sensitivity for the (a) solid and (b) perforated diaphragm pressure sensors. The perforated diaphragm sensors have a higher sensitivity and larger output for identical environmental testing conditions.

These values agree with offsets measured in previous characterization experiments presented in [22]. When the sensors are placed in the 0.15 M PBS solution and at equilibrium the sensors output is stable with noise levels on the order of 1×10^{-6} V. The diaphragm size was shown to have a prominent impact on the sensitivity of individual sensors in the array.

As expected the largest diaphragm sensors have the highest sensitivity due to increased stresses developed in the piezoresistors. Comparing the sensitivities of the two designs at both 0.025 and 0.075 M we can see that for the same experimental conditions the output of the perforated diaphragms sensors is higher as shown in Figure 6.9. The increased sensitivity is due to higher stress induced in the piezoresistors for a particular hydrogel swelling pressure. This is due to a combination of effects. First, the perforations are defined in such a way that they maximize stress within the diaphragm as discussed in [20].

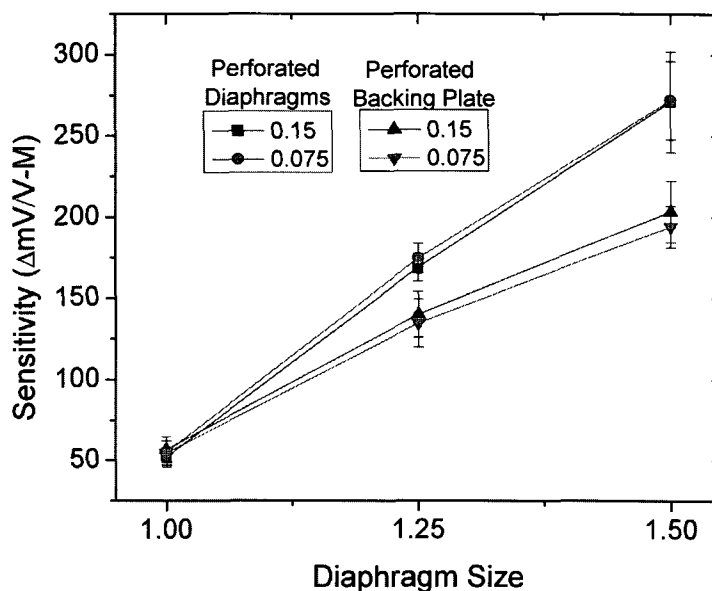


Figure 6.9. Comparison of sensitivities for perforated diaphragm and solid diaphragm sensors placed in 0.025 and 0.075 M PBS solutions. Perforated diaphragm sensors were more sensitive for all sensors in the array.

Additionally, the forces and hence stress exhibited on the diaphragm from loading vary between the two designs. Assuming the hydrogel does not exude through the pores the same total force is applied to the two different diaphragms. This force is determined by swelling pressure times the diaphragm area. For the perforated diaphragm sensors, stresses experienced by the piezoresistors are higher, since there is less diaphragm material to resist the hydrogel swelling pressure. Hence, the perforated diaphragm design experiences higher stress and therefore increased sensitivity. In this scenario the highest forces are witnessed by the diaphragm with the largest pores. The actual amount of deformation of the gel through the pores is difficult to estimate and should be studied empirically since the hydrogel mechanical properties can vary significantly.

6.6.2 Response Time

The sensor response time is influenced by a number of factors including analyte diffusion and hydrogel kinetics. In order for the HPMA/DMA/TEGDMA hydrogels to swell/contract water must be absorbed or released by the gel. This is effectively controlled by the chemical potential of the water which is dependent on ionic strength. At lower ionic strength the water has a higher chemical potential and the gels swell. Therefore the internal sensor cavity where the hydrogel is located requires the exchange of the analytes with the external environment. This process is complicated by the fact that multiple mass transfer mechanisms are occurring concurrently.

Initial preconditioning of the sensors was performed by alternating between the highest (0.15M) and lowest (0.025) ionic concentrations for several cycles. This process step is performed to allow the internal structure to reach steady state conditions prior to sensitivity testing [25]. The arrays output voltage was measured during the

preconditioning cycles to measure the swelling pressure shown in Figure 6.10. These data, representative of all sensors, were taken using the perforated diaphragm $1 \times 1 \text{ mm}^2$ pressure sensor with diaphragm pore sizes of $40 \mu\text{m}$. During the first operation, the hydrogel sensor often showed poor repeat accuracy and a slight drift of the sensor parameters.

It is shown that the first initial couple of cycles of have different response characteristics than subsequent cycles. We found that the repeatability of the sensor response can be significantly increased by performing the conditioning cycles. In general, the conditioning process was complete after 3 to 5 swelling-contracting cycles. Specifically, for the $1 \times 1 \text{ mm}^2$ sensor the first cycle had the slowest response and the lowest swelling pressure of approximately 30 kPa. The second cycle had an improved pressure output of 40 kPa and a slightly faster response. After the second cycle the measured swelling pressure and response time became more reversible and repeatable with an output pressure of roughly 45 kPa. This phenomenon is attributed to the fact that the gels are initially in a partially dry contracted state with little absorbed water. In this state the swelling process is governed by the analyte and polymer chain mobility. The dry contracted state of the hydrogel has reduced diffusion channels size which consequently slows diffusion into the gel. Before testing molecular chains are more tightly bound with a higher crosslinking density. It has been previously reported that the diffusivity of analytes decreases as the crosslinking density increases, size of the analyte increases, and the volume fraction of water within the gel decreases. During the first few cycles the hydrogel absorbs water becoming better situated inside the sensors cavity. This is shown by the reduced baseline value of the output signal.

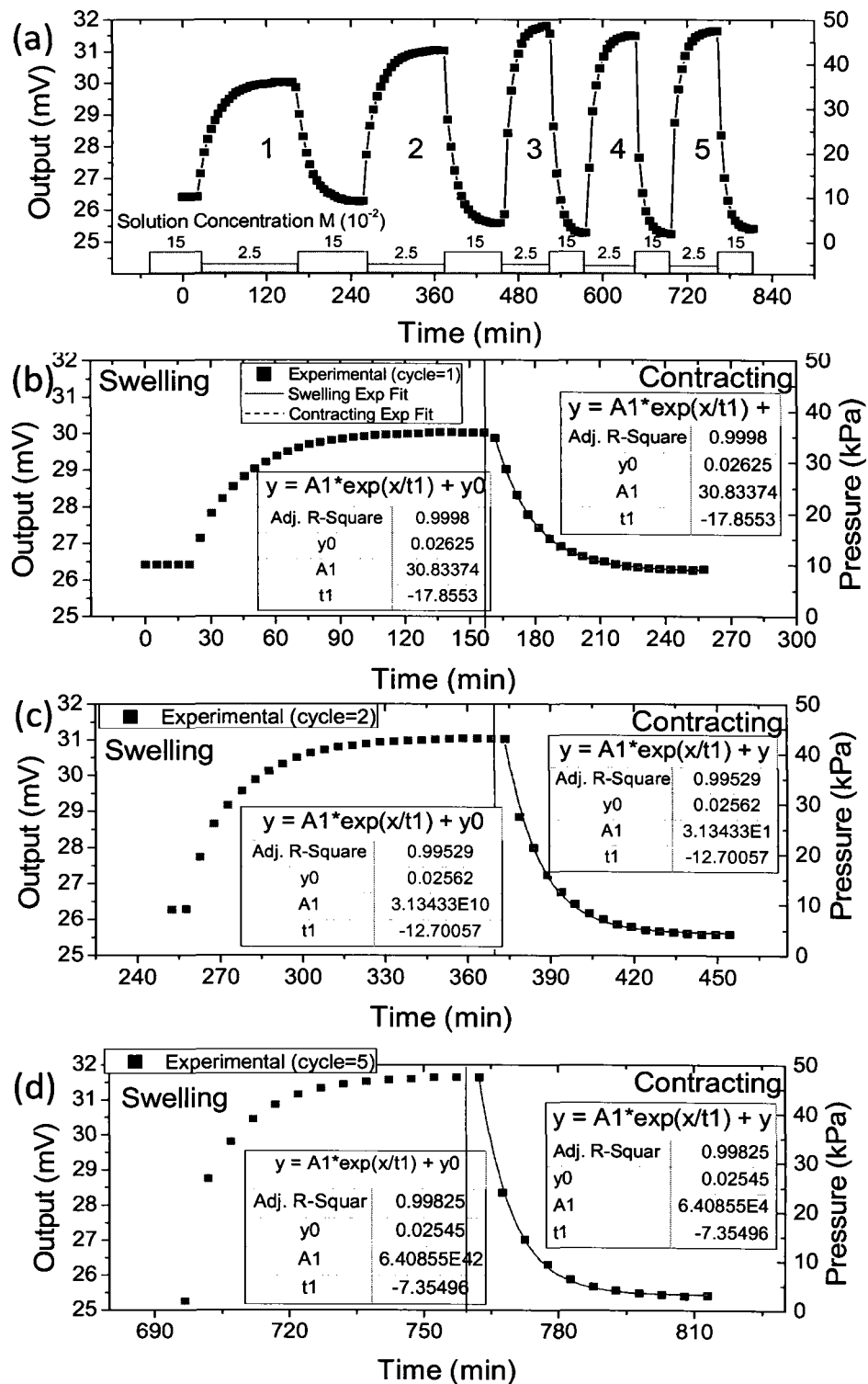


Figure 6.10. Sensor responses during the first five cycles of testing between 0.15 and 0.025 M PBS solution concentrations (a-d). Exponential fits of (b) cycle 1 (c) cycle 2 and (d) cycle 5 for the swelling and contracting half cycles. Data show the initial cycles have the smallest and slowest response.

As the hydrogel is cycled the polymer chains are molecularly reconfigured and response is improved. By fitting the output voltage signal to the exponential growth function described in equation 32 we can quantify the swelling (τ -swelling) and contracting (τ -contracting) time constants.

$$y = y_0 + A_1 e^{(x/t_1)} \quad (32)$$

Figure 6.11 compares the time constants (τ) calculated using the exponential fit for the swelling and contracting of the first five cycles for both sensor types. Results show that the hydrogels initially take more than two times as long to reach equilibrium when comparing the cycle=1 to cycles ≥ 3 .

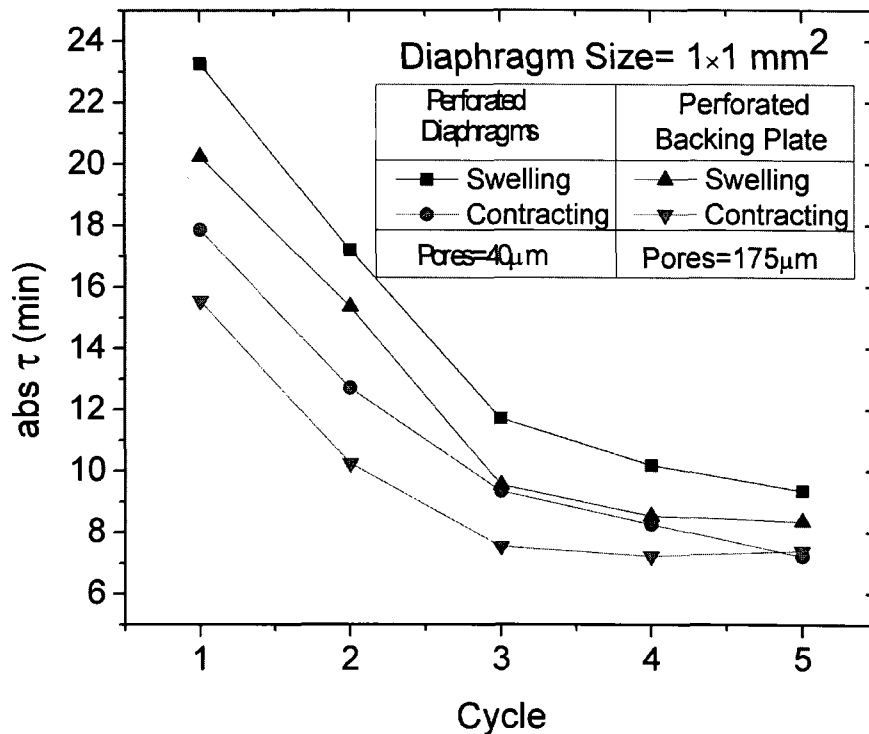


Figure 6.11. Plot of the calculated time constants (τ) with respect to the first five cycles for the two sensor types. The sensors response time shows significant improvement after an initial conditioning period. Response times for the various sensor types are similar.

When comparing the response time between sensors with perforated diaphragms (pore diameter =40 μm) or porous backing plates (pore diameter=175 μm), sensors with porous backing plates had a slightly lower τ_{swelling} and $\tau_{\text{contracting}}$. This means that the sensor reaches equilibrium faster and is likely due to the larger pores allowing a higher diffusion rate of analytes in and out of the hydrogel cavity improving hydrogel swelling response.

According to Figure 6.12, we determined that the contracting time constants were consistently less than that of swelling for both sensors with perforated diaphragms and backing plates. This is likely due to an imbalance of mechanical forces exhibited on the hydrogel from the piezoresistive diaphragm during testing. During swelling the hydrogel volume expands filling all available free space in the sensor cavity then begins to deflect the piezoresistive diaphragm. At equilibrium the swelling pressure of the hydrogel is equal to the pressure applied by the piezoresistive diaphragm. During the contraction the piezoresistive diaphragm applies additional mechanical pressure aiding in the out diffusion of water from the hydrogel. The increased hydrogel loading during contraction improves the response time during contraction half cycle. Figure 6.12 also compares response times of the various sized sensors within the sensor array.

We found that the $1 \times 1 \text{ mm}^2$ sensors have decreased time constants and faster response than the larger $1.25 \times 1.25 \text{ mm}^2$ and $1.5 \times 1.5 \text{ mm}^2$ sensors even though the hydrogel thickness ($\sim 400 \mu\text{m}$) is the same for each sensor. This is likely due to hydrogel loading characteristics. The larger diaphragms are more compliant and sensitive to minute increases in hydrogel swelling pressure while the smaller sensors diaphragms are more rigid.

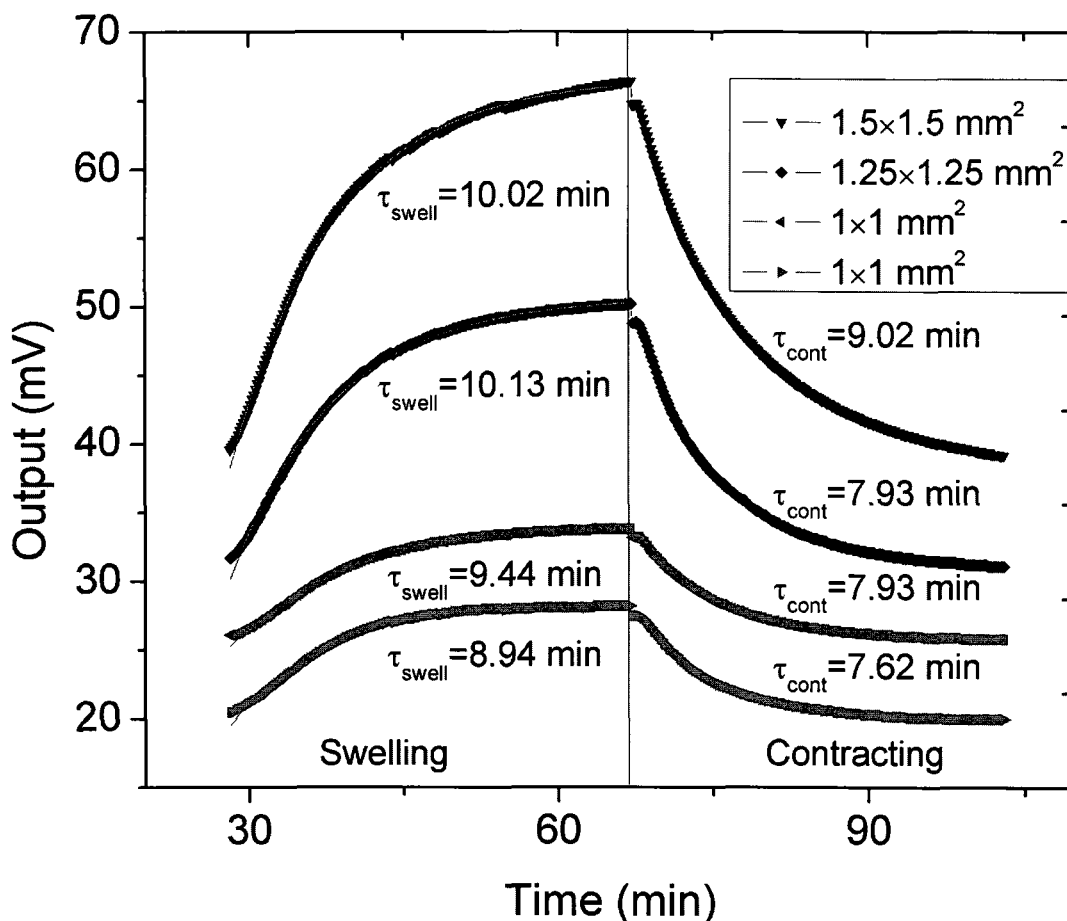


Figure 6.12. Swelling and contracting time constants calculated for the various sized perforated diaphragm sensors within the array after conditioning. The sensors were cycled from 0.15 to 0.025 M PBS and the smaller diaphragms had faster response.

Hence it takes longer to reach equilibrium for the larger sensors, increasing the swelling and contracting time constants. Another reason may be that the larger sensors use hydrogels which have a reduced surface to volume ratio which might lead to decreased analyte diffusion rates.

6.6.3 Stability

Sensor lifetimes of over 400 hours in PBS buffer solution at 23 °C were observed, but the baseline offset started drifting after approximately 50 hours seen in Figure 6.13.

Generally, the sensors fail within a few days of testing due to the premature failure of the encapsulation which can be improved by using a thicker parylene coating, improved deposition parameters, or a new encapsulation material. We observed that on two sensors the parylene passivation on the wire bonds was compromised, indicated by the depositions of salts on the metallization. When analyzing the data of the sensor which lasted the longest we learned that the sensor sensitivity remained stable (~ 135 mV/V-M) while only the baseline drifted. Originally the sensor output was roughly 30 mV but after 200 hours of testing the sensor offset drifted to >50 mV and stabilized.

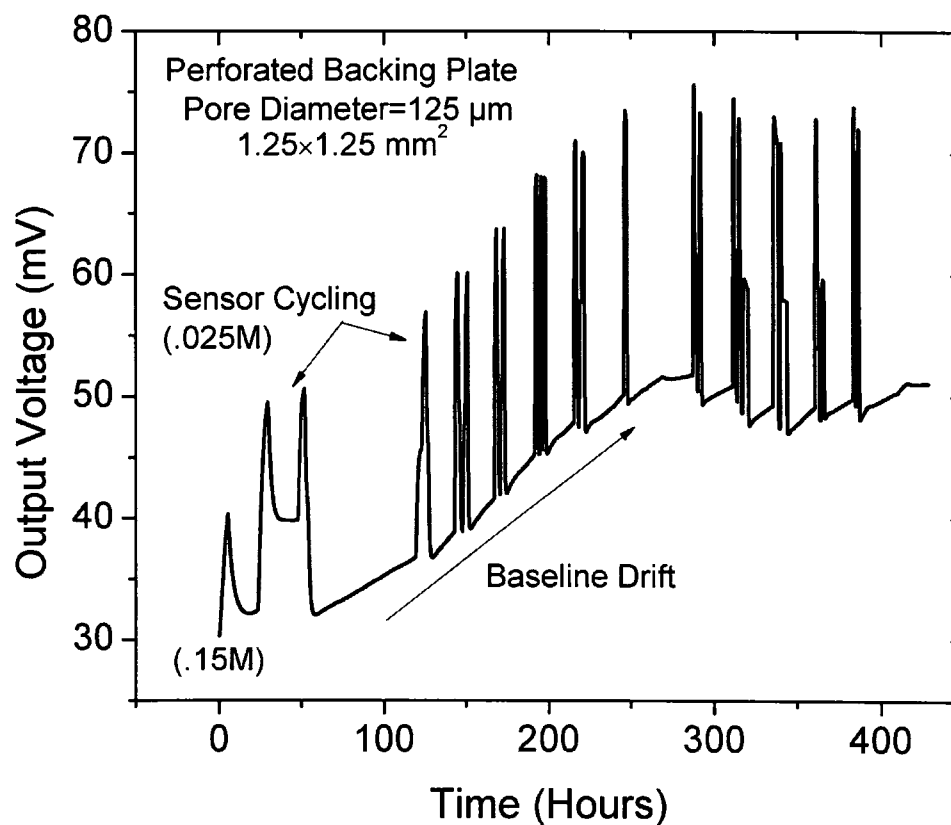


Figure 6.13. Plot illustrating the long term stability of the 1.25x1.25 mm² perforated backing plate sensor with 125 μm pores. The sensor was cycled between 0.15 and 0.025M PBS concentrations and although the sensor responded to changes in ionic strength for ~ 400 hours it the baseline drifted significantly.

Presumably this was due to one or more of the wire bonds being compromised. The resistance was modified on one leg of the Wheatstone bridge creating an imbalance leading to a drifting baseline. Future experiments are planned to validate that hypothesis and to improve passivation performance.

6.7 Conclusions

We have developed two types of sensor arrays used for the detection of hydrogel swelling pressures, one version with perforation, acting as analyte diffusion pores etched directly into the piezoresistive diaphragm, the other with pores etched into the backing plate while using a solid diaphragm. Hydrogels (HPMA/DMA/TEGDMA) which swell in response to changes in ionic strength of PBS solution were integrated into the sensor chips and used in the characterization of the sensors. The sensors were placed into solutions of ionic strengths ranging from 0.025 to 0.15 M. Sensors with pores directly etched into the diaphragm exhibit higher sensitivity. Initial conditioning steps were necessary to precondition the hydrogel within the sensor and stabilize response. The sensor response was fitted to a first order exponential growth function for the swelling and contracting half cycles and $\tau_{\text{swelling}} > \tau_{\text{contracting}}$ was observed for all sensors. The steady state response times of the two sensor version were comparable and improved after 3 to 5 cycles with values of approximately 9 and 7 minutes for τ_{swelling} and $\tau_{\text{contracting}}$. To our knowledge this is the first paper that gives test results for a perforated diaphragm pressure sensor array for the detection of hydrogel swelling pressure used in chemical analysis. We are confident that we can improve long term sensor stability through the optimization of the passivation process, and this sensor design offers a universal platform capable of detecting the swelling pressure of various stimuli responsive hydrogels. We

have demonstrated “proof of concept” of a sensor design that incorporates perforations into a piezoresistive diaphragm for the diffusion of analytes. This design modification was shown to improve sensitivity. In the future experiments are planned to investigate the effect of diaphragm pore size directly on response time and sensitivity.

6.8 References

- [1] M. Lei, A. Baldi, T. Pan *et al.*, "A Hydrogel-Based Wireless Chemical Sensor," *Proceedings of the IEEE International Conference on Micro Electro Mechanical Systems (MEMS)*, pp. 391-394.
- [2] T. Miyata, N. Asami, and T. Uragami, "Preparation of an Antigen-Sensitive Hydrogel Using Antigen Antibody Bindings," *Macromolecules*, vol. 32, no. 6, pp. 2082-2084, 1999.
- [3] T. Miyata, T. Uragami, and K. Nakamae, "Biomolecule-Sensitive Hydrogels," *Advanced Drug Delivery Reviews*, vol. 54, no. 1, pp. 79-98, 2002.
- [4] M. Guenther, D. Kuckling, C. Corten *et al.*, "Chemical Sensors Based on Multiresponsive Block Copolymer Hydrogels," *Sensors and Actuators B: Chemical*, vol. 126, no. 1, pp. 97-106, 2007.
- [5] J. Cong, X. Zhang, K. Chen *et al.*, "Fiber Optic Bragg Grating Sensor Based on Hydrogels for Measuring Salinity," *Sensors and Actuators B: Chemical*, vol. 87, no. 3, pp. 487-490, 2002.
- [6] A. Guiseppi-Elie, S. Brahim, G. Slaughter *et al.*, "Design of a Subcutaneous Implantable Biochip for Monitoring of Glucose and Lactate," *Sensors Journal, IEEE*, vol. 5, no. 3, pp. 345-355, 2005.
- [7] F. W. Scheller, U. Wollenberger, A. Warsinke *et al.*, "Research and Development in Biosensors," *Current Opinion in Biotechnology*, vol. 12, no. 1, pp. 35-40, 2001.
- [8] A. Richter, A. Bund, M. Keller *et al.*, "Characterization of a Microgravimetric Sensor Based on pH Sensitive Hydrogels," *Sensors and Actuators B: Chemical*, vol. 99, no. 2-3, pp. 579-585, 2004.
- [9] G. Gerlach, M. Guenther, G. Suchanek *et al.*, "Application of Sensitive Hydrogels in Chemical and pH Sensors," *Macromolecular Symposia*, vol. 210, no. 1, pp. 403-410, 2004.
- [10] G. Gerlach, M. Guenther, J. Sorber *et al.*, "Chemical and pH Sensors Based on the Swelling Behavior of Hydrogels," *Sensors and Actuators B: Chemical*, vol. 111-112, pp. 555-561, 2005.
- [11] M. Guenther, G. Gerlach, D. Kuckling *et al.*, "Chemical Sensors Based on Temperature-Responsive Hydrogels," *Proc. SPIE*, p. 61670T.
- [12] Q. Thong Trinh, G. Gerlach, J. Sorber *et al.*, "Hydrogel-Based Piezoresistive pH Sensors: Design, Simulation and Output Characteristics," *Sensors and Actuators B: Chemical*, vol. 117, no. 1, pp. 17-26, 2006.

- [13] J. Sorber, G. Steiner, V. Schulz *et al.*, "Hydrogel-Based Piezoresistive pH Sensors: Investigations Using FT-IR Attenuated Total Reflection Spectroscopic Imaging," *Analytical Chemistry*, vol. 80, no. 8, pp. 2957-2962, 2008.
- [14] A. Richter, G. Paschew, S. Klatt *et al.*, "Review on Hydrogel-based pH Sensors and Microsensors," *Sensors*, vol. 8, pp. 561-581, 2008.
- [15] S. Herber, J. Borner, W. Olthuis *et al.*, "A Micro CO₂ Gas Sensor Based on Sensing of pH-Sensitive Hydrogel Swelling by Means of a Pressure Sensor," *Digest of Technical Papers - International Conference on Solid State Sensors and Actuators and Microsystems, TRANSDUCERS '05*. pp. 1146-1149.
- [16] S. Herber, J. Bomer, W. Olthuis *et al.*, "A Miniaturized Carbon Dioxide Gas Sensor Based on Sensing of pH-Sensitive Hydrogel Swelling with a Pressure Sensor," *Biomedical Microdevices*, vol. 7, no. 3, pp. 197-204, 2005.
- [17] S. Herber, W. Olthuis, P. Bergveld *et al.*, "Exploitation of a pH-Sensitive Hydrogel Disk for CO₂ Detection," *Sensors & Actuators: B. Chemical*, vol. 103, no. 1-2, pp. 284-289, 2004.
- [18] S. Herber, W. Olthuis, and P. Bergveld, "A Swelling Hydrogel-Based PCO₂ Sensor," *Sensors and Actuators B: Chemical*, vol. 91, no. 1-3, pp. 378-382, 2003.
- [19] R. ter Steege, S. Herber, W. Olthuis *et al.*, "Assessment of a New Pototype Hydrogel CO₂ Sensor; Comparison with Air Tonometry," *Journal of Clinical Monitoring and Computing*, vol. 21, no. 2, pp. 83-90, 2007.
- [20] M. Orthner, L. Rieth, S. Buetefisch *et al.*, "Design, Simulation and Optimization of a Novel Piezoresistive Pressure Sensor with Stress Sensitive Perforated Diaphragm for Wet Sensing and Hydrogel Applications," *Sensors and Actuators B: Chemical*, vol. Submitted Manuscript, 2009.
- [21] G. Lin, S. Chang, C. H. Kuo *et al.*, "Free Swelling and Confined Smart Hydrogels for Applications in Chemomechanical Sensors for Physiological Monitoring," *Sensors & Actuators: B. Chemical*, pp. 186-195, 2008.
- [22] M. Orthner, L. Rieth, S. Buetefisch *et al.*, "Development, Fabrication, and Characterization of a Piezoresistive Pressure Sensors using Perforated Diaphragms for Chemical Sensing," *Sensors and Actuators A: Physical*, vol. accepted manuscript to be published, 2009.
- [23] D.-Y. Jung, J. J. Magda, and I. S. Han, "Catalase Effects on Glucose-Sensitive Hydrogels," *Macromolecules*, vol. 33, no. 9, pp. 3332-3336, 2000.
- [24] I. S. Han, M. H. Han, J. Kim *et al.*, "Constant-Volume Hydrogel Osmometer: A New Device Concept for Miniature Biosensors," *Biomacromolecules*, vol. 3, no. 6, pp. 1271-1275, 2002.

- [25] B. D. Johnson, D. J. Beebe, and W. C. Crone, "Effects of Swelling on the Mechanical Properties of a pH-Sensitive Hydrogel for Use in Microfluidic Devices," *Materials Science and Engineering: C*, vol. 24, no. 4, pp. 575-581, 2004.

CHAPTER 7

SYNOPSIS OF RESULTS, CONCLUSIONS, AND FUTURE WORK

This chapter discusses the achievements, and drawbacks, as well as potential future work, for hydrogel based micropressure sensor arrays used for chemical sensing. Summarizing conclusions are drawn, followed by a brief discussion of results from preceding chapters. Subsequently, recommendations are given for improvements and future work.

Over the last decade a wide number of sensors presented in literature have relied on stimuli responsive hydrogels for the quantification of chemical analyte concentration. One major advantage lies within their unique transduction mechanism (chemical-mechanical) which provides high specificity to wide range biologically significant chemical analytes. Although numerous transduction methods have been described in literature to detect physical changes in hydrogels, most require sophisticated test equipment and cannot be readily used for chemical sensing or medical diagnostic applications.

This work introduces and demonstrates the first hydrogel based micropressure sensor array (2×2) suitable for chemical testing and medical diagnostics. The primary goal was to reduce sensor response time, size, improve the long-term stability in aggressive environments, increase specificity, and to create a platform sensor technology

which offers flexibility to a wide range of hydrogels. The experimental results show that the new platform technology is a practical solution addressing many key drawbacks of previous sensors

7.1 Overview

Summarizing briefly, chemical sensing technology was expanded by introducing a novel perforated sensor array used to detect the swelling pressure of hydrogels. Modeling and simulation showed that the concept was feasible and had a number of inherent advantages including higher sensor flexibility, reduced size, improved response time, and higher sensitivity. New materials processing technology was developed to create the sensors arrays. Bulge testing showed that the perforated sensors were fully functional and had linear responses over the sensors' specific dynamic range. Bulge testing also demonstrated that the pore geometry directly influences the sensors' performance characteristics and can be used to modify the sensors for a particular application and/or hydrogel. Chemical testing showed that the new sensor designs were more sensitive than their solid diaphragm counterparts when coupled to hydrogels giving proof-of-concept and design validation. Based upon this, a new concept for hydrogel based chemical sensors was presented. Its performance characteristics exceed many of the state of the art solutions previously presented in literature. Below the main conclusions of each chapter are discussed.

7.2 High Speed Wafer Scale Bulge Testing for the Determination of Thin Film Mechanical Properties

A bulge testing system was created to study mechanical properties of thin films, provide valuable simulation parameters for the finite element models, and for characterization of the new hydrogel based chemical sensors. One major advantage over other bulge testing systems is that deflection and curvature of membrane can be simultaneously measured in three dimensions, with nanometer resolution in seconds via the use of an optical profilometer.

The system was characterized and performance tested by measuring the deflection (wafer scale) of square silicon nitride/aluminum membranes (720 nm Si_3N_4 + 20 nm Al) and compare results to analytical and finite element models. Fit of experimental data to simulated and analytical models gave r-square values >99% and a calculated Young's modulus of 454 GPa for a silicon nitride membrane ($1200 \times 1200 \mu\text{m}^2$). The deflections measured with respect to pressure for the smaller diaphragms were in the linear regime and therefore accurate calculations of Young's modulus were unsuccessful. The deflection measurements taken at various locations across the wafer showed little variation.

These preliminary tests were performed primarily to qualify the bulge testing system and determine performance characteristics. This equipment proved essential in order to study diaphragm mechanics, determine pressure limitations, and perform electrical characterization of the sensors.

7.3 Design, Simulation and Optimization of Novel Piezoresistive Pressure Sensors with Stress Sensitive Perforated Diaphragms for Hydrogel Applications

This chapter presents the design specifications, introduces the CAD models, and details the finite element analysis of the new device designs. Finite element analysis of various designs shows that it is not only possible to incorporate perforations into the piezoresistive diaphragm but that these structures can be used to increase mechanical stress within the piezoresistors, leading to higher sensitivity. The perforations also permit the diffusion of analyte into the hydrogel cavity. To our knowledge, this is the first time a perforated diaphragm pressure sensor was modeled and realized for the detection of hydrogel swelling pressure.

A perforated diaphragm design was chosen for the first generation of sensors to show proof-of-concept and that it is feasible to fabricate pores directly into the piezoresistive diaphragm. It should be noted that this conservative design significantly reduced (>60%) the amount of stress located in the perforated regions while only marginally (~5%) increasing the electrical output.

This particular pore geometry was implemented into silicon diaphragms 10 μm in thickness with multiple widths (0.5 to 1.5 mm) in order to measure pressures ranging from 5 to 150 kPa. Three trends were found to exist. First pores located along the midlines reduced stress in the piezoresistive regions due to diaphragm stretching. Secondly, pores close to the midpoint of the diaphragm edges developed extremely high levels of stress. Finally, high densities of large pores (small pitch) develop unacceptable levels of interpore stress, which reduced stiffness in the middle of the diaphragm leading

to higher deflection and less localized piezoresistor stress. Two piezoresistors (a pair) were implemented in both longitudinal and transverse directions, and necessary to obtain the specified bridge resistance of $\sim 3 \text{ k}\Omega$ while keeping stress highly localized.

7.4 Development, Fabrication, and Characterization of Hydrogel Based Piezoresistive Pressure Sensors with Perforated Diaphragms

This chapter further expanded on the optimized sensor design, detailed the fabrication procedure, and gave initial experimental results using the modified bulge testing apparatus. Sensors were front side processed by a commercial foundry using a 14-step fabrication process. KOH and DRIE etching were conducted on the wafer scale, to release diaphragms, and create perforations (10 to 40 μm diameter), respectively. The piezoresistors were within approximately 5% of the 3 $\text{k}\Omega$ design specification, with an average total bridge resistance of $3.09 \pm .054 \text{ k}\Omega$.

Diaphragm deflections (μm) and output voltages (mV) of the sensors were taken with respect to a known applied pressure using the bulge testing apparatus, used to calculate sensitivity (mV/V-Pa). In the absence of applied pressure, diaphragms had a negative deflection which was attributed to compressive stress developed in the silicon oxide and nitride passivation layers. Simulation and empirical results showed that deflection and hence stress distributions were not only a function of diaphragm size but pore size as well. Designs with higher open area (pores = 40 μm) experienced the least total loading force during bulge testing, hence deflections and electrical outputs were lower.

Bulge testing showed that the measured output voltages were approximately 80% less than those approximated by theoretical and numerical simulations. This is presumably due to the fabricated diaphragm thickness being of $15\pm 3\ \mu\text{m}$ instead of the $10\ \mu\text{m}$ that was initially specified. The under etching of the diaphragms not only reduced the stress of the piezoresistors but also changed the location of the diaphragm edge. Although the sensor outputs were smaller than anticipated, the output was easily measurable (mV range) and linear. Sensitivities ranged from 23 to $252\ \mu\text{V}/\text{V-kPa}$ for the perforated diaphragm pressure sensors.

Nonlinearity analysis of the sensors was performed using an End Point Linearity (EPL) model, and determined that the nonlinearity was found to be $< 1\%$ for pressures below 65 kPa which is the range most significant for the pH, ionic strength and glucose sensitive hydrogels. Elevated pressure testing (up to 200kPa) was performed to study broadened sensor nonlinearity and showed diaphragms with the largest pores were also most nonlinear. The calculated nonlinearity is 3.49, 6.30, and 10.02 % for the $1.5 \times 1.5\ \text{mm}^2$ sensors that are solid and perforated with 10 and $40\ \mu\text{m}$ pores, respectively.

7.5 Hydrogel Based Sensor Arrays (2×2) with Perforated Piezoresistive Diaphragms for Metabolic Monitoring (in-vitro)

This chapter detailed the first successful chemical testing results from a solid and perforated diaphragm hydrogel sensor array (2×2) for the detection of hydrogel swelling pressures and hence chemical concentrations.

The sensor assemblies were comprised of three components: the sensors, HPMA/DMA/TEGDMA hydrogels, and backing plates. When sensors were placed in 0.15 M PBS solution and at equilibrium the measured offset was stable ($\sim 20\text{-}30\ \text{mV}$)

with noise levels on the order of 1×10^{-6} V. The sensors were then placed in solutions of PBS with molarities from 0.025 to 0.15M, where a large reversible hydrogel swelling response was recorded. Comparing the sensitivities of both the perforated and solid diaphragm designs, it was shown that for identical experimental conditions the sensitivity of the perforated diaphragms sensors is consistently higher. The sensitivity of the 1.5×1.5 mm² and 1.25×1.25 mm² was 270.9 and 169.1 mV/V-M, respectively, 33% and 20% higher than identical solid diaphragm sensors. As anticipated the largest diaphragms have the highest sensitivity.

It should be noted that response time was improved by performing conditioning cycles, with the process being complete after 3 to 5 swelling-contracting cycles. The response time of sensors with porous backing plates had a slightly lower τ -swelling and τ -contracting, meaning that the sensors reach equilibrium faster. This was likely due to the larger pores allowing a higher diffusion rate of analytes into the hydrogel cavity. Contracting time constants (τ -contracting) were smaller than swelling (τ -swelling) for both sensors with perforated diaphragms and backing plates. Increased hydrogel loading from the diaphragm during contraction likely improved the response time during contraction half cycle. Sensor lifetimes of over 400 hours in PBS buffer solution at 23 °C were observed, but the baseline offset started drifting after approximately 50 hours.

7.6 Comparison of Specifications, Simulations, and Empirical Results

The two versions of sensor arrays (perforated and solid diaphragms) fulfill the vast majority of specified requirements. The behavior of the sensors was extensively studied and appears to be predictable, repeatable, reliable and robust by exceeding all specified pressure

requirements. Table 7.1 compares specifications to simulated and empirically measured data.

7.7 Future Work

There are still a number of issues that need to be addressed in order to demonstrate a practical sensor for commercial chemical and medical diagnostic monitoring. Most of the additional work can be grouped into three distinct areas: hydrogels, sensors, and passivation/encapsulation.

Table 7.1. Comparison of specified and actual device properties measured using bulge and chemical testing.

Sensor Specifications		Units	Finite Element Simulations		Empirical Measurements				
					Bulge		Chemical (ionic strength)		
			Solid	Perforated	Solid	Perforated	Solid	Perforated	
Thickness	10	μm	10	10	15±3	15±3	12±3	12±3	
Pressure Range	0-150	kPa	0-150	0-150	0-200	0-200	~0-50	~0-50	
Burst Pressure	1.5×1.5 mm ²	0-5	kPa	61	54	>200	195±11	>35	>35
	1.25×1.25 mm ²	0-25	kPa	275	254	>200	>200	>35	>35
	1.0×1.0 mm ²	0-50	kPa	585	511	>200	>200	>35	>35
	0.5×0.5 mm ²	0-150	kPa	1342	1143	>200	>200	No Data	No Data
Full Scale Output	1.5×1.5 mm ²	>5	mV	6.0	6.2	1.42 (5kPa)	1.26	29.1 (35 kPa)	40.61
	1.25×1.25 mm ²	>10	mV	25.25	26.5	5.07 (25kPa)	4.375	20.75 (35 kPa)	25.35
	1.0×1.0 mm ²	>10	mV	32.0	33.5	6.90 (50kPa)	4.55	8.81 (35 kPa)	8.82
	0.5×0.5 mm ²	>10	mV	15.75	16.5	3.15 (150 Kpa)	2.25	No Data	No Data
Ave Sensitivity	1.5×1.5 mm ²	>1.0	mV/(V-Kpa)	1.20	1.24	0.284	0.252	0.831	1.16
	1.25×1.25 mm ²	>0.8	mV/(V-Kpa)	1.01	1.06	0.203	0.175	0.592	0.724
	1.0×1.0 mm ²	>0.5	mV/(V-Kpa)	0.64	0.67	0.138	0.091	0.231	0.252
	0.5×0.5 mm ²	>0.1	mV/(V-Kpa)	0.105	0.112	.021	0.015	No Data	No Data
Bridge Resistance	3	kΩ	kΩ	3	3.09±0.054	3.08±0.045	3.09±0.021	3.08±0.045	
Ave Offset voltage (1V)	-40-40	mV	mV	N/A	20-30	20-30	20-40	20-40	
Power Supply (V _{in})	1-10	V	V	1-10	1-10	1-10	1-10	1-10	

7.7.1 Hydrogels

One of the most critical issues for hydrogels based transducers involves the hydrogels' response time. Hydrogels have slow response times, i.e., the amount of time it takes the hydrogel to generate a measureable amount of swelling pressure detected by the sensor array. Although the problem was addressed in our sensor by using small volumes of hydrogels that are relatively thin (400 μm) improvement is still needed since the response times of our sensors are on average > 10 minutes. Thinner hydrogel layers (<100 μm) should be tested to determine the limits of pressure generation, stability, sensitivity, linearity, reliability, and response time.

Furthermore, the hydrogel fabrication process must be integrated in a way that increases repeatability, allows batch production on the wafer scale, possibly utilizing ultra violet (UV) photolithography methods. Methods used to insert the hydrogel into the sensor cavity in this report have proven somewhat unreliable with variability in hydrogel size and preloading pressure. Recent progress has been made in this area using glucose sensitive hydrogels that cure with UV, and initial testing shows the gels are responsive to physiological important glucose concentrations. This method is currently being performed on the chip level by filling the cavities using a micropipette and exposing the dies to a UV lamp. Prehydrogel solution could potential be deposited using a spin-on process, patterned and polymerized on the pressure sensor diaphragms on the wafer level using photolithography. The most important parameters for this process would be spin speed, spin time, viscosity of the prehydrogel solution, and exposure time. To improve the adhesion of the hydrogel to the wafer and diaphragm surfaces an adhesion promoter such as Hexamethyldisilane (HMDS) can be utilized.

7.7.2 Sensor Design and Manufacturing

Several aspects of the fabrication of the sensor assemblies need improvement. First, bulk etching of the diaphragms needs to be controlled more reliably. In the best case scenario, timed KOH etching of the diaphragms realistically can only be used to an accuracy of approximately 1 μm . Our sensors were designed to have a diaphragm thickness of 10 μm and after etching the measured thickness was 15 ± 3 μm which significantly reduced sensitivity of the sensors as determined using bulge testing. The DRIE etching of the thin diaphragms was also difficult since they were first KOH etched and delicate. The use of silicon on insulator (SOI) wafers would alleviate a number of these problems directly by creating diaphragms with accurate thicknesses (<100 nm) and with the buried oxide providing a highly selective etch stop. Figure 7.1 shows the fabrication process envisioned.

The use of the SOI wafers for the fabrication process only alters the diaphragm etching process order. All frontside fabrication processes (oxide, piezoresistor implantation, nitride, and metallization) would remain unaltered. After etching of the oxide and nitride dielectric layers DRIE would be used to etch the pores in the diaphragm. The buried oxide acts as an etch stop ensuring the pores are all etched to the same depth. Studies have shown that for the Bosch process, which uses octafluorocyclobutane (C_4F_8), selectivity between oxide and nitride exceeds 150:1. Accuracy of the bulk etching of the silicon substrate would also be improved using the buried oxide layer as a backside etch stop. The selectivity between silicon oxide and silicon is extremely high, greater than 500:1.

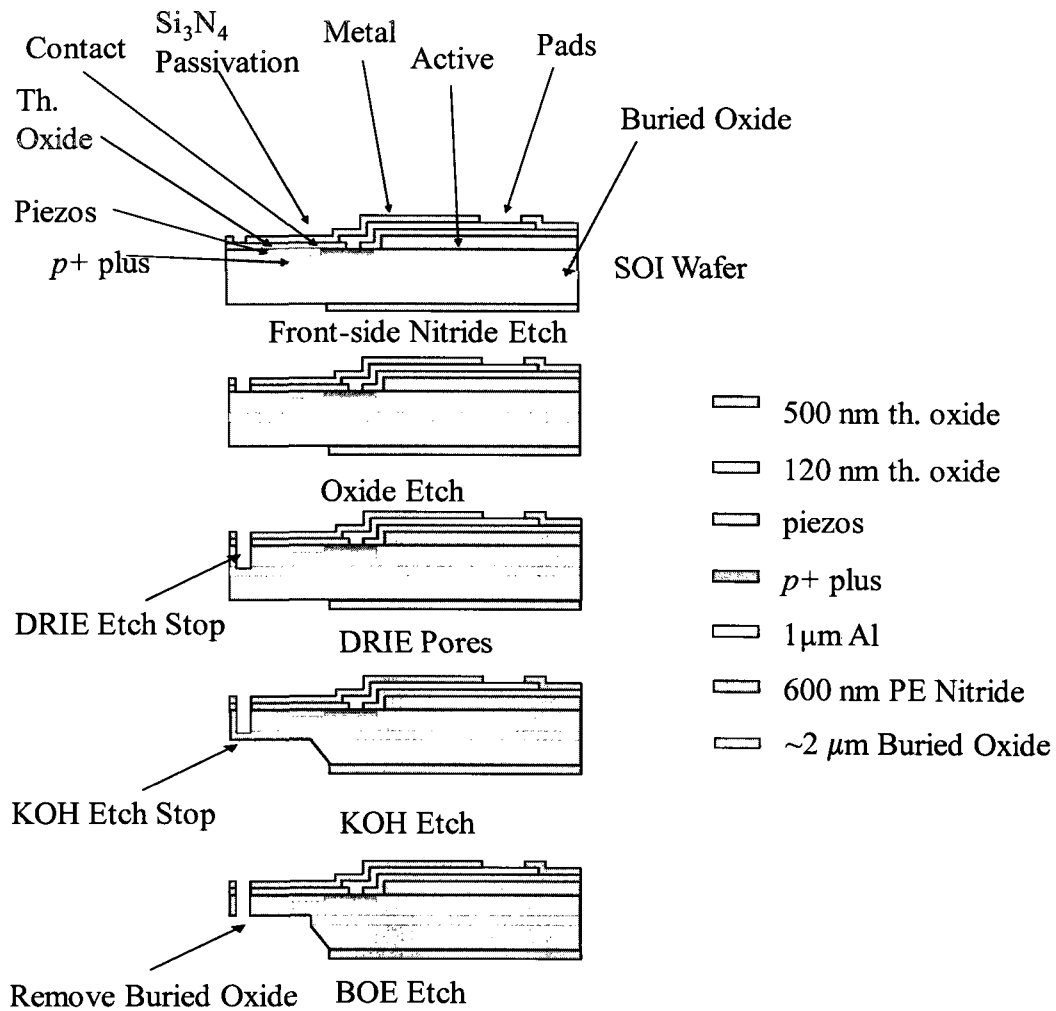


Figure 7.1. Proposed SOI wafer perforated diaphragm sensor fabrication procedure.

An additional advantage of this process is that the buried silicon oxide layer helps support the diaphragm which could be made very thin (<3 μm) determined by the thickness of the silicon overlayer. The silicon overlayer can be specified from silicon wafer manufacturers with thicknesses ranging from 100 nm to >15 μm . This added benefit could directly lead to development of smaller sensors and higher sensitivities. In order to release the diaphragms the buried oxide would be etched using a buffered oxide etch (BOE 7:1, NH_4F :7, HF:1).

7.7.3 Passivation/Encapsulation

Although the critical problem of isolating the resistors, bonding pads, and wiring from the liquid environment to prevent them from shorting has been solved, more work remains on improving the passivation and encapsulation performance. Parylene appears to be a suitable material to isolate the electronics from the conductive surroundings since the sensors have shown to be fully functional in PBS for over 400 hours. In general, most of the sensors failed within a few days of testing. Therefore studies should be performed using thicker parylene coatings, improved deposition parameters, and/or new encapsulation materials to increase sensors lifetime.

7.7.4 In-Vivo Testing

En route to in-vivo animal testing, experiments should first be conducted using various stimuli responsive hydrogels in animal serum, which closely simulates the subcutaneous fluid. This intermediate step will help to further accurately characterize and understand the sensor's behavior in a more realistic physiological monitoring application. Finally a rat is suggested to serve as the first animal model and the previously characterized microsensor array should then be inserted underneath the animal's skin where the objectives will be to:

- a) Determine the sensor's ability to continuously monitor changes within the body (stability) and establish the presence of signal drift, if any.
- b) Expose the animal to various stimuli, in order to determine any cross sensitivities which cause hydrogel to swell, and detect these changes with the sensor (selectivity).
- c) Examine and quantify the performance of the sensor in-vivo (sensitivity).

Successful testing in an animal will be the culmination of this work, which was modeled, successfully fabricated, characterized and presented in this dissertation.

APPENDIX A

**DESIGN AND PERFORMANCE OF AN LPCVD REACTOR FOR
THE GROWTH OF 3C-SILICON CARBIDE**

Reprinted with permission from the Electrochemical Society

Volume 156, pp. D364-D369, 2009



Design and Performance of an LPCVD Reactor for the Growth of 3C-Silicon Carbide

M. P. Orthner,² L. W. Rieth, and F. Solzbacher

Department of Electrical and Computer Engineering, University of Utah, Salt Lake City, Utah 84112, USA

This paper discusses the design of a low pressure chemical vapor deposition (LPCVD) reactor and growth of β silicon carbide (3C-SiC) thin films on Si. The reactor's hot-zone configuration radiatively couples the graphite heater (no physical contact) to Si substrates with realized temperatures $> 1500^\circ\text{C}$. We implemented a four-stage growth procedure using silane and propane precursors and hydrogen as the carrier gas. Temperatures, pressures, and flows varied from 850 to 1325°C , from 300 to 700 mTorr, and from 170 to 870 sccm during growth, respectively. Growth of 3C-SiC was confirmed using X-ray diffraction (XRD) with the observation of a (200) peak located at 41.4° . Activation energies of 21.5 and 2.15 kcal mol⁻¹ were calculated for the kinetically and mass-transport-limited regimes for polycrystalline 3C-SiC growth. The polycrystalline 3C-SiC films with fewest defects and smallest XRD full width at half-maximum were deposited at 300 mTorr with a growth rate of 1.07 $\mu\text{m}/\text{h}$ using flow rates of 5 sccm C_2H_6 , 5 sccm SiH_4 , and 850 sccm of H_2 (conc. 1.16%). The composition of the films measured by X-ray photoelectron spectroscopy shows that the films are slightly carbon rich (Si:C = 1:1.2) with oxygen as the main source of contamination. Voids were observed at the film-substrate interface for samples grown at high precursor concentrations. © 2009 The Electrochemical Society. [DOI: 10.1149/1.3158549] All rights reserved.

Manuscript submitted February 17, 2009; revised manuscript received May 27, 2009. Published July 14, 2009.

β silicon carbide (3C-SiC) is a wide bandgap semiconductor (~ 2.3 eV) that can be used at high temperatures ($> 500^\circ\text{C}$) and in aggressive/corrosive gas and fluid media.^{1,2} This makes it attractive in high power and high radiation applications.³ Silicon carbide thin films are stable at high temperatures, relatively chemically inert, and possess excellent mechanical properties when compared to silicon, making it useful in harsh environment sensors and microelectromechanical systems (MEMS).^{4,5} SiC has over 200 different polytypes often described by the stacking sequences of the Si-C bilayers.⁶ For MEMS applications and sensors, cubic 3C-SiC grown heteroepitaxially on Si substrates can be processed using conventional silicon bulk micromachining techniques.⁷ Due to its chemical inertness, high process selectivity exists between SiC and Si. Therefore wet and dry etching processes can be used to isolate SiC components when fabricated on Si.⁸

Conventionally, 3C-SiC thin films are deposited via chemical vapor deposition (CVD) using precursors containing a silicon precursor (silane) and a hydrocarbon (methane, ethane, or propane). Typically, cracking the hydrocarbons for vapor solid-phase growth requires substrate temperatures above 1000°C .⁹ Achieving these temperatures reliably with good temperature uniformity is a challenging task for reactor design.¹⁰ Two known issues with the growth of epitaxial 3C-SiC on Si is the formation of high stress leading to growth defects because of a 19.7% mismatch in lattice spacing ($a_{3\text{C-SiC}} = 0.436$ nm, $a_{\text{Si}} = 0.543$ nm) and 23% in thermal expansion coefficients at 1350°C .¹¹ Modification of film thickness, growth rate, and precursor concentrations (C:Si ratio) has been shown to reduce defects by manipulation of compressive and tensile stresses as described in Ref. 12 and 13. Films (3C-SiC) are grown on silicon substrates using hot-wall (resistive tube furnace) or cold-wall [radio-frequency (rf) induction heated] CVD reactor configurations.¹⁴⁻¹⁷ Many researchers are investigating growth at temperatures below 1250°C at atmospheric pressure using precursors to enable use of tube furnaces. These organometallic precursors such as methyltrichlorosilane (CH_3SiCl_3), tetramethylsilane [$\text{Si}(\text{CH}_3)_4$], and hexamethyldisilane [$(\text{CH}_3)_6\text{Si}_2$] have been used to grow SiC with some success.¹⁸⁻²⁰ Hot-wall systems are often limited to 1300°C by the quartz tube. The highest quality 3C-SiC films are grown above 1350°C commonly using cold-wall inductively heated reactors.²¹

This paper discusses the design and performance of a "quasi" cold-wall low pressure chemical vapor deposition (LPCVD) reactor that uses a resistive graphite heater for the growth of 3C-SiC on Si and allows lower equipment cost and more flexible processing configurations than conventional systems. We further present the influ-

ence of deposition conditions (temperature, pressure, flow rate, and precursor concentration) on the thin-film quality. Characterization techniques used to investigate the films include scanning electron microscopy (SEM), X-ray diffraction (XRD), and X-ray photoemission spectroscopy (XPS). These techniques studied the film's surface morphology and thickness, crystal structure, and chemical composition, respectively.

Experimental

CVD reactor design.—The LPCVD reactor used in this work made use of low cost resistive heating (instead of rf induction) and was capable of depositing 3C-SiC on Si. Details of the heater system design and validation are not covered in this paper and are found in Ref. 22. Design requirements for the SiC-LPCVD system are listed in Table I.

The reactor main chamber was built using a 12 in. o.d. feedthrough collar made from double-wall 304 stainless steel with integrated water cooling manufactured by Kurt J. Lesker (Pittsburgh, PA). The i.d. of the chamber is 27.5 cm, where graphite hot-zone components are located as shown in Fig. 1. A 16.5 cm graphite sigmoidal heater was mounted to the lid suspended 2.5 cm above a rotating substrate holder. Graphite posts were connected to water-cooled electrical feedthroughs on the lid and acted as the mechanical supports and electrical interconnects. Finite-element analysis performed with Comsol 3.4 (Burlington, MA) was used to optimize the heater geometry with respect to mechanical integrity and temperature uniformity. These simulations validated the reported experimental data and indicated a temperature gradient of $\pm 10^\circ\text{C}$ at 1500°C across the wafer locations. A two-color optical pyrometer (Omega IR2P) was used to measure the surface temperature at the center of the graphite sample holder during growth with an accuracy of 0.2% full scale within the range 600 – 1800°C .

All internal hot-zone components were fabricated from IG-70 high purity graphite (Toyo Tanso, Troutdale, OR) including the heat shields and sample holder. The heat shields minimized thermal radiation and conduction losses to the outer chamber. The shield on

Table I. Initial performance specifications of the LPCVD reactor used for growth of 3C-SiC on Si.

Process parameter	Min	Max
Temperature ($^\circ\text{C}$)	600	1500
Temperature uniformity at 1500°C ($^\circ\text{C}$)	N/A	± 10
Total flow rate (sccm)	10	1200
Pressure (mTorr)	50	1000
Wafer size (mm)	N/A	150

² E-mail: m.orthner@utah.edu

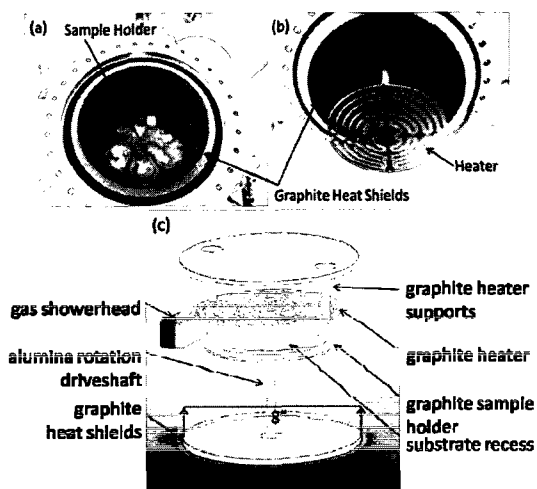


Figure 1. (Color online) Photographs of the (a) double-walled 304 stainless steel vacuum chamber, graphite heat shields, and sample holder. (b) shows the chamber lid with the attached graphite heater. Solidworks rendering of the (c) SiC-LPCVD reactor hot zone. The resistive heater is located 25 mm above the rotating sample holder and capable of temperatures $>1500^{\circ}\text{C}$. Six 2 in. wafers can be loaded in the chamber simultaneously. A series of graphite heat shields was used to isolate temperatures to the growth zone.

the lid and base comprised two layers of graphite separated by 3.175 mm thick alumina washers attached using alumina screws (Superior Technical Ceramics, Vermont). The feedthrough collar shield was a hollow graphite cylinder with 12.7 mm wall thickness used to line the inside of the chamber, with openings created for the gas showerhead inlet and pumping outlet. Growth took place in the hot zone, where the heater was located above the rotating sample holder as illustrated in Fig. 1c. Gases entered the chamber through the horizontal showerhead, flowing horizontally across samples. The exhaust was pumped from the chamber to a water-cooled particulate trap.

This pseudocold-wall design prevents 3C-SiC deposition on the outer steel chamber by confining growth to the hot zone. A computer-controlled stepper motor (IMS MDO34) connected to a water-cooled rotary feedthrough (Rigaku 10C-24041500) was used to rotate the sample holder. Three mass-flow controllers (Celerity 1661) and gas-mixing manifold were mounted inside a 19 in. rack cabinet. Normally closed pneumatic bellows valves (Swagelok, SS-BN8FR8-C) were automated using a personal computer running Labview 7.1 (National Instruments, Austin, TX). Silane, propane, and hydrogen flow was regulated using three mass-flow controllers connected in parallel and mixed in a VCR cross, then travel to a stainless steel showerhead located inside the hot zone. The base pressure of 50 mTorr was limited by the hook claw and roots blower dry pump combination (Alcatel 813B), a throttle valve (MKS 253B-2-50-2) with closed-loop control provided by a capacitance monometer [MKS Baratron (0.1–1000 mTorr)] was used to control deposition pressure. The custom-written Labview virtual instrument interfaces the heating, gas delivery, and pressure control subsystems with interlocks monitoring temperature, cooling water flow, gas flow, and pressure. Procedural interlocks were implemented to ensure proper growth steps and timing.

SiC growth.—Growth runs were carried out on p-type (1–10 Ω cm) c-Si (100) samples (2 \times 2 cm). Precursors consisted of ultrahigh purity (99.999%) silane (SiH_4) and propane (C_3H_8), and hydrogen (H_2) as the carrier gas. Before loading samples in the growth chamber, they were degassed in methanol (30 s) and then

Table II. Experimental plan describing the variation of processing parameters used for 3C-SiC growth. Four variables were studied: the temperature, pressure, flow rate, and precursor concentrations.

Process variable	Temperature	Pressure	Flow rate	Precursor concentration
Temperature ($^{\circ}\text{C}$)	750–1325	1325	1325	1325
Pressure (mTorr)	300	300–700	300	300
H_2 flow (sccm)	850	850	170–850	85–850
C_3H_8 flow (sccm)	5	5	1–5	5
SiH_4 (sccm)	5	5	1–5	5
Total flow ($\text{SiH}_4 + \text{C}_3\text{H}_8$)	860	860	172–860	860
($\text{SiH}_4 + \text{C}_3\text{H}_8 + \text{H}_2$)	1.16	1.16	1.16	1.16–10.6

dipped in a buffered oxide etch (30 s) at room temperature to remove any native oxide. They were then rinsed in deionized water, dried using N_2 , and loaded into the reactor. Each growth run used three 2 \times 2 cm Si samples placed 150 mm from the center of the graphite sample holder. The sample holder was located 25 mm below the graphite heater and rotated at 20 rpm for all growth runs. This rotational speed was chosen to improve temperature homogeneity without allowing the samples to fall off the sample holder. The system was pumped to base pressure (50 mTorr) and backfilled with argon 10 times to decrease any residual gases from sample loading. All SiC films were grown with an identical four-step growth procedure as described in Ref. 19. The silicon samples were heated at $>20^{\circ}\text{C}/\text{s}$ in H_2 (1 slm) to the temperature of 1000°C for 3 min of in situ cleaning at 500 mTorr. After cooling to 600°C , a carbonization process was performed for 2 min flowing H_2 (1 slm) and C_3H_8 (8 sccm) to deposit stoichiometric 3C-SiC buffer layer at 1150°C (500 mTorr). This buffer layer reduced the abruptness of mismatch in thermal expansion coefficient and lattice parameter between the 3C-SiC thin film and silicon substrate. Films grown using carbonization have fewer SiC-Si interface-related defects.^{19,23} To study the film properties after carbonization, three samples were unloaded before the growth stage of different runs. The carbonization process was consistent between runs and, for growth, the chamber was ramped to temperature and then SiH_4 was introduced for 30 min. The reactor heat up ramp in the preliminary experiments was very fast (ca. $10^{\circ}\text{C}/\text{s}$). Within less than a minute the measured temperature on the susceptor increased from 600 to 1150°C , followed by a 2 min settling process in which the temperature stabilized. Following processing, the substrates were cooled to room temperature at 500 mTorr in an Ar ambient. The C:Si ratio for the precursors was constant at 3 in the gas phase based on the following formula

$$\frac{\text{C}}{\text{Si}} = \frac{3[\text{C}_3\text{H}_8(\text{sccm})]}{\text{SiH}_4(\text{sccm})} \quad [1]$$

Preliminary growth runs varied the temperature, pressure, total precursor flow rate, and precursor (SiH_4 and C_3H_8) concentration in H_2 during the growth stage as described by Table II.

Results

Growth rate.—For CVD processes, the relationship between temperature and growth rate needs to be investigated to derive information about the competing chemical reactions. Figure 2 shows the growth rate in relation to deposition temperature using deposition parameters shown in the first column of Table II. The cross-sectional film thickness was determined by cleaving samples through their midpoint using a diamond scribe and then measuring the film using an SEM (FBI Quanta 600F). Vertical error bars define the standard deviation of the growth rate from sample to sample within a particular growth run. Films grown below 1025°C were very thin (<60 nm), which may be due to reduced precursor decomposition at these lower temperatures. For temperatures from

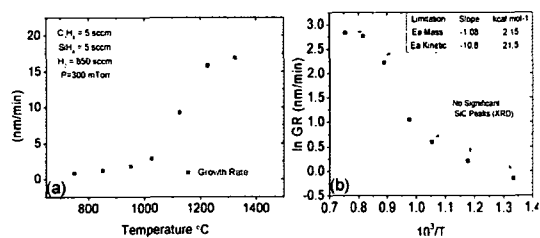


Figure 2. (Color online) (a) Growth rate dependence of the 3C-SiC layers grown at temperatures from 750 to 1325°C. From 1025 to 1225°C the reaction is strongly temperature dependent and kinetically controlled. The slope of the growth rate with respect to temperature becomes smaller between 1225 and 1325°C, indicating that mass transport was the limiting growth mechanism. (b) Arrhenius plot used to determine activation energies of 21.5 and 2.15 kcal mol⁻¹ for the kinetic and mass-transport-limited regimes of the 3C-SiC growth, respectively.

1025 to 1325°C, the growth rate was strongly temperature dependent with a calculated activation energy of 21.5 kcal mol⁻¹ as shown in Fig. 2b. This is consistent with results found in literature for Nishino et al.²⁴ who found an activation energy of 15 kcal mol⁻¹ for a similar process. Above 1025°C, the growth rate is kinetically limited and is essentially constant with increasing temperature to 1225°C. The slope of the growth rate with respect to temperature becomes smaller between 1225 and 1325°C, indicating that the limiting growth mechanism was altered. This can be attributed to the limited mass transport of reactants through a boundary layer above the substrate growth surface. An activation energy of 2.15 kcal mol⁻¹ was found for this region.

Pressure and flow experiments are described by the second and third columns of Table II. These six growth runs performed at 1325°C show that decreasing pressure and increasing flow rate increase 3C-SiC growth rate as shown in Fig. 3. Experimental results from growth runs performed at 1325°C implicate that rate is limited by mass transport of precursors to the growth surface. Using the boundary layer (BL) model, the BL thickness is decreased as precursor flow rates are increased.^{25,26} Therefore, a thinner boundary layer allows a larger flux of precursor molecules to reach the surface, increasing the growth rate. The growth rate was the highest (17.5 nm/min) when using a total flow rate of 860 sccm and pressure of 300 mTorr at 1325°C.

Experimental parameters used to study the influence of precursor concentration are displayed in the fourth column of Table II. The

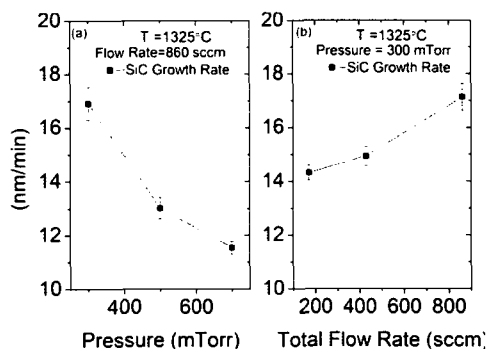


Figure 3. Growth rate dependence on (a) pressure and (b) volumetric gas flow rate of 3C-SiC films grown at 1325°C for 30 min. Pressure increase from 300 to 700 mTorr decreased the growth rate from 16.9 to 11.4 nm/min, respectively. An increase in flow rate from 172 to 860 sccm increased the growth rate from 14.3 to 17.6 nm/min.

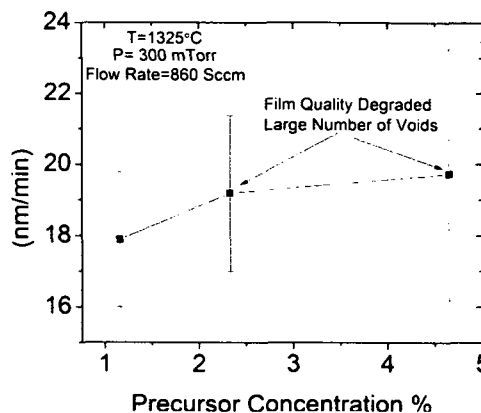


Figure 4. Precursor concentration influence on growth rate at 1325°C (300 mTorr) using a total precursor flow of 860 sccm. Increased concentration from 1.16 to 4.63% increased the growth rate from 17.7 to 19.7 nm/min. Many voids are found at the interface of the film and substrate at concentrations > 1.16%.

flow rates of propane and silane were held constant at 5 sccm, while the hydrogen carrier flow was increased from 85 to 850 sccm. The precursor concentrations had a minor influence on growth rate as shown by Fig. 4 with precursor concentrations ranging from 1.16 to 4.63% at a growth temperature of 1325°C. We observed the formation of voids between the silicon substrate and the 3C-SiC layer at precursor concentrations > 1.16% in hydrogen. Films deposited at elevated precursor concentrations had a higher density of interface defects and growth rate variation. An important observation was that the standard deviation of growth rate increased from 1.9 to 3.53 nm/min at precursor concentrations from 1.16 to 4.65%. We assume that the growth of these films involves Si atoms diffusing from the substrate in the growth region. Kim et al.²⁷ proposed that methyl radicals adsorb on the Si substrate leading to evaporation and out-diffusion creating defects on the surface. Once a defect is formed, evaporation of Si occurs due to the increased charged density, leading to the formation of voids at the interface. The evaporated Si atoms continuously combine with methyl radicals on the surface, enlarging the SiC nuclei that eventually coalesce, capping off the defect.

Film morphology.— Presented in Fig. 5 are plane-view SEM micrographs of the 3C-SiC films grown at 1025, 1125, 1225, and 1325°C using conditions described in the second column of Table II. Deposition temperature and subsequent growth strongly influence the microstructure. SEM analysis showed that films grown at 1025°C had a granular surface and submicrometer-size SiC crystals. It is apparent that an elevated temperature leads to higher growth rates and enlarged SiC crystal size. At 1025 and 1125°C the surface shows particulates that are < 2 μm in diameter. Significant enlargement occurs at 1225°C with surface SiC crystals > 4 μm. The surface morphologies of the films grown at 1325°C are more faceted in character, as shown in Fig. 5d. XRD spectra collected with a Phillips XPERT system determine the microstructure and crystallinity of 3C-SiC films. Continuous scans were carried out using Cu Kα X-ray radiation (0.154 nm) from 10 to 100° with a 0.02° step size and step time of 0.2 s. Temperature had the largest impact on the morphology of SiC thin films seen in Fig. 6. At growth temperatures of 1125, 1225, and 1325°C, the SiC(200) peak is observed at 41.4°. Reduction in growth temperature increased the full width at half-maximum (fwhm) of the 3C-SiC peak from 0.29 to 0.39° at 1325 and 1125°C, respectively. XRD spectra taken from samples deposited at 1025°C exhibit diffraction patterns associated with Si(200) planes (underlying Si substrate) with no significant peaks due to SiC. This silicon

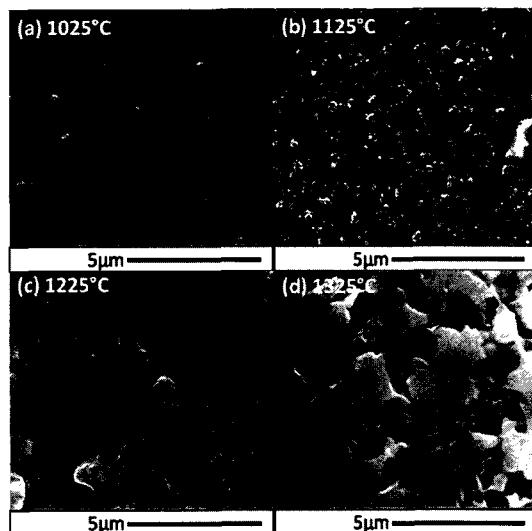


Figure 5. SEM images of SiC surface morphology on Si(100) substrates using propane, silane, and H_2 at (a) 1025, (b) 1125, (c) 1225, and (d) 1325°C. Increasing growth temperatures lead to larger, more rectangular 3C-SiC crystals.

(200) peak appears when the silicon is strained, introducing tetragonal distortion in the lattice. The samples deposited at 1325°C have the highest reflection from the silicon (200) peak, which is caused by the Si lattice distortion. This film was the thickest obtained in all samples and produced at the highest temperature, resulting in the highest substrate stress. Growth temperatures of 1025°C and below appear too low for 3C-SiC formation using the described conditions. Another observed trend was that elevated flow rates increased the intensity of the 3C-SiC peak (41.4°), as shown in Fig. 7. There is a decrease in the fwhm of the 3C-SiC (200) peak from 0.39° to 0.34° with the increase of flow rate, indicating that the crystallinity of 3C-SiC films was slightly improved. Growth rate has an inverse relationship with pressure at a flow rate of 850 sccm, which could be attributed to gas depletion on the growth surface and gas-phase

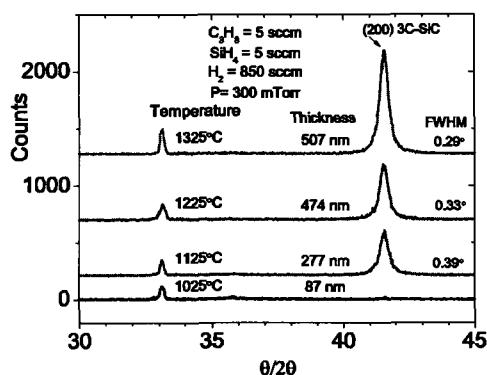


Figure 6. (Color online) XRD spectra of 3C-SiC films grown at temperatures from 1025 to 1325°C at 300 mTorr with flows of 5 sccm of SiH_4 and C_2H_6 and 850 sccm of H_2 . Two distinct peaks are present; the strained silicon substrate peak (200) and the 3C-SiC (200) at 33.3 and 41.4° , respectively.

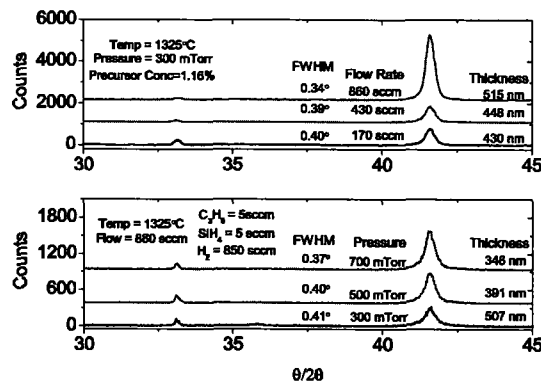


Figure 7. (Color online) XRD spectra of 3C-SiC films deposited at pressures and flows ranging from 300 to 700 mTorr and from 170 to 860 sccm, respectively. At 300 mTorr the flow rate had a large impact on the (200) 3C-SiC peak, while pressure played a less influential role.

nucleation. The fwhm of spectra taken at different pressures does not show a significant trend. Future experiments are necessary to further investigate these effects.

Chemical composition.— A Kratos Axis Ultra DLD XPS system with monochromatic Al $K\alpha$ line X-ray source ($h\nu = 1486.6$ eV) using a 15 keV, 15 mA emission current was used to detect scattered electrons from the 3C-SiC films. After measurements of the film's surface a 3×3 mm square was etched with a 4 kV ($\sim 1 \mu A$, beam current) argon-ion beam to remove any surface contamination. The surface survey spectrum in Fig. 8 clearly shows the photoelectron peaks for F, O, N, C, and Si. Figure 9 shows in detail the C 1s and Si 2p spectra on the surface and after argon etching. The surface of the films shows the presence of carbide bonding recognized from the 283 eV peak along with adventitious carbon at 284.9 eV. The adventitious carbon peak used for system calibration disappears after etching and only carbidic bonding is apparent. Peak shifting occurs

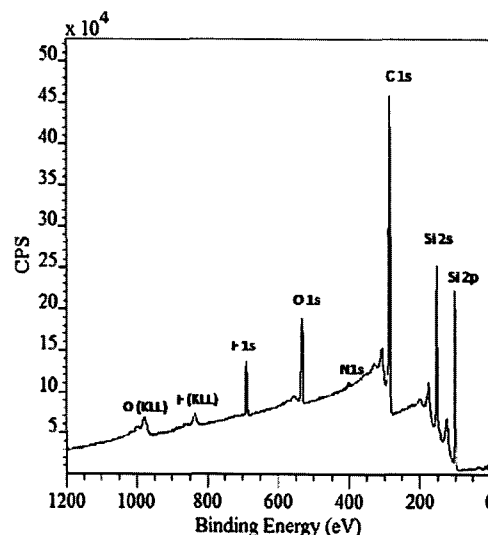


Figure 8. XPS survey spectrum of the sample grown at 1325°C (300 mTorr) at a 1.16% precursor concentration for 30 min. The scan was from 1200 to 0 eV using monochromatic Al $K\alpha$ line X-ray source.

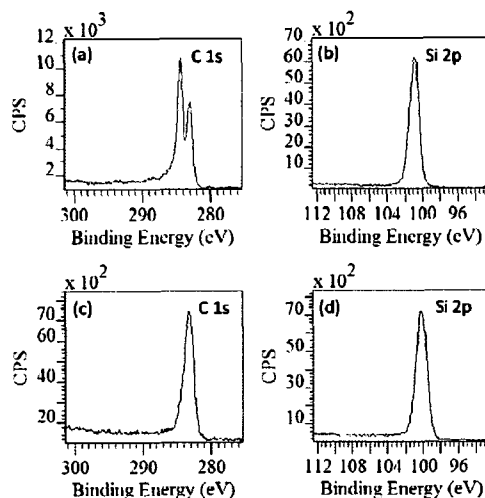


Figure 9. Carbon 1s peaks shown on the (a) surface and (c) after 240 s of Ar etching (<20 nm). The silicon 1p peak is shown shifting from (b) 100.9 eV on the surface to (d) 100.3 eV after etching, indicating an increase in Si-C bonding.

from 100.9 to 100.3 eV after argon etching for the Si 2p bonds. This is explained by improved Si-C bonding after removal of surface carbon and oxide species.⁹ Figure 10 shows that oxygen (O 1s) contamination was more prevalent on the surface and presumably caused from samples' exposure to the atmosphere during sample loading and unloading. The measurements were made on 10 samples which consistently showed O to be higher than N and F in the etched films. The relative sensitivity factor (RSF) for F is relatively high (1.0) and the spectra postetching indicated that F is below

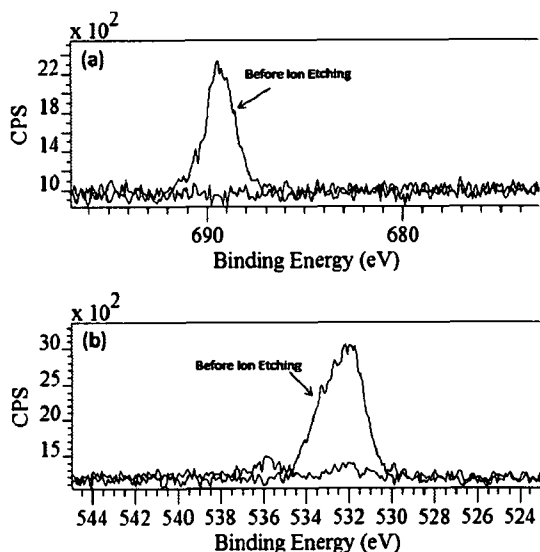


Figure 10. XPS spectra showing surface contamination of the (a) F 1s and (b) O 1s peaks. Sputter etching for 4 min significantly reduced the contamination levels detected, suggesting these were surface contaminants.

Table III. Quantified atomic concentrations (XPS) taken from 3C-SiC grown at 1325°C (300 mTorr) with a precursor concentration of 1.16% and a total flow rate of 860 sccm. The C:Si ratio was 2.46 and 1.21 on the surface and after ion etching, respectively. All films appeared to be carbon rich.

Peak	Surface (atom %)	Ion etched (atom %)
F 1s	2.7	0
O 1s	6.41	0.66
N 1s	0.25	0.43
C 1s	64.48	54.24
Si 2p	26.16	44.67

detection limits. However, we did see high concentrations of F on the surface ~5 to 10% on certain samples. Oxygen has an RSF of 0.78, and clearly discernible O peaks were observed before and after ion etching. Nitrogen has a relatively low RSF factor (0.447) resulting in high detection limits. Nitrogen peaks were seen before etching but were not discernible in the ambient noise after etching. From these data we conclude that oxygen is the primary contaminant while some nitrogen may be present. The oxygen levels observed were ~1 to 2 atom %, but the nitrogen was below the detection limits of the XPS after etching. The average atomic concentration of oxygen was 5.42% before and 1.1% after etching. The source of oxygen contamination is due to impure gases, incomplete purging, or minor chamber leaks during growth. The composition measured by XPS for a sample grown at 1325°C, 300 mTorr, 1.16% precursor concentration, and a total flow rate of 860 mTorr is presented in Table III. This particular sample had the smallest fwhm (0.29°) for the 3C-SiC (200) XRD peak and a 507 nm thickness. The stoichiometry of the etched film is Si:C = 1:1.2, which is slightly carbon rich.

Elevated concentrations (>2 atom %) of F on the surface on several samples was observed and is attributed to outgassing of the chamber's lid fluoropolymer o-ring during the cooling phase. Samples cooled in the presence of argon at elevated pressures showed surface fluorine contamination decrease from 2.4 to 0.11 atom %.

Defects.—One major challenge for heteroepitaxial growth of 3C-SiC on silicon using silane and propane is the large density of voids formed at the SiC/Si interface.²⁷ These voids are pyramidal with a base that is parallel to the (110) direction in the (100) substrates.²⁸ Literature references propose that these structures could be created when silicon from the substrate diffuses to the surface during the initial growth stage.²⁸⁻³² Cross-sectional SEM micrographs used to measure film thickness show evidence of voids at the interface for samples grown from 1125 to 1325°C with a precursor concentration $\geq 2.3\%$. Films grown below these temperatures ($\leq 1025^\circ\text{C}$) were thin (<100 nm), had no interfacial voids, and did not exhibit the 3C-SiC (200) XRD peak. Growth runs performed using a 1.16% precursor concentration did show evidence of voids but were less frequent and submicrometer in size. The largest voids (>5 μm) were found in samples that were grown at 1325°C and precursor concentrations of 4.63%, as shown in Fig. 11b and d. At lower temperatures the voids were generally smaller (<3 μm) (Fig. 11a and c). Steckyl and Li³³ deduced that at high propane flow rates the formation of voids is due to the many nucleation sites available on the growth surface allowing many Si atoms to diffuse from the bulk. The results of Burkland et al.³⁰ showed that voids were created during the carbonization process, and with the addition of silane, they could be significantly reduced. In our experiments, we have not modified the precursor stoichiometric ratio during carbonization or growth. Therefore, we are unable to verify if manipulation of the gas partial pressures have a direct impact on the formation of interface voids. The reduction or elimination of these etch voids is crucial to the success of creating 3C-SiC/Si devices. At elevated precursor

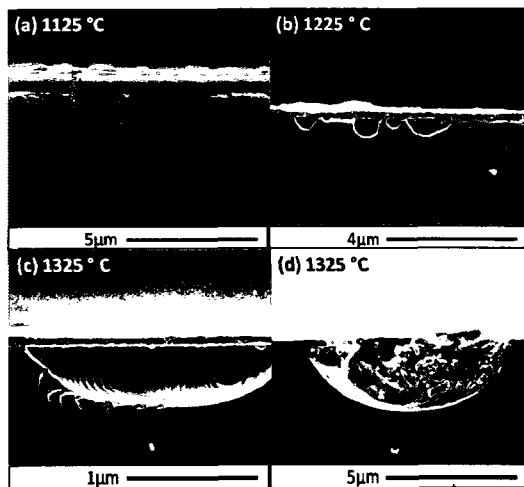


Figure 11. SEM micrographs of voids found at the 3C-SiC/Si interface for films grown at (a) 1125, (b) 1225, and (c, d) 1325°C under various growth conditions.

concentrations (>2.3%) and temperatures (>1225°C), ring-shaped defects with small particles in the center were found on the SiC film surface, as shown in Fig. 12. These ring defects were more frequent at higher pressures (700 mTorr) and best explained by gas-phase nucleation. In literature, it was seen that high SiH₄ concentration, high pressures, and elevated temperatures enhance the probability for homogeneous nucleation in the gas phase to occur.^{15,34,35} At the highest precursor concentration (4.63%) and temperature (1325°C) the films appeared porous on the surface, with voids extending into the substrate (Fig. 12b) with the presence of large ring-like defects (Fig. 12a). A weakly adhered white powdery deposit was also present on these samples. The centers of the ringlike defects resembled particles formed from gas-phase nucleation which landed on the growth surface creating modified growth sites. The ring shape indicates that particles landed during growth and modified the growth mechanism in the surrounding areas.

Conclusions

Polycrystalline β (3C-SiC) silicon carbide thin films were grown on c-Si(100) samples using a resistively heated LPCVD reactor with unique hot-zone geometry. Initial process runs demonstrate that the LPCVD system is capable of controlling temperature, flow, and

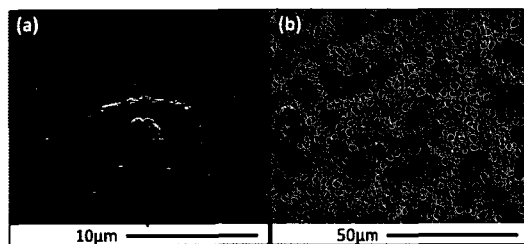


Figure 12. SEM micrographs of samples grown at a precursor concentration of 4.63% and at temperatures of (a) 1225 and (b) 1325°C. These deposition conditions caused (a) gas-phase nucleation with modified growth sites and (b) films that were highly defective with surface voids protruding into the substrate.

pressure in the ranges needed for 3C-SiC growth using silane and propane as precursors. SEM cross-sectional analysis verifies that higher temperatures, lower pressures, and higher flow rates increase the growth rate in our system. XRD results show that films grown at temperatures $\geq 1125^\circ\text{C}$ are primarily 3C in character, indicated by a strong peak at 41.4° . XPS analysis indicates that films are slightly carbon rich and that the main source of contamination within the films is oxygen. Well-oriented rectangular 3C-SiC polycrystalline films were grown at 1325°C with low precursor concentrations (1.16%) and a rate of 16.9 nm/min. All samples had formation of interface pits when precursor concentrations exceeded 1.6% dilution. The largest voids (>5 μm) were found in samples grown at a precursor concentration of 4.63% at 1325°C. At elevated precursor concentrations (>2.3%) particulates formed on the sample surface from gas-phase nucleation, thus modifying growth sites, and created ring-shaped defects. Additional process optimization must be performed to reduce SiC/Si interfacial pitting and overall reduction of defects.

University of Utah assisted in meeting the publication costs of this article.

References

- R. F. Davis, G. Keiner, M. Shur, J. W. Palmour, and J. A. Edmond, *Proc. IEEE*, **79**, 677 (1991).
- M. R. Werner and W. R. Fahrner, *IEEE Trans. Ind. Electron.*, **48**, 249 (2001).
- M. Bhatnagar and B. J. Baliga, *IEEE Trans. Electron Devices*, **40**, 645 (1993).
- M. Mehregany, T. Lijun, L. G. Mathis, and D. J. Larkin, *IEEE Trans. Electron Devices*, **44**, 74 (1997).
- M. Mehregany and C. A. Zorman, *Thin Solid Films*, **355-356**, 518 (1999).
- H. Matsunami and T. Kimoto, *Mater. Sci. Eng. R.*, **20**, 125 (1997).
- P. M. Sarro, *Sens. Actuators, A*, **82**, 210 (2000).
- P. H. Yih, V. Saxena, and A. J. Steckl, *Phys. Status Solidi B*, **202**, 605 (1997).
- D. C. Lim, H. G. Jee, J. W. Kim, J. S. Moon, S. B. Lee, S. S. Choi, and J. H. Boo, *Thin Solid Films*, **459**, 7 (2004).
- A. Ellison, J. Zhang, J. Peterson, A. Henry, Q. Wahab, J. P. Bergman, Y. N. Makarov, A. Vorobe'ev, A. Vehanen, and E. Janz n, *Mater. Sci. Eng. B*, **61-62**, 113 (1999).
- G. Ferro, N. Planes, V. Papaioannou, D. Chaussende, Y. Monteil, Y. Stoemenos, and J. Camassel, *Mater. Sci. Eng. B*, **61-62**, 586 (1999).
- M. Zielinski, *Phys. Status Solidi A*, **204**, 981 (2007).
- S. R. Nutt, D. J. Smith, H. J. Kim, and R. F. Davis, *Appl. Phys. Lett.*, **50**, 203 (1987).
- J. Zhang, U. Fowberg, M. Isacson, A. Ellison, A. Henry, O. Kordina, and E. Janz n, *J. Cryst. Growth*, **241**, 431 (2002).
- E. L. Myers, Y. Shishkin, O. Kordina, and S. E. Saddow, *J. Cryst. Growth*, **288**, 486 (2005).
- R. Rupp, *Phys. Status Solidi B*, **202**, 281 (1997).
- R. Rupp, P. Lanig, J. V. Iki, and D. Stephani, *J. Cryst. Growth*, **146**, 37 (1995).
- S. Madapura, A. J. Steckl, and M. Loboda, *J. Electrochem. Soc.*, **146**, 1197 (1999).
- G. Ferro, J. Camassel, S. Juillaguet, C. Balloud, E. K. Polychroniadis, Y. Stoemenos, J. Dazord, H. Peyre, Y. Monteil, S. A. Rushworth, et al., *Semicond. Sci. Technol.*, **18**, 1015 (2003).
- A. J. Steckl, J. Devrajan, S. Tlali, H. E. Jackson, C. Tran, S. N. Gorin, and L. M. Ivanova, *Appl. Phys. Lett.*, **69**, 3824 (1996).
- K. Tekar, C. Jacob, J. Chung, and M. H. Hong, *Thin Solid Films*, **371**, 53 (2000).
- M. Orthner, L. Rieth, and F. Solzbacher, *52nd Annual Technical Conference Proceedings of the Society of Vacuum Coaters, Society of Vacuum Coaters* (2009).
- S. Nishino, J. A. Powell, and H. A. Will, *Appl. Phys. Lett.*, **42**, 460 (1983).
- S. Nishino, Y. Hazuki, H. Matsunami, and T. Tanaka, *J. Electrochem. Soc.*, **127**, 2674 (1980).
- E. L. Choy, *Prog. Mater. Sci.*, **48**, 57 (2003).
- H. Schlichting and K. Gersten, *Boundary-Layer Theory*, Springer, New York (2000).
- K. C. Kim, C. I. Park, J. I. Roh, K. S. Nahm, and Y. H. Seo, *J. Vac. Sci. Technol. A*, **19**, 2636 (2001).
- J. A. Powell, G. M. Lawrence, and A. K. Maria, *J. Electrochem. Soc.*, **134**, 1558 (1987).
- C. C. Tin, R. Hu, R. L. Coston, and J. Park, *J. Cryst. Growth*, **148**, 116 (1995).
- B. Burkland, Z. Y. Xie, J. H. Edgar, M. Ervin, J. Chaudhuri, and S. Farsinivas, *J. Electrochem. Soc.*, **149**, 550 (2002).
- P. Linw and R. F. Davis, *J. Electrochem. Soc.*, **132**, 642 (1985).
- K. Kwang Chul, P. Chan Il, R. Jae Il, N. Kee Suk, H. Yoon Bong, L. Youn-Sik, and L. Kee Young, *J. Electrochem. Soc.*, **148**, C383 (2001).
- A. J. Steckl and J. P. Li, *IEEE Trans. Electron Devices*, **39**, 64 (1992).
- H. O. Pierson, *Handbook of Chemical Vapor Deposition (CVD): Principles, Technology, and Applications*, Noyes, Park Ridge, NJ/William Andrew, Norwich, NY (1999).
- Z. M. Qian, H. Michiel, A. V. Ammel, J. Nijs, and R. Mertens, *J. Electrochem. Soc.*, **135**, 2378 (1988).

APPENDIX B

EXAMPLE COMSOL CODE FOR PERFORATED DIAPHRAGM

SIMULATIONS

```
% COMSOL Multiphysics Model M-file
% Generated by COMSOL 3.5a (COMSOL 3.5.0.603, $Date: 2008/12/03 17:02:19 $)
% Some geometry objects are stored in a separate file.
% The name of this file is given by the variable 'flbinaryfile'.
```

```
flclear fem
```

```
% COMSOL version
clear vrsn
vrsn.name = 'COMSOL 3.5';
vrsn.ext = 'a';
vrsn.major = 0;
vrsn.build = 603;
vrsn.rcs = '$Name: $';
vrsn.date = '$Date: 2008/12/03 17:02:19 $';
fem.version = vrsn;
```

```
flbinaryfile='Simulation_Code.mphm';
```

```
% Geometry
clear draw
g12=flbinary('g12','draw',flbinaryfile);
draw.s.objs = {g12};
draw.s.name = {'CO1'};
draw.s.tags = {'g12'};
fem.draw = draw;
fem.geom = geomcsg(fem);
fem.mesh = flbinary('m1','mesh',flbinaryfile);
```

```
% (Default values are not included)
```

```
% Application mode 1
clear appl
appl.mode.class = 'SmeSolid3';
appl.module = 'SME';
appl.gporder = 4;
appl.cporder = 2;
appl.assignsuffix = '_smsld';
```



```

'mat3_Delatic3D_6_1_', 'mat3_Delatic3D_6_2_', 'mat3_Delatic3D_6_3_', 'mat3_Delatic3D_6_4_',
...
'mat3_Delatic3D_6_5_', 'mat3_Delatic3D_6_6_'});
equ.Tempref = 0;
equ.alphadM = 1;
equ.Temp = 0;
equ.name = {'', 'SingleCrystalSi'};
equ.alphavector = {'mat2_alphavector3D_1_', 'mat2_alphavector3D_2_', 'mat2_alphavector3D_3_', ...
'mat2_alphavector3D_4_', 'mat2_alphavector3D_5_', 'mat2_alphavector3D_6_', ...
{'mat3_alphavector3D_1_', 'mat3_alphavector3D_2_', 'mat3_alphavector3D_3_', ...
'mat3_alphavector3D_4_', 'mat3_alphavector3D_5_', 'mat3_alphavector3D_6_'});
equ.ind = [1.];
appl.equ = equ;
fem.appl{1} = appl;
fem.sdim = {'x', 'y', 'z'}, {'x2', 'y2', 'z2'});
fem.frame = {'ref', 'deform'};
fem.border = 1;
clear units;
units.basesystem = 'SI';
fem.units = units;

% Library materials
clear lib
lib.mat{1}.name='Silicon';
lib.mat{1}.varname='mat1';
lib.mat{1}.variables.nu='0.27';
lib.mat{1}.variables.E='131E9[Pa]';
lib.mat{1}.variables.mur='1';
lib.mat{1}.variables.sigma='1e-12[S/m]';
lib.mat{1}.variables.epsilon='12.1';
lib.mat{1}.variables.alpha='4.15e-6[1/K]';
lib.mat{1}.variables.C='703[J/(kg*K)]';
lib.mat{1}.variables.n='3.48';
lib.mat{1}.variables.rho='2330[kg/m^3]';
lib.mat{1}.variables.k='163[W/(m*K)]';
lib.mat.name='Silicon (single-crystal)';
lib.mat.varname='mat2';
lib.mat.variables.Delatic2D={'166[Pa]', '64[Pa]', '64[Pa]', '0'}, {'166[Pa]', '64[Pa]', '0[Pa]'}, {'1
66[Pa]', '0[Pa]'}, {'80[Pa]'});
lib.mat.variables.Delatic3D={'166[Pa]', '64[Pa]', '64[Pa]', '0[Pa]', '0[Pa]', '0[Pa]'}, {'166[Pa]
', '64[Pa]', '0[Pa]', '0[Pa]', '0[Pa]'}, {'166[Pa]', '0[Pa]', '0[Pa]', '0[Pa]'}, {'80[Gpa]', '0[GPa]', '0[G
Pa]'}, {'80[Gpa]', '0[GPa]'}, {'80[Gpa]'});
lib.mat.variables.alphavector2D={'2.6e-6[1/K]', '2.6e-6[1/K]', '2.6e-6[1/K]', '0[1/K]'};
lib.mat.variables.alphavector3D={'2.6e-6[1/K]', '2.6e-6[1/K]', '2.6e-6[1/K]', '0[1/K]', '0[1/K]', '0[1/K]'};
lib.mat.variables.rho='2330[kg/m^3]';
lib.mat{3}.name='Silicon (single-crystal)_1';
lib.mat{3}.varname='mat3';
lib.mat{3}.variables.Delatic2D={'166[Pa]', '64[Pa]', '64[Pa]', '0'}, {'166[Pa]', '64[Pa]', '0[Pa]
'}, {'166[Pa]', '0[Pa]'}, {'80[Pa]'});
lib.mat{3}.variables.Delatic3D={'166[Pa]', '64[Pa]', '64[Pa]', '0[Pa]', '0[Pa]', '0[Pa]'}, {'166[G
Pa]', '64[Pa]', '0[Pa]', '0[Pa]', '0[Pa]'}, {'166[Pa]', '0[Pa]', '0[Pa]', '0[Pa]'}, {'80[Gpa]', '0[GPa]',
'0[GPa]'}, {'80[Gpa]', '0[GPa]'}, {'80[Gpa]'});
lib.mat{3}.variables.alphavector2D={'2.6e-6[1/K]', '2.6e-6[1/K]', '2.6e-6[1/K]', '0[1/K]'};

```

```
lib.mat{3}.variables.alphavector3D={'2.6e-6[1/K]','2.6e-6[1/K]','2.6e-6[1/K]','0[1/K]','0[1/K]','0[1/K]','0[1/K]'};  
lib.mat{3}.variables.rho='2330[kg/m^3]';
```

```
fem.lib = lib;
```

```
% Multiphysics  
fem=multiphysics(fem);
```

```
% Extend mesh  
fem.xmesh=meshextend(fem, ...  
                    'linshape',[], ...  
                    'dofversion',1);
```

```
% Retrieve solution  
fem.sol=fbinary('sol1','solution',fbinaryfile);
```

```
% Save current fem structure for restart purposes  
fem0=fem;
```